NON-EQUILIBRIUM PHASE TRANSFORMATIONS IN CHARGE-DENSITY WAVE AND STRONGLY CORRELATED SYSTEMS STUDIED BY COHERENT FEMTOSECOND ELECTRON DIFFRACTION

By

Faran Zhou

A DISSERTATION

Submitted to
Michigan State University
in partial fulfillment of the requirements
for the degree of

Physics – Doctor of Philosophy

2019

ABSTRACT

NON-EQUILIBRIUM PHASE TRANSFORMATIONS IN CHARGE-DENSITY WAVE AND STRONGLY CORRELATED SYSTEMS STUDIED BY COHERENT FEMTOSECOND ELECTRON DIFFRACTION

By

Faran Zhou

By photo-exciting electrons in a material causing subsequent electron-electron and electron-phonon interactions, an energy landscape is created that is very different from that in thermal equilibrium. This distinction sets the baseline that photo-induced phase transitions (PIPT) could go through very different pathways compared with the thermally-induced phase transitions in equilibrium. This opens up a new dimension for complex materials research in non-equilibrium with ultrafast tools. In recent years, with the discovery of photo-induced superconductivity (SC) and other hidden quantum states, the study of these metastable and hidden phases in quantum materials has drawn intense interest in the ultrafast community.

With femtosecond electron diffraction, we have observed intriguing phenomena in a few charge-density wave (CDW) materials ($CeTe_3$, $ErTe_3$ and 1T-TaS_2) and iron chalcogenide systems (FeTe, $FeSe_{0.44}Te_{0.56}$ and FeSe). We explore the metastable hidden phases and observe universal dynamics in these materials far from equilibrium.

$CeTe_3$ exhibits uni-directional stripe CDW order in thermal equilibrium. Bi-directional CDW is thermodynamically forbidden. After femtosecond laser pulse excitation, the system is driven to a bi-directional order as it crosses a nonthermal fixed point. The new state is formed through associated symmetry changes that cause softening/hardening of CDW-related phonons. The CDW wavevector change proves that Fermi surface nesting (FSN)-enhanced electron-phonon coupling plays a central role in driving the CDW instabilities. Based on these results, we propose a nonthermal phase transition pathway in the non-

equilibrium phase diagram.

The work in $ErTe_3$ is one step further based on the $CeTe_3$ results. $ErTe_3$ is on the opposite side of the rare-earth tritelluride ($RETe_3$) series to host two orthogonal CDW orders at low temperature. Together with $CeTe_3$ data, the ultrafast results at various temperatures in $ErTe_3$ indicate that the system becomes more symmetric after laser excitation. Given the robustness of the data, the conclusion here may be extended to similar systems as well.

The generic features of CDW dynamics in 1T-TaS_2 are very similar to those in the quench dynamics of isolated quantum systems (e.g. cold atoms). After laser excitation, the system goes to the prethermalization plateau region before the thermalization stage. We find that both regimes follow universal scalings due to the existence of two nonthermal fixed points. Microscopically, we propose a chiral-symmetry-breaking mechanism that mediates the phase transformation. With a 2500 nm excitation laser, we emphasize the photo-doping, instead of the photo-thermal effect, in driving the phase transition. Due to the lack of thermal energy, the phase transition induced by the 2500 nm laser is more first order-like with faster switching speeds than 800 nm excitation. This high-speed switching with little thermal energy deposition holds promise for better future optoelectronic applications.

In FeTe, we directly observed the ultrafast structural transition by ultrafast electron diffraction (UED) for the first time. In the studies of optimally-doped compound $FeSe_{0.44}Te_{0.56}$, we observed the large-amplitude acoustic phonon excitations at right above the transition temperature T_c. While experiments with better spatial-temporal resolutions are needed, the acoustic phonon observed here might be important for SC in iron chalcogenide. In FeSe, we observed the laser-enhanced local stress that is known to be coupled to the nematic phase and superconductivity. Future UED experiments targeted for understanding the local stress would be very helpful.

To my family

ACKNOWLEDGMENTS

First of all, I would like to thank my advisor Prof. Chong-Yu Ruan for his guidance and support. He taught me how to do research and how to manage a project. I don't have much research experience before joining the group and learned significantly from Prof. Ruan over the years. I am grateful to him for all the guidance and encouragement.

My Ph.D. work can not be done without the collaboration and help of my lab colleagues. Tzong-Ru Han taught me most of the things in the lab when I first joined the group and he is also a great mentor to me in life. I also learned a lot from Zhensheng Tao and Kiseok Chang. Great thanks to my colleague Joseph Williams who I worked with for a few years and helped me a lot in the lab. Also thank other labmates that I worked with: Dr. Tianyin Sun, Dr. Yingjie Li, Dr. Shuaishuai Sun, Xiaoyi Sun, Alan McLean, Anna Turnbull, Daniel Bartles, Elliot Wozniak, and Nicholas Breslin, etc.

To my committee members who give me great advice on improving myself and finishing the Ph.D. program: Prof. Phillip Duxbury, Prof. Norman Birge, Prof. Pengpeng Zhang, Dr. Frederique Pellemoine. Also, I would like to thank my collaborators who contributed to my Ph.D. work in different ways. Thanks to Prof. Mercouri G. Kanatzidis and Dr. Christos D. Malliakas for providing us high quality samples for the experiments reported in chapters 3 to 5. Thank Prof. Zhiqiang Mao for providing the iron chalcogenides samples. Thank Prof. Nelson Sepulveda and David Torres for providing VO_2 thin film samples. Thank Prof. Alexander F. Kemper from North Carolina State University for the collaboration in $CeTe_3$ project. Thank Prof. Mohammad Maghrebi for the help in 1T-TaS_2 project. I would also like to thank Dr. Kai Sun from University of Michigan for his help in $CeTe_3$ measurements.

Dr. Reza Lolloee and Dr. Baokang Bi are of great help in teaching me how to use

various instruments and gives very helpful advice when I come into a problem in the lab. To the machine shop staff Tom Palazzolo, Tom Hudosn, Jim Muns and Rob Bennett for their friendliness and patience when I seek them for help. Also, thank Dr. Xudong Fan in the electron microscopy center for teaching me how to use TEM and giving me helpful advice. Barry Tigner from the electronics shop is the guy that I would first think of and turn to whenever I have anything related with electronics and he is always very patient to help. I am very grateful to Art Camire from Spectra Physics who taught me quite a lot in laser technology. I would also like to thank our secretaries for their support: Cathy Cords, Jessica Cords, Kim Crosslan.

To a lot of friends who supported me along the way and made my life more interesting: Xukun Xiang, Nan Du, Mengze Zhu, Jie Guan, Didi Luo, Xueying Huyan, Yanhao Tang, Dan Liu, Zheng Gu, Zixi Chen, Li Ke, Jun Zhang, Jie Yang, and many others.

On my personal side, I would thank my parents, uncle, grandma, and sisters for their unconditional love and support. I would not be me today without their consistent support and encouragement. I also thank my love Shanshan Wang who has been always on my side encouraging me and always has faith in me. I always owe them for not being able to be get together with them. Thank them all for their support and understanding.

Studying at MSU is a life-changing experience for me. I am so grateful to get to know so many colleagues and friends who have helped me along the way. Finally, sincere thank you to all of them.

TABLE OF CONTENTS

LIST OF TABLES

LIST OF FIGURES

KEY TO ABBREVIATIONS

Here are some abbreviations and acronyms that appear in this dissertation. The full name is shown in the first appearance of each abbreviation. For a better reading experience and ease of reference, the list of abbreviations used in this work are summarized below in alphabetical order.

AFM ..... Anti-ferromagnetic

ARPES..... Angle-resolved photoemission

BCS ..... Bardeen-Cooper-Schrieffer

BS ..... Beam splitter

BZ ..... Brillouin zone

CDW ..... Charge-density wave

DWF ..... Debye-Waller factor

EELS ..... Electron energy loss spectroscopy

FEL ..... Free electron laser

FO ..... Friedel oscillation

fs ..... Femtosecond

FS ..... Fermi surface

FT ..... Fourier transform

FWHM..... Full width at half maximum

IC ..... Incommensurate

IMT ..... Insulator to metal transition

KZM ..... Kibble-Zurek mechanism

MFT ..... Mean field theory

NC . . . . . Nearly-commensurate

PIPT . . . . . Photo-induced phase transition

PD . . . . . Photo diode

PT . . . . . Phase transition

QCP . . . . . Quantum critical point

RF . . . . . Radio-frequency

rms . . . . . Root mean square

RG . . . . . Renormalization group

RT . . . . . Room temperature

SC . . . . . Superconductivity

SSB . . . . . Spontaneous symmetry breaking

T_c . . . . . Critical temperature

TEM . . . . . Transmission electron microscopy

THG . . . . . Third harmonic generation

TMD . . . . . Transition metal dichalcogenides

UED . . . . . Ultrafast electron diffraction

UEM . . . . . Ultrafast electron microscopy

UHV . . . . . Ultra-high vacuum

WRT . . . . . With respect to

Chapter 1

Introduction

In modern physics, nearly all physical processes and phenomena can be explained under the framework of quantum mechanics. Although in many cases quantum effects can be approximated to classical descriptions on the macroscopic level, in recent years, more and more materials and exotic phenomena are discovered to exhibit effects that might only be explained quantum mechanically, such as unconventional superconductors, topological insulators, quantum spin liquids, etc. In many complex quantum materials, often referred to as strongly correlated electron systems, the interplays between charge, spin, orbital, and lattice degrees of freedom result in multiple competing ground states such as anti-ferromagnet, superconductor, and density waves.

By tuning the external parameters, phase transitions between different quantum phases can be realized. Instead of just tuning the system's temperature that usually causes thermal fluctuations, one can also manipulate the system in a nonthermal fashion by applying external pressure, magnetic field, or changing the electron density distribution by doping. Ultrafast excitation of the electron systems by intense femtosecond (fs) laser pulses could be another way of driving the system nonthermally under non-equilibrium conditions. In the past 3 decades, fs lasers have been developed to cover almost all the energy scales comparable to physical processes in condensed matter physics, varying from milli-electron-volt (meV) teraherz wave generation to tens of keV hard X-ray in the free-electron laser facili-

ties. The ultrafast laser holds a special position in studying quantum materials in that it can selectively excite certain modes or subsystems and also track, in real time, the subsequent order parameter evolution through the associated laser-based probes.

The work presented here focuses on understanding phase transitions between different symmetry-broken ground states in quantum materials and exploring the phase diagrams under non-equilibrium conditions. In these studies, we excite the systems with fs laser pulses and track the structural order parameter changes and associated instabilities by the ultrafast electron diffraction method.

In this chapter, the background and an overview of the complex quantum materials are given in Sec. 1.1. In Sec. 1.2, phase transition is first introduced based on simple Landau's theory. Then the development of renormalization group theory to address the limitations of the mean-field theory is discussed. We will also describe phase transitions under non-equilibrium, especially on photo induced phase transitions. In Sec. 1.3, a general theoretical description of charge-density wave (CDW) is formulated based on mean-field theory in the weak coupling limit.

1.1 Complex quantum materials

In condensed matter physics, complex quantum materials are a class of materials in which quantum effects are non-negligible due to strong electron-electron, electron-phonon, or spin-orbital interactions [17]. They include, but are not limited to superconductivity, ferro- and antiferromagnetism, charge- and spin-density waves, topological insulators, Weyl semimetal, Mott insulators, etc.

Due to the intricate interactions between different degrees of freedom in quantum mate-

rials, perturbations can suppress or enhance certain interactions or order. Above a certain threshold, phase transitions would occur between different quantum states. These occur via tuning of the control parameter and the phase transition could be either thermal (i.e. via temperature change) or nonthermal (e.g. through externally applied pressure, magnetic field, or doping).

For a thermally-induced phase transition, it is driven by the competitions between the interaction energies of the system and the entropy of its thermal fluctuations. By contrast, a nonthermal phase transition is achieved by varying other external parameters instead of temperature. More interestingly, there is a type of transition called *quantum phase transition* that happens at absolute zero temperature. Under this condition, thermal fluctuations are completely absent and the transition is purely driven by quantum fluctuations, which follow explicitly the Heisenberg uncertainty principle [2,17]. In the quantum phase transition, there is usually a interaction-mediated threshold at which the phase transition happens and this threshold at zero temperature is called the quantum critical point (QCP). Of course, the QCP is not accessible experimentally because it is at absolute zero temperature. But its influence extends way above zero temperature to a region above it usually referred to as the quantum critical region.

Fig. 1.1 provides an example schematic drawing of the phase diagram near a QCP [2]. The horizontal axis r is the nonthermal control parameter and the vertical axis is temperature. The solid line crosses the vertical axis at the transition temperature in a classical phase transition. With increasing r, the transition temperature is suppressed until all the way down to zero temperature at the critical threshold r_c at QCP. Above the QCP, the shaded area is the quantum critical region whose character is governed by both thermal and quantum fluctuations. It is widely believed that the quantum critical region and QCP hold the key

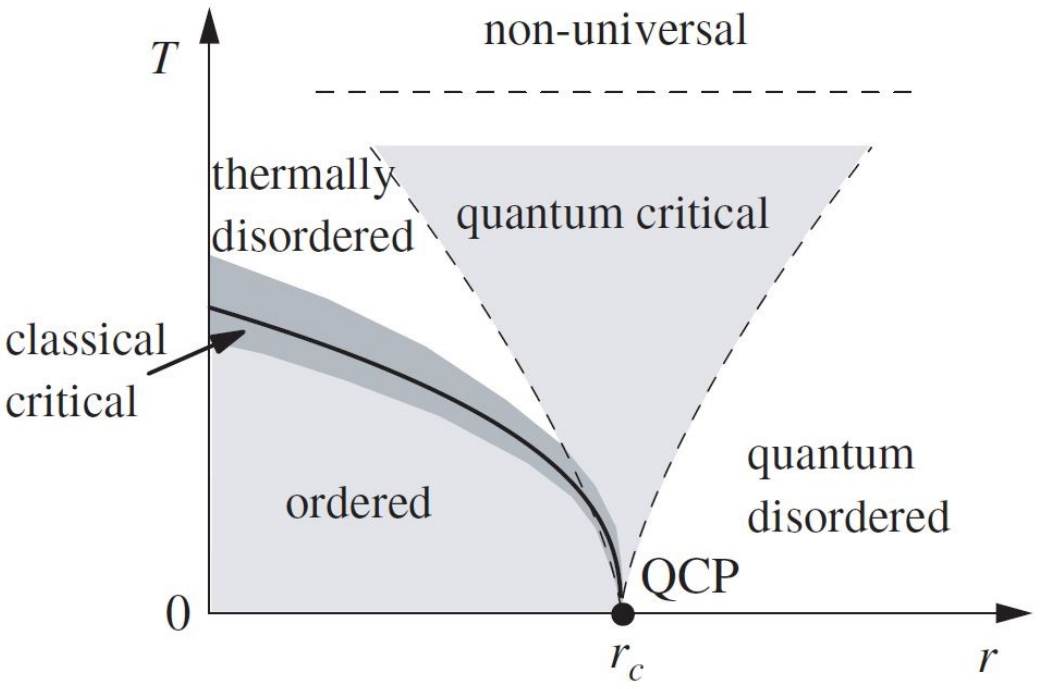

Figure 1.1: The schematic phase diagram near the quantum critical point. Adapted from Ref. [2].

to understanding these complex quantum materials.

Fig. 1.2 is another example of a general phase diagram of quantum materials, hosting high-temperature (high-T_c) superconductivity, adapted from Ref. [18]. In a phase diagram, for high-T_c cuprate superconductors, the unknown phase X usually exhibits the pseudogap character that competes with superconductivity.

1.2 Phase transitions

A phase transition is a transformation of a thermodynamic system from one state to another. The discontinuous jump in the thermodynamic behavior is indicative of a phase transition. Classification of phase transitions is the following: when there is a discontinuity in the first order derivative of the Gibbs free energy (i.e. a jump in entropy), it is called a *first order*

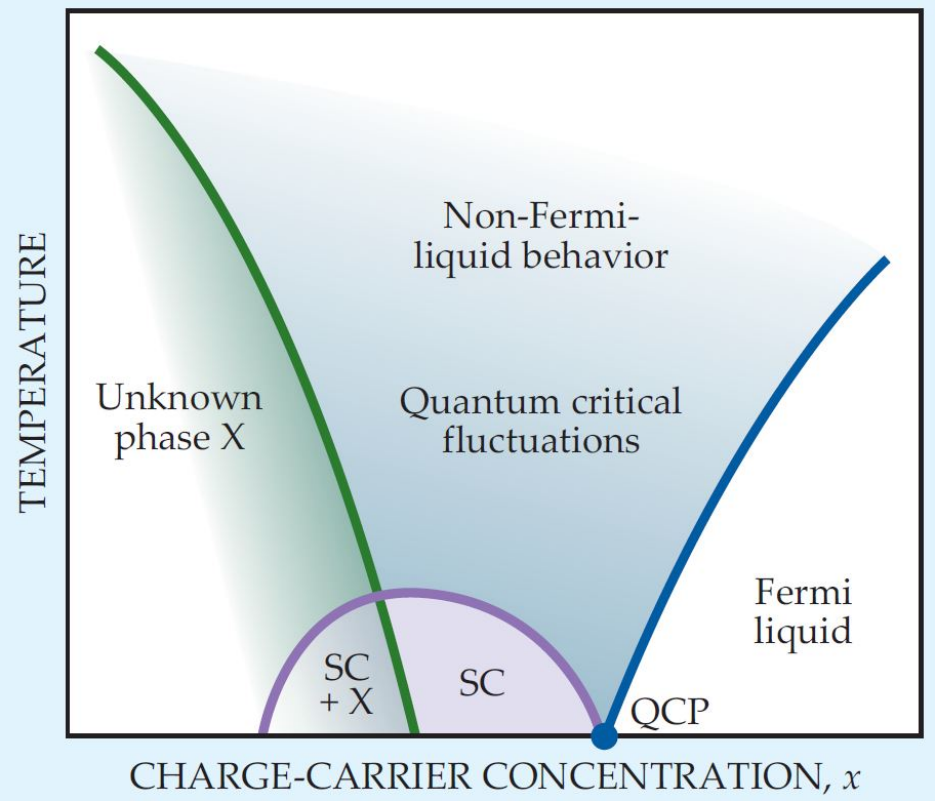

Figure 1.2: A generic phase diagram for high-T_c superconductors.

phase transition; when there is a discontinuity in the second order derivative of the Gibbs free energy (i.e. entropy is continuous but a jump in specific heat), it is called a *second order phase transition*, or a *continuous phase transition*. The position in the phase diagram where a continuous phase transition occurs is called the *critical point*.

Condensed matter physicists are dealing with systems that have atom numbers on the order of 10^{23}. Such complicated many-body systems consist of many small individuals interacting with each other. The many-body problem is generally very difficult to solve precisely except in some special cases like the one-dimensional (1D) Ising model. With *mean-field theory*, or mean-field approximations, the interactions from all other individuals on a specific individual are approximated by an averaged effect, thus reducing the many-body problem to a single-body problem. In condensed matter physics, mean-field theory (MFT)

is one of the most successful ideas that has applications in many contexts, for example the Ising model, the Landau's theory of phase transitions, and the Bardeen–Cooper–Schrieffer (BCS) theory.

Phase transitions are fascinating in that they involve changes in the atomic arrangements and also changes of the electronic parameters such as electronic density or magnetic moment. Ever since the development of thermodynamics, researchers have been trying to theoretically formulate, describe, or even predict phase transitions. In the late 19^{th} and early 20^{th} centuries, pioneering work on phase transitions was done by Johannes van der Waals, Pierre Curie, James Clerk Maxwell, Paul Ehrenfest, Ernst Ising, etc., all under the framework of MFT. Their work was typically related to transitions such as the gas-liquid transition, or the magnetic transition. In 1937 [19, 20], Landau realized many kinds of phase transitions are just manifestations of broken symmetries. He used the concept of *order parameter* to describe the extent of symmetry breaking: the order parameter is non-zero in the symmetry-broken phase and zero otherwise.

As we will show later on, Landau's theory is essentially a mean-field model, meaning that it treats the system as spatially uniform and no fluctuations exist. It was designed to predict behaviors near the critical point based on a free energy landscape, but ironically, near the critical point, fluctuations diverge and dominate the behavior of phase transitions. So Landau's theory of phase transitions can provide a qualitative but numerically inaccurate description near the critical point. It fails to explain the lack of phase transition in a finite system, or an infinite but 1D system. For example, independent of the dimensions of the systems or the interaction range, MFT always predicts a 1/2 critical exponent in order parameter change, which also contradicts many experimental observations. On the other hand, Landau's theory is mathematically simple and explains the general scaling and

universal behaviors of the seemingly very different types of transitions. It is typically the starting point in most textbooks that explain phase transitions.

Landau's theory does not specify which dimension it should be applied to. But as we know, the dimension of a system affects the number of the nearest neighbors. With increasing dimension, each particle has more nearest neighbors, thus more interaction constraints, so it is easier for them to line up. Effectively speaking, there is less freedom for fluctuations to play a role. Ginzburg's calculations show that if the dimension is below an upper critical dimension d_c, phase transition near the critical point is dominated by fluctuations and mean-field theory fails to predict correct critical exponents, which is a power-law evolution during phase transition. But when the dimension is greater than d_c, mean-field theory is self-consistent and predicts the precise scaling behavior. This is called the *Ginzburg criterion*. See Table 1.1, for the Ising model, O(n) model, and directed percolation model, the upper critical dimension d_c is 4 while for standard percolation d_c is 6.

To better understand and predict the scaling and universal behaviors near a phase transition, different approaches were tried and breakthrough happened in 1971 [21, 22], when Kenneth Wilson came up with an approach called *renormalization group*, in which he included many parameters and coupling terms and performed repeated renormalization transformations until a *fixed point* was reached. This fixed point is where the phase transition occurs. Wilson's renormalization group (RG) theory successfully predicted phase transitions and explained the critical phenomena that mean-field theory failed to do. But it is mathematically very complicated. Given that mean-field theory is mathematically simple and yet predicts qualitatively most of the critical behaviors of phase transition, in the Sec. 1.2.1, we first introduce Landau's theory.

1.2.1 Landau's theory of phase transitions

In Landau's mean-field theory of phase transitions, the order parameter is built on the macroscopic quantity that is zero on the high temperature side, but non-zero on the lower temperature side of the phase transition. For example, for the ferromagnetic to paramagnetic transition, the order parameter is magnetization; for the gas-liquid-solid transition, the order parameter is usually the density difference; for the orthorhombic-to-tetragonal structural transition, the order parameter is the difference between two lattice constants.

When it is near a phase transition, the order parameter is usually small so one can perform power expansion on the free energy with respect to (WRT) the order parameter Ψ. The free energy f has the following expression

$$f(\Psi, T) = f_0(T) + a_1(T)\Psi + \frac{1}{2}a_2\Psi^2 + \frac{1}{3}a_3\Psi^3 + \frac{1}{4}a_4\Psi^4 + \frac{1}{5}a_5\Psi^5 + \frac{1}{6}a_6\Psi^6 + ... \qquad (1.1)$$

where $f_0(T)$ is free energy for the high-temperature state; a_0, a_1, etc., are the coefficients. The values of both coefficients a_n and order parameter Ψ depend on temperature (T).

To have a stable state, free energy requires minimum(s). Mathematically, this means the following two conditions have to be met:

(1), The first derivative of f WRT to Ψ is zero:

$$\frac{\partial f(\Psi, T)}{\partial \Psi} = a_1 + a_2\Psi + a_3\Psi^2 + a_4\Psi^2 + a_5\Psi^4 + a_6\Psi^5 + ... = 0. \qquad (1.2)$$

(2), The second derivative of f WRT to Ψ is larger than or equal to zero:

$$\frac{\partial^2 f(\Psi, T)}{\partial \Psi^2} = a_2 + 2a_3\Psi + 3a_4\Psi^2 + 4a_5\Psi^3 + 5a_6\Psi^4 + ... \geq 0. \qquad (1.3)$$

At a high temperature where $\Psi = 0$, the system is a stable state, so $\frac{\partial f(\Psi=0,T)}{\partial \Psi} = a_1 = 0$. This means the linear term cannot exist in the expansion series. Another obvious conclusion to make is the highest order of the expansion must be an even number. If it is an odd number, *f(Ψ, T)* would go to $-\infty$ as Ψ goes to $-\infty$ or $+\infty$. This condition yields no stable state globally. For the same reason, the coefficient for the highest even order should be positive and the highest order in the expansion should be the 4^{th} order or higher. Next we will consider two classical forms of the expansion to the 4^{th} and 6^{th} orders, respectively:

$$f(\Psi, T) = f_0(T) + \frac{1}{2}a_2\Psi^2 + \frac{1}{4}a_4\Psi^4, \tag{1.4}$$

and

$$f(\Psi, T) = f_0(T) + \frac{1}{2}a_2\Psi^2 + \frac{1}{4}a_4\Psi^4 + \frac{1}{6}a_6\Psi^6. \tag{1.5}$$

In Eq. 1.4, where $a_4 > 0$, the free energy has the forms as illustrated in Fig. 1.3.

When $a_2 > 0$, the system is convex and there is only one minimum at $\Psi = 0$. But when a_2 becomes negative, the original minimum at $\Psi = 0$ is no longer the minimum of the free energy, so the system would spontaneously move to new minimum positions. This process is also called *spontaneous symmetry breaking* (SSB).

To a first order approximation, a_2 can be written as $a_2 = a_2^0(T - T_c)$, where a_2^0 is a positive constant; T_c refers to the critical temperature. So

$$\frac{\partial f(\Psi, T)}{\partial \Psi} = a_2\Psi + a_4\Psi^3 = \Psi[a_2^0(T - T_c) + a_4\Psi^2] = 0. \tag{1.6}$$

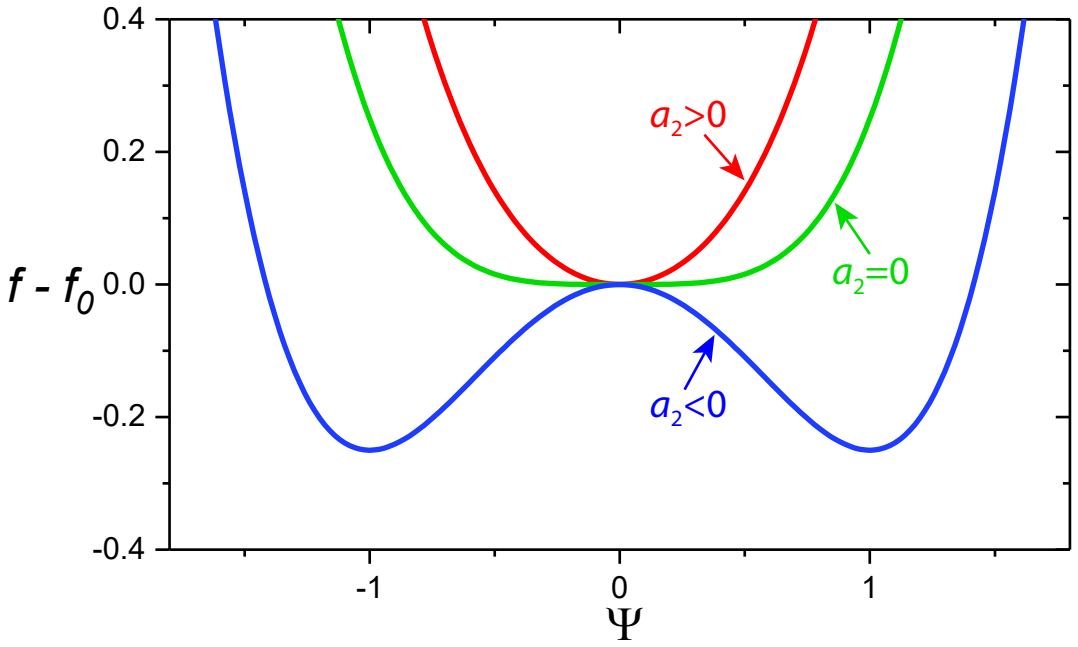

Figure 1.3: The profiles of free energy as a function of the order parameter at different a_2 values.

The solution for Eq. 1.6 is

$$\Psi = \begin{cases} \pm\sqrt{\frac{a_2^0(T_c - T)}{a_4}}, & T < T_c \\ 0, & T \geq T_c. \end{cases} \tag{1.7}$$

The evolution trend for Ψ is shown in Fig. 1.4. Below T_c, Ψ is continuously approaching the critical point with the exponent of 1/2; above T_c, there is no jump in the order parameter so the expression in Eq. 1.4 corresponds to a second order transition.

Plugging the solution in Eq. 1.7 to the free energy terms in Eq. 1.4, we can get free energy expression wrt temperature only. With this free energy form, other parameters, such as entropy, latent heat, specific heat, etc., can be readily obtained. It is easy to show that for a second order phase transition, entropy is continuous across the phase transition so the latent heat is zero.

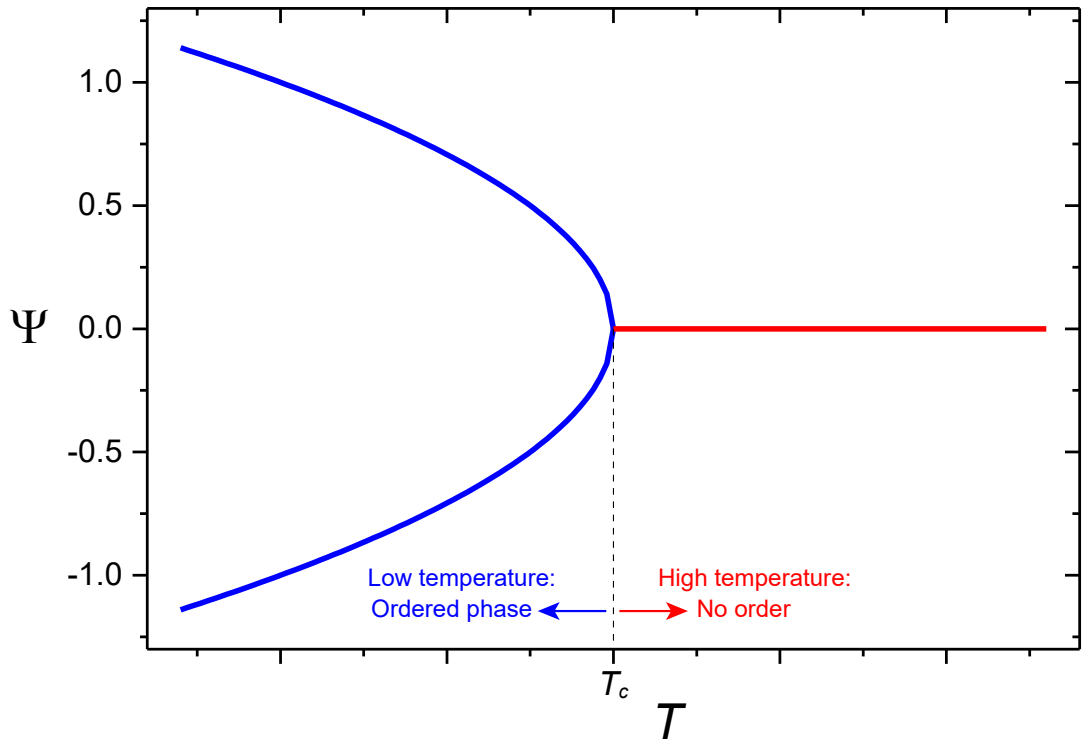

Figure 1.4: The order parameter Ψ evolution as a function of temperature T, at both below and above T_c

We have shown the 1/2-scaling behavior of the order parameter near a phase transition. Next, we will consider applying a magnetic field B during, for example, a paramagnetic-to-ferromagnetic transition. Here, the free energy has an additional magnetic field term compared to Eq. 1.4

$$f(\Psi, T) = f_0(T) + \frac{1}{2}a_2^0(T - T_c)\Psi^2 + \frac{1}{4}a_4\Psi^4 - \Psi B. \tag{1.8}$$

Similarly, to minimize the free energy, its first derivative wrt to Ψ is zero

$$\frac{\partial f(\Psi, T)}{\partial \Psi} = a_2^0(T - T_c)\Psi + a_4\Psi^3 - B = 0. \tag{1.9}$$

Since Ψ is small near the critical point, we can ignore the Ψ^3 term. Then the order parameter becomes

$$\Psi = \frac{B}{a_2^0(T - T_c)}. \tag{1.10}$$

As mentioned, in a paramagnetic-to-ferromagnetic transition, Ψ usually corresponds to the magnetic moment. So the magnetic susceptibility would have the following form

$$\chi = \frac{\Psi}{B} = \frac{1}{a_2^0|T - T_c|}. \tag{1.11}$$

The magnetic susceptibility χ diverges at $T = T_c$ and on either side of phase transition, its decay follows power of - 1, as shown in Fig. 1.5.

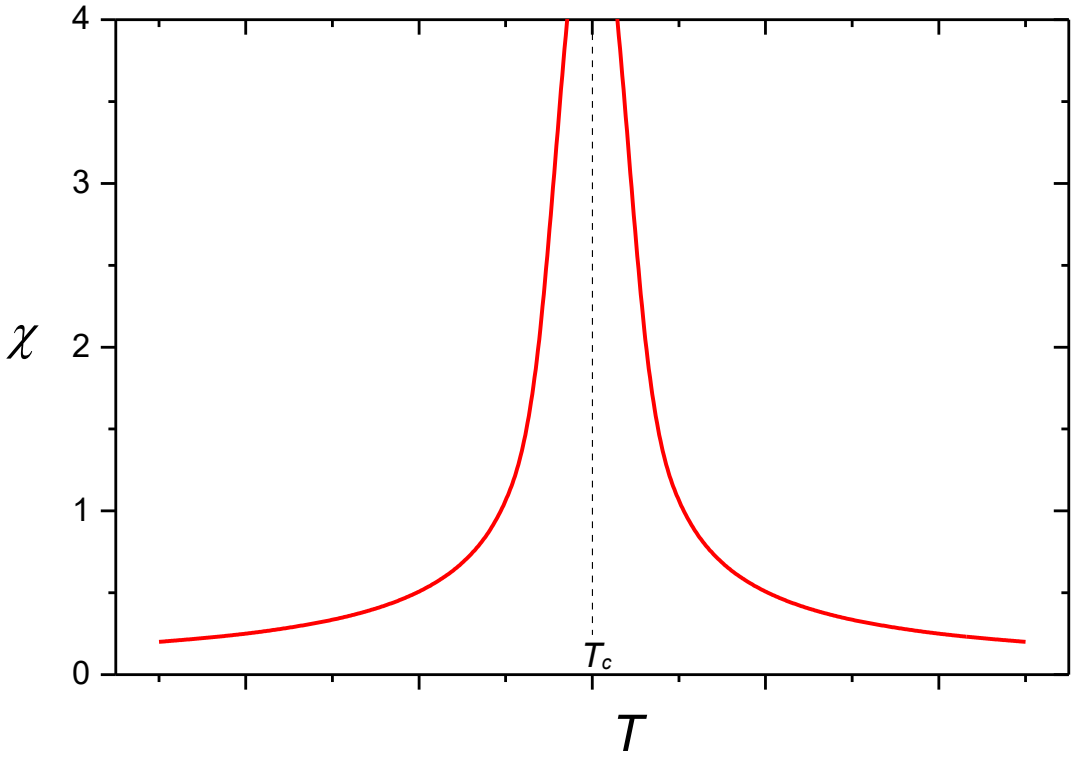

Figure 1.5: The magnetic susceptibility χ evolution as a function of temperature near the critical point. On both sides of T_c, χ is inversely proportional to the distance from T_c and diverges at T_c.

For a second order phase transition, the critical scaling behavior is demonstrated from order parameter and the divergence in susceptibility. But for a first order transition, which, as we will show later, takes the form of Eq. 1.5, where there is no such scaling behavior due to the jump in the order parameter. We take first derivative of Eq. 1.5 wrt Ψ to minimize the free energy

$$\frac{\partial f(\Psi, T)}{\partial \Psi} = a_2^0(T - T_c)\Psi + a_4\Psi^3 + a_6\Psi^5 = 0. \tag{1.12}$$

The solution for this is

$$\Psi^2 = \begin{cases} \frac{-a_4+\sqrt{a_4^2-4a_6a_2^0(T-T_c)}}{2a_6}, & T < T_c \\ 0, \frac{-a_4+\sqrt{a_4^2-4a_6a_2^0(T-T_c)}}{2a_6}, & T_c < T < T_1 \\ 0, & T > T_1, \end{cases} \tag{1.13}$$

where $T_1 = \frac{a_4^2}{4a_2^0a_6} + T_c$, $a_2^0 > 0, a_4 < 0, a_6 > 0$.

The temperature dependence of the order parameter Ψ is plotted in Fig. 1.6.

As we can see from the plot, there is a jump in the order parameter at the phase transition. It is easy to show that there is also a jump in the entropy curve, so the latent heat is nonzero for a first order phase transition. Due to the existence of latent heat, first order transitions are harder to study/formulate than second order. This is because Landau's theory is based on power-law expansion. It is thus a question of whether the expansion method would work well for a first order transition, when the order parameter is not necessarily small enough for power expansion near T_c. So in the following sections we will focus on second order transitions.

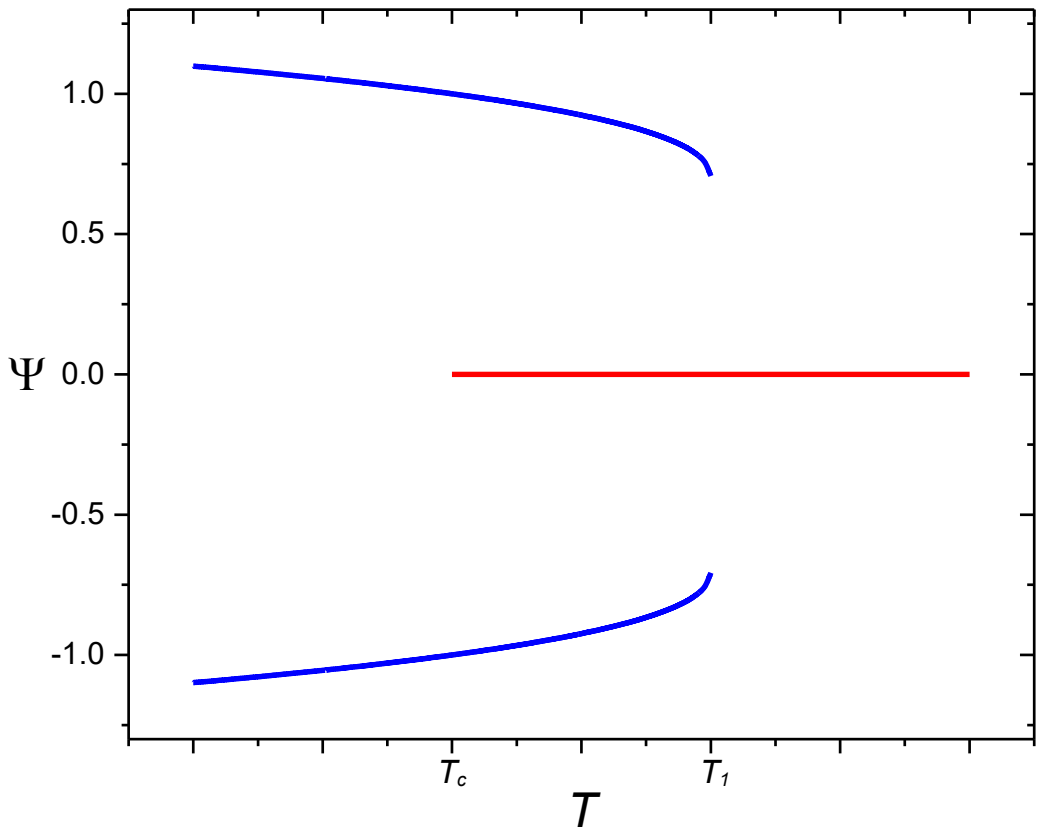

Figure 1.6: The order parameter evolution as a function of temperature for first-order phase transition near T_c. Cooling from high temperature, the system follows the red curve until $T = T_c$ where it becomes unstable and phase transition will happen. The system jumps to one of the blue curves. If the system is heated from low temperature, then the system would remain on the blue curve until $T = T_1$, after which it jumps to the red curve and phase transition occur.

1.2.2 From mean-field theory to renormalization group

In the previous section, we discussed how Landau used a simple formulation to explain the critical phenomena and the universality of different phase transitions. His theory is general, simple, and elegant in many ways. But as we mentioned, it can only give a qualitative but not quantitative description of phase transitions, especially for the critical scaling.

Landau's theory predicts a universal critical exponent of 1/2, independent of the interactions or dimension of the system. But this is not always true experimentally and also

conflicts with other theories. For example, in 1945, E. A. Guggenheim summarized different types of gas-liquid transitions [23] and fitted the universal critical exponent to be 1/3 instead of 1/2.

When studying magnetic transitions, one usually refers to the Ising model. By solving the 2D Ising model [24, 25], the critical exponent is determined to be 1/8. For 3D, it is determined to be about 0.33. The critical exponents for both 2D and 3D Ising models disagree with the MFT.

Another aspect is that MFT predicts a discontinuous but finite jump in specific heat. But experimentally, for example in reference [26], the authors studied the normal-superfluid transition in He^4 and liquid-vapor transition of He^3 and He^4, where the specific heat is observed to have singularities and divergent behaviors near the critical points.

The validity of MFT is constrained by the Ginzburg criterion, which states that mean-field theory is self-consistent and valid only for dimensions greater than d_c. So for experiments in system whose dimension is below d_c, MFT can not predict the precise scaling behaviors.

Critical scaling means that the system appears the same at different scales (the so-called self-similarity or scale invariance). Consider a 2D spin system, each spin interacts with its nearest neighbors with certain coupling J at temperature T. The physics of this system is described by Hamiltonian $H(T, J)$. Then we divide the 2D lattice into 2x2 blocks and try to describe the system in terms of the blocks instead of individual spin. We assume the block variables are described by Hamiltonian with different temperature and coupling: $H(T', J')$. Originally we may have too many problems and degrees of freedom, now with the "block spin" method [27], in the renormalized problem we have only 1/4 of them. By doing another iteration, we will reduce the problem down to 1/16 of the original value. With each RG step, we are increasing the observable scale and decreasing the degrees of freedom. This iteration

process is equivalent of finding the long range behavior of RG transformation from (T, J) to (T', J'), (T', J') to (T'', J''), etc. Often, when iterated enough times, the RG transformation will lead to a certain number of *fixed points*. For a magnetic system, the coupling term J has a tendency of aligning neighboring spins while the temperature term T tends to disorder the spins. For many models of this kind, there are three fixed points:

1. $T = 0$ and $J \to \infty$, meaning that disorder disappear and the spin system is aligned in the large scale. This is the ferromagnetic phase.

2. $T \to \infty$ and $J = 0$, meaning that the high temperature and disorder dominate. This is the so-called paramagnetic phase.

3. $T = T_c$ and $J = J_c$. At this point, changing scales does not change the properties of the system and the system is in a self-similar or fractal state. It corresponds to the critical point at a Curie ferromagnetic to paramagnetic phase transition.

This block spin idea was brought up by Leo Kadanoff in 1966 [27] whereas the fixed point concept was Kenneth Wilson's genius idea to bridge RG with phase transitions [21,22]. Wilson considered many couplings in a system in repeated RG transformations. Each transformation increases the size of length scale and the phase transition would occur when the transformation is brought to a fixed point. That is, after enough transformations, the couplings will not further modify the system and the system becomes scale-invariant. Furthermore, the correlation length remains unchanged under transformations at the fixed point. Wilson pointed out two ways of stabilizing the correlation length: for a continuous phase transition, correlation length is infinite at the critical point; for a first order phase transition, correlation length is finite, reflecting that the local interactions drive the phase transition.

To generalize the RG theory to phase transitions, in 1972, K. Wilson worked with M. Fisher [28] to apply the RG theory on a system that has dimension of $d = 4 - \epsilon$ to calculate

the critical exponents. This method, later known as epsilon-expansion, was generalized not just to small ϵ but also to three dimensions and beyond.

Regarding critical scaling near the critical point, we have mentioned the scaling of the order parameter, susceptibility and specific heat based on Landau's theory of phase transitions. Next we will summarize the key scaling orders and scaling exponents in 2D and 3D Ising models. Following conventions in this field, we define parameters as follows:

Ψ: order parameter. It can be density for liquid-gas transition, or magnetization for paramagnetic to ferromagnetic transition

τ: reduced temperature, $\tau = \frac{T-T_c}{T_c}$, distance away from the critical point

f: free energy

C: specific heat, $C = -T\frac{\partial^2 f}{\partial T^2}$

J: source field, it could be magnetic field, reduced chemical potential, or pressure, etc.

χ: susceptibility, compressibility, etc., $\chi = \frac{\partial \Psi}{\partial J}$

ξ: correlation length

d: spatial dimension of a system

$\langle \psi(\overrightarrow{x})\psi(\overrightarrow{y})\rangle$: the correlation function

r: spatial distance

Then, there will be the following scaling relations:

$$\Psi \propto |\tau|^{\beta}, \text{for } \tau < 0 \text{ only; } \Psi = 0 \text{ when } \tau \geq 0, \tag{1.14}$$

$$\xi \propto |\tau|^{-\nu}, \tag{1.15}$$

$$\chi \propto |\tau|^{-\gamma}, \tag{1.16}$$

$$C \propto |\tau|^{-\alpha}, \tag{1.17}$$

$$J \propto \Psi^{\delta}, \tag{1.18}$$

$$\langle \psi(\overrightarrow{x})\psi(\overrightarrow{y})\rangle \propto r^{-d+2-\eta}. \tag{1.19}$$

From Eq. 1.14 to Eq. 1.19, there are 6 critical exponents shown in the scaling powers: $\alpha,\ \beta,\ \gamma,\ \delta,\ \nu,\ \eta$. Due to the confinements and definition of the physical parameters, the critical exponents have the following scaling relations (Note: the relations apply for $d < d_c$, where d_c is the upper critical dimension; above d_c, some of the exponents are no longer spatial dimension-dependent and some of the relations will no longer hold):

$$\nu d = 2 - \alpha = 2\beta + \gamma = \beta(\delta + 1) = \gamma\frac{\delta + 1}{\delta - 1} = \frac{\gamma d}{2 - \eta}. \tag{1.20}$$

Therefore, for a $d-$dimension system, of the 6 critical exponents $(\alpha, \beta, \gamma, \delta, \nu, \eta)$, only two of them are independent. These exponents are universal in a sense that they only depend on the *spatial dimension d* and the *type of model* used. Systems very different from each other could share a set of critical exponents and such systems together are said to belong to the same *universality class*.

Table 1.1 is a summary of critical exponents for some well-known models at different dimensions. In the table, the O(n) model is also called n-vector model. It is a generalization of the Ising model, XY model, and Heisenberg model. The majority of these models are calculated based on RG theory which laid the foundation for quantum field theory in particle physics and the theory of continuous phase transition in condensed matter physics.

Model/Class	d	α	β	γ	δ	ν	η	**Ref.**
Mean-field	all d	0	1/2	1	3	1/2	0	[19,29]
2D Ising	2	0	1/8	7/4	15	1	1/4	[24,25]
4D Ising	4	0	1/2	1	3	1/2	0	[30]
Self-avoiding walk/ O(0)	3	0.2350	0.3024	1.1596	4.8347	0.5882	0.0284	[31]
3D Ising / O(1)	3	0.1090	0.3258	1.2396	4.8048	0.6304	0.0335	[31]
XY model / O(2)	3	- 0.011	0.3470	1.3169	4.7951	0.6703	0.0354	[31]
Heisenberg / O(3)	3	- 0.122	0.3662	1.3895	4.7944	0.7073	0.0355	[31]
O(4)	3	- 0.223	0.3830	1.456	4.8016	0.7410	0.0350	[31]
Standard percolation	1	1	0	1	∞	1	1	[32]
Standard percolation	2	- 2/3	5/36	43/18	91/5	4/3	5/24	[33]
Standard percolation	3	- 0.616	0.4050	1.8050	5.4593	0.8720	- 0.070	[34]
Standard percolation	4	- 0.712	0.6390	1.4350	3.2441	0.6780	- 0.120	[34]
Standard percolation	5	- 0.855	0.8350	1.1850	2.4192	0.5710	- 0.075	[34]
Standard percolation	≥ 6	- 1	1	1	2	1/2	0	[32]
Directed percolation	1	0.1595	0.2765	2.2777	0.1595	1.0969	0.3137	[35]
Directed percolation	2	0.4505	0.5834	1.5950	0.4505	0.7330	0.2295	[36]
Directed percolation	3	0.7320	0.8130	0.7320	1.2370	0.5840	0.1200	[37]
Directed percolation	≥ 4	- 1	1	1	2	1/2	0	[38]

Table 1.1: Critical exponents for different models at different dimensions. References are included in the last column for different models. For cell values that are integer or fraction, they come from exact solutions. For cells with decimal values, they usually come from RG based field theory methods.

1.2.3 Systems driven far from equilibrium and photo-induced phase transitions

Thus far the phase transitions are discussed under equilibrium conditions. But everything in nature is moving, interacting, or evolving even in equilibrium state. Much less is understood about phase transitions for systems driven out of equilibrium, both theoretically and experimentally.

Generally, dynamical systems can be classified into several categories based on whether the order parameter is conserved or not, the dimensionality, and symmetry of the system. Table 1.2 shows such classification of currently known dynamical models treated by the RG method (from Ref. [1]).

It is generally believed that many concepts and techniques used in describing the equilibrium phase transitions, such as scaling and universality, can still be applied to the non-equilibrium dynamical systems. Systems of the the same universality class share the same scaling exponents and sometimes even the same scaling function. However, non-equilibrium systems have an additional degree of freedom: time. Not only does this gives more freedom for expressing universality, it also allows one to actively manipulate and predict the behavior of the systems following universal dynamics. In terms of the universality and scaling, besides the aforementioned 6 static critical exponents (2 independent exponents), there are additional critical exponents for the non-equilibrium systems defined as below.

The divergences of the relaxation time τ and correlation length ξ are related by the dynamical exponent z

$$\tau \propto \xi^z. \tag{1.21}$$

The dynamical exponent z can also be defined as the ratio of the temporal ($\nu_{||}$) and spatial

Model	**No.**	**System**	D	**N.C. fields**	**Cons. fields**	**Non-vanishing Poisson bracket**
Relaxational	A	Kinetic Ising anisotropic magnets	n	Ψ	None	None
Relaxational	B	Kinetic Ising uniaxial ferromagnet	n	None	Ψ	None
Relaxational	C	Anisotropic magnets structural transition	n	Ψ	m	None
Fluid	H	Gas—liquid binary fluid	1	None	Ψ, j	$\{\Psi, j\}$
Symmetric planar magnet	E	Easy-plane magnet, $h_z = 0$	2	Ψ	m	$\{\Psi, m\}$
Asymmetric planar magnet	F	Easy-plane magnet, $h_z \neq 0$, superfluid helium	2	Ψ	m	$\{\Psi, m\}$
Isotropic antiferromagnet	G	Heisenberg antiferromagnet	3	Ψ	m	$\{\Psi, m\}$
Isotropic ferromagnet	J	Heisenberg ferromagnet	3	None	Ψ	$\{\Psi, \Psi\}$

Table 1.2: Classification of non-equilibrium dynamical systems based on alphabetical order [1]. In the first row title line, the "No." refers the designation of alphabet for each model. "D" is the dimension of the system. "N.C. fields" represents the non-conserved fields. "Cons. fields" represents "conserved fields".

($\nu_\perp$) correlation length exponents: $z = \nu_{||}/\nu_\perp$.

To describe the two-time correlations in a spin system $\{s_i\}$ of size L relaxing to the

critical state from a disordered initial condition, another dynamical exponent λ is needed

$$A(t,0) = \frac{1}{L^d}\langle \sum_i s_i(0)s_i(t)\rangle \propto t^{-\lambda/z}. \tag{1.22}$$

Persistence exponent θ is introduced by Derrida *et al* in Ref. [39] to describe a quench to the critical point. The probability $p(t)$ that the local or global order parameter does not change sign at time t after the quench follows a power-law: $p(t) \propto t^{-\theta}$.

Of the several dynamical critical exponents, z is the most common and widely discussed. The same universality classes share the same critical exponents. For example, in the Ising model of model A dynamics, dynamic exponent z is around 2 for all dimensions [40]. With dynamic exponent z, the relaxation time τ diverges as the system approaches the critical point. This is usually called *critical slowing down*. Critical slowing down enforces a local choice of the broken symmetry and leads to the formation of topological defects [41].

One classical example of non-equilibrium dynamics is the relaxational dynamics after quenching the system from a homogeneous phase to a broken-symmetry phase. The phase ordering kinetics can be understood in terms of domain coarsening processes, in which the domain size grows with time following the relation: $L(t) \propto t^{1/z}$. Such a dynamical process involving spontaneous symmetry breaking (SSB) was studied in cosmology in the 1970s and also in condensed matter physics. According to Tom W. B. Kibble [42, 43], right after the "big bang", the universe is in a high-temperature "normal" phase with high symmetry. Then the universe expands and cools down and at a certain point when the temperature drops below the transition temperature T_c, the symmetry is spontaneously broken and domains are expected to form. Under certain conditions, the universe is expected to form domain walls, cosmic strings, or "monopoles", all of which are called topological defects. The evolution of

the universe can be understood in such a way that it is similar to phase transitions in condensed matter physics. For example, in a paramagnetic-to-ferromagnetic phase transition, it also involves SSB and formation of domains.

To quantitatively investigate the effects of topological defects on structural evolution, Wojciech H. Zurek studied the domain coarsening process in the context of dynamical scaling [44, 45]. The defined criticality is by a reduced temperature ϵ: $\epsilon = \frac{T_c - T}{T_c}$, where T_c is the critical temperature and T is system temperature. As discussed earlier, near critical point, the equilibrium correlation length and relaxation time τ diverge: $\xi = \frac{\xi_0}{\epsilon^{\nu}}, \tau = \frac{\tau_0}{\epsilon^{z\nu}}$. Now consider a linear (in time) quench that drives the system across the critical point. When the system is far away from the critical point, the relaxation time is small and system can catch up with the quench, so the dynamics is adiabatic. On the other hand, when the system is close to the critical point, dynamics become almost frozen due to divergence of the relaxation time in critical slowing down, the adjustment of the system is unable to catch up with the quench. Such a non-adiabatic time is called *Kibble-Zurek freeze-out time*.

Near the critical point, the reduced temperature $\epsilon(t)$ is written linear with respect to time

$$\epsilon(t) = \frac{t}{\tau_Q}, \tag{1.23}$$

where τ_Q is the quench period. The process starts at negative time. At time-zero, $\epsilon(0) = 0$ and it is at critical point. To estimate the Zurek freeze-out time, the relaxation time is equal to the time elapsed (t)

$$\tau(\epsilon(t)) = \frac{\tau_0}{\epsilon(t)^{z\nu}} = \tau_0 (\frac{t}{\tau_Q})^{-z\nu} = t. \tag{1.24}$$

With this, we can estimate the freeze-out time (t_{KZ}) to be

$$t_{KZ} = (\tau_0 \tau_Q^{z\nu})^{\frac{1}{1+z\nu}}. \tag{1.25}$$

Correspondingly, the order parameter at this non-adiabatic-to-adiabatic transition is

$$\epsilon_{KZ} = \epsilon(t_{KZ}) = (\frac{\tau_0}{\tau_Q})^{\frac{1}{1+z\nu}}. \tag{1.26}$$

The corresponding correlation length at ϵ_{KZ} is

$$\xi^{KZ} = \xi(\epsilon_{KZ}) = \xi_0(\frac{\tau_Q}{\tau_0})^{\frac{\nu}{1+z\nu}}. \tag{1.27}$$

With this correlation length, the density of topological defects is estimated to be

$$n \sim \frac{\xi_{KZ}^d}{\xi_{KZ}^D} = \frac{1}{\xi_0^{D-d}}(\frac{\tau_0}{\tau_Q})^{(D-d)\frac{\nu}{1+z\nu}}, \tag{1.28}$$

where D and d are dimensions of the system and defects, respectively. The results above from Eq. 1.25 to Eq. 1.28 are the main predictions by theory, which is frequently referred to as the so-called *Kibble-Zurek mechanism* (KZM). KZM can be experimentally tested by examining whether the defect density follows the scaling law described in Eq. 1.28.

Photo-induced phase transitions (PIPT), by definition, are phase transitions initiated by laser pulses and typically involve non-equilibrium, non-thermal processes. After laser excitations, the system is initially driven far from equilibrium then relaxes. The relaxation process could exhibit scaling behaviors that can be described with different universality classes. Fig. 1.7 is an example of PIPT from Ref. [3], in which the authors performed transient fs optical

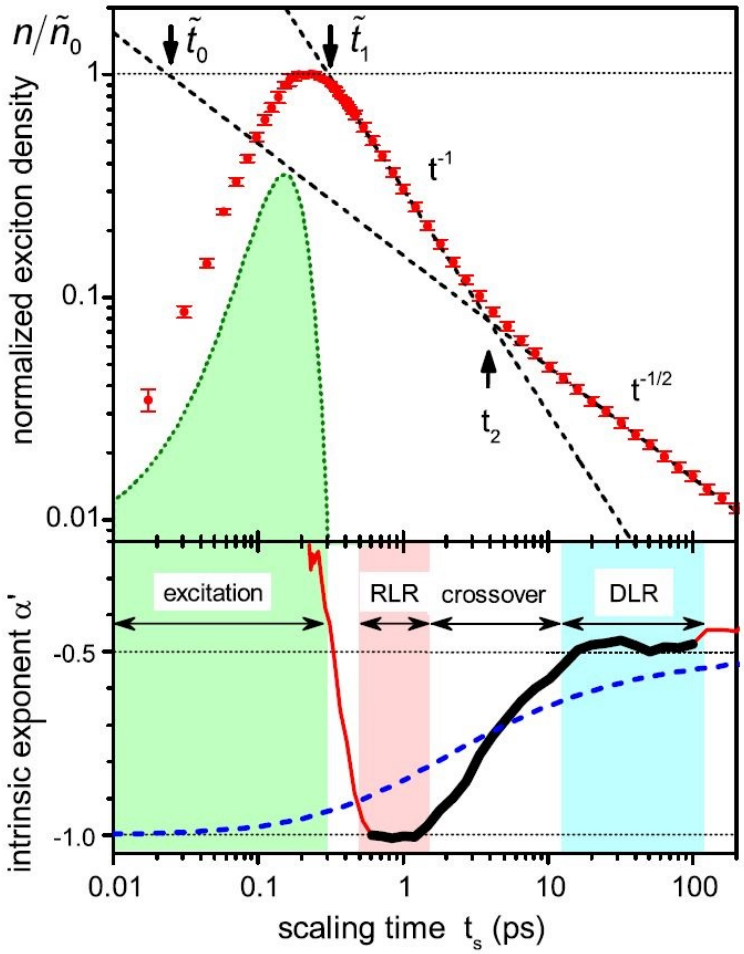

Figure 1.7: The evolution of the exciton density observed in photo-excited carbon nanotubes [3]. In the log-log plot, the system switches from a - 1 power-law decay to a - 1/2 exponent, indicating a transition from the reaction-limited regime (RLR) to diffusion-limited regime (DLR).

transmission measurements on carbon nanotubes and determined the power-law decay of the exciton density. It is found that the exciton-exciton recombination process switches from the reaction-limited to a diffusion-limited process, belonging to different universality classes.

1.3 Charge-density wave

Charge-density wave (CDW) is a symmetry-broken ground state of metals and its formation has been usually described by Fermi surface nesting that enhances electron-phonon coupling.

At the wave-vector of the CDW, the translational symmetry is broken and the charge-density system is characterized by periodic modulation, which couple to the lattice in terms of periodic lattice distortion.

The idea of CDW was first proposed by Rudolf Peierls [46] in 1955 via a mechanism later know as Peierls transition. When Peierls was studying an ideal 1D atomic chain, he found that a one-dimensional metallic chain is intrinsically unstable at low temperatures: the electrons prefer to open up a gap at the Fermi surface (FS) and atomic ions will periodically distort to form a new symmetry-broken ground state. Such a state is called the charge-density wave state and the transition is called the *Peierls transition*.

Due to the formation of CDW, the phonon spectrum is strongly renormalized. At the wave-vector of the CDW, the phonon is frozen into a static atomic distortion. In 1959, Walter Kohn [47] proposed that in the phonon dispersion relation for a metal, the frequency of the phonon at specific wave-vector is lowered when there is a discontinuity in the derivative of phonon dispersion relations. Such a phenomenon is called *Kohn anomaly*. The CDW state is an extreme case of a Kohn anomaly with phonons softened to zero frequency.

Experimentally, CDWs were first found in a 1D conductor compound $K_2Pt(CN)_4Br_{0.30x}H_2O$ [48] by X-ray diffraction in 1973. In the following several years, CDWs were found in the 1D charge-transfer organic salt tetrathiafulvalene-tetracyanoquinodimethane (TTF-TCNQ) [49], blue bronze $K_{0.3}MoO_3$ [50], transitional metal tri-chalcogenide $NbSe_3$ [51], and also in two-dimensional (2D) layered compounds [52, 53].

According to Peierls' theory, CDW formation usually happens in low dimensional materials or materials with very high anisotropy. In the following part of this section, the simplest and most classical theoretical description of CDW will be formulated based on a 1D metallic atomic chain.

1.3.1 One-dimensional electron gas

One-dimensional (1D) electron gas refers to electrons arranged in a 1D array. Consider such a system with length of L, the Fermi energy is given by

$$\epsilon_F = \frac{\hbar^2 k_F^2}{2m_e}, \tag{1.29}$$

where m_e is electron mass and k_F is the Fermi wave-vector, $k_F = \frac{N_0 \pi}{2L}$.

The electron density ρ changes in the presence of an external potential ϕ, such that

$$\rho(\vec{q}) = \chi(\vec{q})\phi(\vec{q}), \tag{1.30}$$

where $\chi(\vec{q})$ is the electronic susceptibility defined by Lindhard response function

$$\chi(\vec{q}) = \int \frac{1}{(2\pi)^d} \frac{f_k - f_{k+q}}{\epsilon_k - \epsilon_{k+q}} d\vec{k}, \tag{1.31}$$

where $f_k = f(\epsilon_k)$ is the Fermi function, d is dimension of the system [54].

For 1D electron gas, the dispersion relation near the FS can be approximated to the following relation:

$$\epsilon_k - \epsilon_F = \hbar v_F (k - k_F), \tag{1.32}$$

where v_F is Fermi velocity.

From Eq. 1.32, susceptibility in Eq. 1.31 is calculated to be

$$\chi(q, T = 0) = \frac{-e^2}{\pi \hbar v_F} ln|\frac{q + 2k_F}{q - 2k_F}| = -e^2 n(\epsilon_F) ln|\frac{q + 2k_F}{q - 2k_F}|, \tag{1.33}$$

where $n(\epsilon_F)$ is the density of states at the Fermi level. Here we consider $T = 0$ for χ, but generally χ should also depend on temperature.

Immediately we can see that susceptibility diverges at $q = 2k_F$, meaning that at $q = 2k_F$ the electron density can reorganize even without any external field. So the 1D electron gas is intrinsically unstable at zero temperature. The 1D susceptibility is plotted in Fig. 1.8 along with the 2D and 3D cases, where the curves are generated based on expressions in Ref. [55]. Divergence of the susceptibility for 1D case clearly stands out.

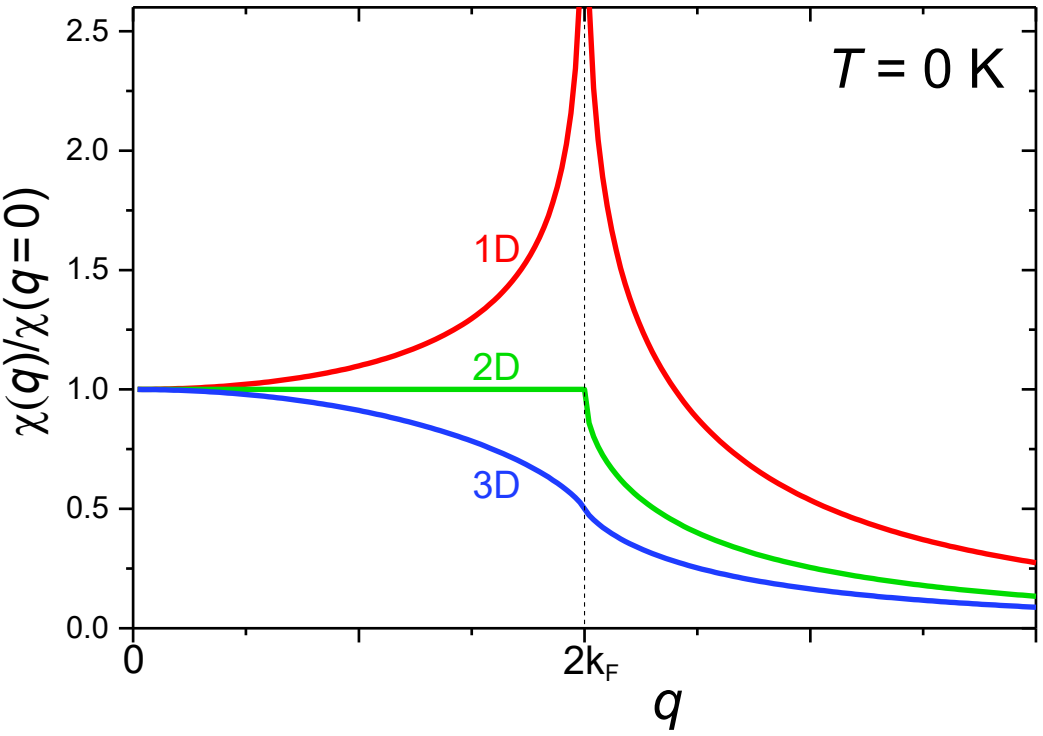

Figure 1.8: The electron susceptibility for 1D, 2D, and 3D systems at zero temperature.

When a large segment of the FS can be connected to another large segment of FS via a reciprocal lattice vector, we call this phenomenon *Fermi surface nesting* (FSN) and the wave-vector is called FSN vector q_χ. If there is strong FSN in a large portion of FS, then by examining the Lindhard response function in Eq. 1.31, one usually sees a peak in electron

dispersion or divergence of $\chi(\vec{q})$ at $q = q_\chi$. So a strong FSN always results in divergence in susceptibility and increased instabilities in the electron system.

For 1D linear chain, the FS is just two points, so one can completely connect the entire FS with a single wave-vector $q = 2k_F$. This is the case of perfect FSN. For 2D or 3D cases, the FS topology is more complicated and exhibits much less symmetry, so only partial FSN occurs. Fig. 1.9 shows examples of FSN for different FS topologies.

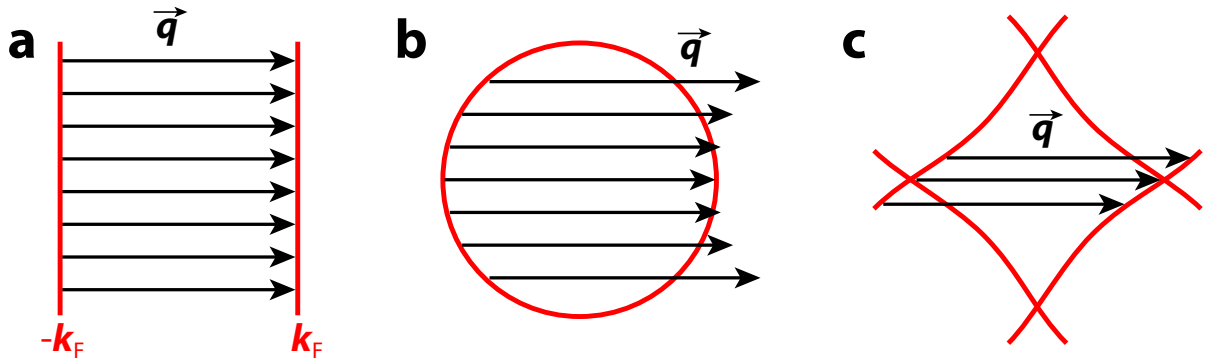

Figure 1.9: Examples of Fermi surface nesting for different Fermi surface topologies. **a**, 1D electron gas, perfect FSN occurs. **b**, 2D free electron gas. There is no "parallel" parts in the circular FS, so no FSN. **c**, FS of a 2D square lattice. The diamond shape of FS results in relatively good FSN.

At a finite temperature T, the susceptibility can be calculated based on the finite-temperature Fermi function for density of state $n(\epsilon_F)$ [54]

$$\chi(q = 2k_F, T) = -e^2 n(\epsilon_F) \int_0^{\epsilon_0/2k_B T} \frac{\tanh(x)}{x} dx, \tag{1.34}$$

where ϵ_0 is the cutoff energy of the integral, which is usually taken to be equal to the Fermi energy ϵ_F.

The integral can be calculated to be

$$\chi(q = 2k_F, T) = -e^2 n(\epsilon_F) \ln \frac{1.14\epsilon_0}{k_B T}. \tag{1.35}$$

This temperature-dependent susceptibility is a finite value at finite temperatures and diverges only when $T \to 0$.

1.3.2 Coupled one-dimensional electron-phonon linear chain

Next, we will consider a 1D free electron gas coupled to the underlying chain of ions through electron-phonon coupling. The Hamiltonian for the electron gas can be written as

$$\hat{\mathcal{H}}_{el} = \sum_k \epsilon_k a_k^\dagger a_k, \tag{1.36}$$

where $a_k^\dagger$ and a_k are the creation and annihilation operators for the electron state with energy $\epsilon_k = \hbar^2 k^2 / 2m$.

The Hamiltonian for the lattice can be written as

$$\hat{\mathcal{H}}_{ph} = \sum_q \hbar\omega_q (b_q^\dagger b_q + \frac{1}{2}), \tag{1.37}$$

where $b_q^\dagger$ and b_q are the creation and annihilation operators for the phonons at frequency ω_q.

For the electron-phonon interaction term, the Hamiltonian can be written as

$$\hat{\mathcal{H}}_{ph} = \sum_{k,q} g_q (b_{-q}^\dagger + b_q) a_{k+q}^\dagger a_k, \tag{1.38}$$

where g_q is the electron-phonon coupling constant defined as

$$g_q = i(\frac{\hbar}{2M\omega_q})^{1/2}|q|V_q, \tag{1.39}$$

where M is the ionic mass, V_q is the ionic potential. For detailed derivation check Ref. [54].

So summing up Eqs. 1.36, 1.37, 1.38, we get the total Hamiltonian of the system:

$$\hat{\mathcal{H}} = \sum_k \epsilon_k a_k^\dagger a_k + \sum_q \hbar\omega_q(b_q^\dagger b_q + \frac{1}{2}) + \sum_{k,q} g_q(b_{-q}^\dagger + b_q)a_{k+q}^\dagger a_k. \tag{1.40}$$

Based on Heisenberg equation of motion, assuming Q_q is the atomic position, for small displacements, the equation of motion is

$$\hbar^2\ddot{Q}_q = -[[Q_q, \hat{\mathcal{H}}], \hat{\mathcal{H}}]. \tag{1.41}$$

Then based on commutation relations of $[Q_q, P_{q\prime}] = i\hbar\delta_{q,q\prime}$, Eq. 1.41 becomes

$$\hbar^2\ddot{Q}_q = -\omega_q^2 Q_q - g(\frac{2\omega_q}{M\hbar})^{1/2}\rho_q, \tag{1.42}$$

where ρ_q is the electron density determined by susceptibility: $\rho_q = \chi(q,T)g(\frac{2M\omega_q}{\hbar})^{1/2}Q_q$, so the equation of motion becomes

$$\ddot{Q}_q = -[\omega_q^2 + \frac{2g^2\omega_q}{\hbar}\chi(q,T)]Q_q. \tag{1.43}$$

This gives a normalized phonon frequency of $\omega_{ren,q}^2 = \omega_q^2 + \frac{2g^2\omega_q}{\hbar}\chi(q,T)$. At FS nesting vector of $q = 2k_F$, plugging in the susceptibility expression in Eq. 1.35, the phonon frequency

becomes

$$\omega^2_{ren,2k_F} = \omega^2_{2k_F} - \frac{2g^2 n(\epsilon_F)\omega_{2k_F}}{\hbar} \ln\left(\frac{1.14\epsilon_0}{k_B T}\right). \tag{1.44}$$

From Eq. 1.44, we can see with decreasing temperature, the renormalized phonon frequency goes down to zero to form "frozen" phonons. This defines the transition temperature

$$k_B T^{MF}_{CDW} = 1.14\epsilon_0 e^{-1/\lambda}, \tag{1.45}$$

where λ is a dimensionless electron-phonon coupling constant defined as $\lambda = \frac{g^2 n(\epsilon_F)}{\hbar\omega_{2k_F}}$.

This Kohn anomaly effect can be visualized in Fig. 1.10, which is adapted from Ref. [54].

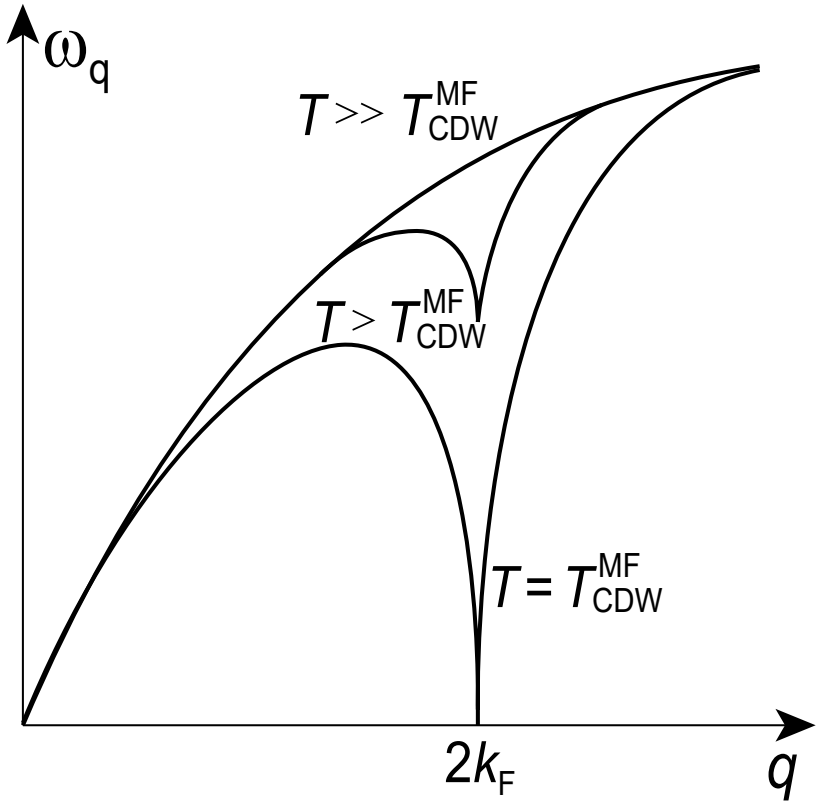

Figure 1.10: The phonon softening effect when the temperature is close to T^{MF}_{CDW}. It becomes frozen phonon when $T = T^{MF}_{CDW}$.

We can define an order parameter (Δ is actually the CDW gap) as

$$|\Delta|e^{i\phi} = g(\langle b_{2k_F}\rangle + \langle b^{\dagger}_{-2k_F}\rangle). \tag{1.46}$$

Replace the electronic part Hamiltonian in Eq. 1.36 with this order parameter and with some algebra transformations (Ref. [54]), in the weak coupling limit, the energy loss by the electron system due to CDW formation is

$$E_{el} = n(\epsilon_F)[-\frac{\Delta^2}{2} - \Delta^2 \log\left(\frac{2\epsilon_F}{\Delta}\right)]. \tag{1.47}$$

On the other hand, the energy gain due to lattice distortion is

$$E_{latt} = \frac{N}{2} M\omega^2_{2k_F}\langle u(x)\rangle^2 = \frac{\hbar\omega_{2k_F}\Delta^2}{2g^2} = \frac{\Delta^2 n(\epsilon_F)}{2\lambda}, \tag{1.48}$$

where the lattice distortion amplitude u is actually directly connected to the CDW gap Δ as $\langle u(x)\rangle = (\frac{\hbar}{2NM\omega_{2k_F}})^{1/2}\frac{2|\Delta|}{g}\cos(2k_F x + \phi)$. That is why in Eq. 1.48 there is that replacement.

Consider the total energy change by summing up Eq. 1.47 and Eq. 1.48

$$E_{tot} = E_{el} + E_{latt} = n(\epsilon_F)[-\frac{\Delta^2}{2} - \Delta^2 \log\left(\frac{2\epsilon_F}{\Delta}\right) + \frac{\Delta^2}{2\lambda}]. \tag{1.49}$$

Minimizing this energy, we get the CDW gap

$$\Delta = 2\epsilon_F e^{-1/\lambda} \tag{1.50}$$

and the condensation energy

$$E_{cond} = E_{normal} - E_{CDW} = \frac{n(\epsilon_F)}{2}\Delta^2. \tag{1.51}$$

This positive condensation energy indicates that the formation of CDW reduces the total energy and the CDW is now a stable ground state.

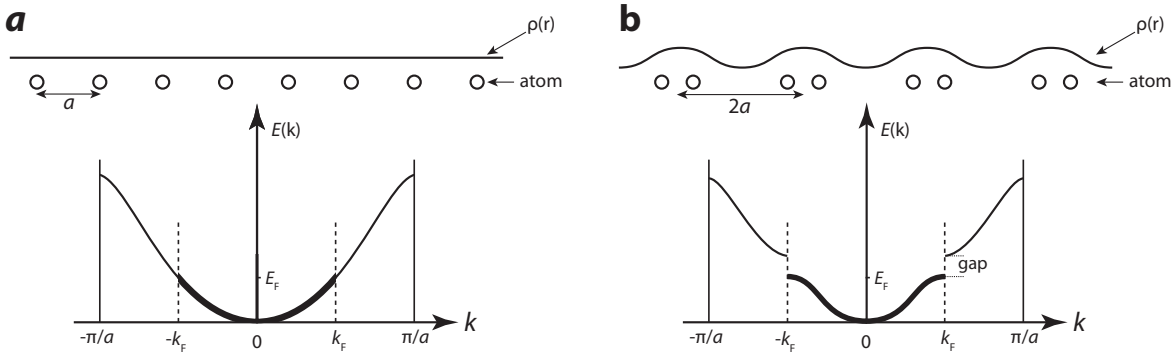

Figure 1.11: An example of CDW formation in a half-filled 1D linear chain. **a**, Metallic state. Charge-density is uniform and atomic ions are undistorted. Electrons fill up to half of the band and it is a metal. **b**, CDW state. The charge-density re-modulate and atomic ions distort every pair. The band opens up a gap at $\pm\, k_F$.

Comparing Eq. 1.50 and Eq. 1.45, we can get the well-known relation between the zero-temperature gap and the transition temperature

$$2\Delta(T=0) = 3.52 k_B T_{CDW}^{MF}. \tag{1.52}$$

The temperature-dependent gap can be deduced by integrating the Fermi function that defines T_{CDW}^{MF} in Eq. 1.45, yielding the BCS-like order parameter temperature evolution

$$\frac{|\Delta(T)|}{|\Delta(T=0)|} = 1.74\sqrt{1 - \frac{T}{T_{CDW}^{MF}}}, \text{ for } T < T_{CDW}^{MF}. \tag{1.53}$$

1.3.3 Fluctuation effect versus mean-field model

As we have discussed in Sec. 1.2, mean-field theory ignores fluctuations. On the other hand, RG theory predicts that the fluctuation will diverge at the fixed point. At low dimensions where atomic motions are less constrained by fewer nearest neighbors, the fluctuation effect is expected to be more dominant. The divergence of correlation length in the fluctuating order parameter near the critical point is discussed here.

For a 1D chain described by Hamiltonian in Eq. 1.40, the order parameter is complex. So both the phase and amplitude should be considered when calculating the correlation length. As drawn in Fig. 1.3, when temperature is above T^{MF}, the potential has one minimum in the middle, and the system moves inside like a pendulum, the amplitude fluctuation dominates over phase; when T is below T^{MF}, the system's orbit is more likely along the minimum circle, so phase fluctuation dominates.

The phase-phase correlation length for $T < T^{MF}$ can be written as the following (for detailed derivation, check Ref. [54])

$$\xi_{1D} = \frac{\hbar v_F}{\pi k_B T}. \tag{1.54}$$

On the other hand, at high temperature, the correlation length due to amplitude fluctuation takes the form of

$$\xi_{1D} = \frac{[7\zeta(3)]^{1/2} v_F}{4\pi k_B T}, \tag{1.55}$$

where $\zeta(3)$ is the third-order zeta function and this equation is derived from Ref. [56].

In real systems, a 1D chain does not exist and it is always multiple chains coupled together with some kind of interactions. Due to this interaction, CDW fluctuations are

better stabilized and this leads to a transition to a ground state with 3D long range order. Assuming a square lattice chain with lattice constant $d_\perp$, the inter chain interaction can be written as

$$E_{int} = n(\epsilon_F)\frac{2}{d_\perp^2}c_\perp \sum_{i,j} dx Re[\Delta_i^*(x), \Delta_j(x)], \tag{1.56}$$

where $n(\epsilon_F)$ is density of states at the Fermi level, $c_\perp$ is the inter chain interaction, Δ is complex order parameter, i, j are the chain index.

In the mean-field approximation, the susceptibility can be generally written as

$$\chi(q_\parallel, q_\perp) = \frac{\chi_{1D}(q_\parallel)}{1 - Zc_\perp(0)\chi_{1D}(q_\parallel)T}, \tag{1.57}$$

where Z is the number of the nearest neighbors, $\chi_{1D}(q_\parallel)$ is the common susceptibility in a 1D chain discussed in Sec. 1.2. The divergence of $\chi(q_\parallel, q_\perp)$ defines a transition temperature T_{3D}

$$1 - Zc_\perp(0)\chi_{1D}(q_\parallel)T_{3D} = 0. \tag{1.58}$$

According to Ref. [54], the correlation length parallel and perpendicular to the chains can be defined as

$$\xi_\parallel = (\frac{c}{a'})^{1/2}(T - T_{3D})^{-1/2} \tag{1.59}$$

$$\xi_\perp = (\frac{c_\perp}{a'})^{1/2}(T - T_{3D})^{-1/2}, \tag{1.60}$$

where $c, c_\perp$ are the interaction terms, a is a parameter related to temperature and order parameter, detailed definitions can be seen in chapter 5 of Ref. [54].

From Eq. 1.59 and Eq. 1.60, in directions both parallel and perpendicular to the chain, the correlation length diverges at $T = T_{3D}$. At near T_{3D}, both correlation length is large

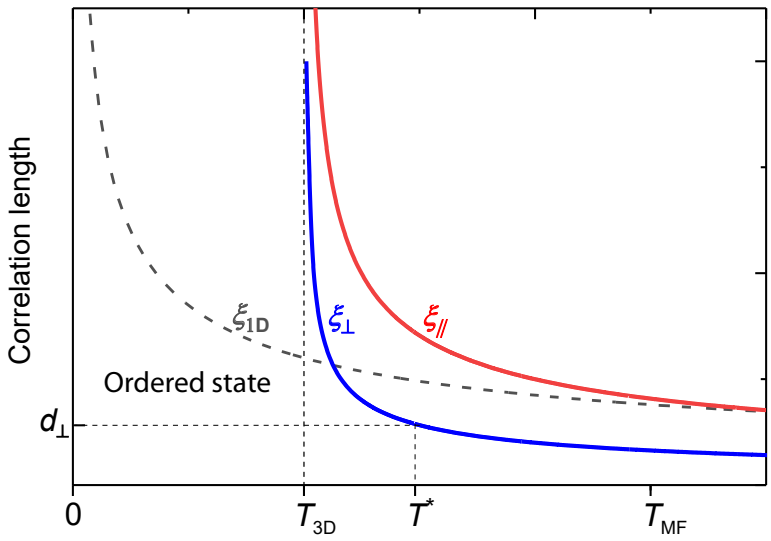

Figure 1.12: The temperature-dependent correlation length of the parallel and perpendicular to the chains as well as single 1D chain correlation length. T_{3D} is the real transition temperature in materials, below which is CDW state. T_{MF} is the mean-field transition temperature based on mean-field models.

and $\xi_{\perp}$ is larger than $d_{\perp}$, which is the inter chain distance. So in this region, the neighboring chains are strongly coupled and it is more 3D like. At high temperature where $\xi_{\perp}$ is smaller than $d_{\perp}$, each chain is decoupled and it is more 1D character. From 3D to 1D, the crossover happens when

$$d_{\perp} = \xi_{\perp} = (\frac{c_{\perp}}{a'})^{1/2}(T^* - T_{3D})^{-1/2}. \tag{1.61}$$

Thus the crossover temperature T^* is

$$T^* = T_{3D} + \frac{d_{\perp}^2 a'}{c_{\perp}}. \tag{1.62}$$

The correlation length of 3D $\xi_{\|}$, $\xi_{\perp}$ and 1D ξ_{1D} is plotted in Fig. 1.12 for comparison. Crossover temperature T^* is also labeled in the plot.

In Table 1.2, the CDW transition temperature T_{3D} and MFT predicted temperature T_{MF} are compared for several different CDW materials. From the table, we can see all the T_{3D}

is smaller than the mean-field value, thus confirming the point of inter-chain interactions.

Materials	T_{3D} (K)	T_{MF} (K)	**Ref.**
$K_2Pt(CN)_4Br_{0.3}\cdot 3H_2O$	100	650	[57]
TTF-TCNQ($2k_F$)	54	150	[58]
TTF-TCNQ($4k_F$)	49	600	[59]
$NbSe_3$	145	700	[60]
$BaVS_3$	70	170	[61]
$K_{0.3}MoO_3$	180	500	[62]
$CeTe_3$	> 500	2700	[63, 64]
1T-TaS_2	543	700-2700	[65]

Table 1.3: Comparison of the CDW transition temperature T_{3D} and the temperature predicted by mean-field theory T_{MF} in several materials. The T_{MF} is estimated based on CDW gap in Eq. 1.52. For $CeTe_3$, the CDW gap is 400 meV. For 1T-TaS_2 at zero temperature, there are both the CDW gap and Mott-Hubbard gap. The CDW gap based on different measurements are estimated to be 100-400 meV.

1.3.4 Origin of charge-density wave: Fermi surface nesting and beyond

Based on Peierls' theory of CDW, CDW formation is initially driven by electronic instabilities (Fermi surface nesting and thus divergence of electron susceptibility) then stabilized through electron-phonon coupling. In this picture, the lattice distortion is just a secondary "side effect" of CDW formation but not the driving force. The CDW Q-vector matches well with the FSN vector, especially in 1D chains where there is a perfect FSN.

But in many 2D or higher dimensional CDW materials, researchers have shown [55,66,67]

that FSN could be weakened by carrier scattering and Fermi function broadening and FSN alone is not sufficient to drive the CDW. Instead, strong momentum-dependent electron-phonon interactions are attributed strongly to drive CDW formation. Examples of this type include $NbSe_2$, $TaSe_2$, etc.

In some strongly correlated materials, for example VO_2, the metal-insulator transition involves a large gap opening and lattice atomic distortion (e.g. dimerization). Sometimes this is also called CDW formation. But this type of transitions is completely different from the Peierls mechanism, more to do with electron-electron interactions and Mott physics.

The CDW is also found to form in some high-temperature superconductors in cuperates [68, 69]. But it is still debated whether FSN or strong electron phonon interactions is the driving force of CDW [55].

Chapter 2

Diffraction theory and ultrafast electron diffraction

Scattering is one of the most powerful experimental tools to study physics throughout history. In scattering experiments, probe particles are shot onto the target material and interact with the target, then the probe particles are collected for detection. By monitoring the probe particle's momentum or energy change, information about the target material can be revealed. Such a probe could be photons (from THz to hard X-ray), electrons, neutrons, alpha particles or other charged particles, etc.

Different probe particles interact differently with the materials being tested. For example, X-ray photons mainly interact with electrons in a material through their electromagnetic (EM) field. Electrons in the specimen oscillate with the EM field in an X-ray beam then emit their own EM field that is identical in wavelength and phase to the incident X-ray. Hence, X-ray diffraction can be used to map the electron density of the material. Electrons are light, negatively charge particles. They interact with materials by passing through the Coulomb potential formed by both electrons and core ions in the materials. So electron diffraction is a measure of the Coulomb potential of the material. On the other hand, neutrons are heavy, charge-neutral but non-zero spin particles. Therefore, neutrons interact with materials either through strong nuclear force with nucleus or through magnetic interactions with outer shell

electrons.

In this chapter, the basic formulations of (electron/X-ray) diffraction are discussed in Sec. 2.1, from atomic scattering to crystal scattering. Factors that affect scattering will also be discussed, especially the structural factor and the Debye-Waller factor (DWF). Following this, the pump-probe technique and ultrafast electron diffraction will be introduced in Sec. 2.2.

2.1 Basic formulation of diffraction

Diffraction is a process of wave interference from multiple scattered waves. Crystalline materials consist of atoms arranged in a certain periodic way. First scattering from single atom will be discussed, then we will extend it to crystalline materials.

2.1.1 Scattering from a point target: atomic form factor

When a probe particle, either X-ray photon or electron, is scattered by an isolated atom, the scattering amplitude depends on the type of interaction, properties of the probe and target atom, scattering angle, etc. Such a scattering amplitude is called *atomic form factor*.

For X-rays, the atomic form factor involves a Fourier transform of the spatial density distribution of the scattering target from real space to reciprocal space. For a target atom with spatial density distribution of $\rho(r)$, the form factor $f(s)$ is defined as

$$f(\mathbf{s}) = \int \rho(\mathbf{r}) e^{i\mathbf{s}\cdot\mathbf{r}} d^3\mathbf{r}, \tag{2.1}$$

where $\mathbf{s}$ is called momentum transfer defined below.

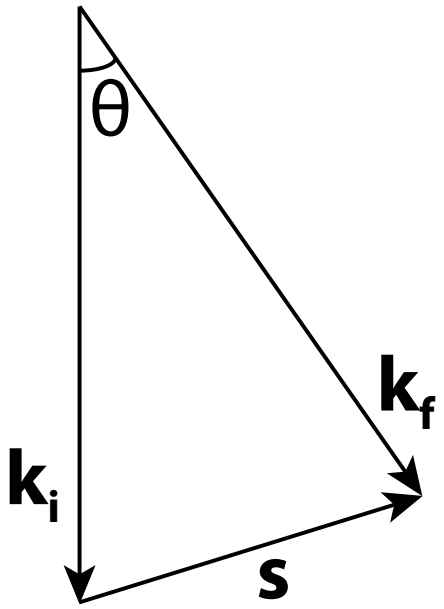

Figure 2.1: Diagram of the momentum transfer in a single atom scattering event. $\mathbf{k}_i$ and $\mathbf{k}_f$ are the incident and scattered wave-vector, respectively, defined as $\mathbf{k}_i = 2\pi/\lambda_i$ and $\mathbf{k}_f = 2\pi/\lambda_f$, where λ_i and λ_f are the incident and scattered wavelengths of the probe particles. $\mathbf{s}$ is the momentum transfer. θ is the scattering angle, $\theta/2$ is equal to the so-called Bragg angle θ_b in the Bragg's law.

As shown in Fig. 2.1, for elastic scattering where there is no energy exchange, the incident and scattered wave-vectors are k_i and k_f, respectively. $k_i = k_f = 2\pi/\lambda$. Using trigonometric relation, it is easy to prove that

$$\mathbf{s} = \mathbf{k_f} - \mathbf{k_i} = \frac{4\pi}{\lambda}\sin\left(\frac{\theta}{2}\right)\hat{\mathbf{s}}, \tag{2.2}$$

with $\hat{\mathbf{s}}$ being the unit length vector along $\mathbf{s}$ direction.

The scattering intensity $\mathbf{I}$ is proportional to atomic form factor squared: f^2.

The electron charge density about nucleus $\rho(\mathbf{r})$ in Eq. 2.1 can be assumed to be a spherical distribution. For X-ray scattering, the atomic form factor is usually written as sum of

Gaussians [70]

$$f_x(s) = \sum_{i=1}^{4} a_i \exp\Big(-b_i(\frac{s}{4\pi})\Big) + c, \tag{2.3}$$

where a_i, b_i, and c are parameters from different atomic species. Their values can be found in Ref. [71].

For electron scattering, the atomic form factor is different but is related to that of X-rays by the Mott–Bethe formula [72]

$$f_{el}(s) = \frac{me^2}{32\pi^3\hbar^2\epsilon_0}\frac{1}{s^2}(Z - f_x(s)), \tag{2.4}$$

where m and e are electron mass and charge, respectively, ϵ_0 is vacuum permittivity, Z is atomic number of the target atom.

The electron atomic form factor in Eq. 2.4 can be plotted in Fig. 2.2, which is adapted from Ref. [4].

2.1.2 Scattering from a crystal: Bragg's law and Laue condition

Consider two atoms separated by distance a as shown in Fig. 2.3a, an incident plane wave with wavelength λ and incidence angle θ_i (relative to the atomic line) scattered by the two atoms. The scattered angle is θ_f. In order to have constructive interference, the path difference of the two rays should be equal to

$$a(\cos\theta_f - \cos\theta_i) = h\lambda, \tag{2.5}$$

where h is an integer number.

For a 3D lattice with lattice constants a, b, c forming constructive interferences along all

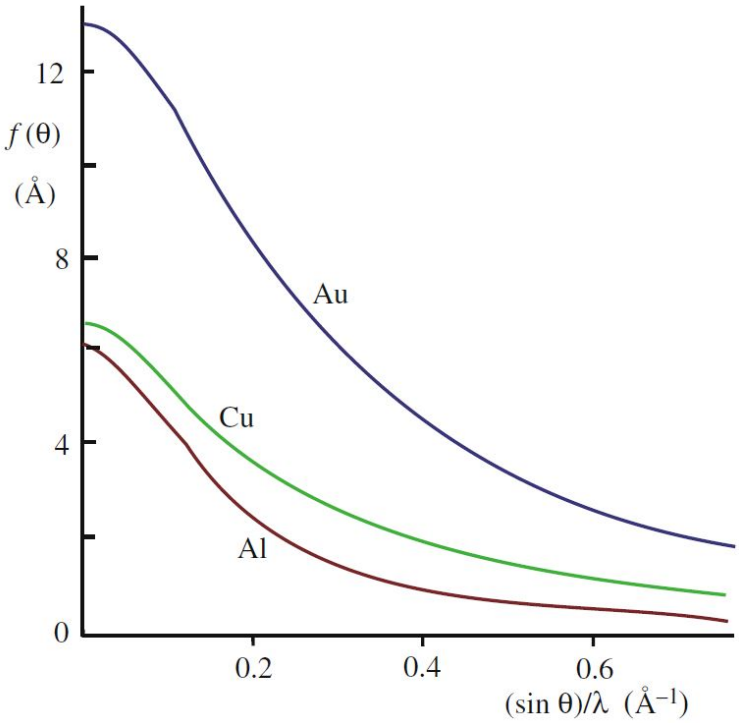

Figure 2.2: The atomic form factor $f_{el}(s)$ evolutions for electron scattering at different s and for different atoms [4]. The atomic form factor decreases with the increasing scattering angle and increases with the increasing target atomic number.

3 crystal periodicities, it requires

$$\begin{aligned} a(\cos\theta_f - \cos\theta_i) &= h\lambda \\ b(\cos\theta_f - \cos\theta_i) &= k\lambda \\ c(\cos\theta_f - \cos\theta_i) &= l\lambda, \end{aligned} \tag{2.6}$$

where h, k, l are all integer numbers. These equations are called Laue equations. Sometimes Laue equations are written in a vector form. We can rewrite Eq. 2.6 in the wave-vector format

$$\begin{aligned} a(\frac{2\pi}{\lambda})\cos\theta_f - a(\frac{2\pi}{\lambda})\cos\theta_i = \boldsymbol{a}(\mathbf{k}_f - \mathbf{k}_i) = \boldsymbol{a}\cdot\boldsymbol{s} &= 2\pi h \\ \boldsymbol{b}\cdot\boldsymbol{s} &= 2\pi k \\ \boldsymbol{c}\cdot\boldsymbol{s} &= 2\pi l. \end{aligned} \tag{2.7}$$

This is equivalent to Eq. 2.6.

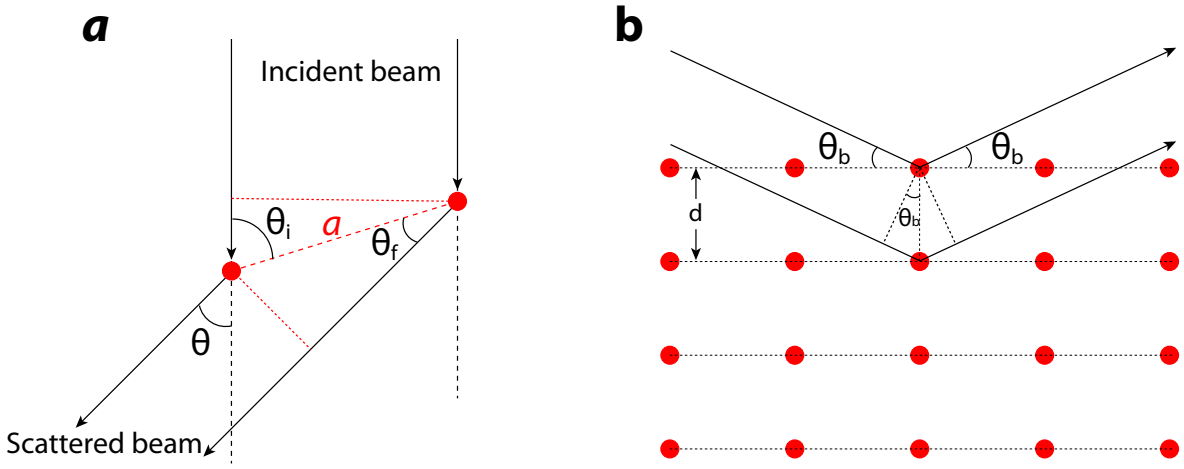

Figure 2.3: The schematic drawing of scattering diagram for the Laue condition (**a**) and the Bragg's Law (**b**).

The Laue condition is a general form of identifying diffraction spots. By contrast, Bragg's law is built on reflection from the lattice plane. Consider the schematic drawing of Fig. 2.3(b), the incident beam hits on a lattice plane, then gets "reflected" from the surface. Both the incident angle and scattering angle are the same θ_b, the so-called Bragg angle. It equals half the scattering angle θ that we mentioned in Fig. 2.1. Similarly, to have a constructive interference, the path difference should be equal to integer numbers of the probe wavelength

$$2d\sin(\theta_b) = n\lambda, \tag{2.8}$$

where n is an integer number. It is easy to prove that Bragg's Law is a special case of the Laue equations. Bragg's law reduces Laue's three equations into only one and has been widely used.

2.1.3 Reciprocal space and Ewald's sphere

When discussing diffraction, we are talking about momentum transfers and wave interferences. It is actually easier to treat it in a new imaginary space called momentum space or reciprocal space.

Consider a 3D lattice that has basis vectors of $\boldsymbol{a}$, $\boldsymbol{b}$, $\boldsymbol{c}$. Any atomic positions in the lattice can be written as $\boldsymbol{r} = l\boldsymbol{a} + m\boldsymbol{b} + n\boldsymbol{c}$, where l, m, n are integers. Then we can define a new set of basis vectors $\boldsymbol{a^*}$, $\boldsymbol{b^*}$, $\boldsymbol{c^*}$ such that they represent the reciprocal space:

$$\begin{aligned} \boldsymbol{a}^* &= 2\pi \frac{\boldsymbol{b} \times \boldsymbol{c}}{\boldsymbol{a} \cdot (\boldsymbol{b} \times \boldsymbol{c})} \\ \boldsymbol{b}^* &= 2\pi \frac{\boldsymbol{c} \times \boldsymbol{a}}{\boldsymbol{b} \cdot (\boldsymbol{c} \times \boldsymbol{a})} \\ \boldsymbol{c}^* &= 2\pi \frac{\boldsymbol{a} \times \boldsymbol{b}}{\boldsymbol{c} \cdot (\boldsymbol{a} \times \boldsymbol{b})}. \end{aligned} \tag{2.9}$$

In such a definition, $\boldsymbol{a}^*$ is perpendicular to the $(\boldsymbol{b}, \boldsymbol{c})$-plane; $\boldsymbol{b}^*$ is perpendicular to the $(\boldsymbol{c}, \boldsymbol{a})$-plane; $\boldsymbol{c}^*$ is perpendicular to the $(\boldsymbol{a}, \boldsymbol{b})$-plane.

We can define a reciprocal lattice vector $\boldsymbol{G}$ to be

$$\boldsymbol{G} = h\boldsymbol{a}^* + k\boldsymbol{b}^* + l\boldsymbol{c}^*. \tag{2.10}$$

By comparing $\boldsymbol{G}$ with Eq. 2.7, we find that $\boldsymbol{G} = \boldsymbol{s}$: the reciprocal lattice vector coincides with the momentum transfers in diffraction. Based on this idea, we use a 2D square reciprocal lattice as shown in Fig. 2.4a as an example. If we draw a circle of radius $R = \frac{2\pi}{\lambda} = k_i$ in such a way that the incident wave-vector $\boldsymbol{k}_i$ starts from circle center and points to a reciprocal lattice point, then any other points that fall onto the circle would define a $\boldsymbol{k}_f$ that can be shown to produce constructive diffraction spot. This circle (or sphere in 3D) is called Ewald's

sphere. This Ewald's sphere construction is very useful in identifying diffraction spots once we know the lattice orientation, beam energy, and beam direction.

Fig. 2.4b shows a more realistic example of the Ewald's sphere cutting reciprocal lattice spots for high-energy beams. The wavelength of 100 keV electron beam is 0.037 Å. Thus, the Ewald's sphere radius will be $2\pi/\lambda = 167$ Å^{-1}. For a real material, for example $CeTe_3$, the lattice constant is $\boldsymbol{a} = 4.4$ Å. The corresponding reciprocal lattice spot distance is $2\pi/a = 1.4$ Å^{-1}. So the Ewald's sphere is about 100 times larger than the reciprocal lattice unit. Given the Fourier relationship between real space and reciprocal space, if we have a finite object, the diffraction spots would not be infinitesimal but instead be finite-sized. For a very thin specimen, the diffraction spots will be elliptical as shown in Fig. 2.4b. If the probe beam is tilted or has a finite angle (e.g. convergent beam electron diffraction), then we need to tilt the Ewald's sphere to see how the cutting is changed to derive the diffraction intensity based on the overlap. On the other hand, if sample is tilted, we just need to correspondingly rotate the reciprocal lattice.

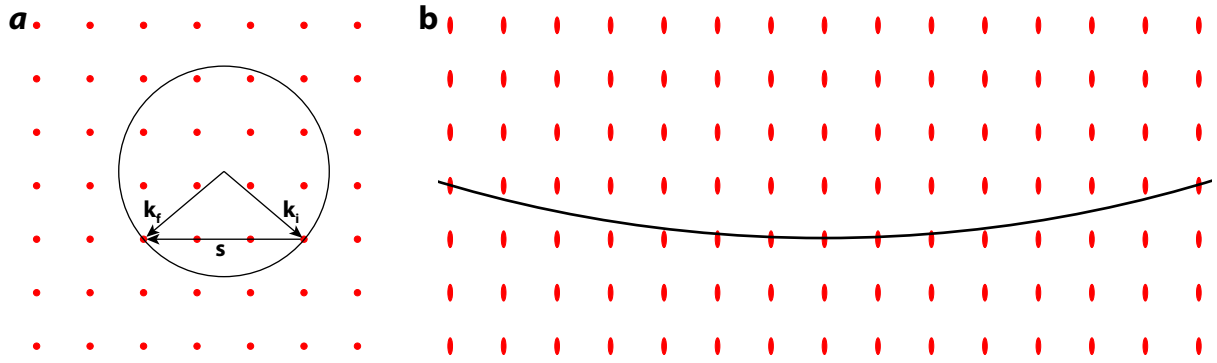

Figure 2.4: The Ewald's sphere intersecting with reciprocal lattice points. **a**, Ewald's sphere for a square 2D lattice. **b**, A more realistic scale for the Ewald's sphere and reciprocal spots.

2.1.4 Structure factor

With Laue equations, Bragg's Law, and Ewald's sphere reconstruction, we can quantitatively determine where and how strong a diffraction spot would show up. Similarly, if one measures the position, intensity, and peak width of the diffraction spot, then periodicity, orientation and size of the sample may be determined.

Consider a system with N atoms and the j^{th} atom is at position $\boldsymbol{r}_j$. f_j is the atomic form factor of the j^{th} atom. Then the scattered wave equals to the sum from all atoms

$$\Psi(\boldsymbol{s}) = \sum_{j=1}^{N} f_j e^{-i\boldsymbol{s}\cdot\boldsymbol{r}_j}, \tag{2.11}$$

where $\boldsymbol{s}$ is the momentum transfer defined earlier in Eq. 2.2.

Then the scattering intensity is obtained by the following expression:

$$\begin{aligned} I(\boldsymbol{s}) = \Psi(\boldsymbol{s}) \cdot \Psi^*(\boldsymbol{s}) &= \sum_{j=1}^{N} f_j e^{-i\boldsymbol{s}\cdot\boldsymbol{r}_j} \times \sum_{k=1}^{N} f_j e^{i\boldsymbol{s}\cdot\boldsymbol{r}_k} \\ &= \sum_{j=1}^{N}\sum_{k=1}^{N} f_j f_k e^{-i\boldsymbol{s}\cdot(\boldsymbol{r}_j - \boldsymbol{r}_j)}. \end{aligned} \tag{2.12}$$

The structure factor for this system is defined as intensity normalized by $1/\sum_{j=1}^{N} f_j^2$

$$S(\boldsymbol{s}) = \frac{1}{\sum_{j=1}^{N} f_j^2} \sum_{j=1}^{N}\sum_{k=1}^{N} f_j f_k e^{-i\boldsymbol{s}\cdot(\boldsymbol{r}_j - \boldsymbol{r}_k)}. \tag{2.13}$$

If the object is randomly oriented, define $r_{jk} = |\boldsymbol{r}_j - \boldsymbol{r}_k|$. After averaging over all

orientations, Eq. 2.13 becomes what is known as the Debye scattering equation

$$S(\boldsymbol{s}) = \frac{1}{\sum_{j=1}^{N} f_j^2} \sum_{j=1}^{N} \sum_{k=1}^{N} f_j f_k \frac{\sin(sr_{jk})}{sr_{jk}}. \tag{2.14}$$

For scattering from crystalline sample, we consider the lattice unit cell has n atoms. The j^{th} atom has an atomic coordinate of (x_j, y_j, z_j) and $\boldsymbol{G} = h\boldsymbol{a}^* + k\boldsymbol{b}^* + l\boldsymbol{c}^*$ for the Bragg reflection. Then the structure factor can be written as

$$F_{hkl} = \sum_{j=1}^{n} f_j e^{-2\pi i(hx_j + ky_j + lz_j)}. \tag{2.15}$$

The intensity of diffraction spot (h k l) is square of the structural factor

$$I_{hkl} = F_{hkl}^2. \tag{2.16}$$

So, for a crystal with specific symmetry, the structural factor for a certain Bragg peak (h k l) could be zero. Such peaks are referred to as symmetry forbidden or symmetry absent peaks. For example, for a body-centered cubic (BCC) Bravais lattice, there are two atoms per unit cell. Coordinates for the two atoms are $x_j, y_j, z_j = (0, 0, 0)$ and $(1/2, 1/2, 1/2)$. The structural factor becomes

$$F_{hkl} = f[1 + e^{-i\pi(h+k+l)}] = f[1 + (-1)^{h+k+l}]. \tag{2.17}$$

So,

$$\begin{cases} F_{hkl} = 2f, I_{hkl} = 4f^2 & \text{, when } (h{+}k{+}l) \text{ is even,} \\ F_{hkl} = 0, I_{hkl} = 0 & \text{, when } (h{+}k{+}l) \text{ is odd.} \end{cases} \tag{2.18}$$

Now, we consider another example of the structure factor for a dimerized 1D atomic chain. As shown in Fig. 2.5a, assume a 1D lattice with N atoms, where each atom is separated by length a. Every other atom is distorted to form dimerization with a period of $2a$. The atomic distortion is u. Each unit cell contains two atoms. The structure factor can be written as

$$F = \sum_{j=1}^{2} f_j e^{-i\boldsymbol{q}\cdot\boldsymbol{r}}. \tag{2.19}$$

Consider two conditions:

1, at wave-vector $\boldsymbol{q} = \frac{2\pi}{a}h$, the h^{th} Bragg peak (h is an integer)

$$F_{Bragg} = f[e^{-2\pi i h\frac{u}{a}} + e^{-2\pi i h(1-\frac{u}{a})}] = 2f\cos\Big(2\pi h\frac{u}{a}\Big). \tag{2.20}$$

So the Bragg peak intensity is

$$I_{Bragg} = 4f^2\cos^2\Big(2\pi h\frac{u}{a}\Big) = 2f^2[1+\cos\Big(4\pi h\frac{u}{a}\Big)] \approx 4f^2[1-4\pi^2h^2(\frac{u}{a})^2], \tag{2.21}$$

where in the last step, for small $\frac{u}{a}$, we use approximation $\cos\big(4\pi h\frac{u}{a}\big) = 1 - \frac{1}{2}(4\pi h^2\frac{u}{a})^2$. From this result, the Bragg peak intensity is decreasing as distortion u increases and for the same distortion u Bragg peak intensity change also increases as the order of the Bragg peak increases (h^2).

2, at wave-vector of $\boldsymbol{q} = \frac{2\pi}{a}(h+\frac{1}{2})$ (satellite peak)

$$F_{CDW} = f[e^{-2\pi i(h+\frac{1}{2})\frac{u}{a}} + e^{-2\pi i(h+\frac{1}{2})(1-\frac{u}{a})}] = -i2f\sin[2\pi(h+\frac{1}{2})\frac{u}{a}]. \tag{2.22}$$

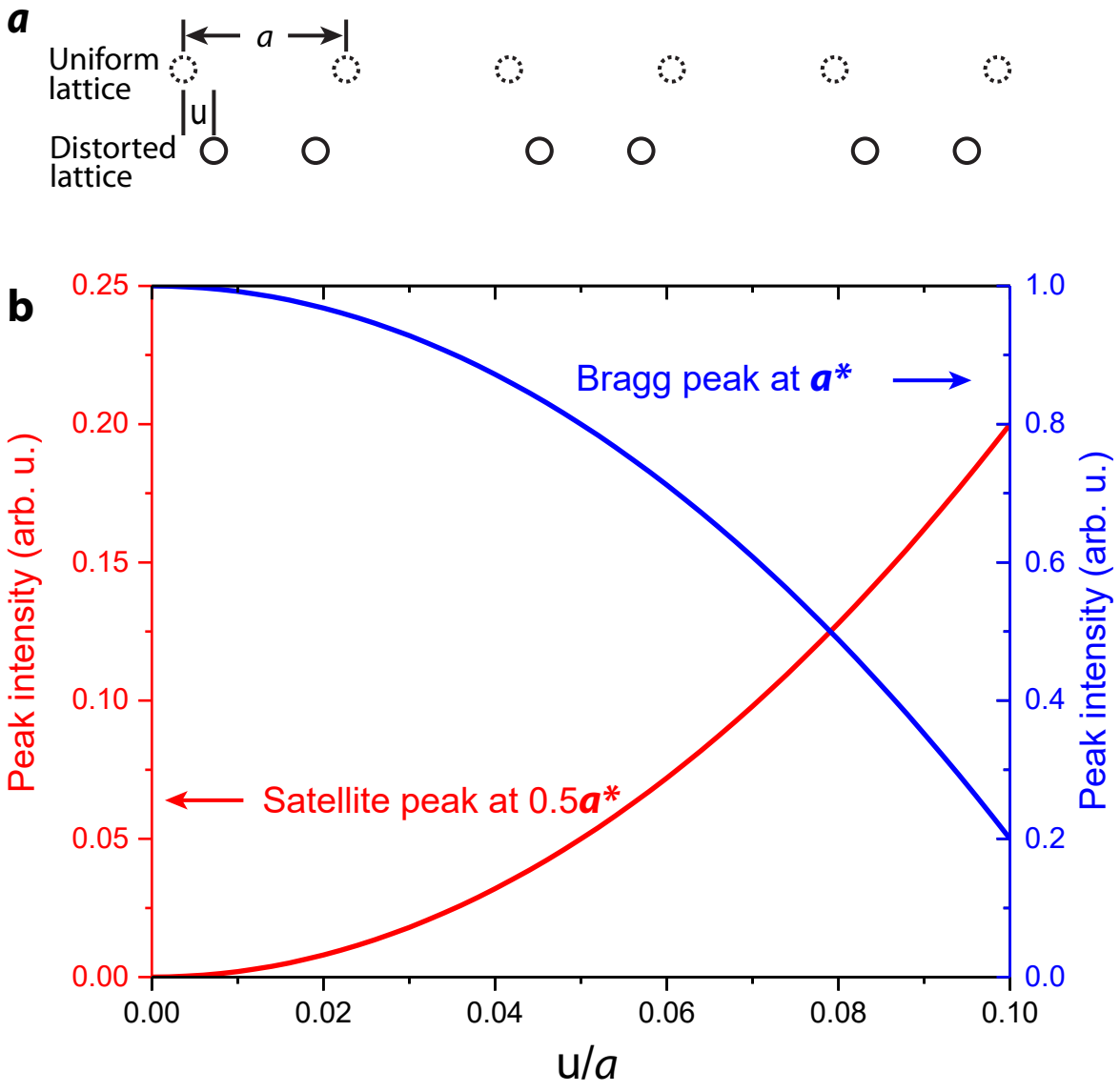

Figure 2.5: The intensities of Bragg peak and satellite peak for a dimerized 1D atomic chain. **a**, Dimerization of a linear atomic chain. **b**, Bragg peak and satellite peak intensity evolutions as a function of relative distortion amplitude u/a.

So the satellite peak is

$$\begin{aligned} I_{CDW} &= 4f^2 \sin^2\left(2\pi(h+\frac{1}{2})\frac{u}{a}\right) = 2f^2[1-\cos\left(4\pi(h+\frac{1}{2})\frac{u}{a}\right)] \\ &\approx 4f^2[4\pi^2(h+\frac{1}{2})^2\frac{u^2}{a^2}], \end{aligned} \tag{2.23}$$

where an approximation is made for small distortions: $1-\cos\left(4\pi(h+\frac{1}{2})\frac{u}{a}\right) = \frac{1}{2}[4\pi(h+\frac{1}{2})\frac{u}{a}]^2$. From this result, the satellite peak intensity is proportional to distortion squared. For the same distortion u, the satellite peak intensity also changes more with increasing scattering angle $(h+\frac{1}{2})^2$.

The intensity evolution of the Bragg peak and satellite peak is plotted in Fig. 2.5 as a function of the relative distortion amplitude u/a.

2.1.5 Diffraction from imperfect crystals

In previous discussions, diffraction is on perfect crystals: the sample has no atomic vibrations; lateral size is infinitely large; the sample is thin enough to justify that there is only single elastic scattering events; there is no defects or disorders in the sample.

Here, we will discuss three aspects of lattice imperfections:

1, temperature effect, lattice vibrations, or in other words, Debye-Waller effect;

2, finite sample size effect;

3, effect of strains, disorder, or defects.

Debye-Waller Effect:

Consider the structure factor in Eq. 2.11, the atomic coordinate now is no longer a constant but instead time-dependent: $\boldsymbol{r}_j(t) = \boldsymbol{r}_j + \boldsymbol{u}_j(t)$, where $\boldsymbol{u}_j(t)$ is the j^{th} atomic distortion away from equilibrium position $\boldsymbol{r}_j$. Since they are random atomic vibrations and each atom is independent, the time average of the structure factor can be written as

$$\Psi(\boldsymbol{s}) = \sum_{j=1}^{N} f_j e^{-i\boldsymbol{s}\cdot\boldsymbol{r}_j}\langle e^{-i\boldsymbol{s}\cdot\boldsymbol{u}}\rangle. \tag{2.24}$$

The scattering intensity has an additional factor compared with Eq. 2.12

$$I_{DWF}(\boldsymbol{s}) = \langle e^{-i\boldsymbol{s}\cdot\boldsymbol{u}}\rangle^2 \sum_{j=1}^{N}\sum_{k=1}^{N} f_j f_k e^{-i\boldsymbol{s}\cdot(\boldsymbol{r}_j-\boldsymbol{r}_j)} = \langle e^{-i\boldsymbol{s}\cdot\boldsymbol{u}}\rangle^2 I_0(\boldsymbol{s}). \tag{2.25}$$

Mathematically, if $\boldsymbol{s}\cdot\boldsymbol{u}$ is small or u follows a Gaussian distribution, then $\langle e^{-i\boldsymbol{s}\cdot\boldsymbol{u}}\rangle = e^{-\frac{1}{2}\langle(\boldsymbol{s}\cdot\boldsymbol{u})^2\rangle}$. So the term $\langle e^{-i\boldsymbol{s}\cdot\boldsymbol{u}}\rangle^2$ in Eq. 2.25 becomes: $e^{-\langle(\boldsymbol{s}\cdot\boldsymbol{u})^2\rangle}$. This term is called the Debye-Waller factor (DWF)

$$DWF = e^{-\langle(\boldsymbol{s}\cdot\boldsymbol{u})^2\rangle}. \tag{2.26}$$

If the system is isotropic, then the average of $\langle(\boldsymbol{s}\cdot\boldsymbol{u})^2\rangle = s^2\langle u^2\rangle|\cos\theta|^2$ over spherical 4π is $\frac{1}{3}s^2\langle u^2\rangle$. The DWF is reduced to a simpler form

$$DWF = e^{-\frac{1}{3}s^2\langle u^2\rangle}. \tag{2.27}$$

From the DWF expression, we can see it is s- or q-dependent. At large s, the DWF is smaller so Bragg peak intensity is attenuated more. In the $-\ln(I(s))$ vs. s plot, the curve is quadratic.

Another important thing to note is that thermal vibrations or DWF only attenuates the Bragg peak intensity. It does not broaden the peak.

Finite sample size effect:

Consider a lattice of finite size consisting of N parallel planes with each neighboring plane separated by distance a. Then calculated structure factor is the same as shown in Eq. 2.14. With some transformation, it can be written as

$$S(s) = \frac{1}{N}\frac{\sin^2(Nsa/2)}{\sin^2(sa/2)}, \tag{2.28}$$

which gives a series of Bragg peaks at $s_{PK} = 0, 2\pi/a, 4\pi/a, ...$, and peak height N.

To determine the peak width (FWHM), assume at $s = s_{PK} + \Delta s$, the peak is at half height of $N/2$. The solution for this would be: $Na\Delta s = 5.56$.

The peak's FWHM β (after deconvoluting the instrumental width) in radians is correlated with Δs by: $\beta = 2\Delta s / \frac{ds}{d\theta} = 2\Delta \frac{4\pi}{\lambda} \cos(\theta_b)$, where θ_b is the Bragg angle. Comparing this with $Na\Delta s = 5.56$, we get the following relation

$$\text{particle size: } p = \frac{0.88\lambda}{\beta \cos(\theta_b)}. \tag{2.29}$$

This equation is called the Scherrer equation. This can be generalized to equation

$$\text{particle size: } p = K \frac{\lambda}{\beta \cos(\theta_b)}, \tag{2.30}$$

where K is dimensionless shape factor. The typical value of K is 0.9 but varies with the actual shape of crystalline and crystal symmetries.

With finite particle size, from Eq. 2.28 and Eq. 2.30, we can conclude that with decreasing crystal size, peak amplitude is decreasing while peak width is increasing.

Effect of strains, disorder, or defects:

In materials with defects or disorder, there will be strains around the defects. Such strain will cause atoms to move away from perfect positions, thus broadening the Bragg peak.

Quantitatively, there have been a lot of derivations on the strain effect, refer to Refs. [73–75]. The effect can be summarized by the following relation

$$e = \frac{\beta}{2 \tan \theta_b}, \tag{2.31}$$

where e is a measure of the micro-strain distribution, β is the FWHM of the Bragg peak in radians after deconvoluting instrumental width, θ_b is the Bragg angle.

With a perfect crystal and ideal scattering event, the Bragg peak is an infinitely sharp Delta function. But with these crystal imperfections, the peak is broadened to finite width with some kind of profile. A lot of times, assuming a Lorentzian profile of the finite size and strain effect gives a relatively good fit. By combining the instrumental broadening, which is usually a Gaussian profile, the real peak profile is usually a combination of Gaussian and Lorentzian, i.e. a Voigt function. So in the following chapters when fitting peak width to extract correlation length, etc, a Voigt function is used for the fitting.

2.2 Ultrafast electron diffraction

One of the ultimate dreams in the scientific community is to watch the motion of atoms or electrons. To fulfill such a dream, scientists have been designing experimental tools to improve the time resolution of various measurements.

After the construction of the first laser in 1960, the field of lasers grew exponentially from the 1960s to 1980s. The idea of using ultrafast electron diffraction (UED) to study chemical reactions was first proposed by Prof. Ahmed Zewail in 1991 [76], then experimentally demonstrated in the following several years [77–80]. Over the past 25 years, UED has blossomed into a multi-disciplinary field that has been applied to chemistry, biophysics, condensed matter physics, accelerator physics, and material science, etc.

Ultrafast electron diffraction is a pump-probe technique that uses a laser pulse to excite the sample, which defines the *time-zero*, then uses a short electron bunch to probe the subsequent structural changes induced by the laser in real time.

2.2.1 Pump-probe technique

Particles (electrons, atomic ions or phonons, etc.) in materials can get excited, interact with each other, or propagate through the sample medium to transport heat or electricity. Such excitation or interaction processes take place from fs to ns scales. To better understand these ultrafast processes at microscopic scales, there is a need for a tool that is fast enough to capture these processes.

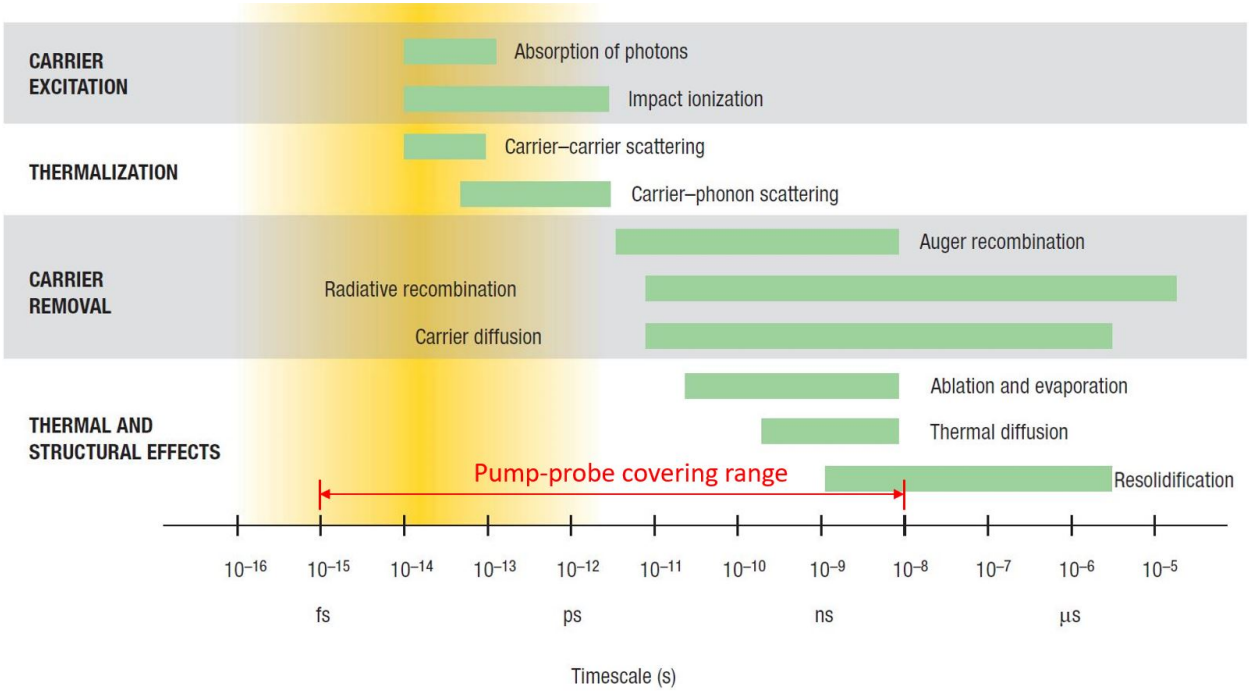

Figure 2.6: Timescales of different electron and lattice processes after laser excitation [5]. Each green bar represents the typical time scales and may vary for different materials and different excitation conditions.

A famous example in history similar to this is the "horse galloping" problem in 1878. People at the time were trying to solve the argument of whether a race horse's feet were actually all off the ground at any single time during a gallop. This problem was solved by the development of instantaneous photography technology, with which they could actually capture the whole course of the horse's motion in real time and solve the debate definitely.

Similarly, to capture the microscopic interaction processes in real time, we need to have a "camera" that is fast enough to resolve the material responses in fs scales. Fig. 2.6 (adapted from Ref. [5]) summarizes the characteristic timescales of microscopic interaction processes after fs laser pulse excitation.

Of course, there is not a mechanical camera capable of such a fast response. To achieve fs resolution, scientists have come up with the idea of a "pump-probe" scheme, in which one uses a fs laser pulse to first perturb the system, which defines a *time-zero*, then uses another short pulse to probe the subsequent parameter changes. The probe pulse could be a fs laser pulse (THz pulse, visible, or X-ray, etc.), or a fs electron pulse. The overall time resolution of this pump-probe technique is the convolution of pump and probe pulse lengths. After deconvoluting the instrumental resolution width from the experimental data, we can get the intrinsic response of the material.

The typical interaction between probe pulse and material depends on the probe type and the interpretation could be different. For example, THz pulses mainly interact with conduction electrons, thus giving direct information on a material's conductivity. UV or soft X-ray pulses can photo-emit electrons from the material surface, the energy vs. momentum relation of the photo-electrons is key to resolve electronic behavior near the Fermi surface. On the other hand, hard X-rays or high energy electron pulses directly map out the lattice vibrations and atomic movements.

Fig. 2.7 is a simplified schematic drawing of the UED setup.

In conventional transmission electron microscopy (TEM), the system has been optimized in the source, optics, and detector such that it can routinely obtain an image spatial resolution of 0.4 Å (Ref. [81]) and an energy resolution of sub-20 meV (Ref. [82]). But the time resolution in conventional TEMs is typically limited to the camera's acquisition speed.

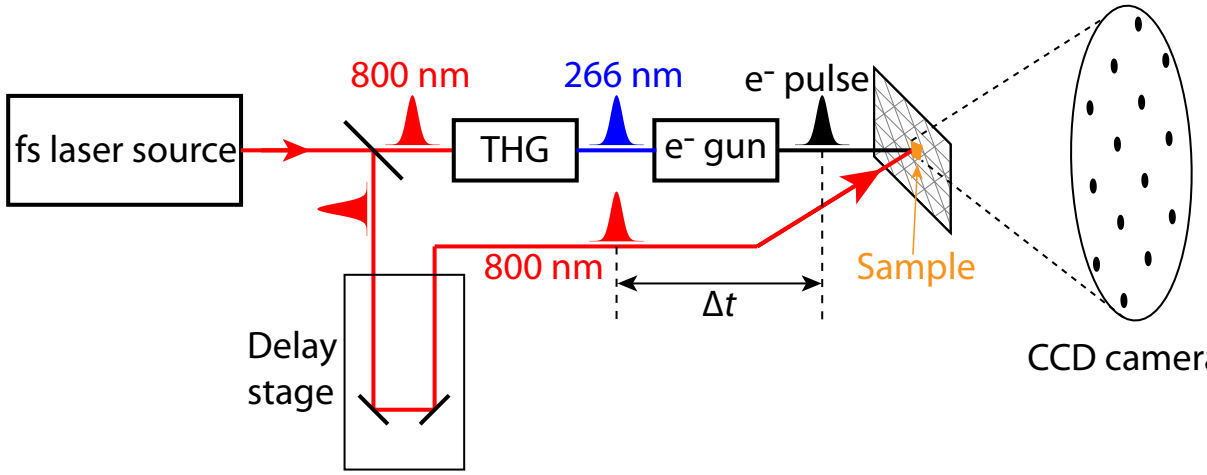

Figure 2.7: The schematic drawing of ultrafast electron diffraction experimental setup. Near-infrared 800 nm laser pulse is split into two paths: one goes through an optical delay stage to serve as a pump pulse, the other goes through third-harmonic generation (THG) to generate ultraviolet (UV) laser pulse for electron pulse generation. Of course, this is just a way simplified schematic drawing. Electron gun, sample, and CCD camera have to be in ultra-high vacuum (UHV) chamber. The electron optics, such as magnetic lens and radio-frequency (RF) cavity, are also omitted out in here.

In a UED setup, to achieve a good time, spatial, energy resolution, the key lies in improving the probe electron pulse characteristics. Several different approaches are adopted to improve on this. For example, to have a good time resolution, one can employ an RF cavity to longetudinally compress the electron pulse to overcome the space charge effect, or accelerate electrons to relativistic energies. To have a high coherence length or high brightness, we can either use a tip source or optimize the photo-emitted laser pulse and electron optics. Table 2.1 lists a few approaches in optimizing the UED and UEM (ultrafast electron microscopy) systems.

A compact UED setup has the advantage of a relatively simple instrumental design, and a moderate bunch electron number. But the time resolution is usually limited by the space charge effect when pushing for a high intensity.

The few-electron UEM system takes advantage of the existing TEM electron optics and

Method	**Groups**	**Rep. Rate**(kHz)	N_e	E_k(keV)	τ (ps)
Compact UED	MSU/Toronto-Max Planck Inst.	1	10^3	50	≤ 0.5
Few e^- UEM	Caltech	10^4	5	100	0.8
RF UED(M)	MSU/McGill	1	10^6	100	≤ 0.1
Low-energy UED	Göttingen	10	100	0.4	2
MeV UED	SLAC	0.12	10^5	3000	≤ 0.1
DTEM	LLNL	10^{-3}	$> 10^9$	200	10^4
FEL (X-ray)	SLAC	0.12	$\sim 10^{13}$	5	0.05

Table 2.1: Comparison of several typical UED/UEM techniques and some typical parameters. The Group column just list one or two groups as examples and definitely not a complete list. All the numbers are typical numbers and may not represent a specific system. N_e is electron number per pulse. E_k is the electron kinetic energy. τ is electron pulse duration.

has a relatively good time resolution. The disadvantage lies in the low bunch electron number and the required high repetition rate that may not be suitable for some experiments.

The RF-enabled UED or UEM utilizes a large number of electrons per bunch and can also achieve a very good time resolution. It is one of the actively developed forefront techniques in the ultrafast community.

For a low-energy UED system with a sharp electron source, it has a relatively high transverse brightness to afford a high coherence length beam without demanding electron optics. The disadvantage lies in relatively poor time resolution, a low electron number, and the electron-laser velocity mismatch problem.

The relativistic MeV UED system is proven to be capable of delivering high-intensity

beams with a very good time resolution. It is also one of the cutting edge techniques at the current stage. The disadvantages may lie in the high-cost instrumentation, the high demand on electron optics, and a relatively low repetition rate compared with the RF-enabled UEM.

The dynamical-TEM (DTEM) is a different branch compared with the above described methods. DTEM pushes for a high bunch electron number, a high spatial resolution, and capabilities for the single-shot imaging or diffraction experiments by operating in the ns timescales.

In Table 2.1, the free electron laser (FEL) is also listed mainly for comparison. The FEL is the state-of-the-art facility-based technique that generates extremely high-brightness and ultrashort pulsed X-rays. The FEL X-ray source can be used for both spectroscopy and diffraction.

2.2.2 Data interpretation in ultrafast electron diffraction

Diffraction patterns are Fourier transform of the real space lattice distribution. So in theory, any change induced by a pump laser will be reflected in the diffraction pattern. Up to now, we have discussed a few key aspects related to diffraction. These are the guiding principles for analyzing diffraction data. For example, for single crystal diffraction patterns, peak shift usually corresponds to lattice constant change; Bragg peak intensity change usually comes from either the structure factor change or the DWF. Peak width would usually correspond to the formation of defects and correlation length change. Diffusive background in-between Bragg peaks is from inelastic scattering and has valuable information on lattice phonons. Next I will give a few UED experiments from other groups to demonstrate each case.

Peak position shift:

Laser excitation may result in sample symmetry change. For example from orthorhombic

to tetragonal lattices, such a transition involves a lattice constant change and results in Bragg peak position shift. Sometimes, optical excitation can also cause lattice expansion or contraction. As shown in Fig. 2.8 (Ref. [6]), the authors performed experiments on graphite. The incident electron beam has a certain angle relative to the graphite c-axis, so the peak with (hkl) indexes of $l \neq 0$ can be monitored to check the inter-layer spacing change. In this case, they observed inter-layer spacing, c ,increases, accompanied by the lowest order longitudinal acoustic phonon mode (sometimes called the breathing mode).

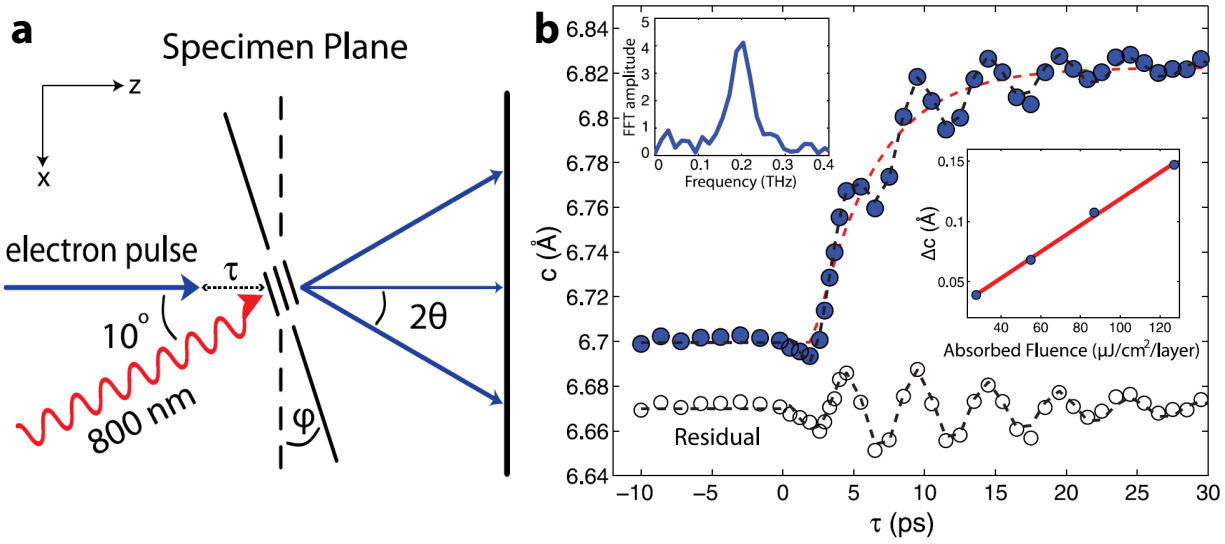

Figure 2.8: The laser-induced lattice constant change in graphite captured by ultrafast electron diffraction [6]. **a**, Experimental geometry. **b**, Lattice constant c change and the excitation of the breathing mode phonon.

Peak intensity structure factor analysis:

Atoms are confined in the lattice with specific arrangements by Coulomb interactions. After absorbing photons with electronic excitation, the overall energy landscape will change, so as the atomic positions. Such atomic movement can be tracked in diffraction patterns and simulated based on structure factor calculations. In Fig. 2.9 (Ref. [7]), the authors examined the intensity change of many Bragg peaks and came up with the idea of inter-layer

shear phonon modes. By writing down the structure factor considering shear phonon modes, the simulated peak intensity changes agree with the experimental data quite well. So the shear displacement can be extracted and further used to explore the intricate physics in this topological quantum material.

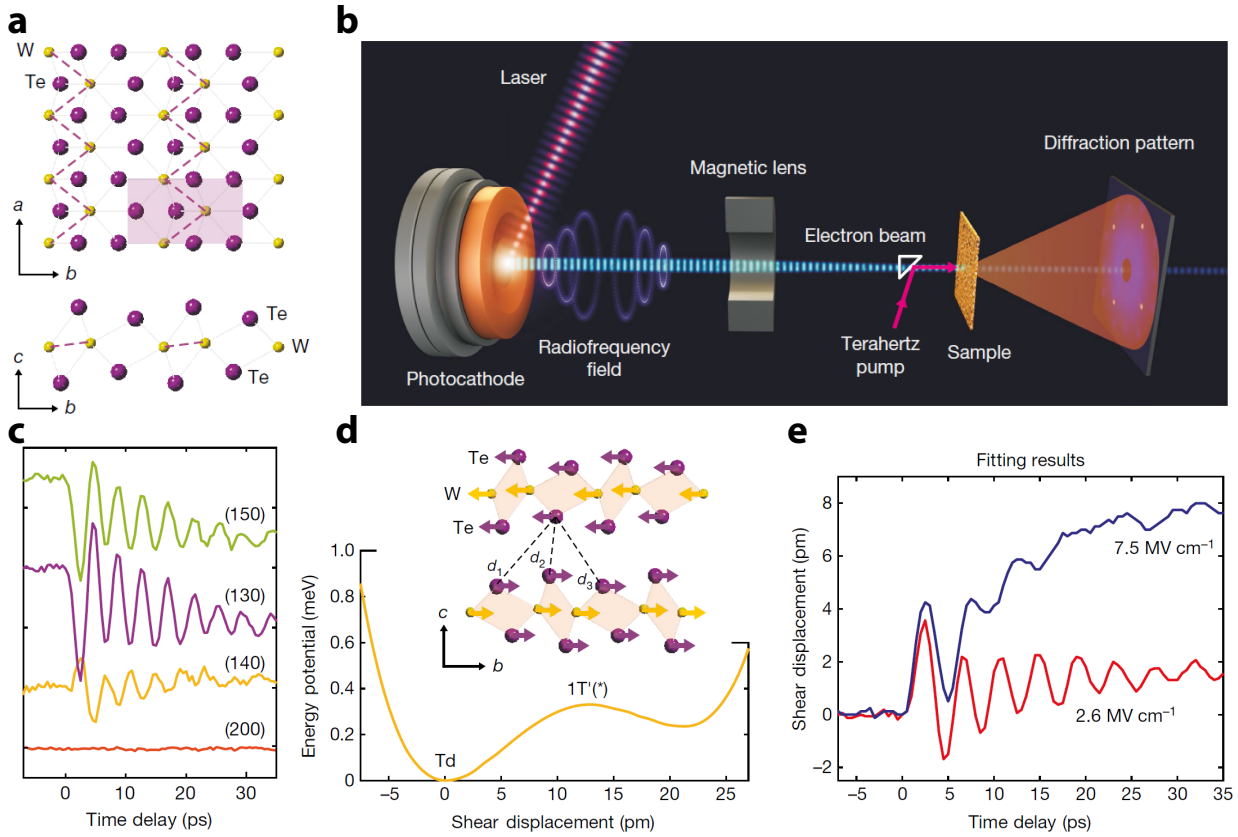

Figure 2.9: MeV ultrafast electron diffraction experiment on Weyl semimetal WTe_2 [7]. **a**, Lattice structure of layered WTe_2. **b**, Experimental setup. THz pump, MeV electron probe is employed in the experiment. **c**, Responses of different Bragg peaks. **d**, Schematic drawing of the energy potential with changes of the shear distortion. **e**, The time-dependent shear distortion at two different pump fluences.

Peak intensity Debye-Waller analysis:

As discussed earlier, in photo-induced phase transitions (PIPT) in almost any system, electron phonon coupling will show up as an electronic energy relaxational channel. Such a coupling results in coherent or incoherent phonon excitations and thermal heating in the

system. The thermal effect is manifested as Debye-Waller effect in the diffraction patterns. In Fig. 2.10 (Ref. [8]), the authors study a simple system, polycrystalline copper. By examining the Bragg peak intensity changes at different q values and different time delays, they are able to track the sample temperature evolution at different times and fluences with a simple two-temperature model. Such a study allows them to determine the electron phonon coupling strength and thermal transport rate for copper.

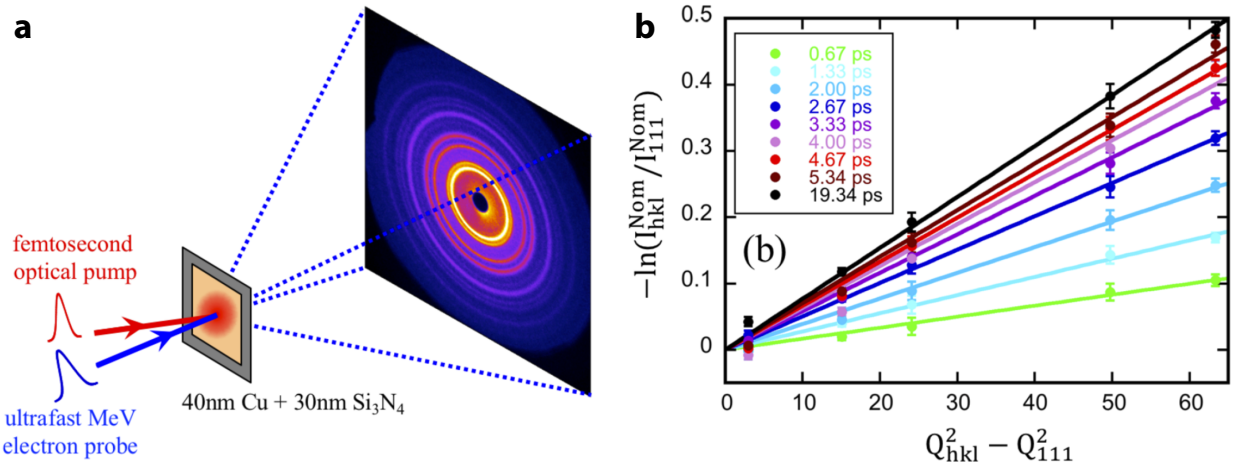

Figure 2.10: The Debye-Waller effect and electron-phonon coupling analyses in polycrystalline copper [8]. **a**, MeV UED pump-probe experimental setup. **b**, The Debye-Waller analysis of Bragg peaks at different q-values and different time delays.

Peak width correlation length analysis:

Crystal defects induce strains in the sample and reduce the correlation length of the system. Such an effect manifests as peak broadening in diffraction. Correlation length is one of the key parameters in tracking phase transitions and it can be deduced from the peak width analysis. In Fig. 2.11 (Ref. [9]), the authors used an ultrafast low-energy electron diffraction method to study phase transitions in a CDW material 1T-TaS_2, in which they monitored the peak width evolution and extracted the corresponding correlation length of the new phase. It is found that a 1/2 power-law increase is independent of the pump fluence. Such

a correlation growth is attributed to decay of CDW dislocations based on a time-dependent Landau-Ginzburg theoretical modeling.

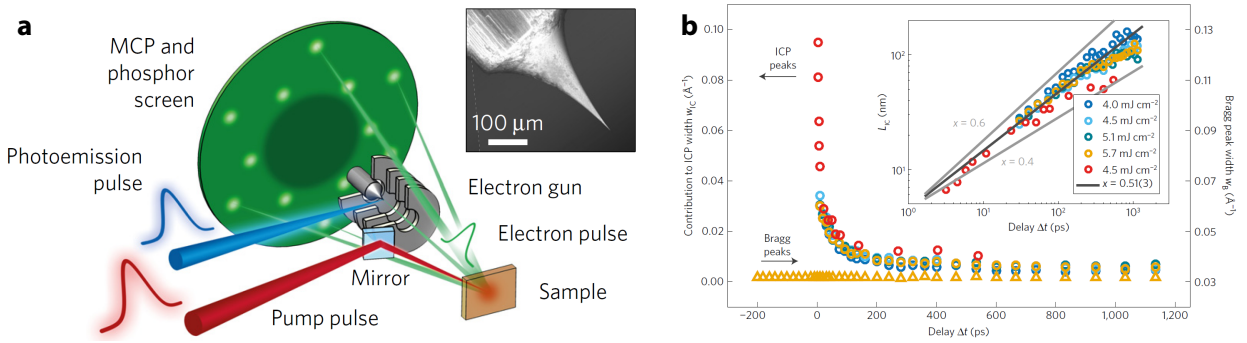

Figure 2.11: The correlation length analysis in a phase transition in CDW material 1T-TaS_2 [9]. **a**, The ultrafast low-energy electron diffraction setup. **b**, The growth of correlation length follows a 1/2 power-law scaling growth.

Diffusive scattering background phonon analysis:

Phonons are lattice vibrations with certain energy and momentum. They interact and transfer energy/momentum with probing particles like X-ray photons, electrons or neutrons. For example, one of the most noticeable phonons in graphite is the in-plane E_{2g} phonon at Γ point. It shows up in the Raman spectrum and has a frequency of 1582 cm^{-1}, corresponding to an energy of 190 meV. This is among the highest energy phonons. Other phonons could have energy of less than 1 meV. For phonons with such energies, the transferred energy or momentum to the high-energy electron probe particles is very small and hard to detect. So normally, such optical phonons are be detected by Raman spectrum. Meanwhile, the phonon spectrum can be mapped out by low-energy (meV) neutron scattering or high precision inelastic X-ray scattering. An alternative approach to probe phonons is through diffusive scattering. With ultrafast electron diffraction, it is now possible to map out the momentum-dependent phonon responses in the Brillouin zone (BZ) through the differential difference method.

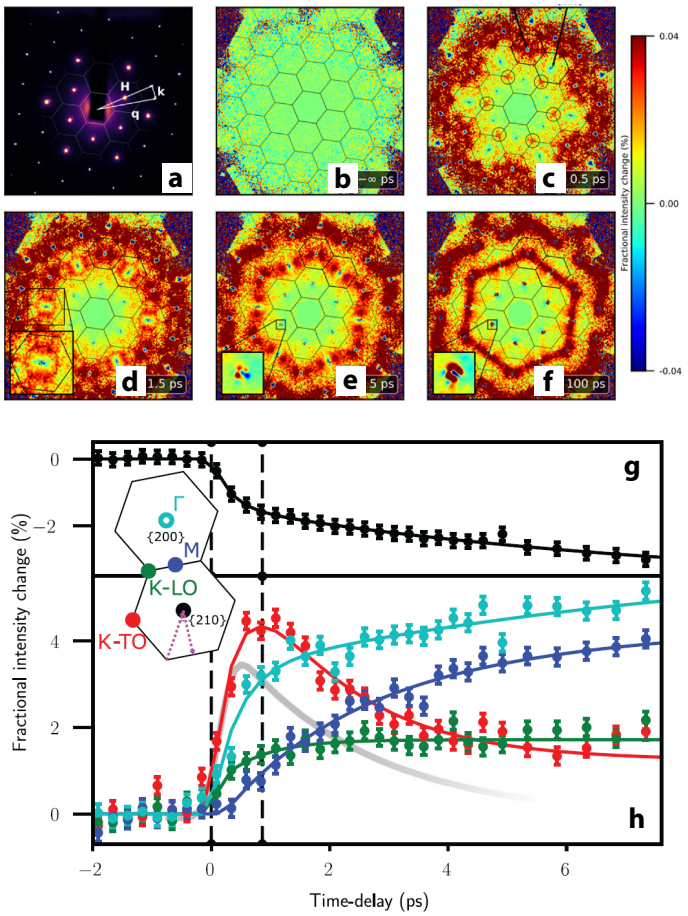

Figure 2.12: The diffusive scattering background phonon analyses in graphite [10]. **a**, Original diffraction pattern of graphite with electron beam along the *c* axis. (**b-f**), The difference of diffraction patterns at different time delays showing diffusive scattering background evolution. **g**, The dynamics of Bragg peak (2 1 0). **h**, The dynamics of diffusive scattering background at different points of the Brillouin zone, corresponding to different phonon branches in graphite.

In Ref. [10], the authors demonstrated the ability of UED for mapping the momentum-dependent phonon relaxations across the entire BZ by following the diffusive scattering patterns. As shown in Fig. 2.12, the phonon momentum transfer at different BZ positions are identified along with their time evolution. Such a time-dependent study may reveal the energy flow in graphite.

Chapter 3

Observation of an emergent bi-directional order in $CeTe_3$

Spontaneous symmetry breaking (SSB) is one of the most common phenomena in physics. For example, during metal-to-superconductor, paramagnetic-to-ferromagnetic, metal-to-charge or spin-density wave transitions, they all involve SSB by breaking a certain kind of symmetry. By lowering the system temperature across T_c, the system goes to a lower symmetry and lower energy state. On the other hand, with laser excitations, the system absorbs energy and typically goes to a higher symmetry state. For instance, with fs laser excitation, researchers studied ultrafast melting of the charge- or spin-density waves, or melting of certain magnetic orders. However, it is rare to see laser-induced superconductivity, laser-induced charge or spin-density waves, etc. Here in this chapter, we will show such an example of laser-induced new symmetry-breaking route and exploration of the hidden states in a CDW system.

In this chapter, I will first give a little background on the materials in Sec. 3.1. The ultrafast results will be presented in Sec. 3.2. More discussions will follow in Sec. 3.3. Then a quick summary is given in Sec. 3.4.

3.1 Background and properties of $CeTe_3$

$CeTe_3$ belongs to a class of materials called rare-earth tritellutrides ($RETe_3$), with rare-earth elements in the lanthanide series. The $RETe_3$ series share the same structure, as shown in Fig. 3.1a. It consists of Te square nets sandwiching the corrugated RETe plane and CDW emerges within the Te planes (Fig. 3.1b). Bands near the Fermi surface (FS) in the Te layer are partially filled by Te 5p electrons. Due to the perpendicular hopping ($t_\perp$ in Fig. 3.1c), the FS (Fig. 3.1d) is in a warped diamond shape rather than perfect square. From photoemission studies [83, 84], the FS structure has parallel portions and the FS nesting vector matches well with the CDW wave-vector, suggesting that the CDW is most likely driven by FS nesting. The nesting vector is drawn in the figure.

The crystal structure of $RETe_3$ is slightly orthorhombic such that a and c axes are not equivalent. For light rare-earth elements like La, Ce, Sm, and Gd, the atomic radius is large and only one CDW is observed along c axis. For heavier elements with smaller atomic radius, the CDW is observed to be shown in both directions at different temperatures (see Fig. 3.1e). There is a well defined trend of transition temperature under chemical pressure [85]. For $CeTe_3$ studied here, as seen in Fig. 3.1e, there is only one CDW formed along the c-axis (stripe phase).

In the $CeTe_3$ experiment, we perform experiments on the freestanding thin flakes of single-crystal (Fig. 3.1f), prepared by the scotch tape exfoliation method (details about sample preparation can be found in Appendix A). The sample is exfoliated and transferred to the 1000-mesh gold TEM grid. The sample thickness is characterized by TEM zero-loss EELS to be 30 ± 5 nm. The electron beam is along the crystal b axis [0 1 0], perpendicular to the a-c plane. The high quality sample yields very high signal-noise-ratio (s/n) diffraction

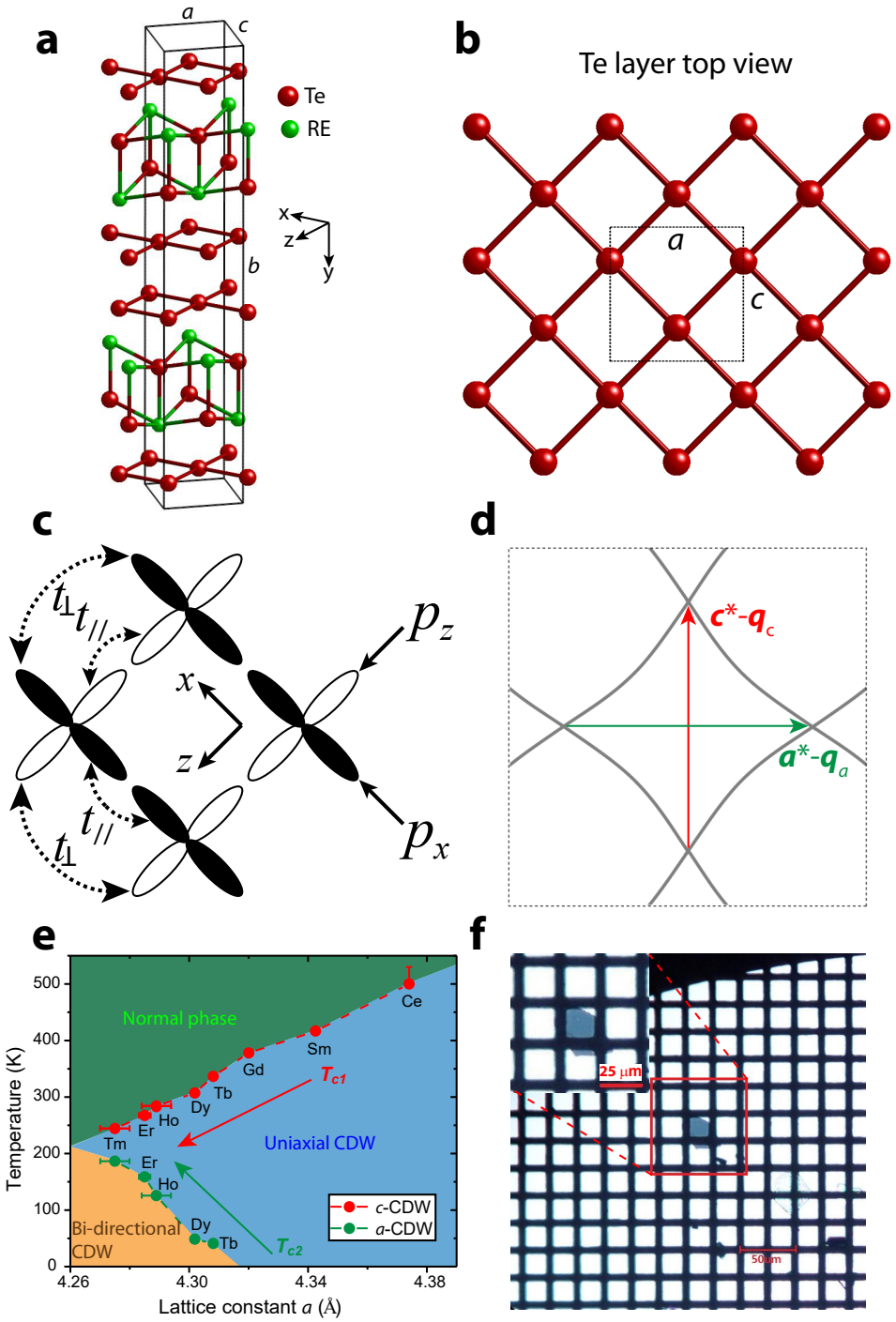

Figure 3.1: Structure, FS, and CDW formation in the $RETe_3$ series. **a**, Ball-stick model of $RETe_3$ structure. The solid cuboid is the unit cell with *a, b, c* labeled. **b**, Top view of the square net Te layer in which CDW is formed. **c**, The electron orbitals in the Te layer are $5p_x$ and $5p_z$ orbitals from Te atoms. **d**, The schematic FS of the square Te net. Dashed line is the BZ boundary. **e**, The transition temperature of different RE elements. **f**, Freestanding thin sample flakes on 1000-mesh gold TEM grid.

patterns, as shown in Fig. 3.2a.

The diffraction pattern of $CeTe_3$ consists of alternating weak and strong lattice Bragg peaks due to its unit cell structure factor: for peak (h 0 l), if $h + l$ is even, then it is a strong Bragg peak; otherwise the Bragg peak is weak, as seen from Fig. 3.2b. In addition, there is a pair of satellite peaks along the weak Bragg peak in the $\boldsymbol{c}^*$ direction, indicating CDW formation along the c-axis. This CDW wave-vector agrees with what was reported earlier [86]: $\boldsymbol{q}_c \approx 0.28\boldsymbol{c}^*$.

Figs. 3.2c&d show the scaled-up view of CDW satellites on the same color scale. Before laser excitation (- 1 ps), satellite peaks only exist at along the $\boldsymbol{c}^*$ axis. After laser excitation (+ 1 ps), the original CDW peaks become weaker. But at the same time, a pair of new satellite peaks are observed along the $\boldsymbol{a}^*$ axis. Such new satellite peak formation is a direct signature of new CDW order along the $\boldsymbol{a}^*$ axis, thus forming a bi-directional CDW that is thermodynamically forbidden.

From the Bragg peak distance analysis, the lattice constant changes in a and c are both within the instrument resolution of 0.05% — much less than the required 1.4% lattice constant change to form bi-directional CDW order (from $CeTe_3$ to $TbTe_3$ in Fig.3.1e). So there is no way that the new CDW formation is due to laser-induced stress or lattice constant change.

3.2 Ultrafast dynamics of $CeTe_3$

The observation of this new CDW order is surprising because such bi-directional CDW order in $CeTe_3$ has been ruled out in the steady-state phase diagram as shown in Fig. 3.1e. We examined the full dynamical evolution of the order parameters. From the result in Fig. 3.3,

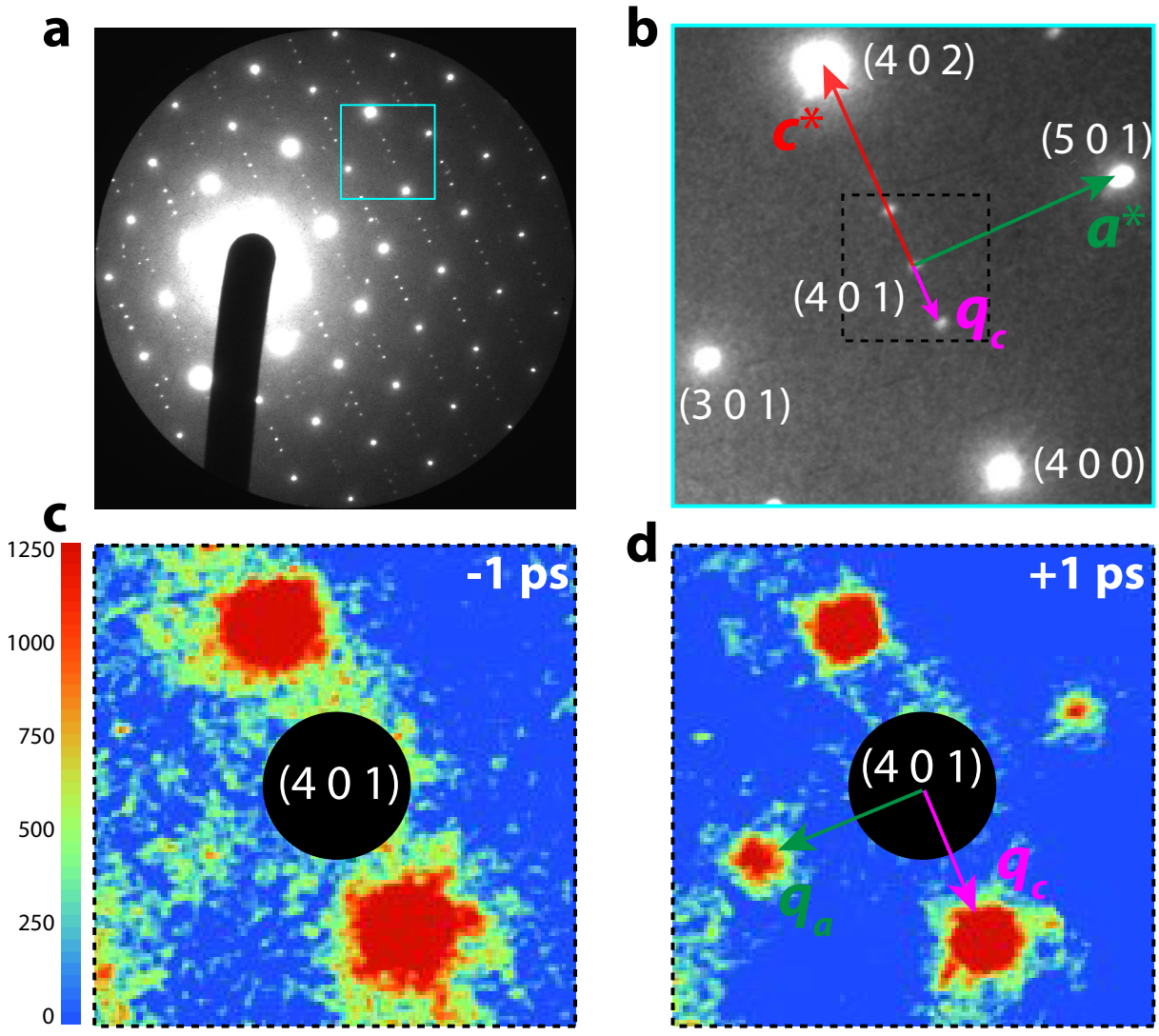

Figure 3.2: The diffraction patterns of $CeTe_3$. **a**, Ground state full diffraction pattern of $CeTe_3$ at RT. **b**, Zoom-in view of the cyan square box in **a**. The Bragg peaks are labeled and Bragg and CDW wave-vectors are also indicated. **c**, Zoom-in view of the black dashed square box in **b** at negative time delay. **d**, The same area as in **c**, but at $+1$ ps after laser excitation. **c** and **d** are in the same scale as indicated by the scale bar on the left. New emergent CDW satellite peaks are clearly observed along the $\mathbf{a}^*$ axis (a-CDW).

the c-CDW peaks get suppressed to $\approx 15\%$ in less than 500 fs then partially recovers to 70% in a time scale of 4 ps. Note, the full recovery to the same state as negative time takes beyond ns range but within 1 ms before the next pump-probe cycle starts. For a-CDW, with a delay of ~ 300 fs after time-zero, it starts to form and the maximum intensity at this

fluence is $\approx 10\%$ of c-CDW intensity at the negative time. As the c-CDW peak partially recovers, the a-CDW intensity also decays, suggesting that the two symmetry-broken ground states are competing.

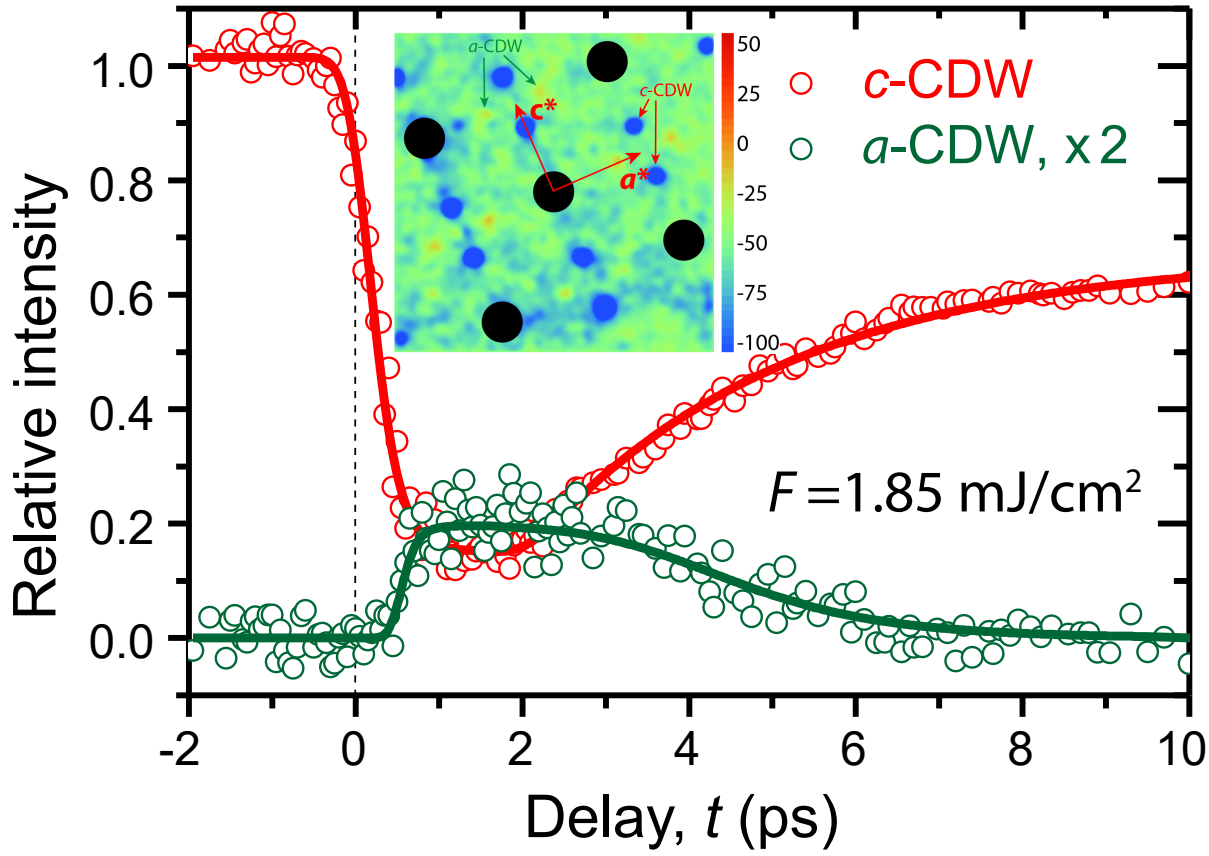

Figure 3.3: The integrated intensity changes of c- and a-CDW peaks. Both c- and a-CDW peak intensities are normalized to the c-CDW intensity at negative time delay. Inset is the difference diffraction pattern: diffraction pattern at $+1$ ps minus that of -1 ps.

Scattering experiments with X-ray, neutrons or high coherence length electrons could measure both the static and fluctuating orders. To better understand this, the peak width, which is a direct representation of the corresponding order's correlation length, is examined. As discussed in Sec. 2.1.5, due to crystal defects, the diffraction peak will be broadened instead of infinitely sharp. In theory, the broadened profile due to imperfections could be

Gaussian, Lorentzian, or more complicated functions, depending on the type of imperfections and assumptions made. But most of the time, broadening with a Lorentzian profile gives a good fit for the presence of inhomogeneities [74]. In this case, while the instrument resolution is typically described by a Gaussian, the CDW peak can be described by a Voigt function, which is a Lorentzian function convoluted with a Gaussian. The CDW peak in Fig. 3.4a would neither be fitted with a Gaussian nor Lorentzian. Only a Voigt function can fit the profile well.

In Fig. 3.4b, the black curve represents a lattice Bragg peak. Due to the infinite correlation length of Bragg peak, the broadened width (Lorentzian width) is close to zero and a Gaussian function can fit the entire peak relatively well. This Gaussian function is set as the instrumental width for deconvoluting other correlation lengths. The other several colored curves in Fig. 3.4b are examples of several peak profiles with different correlation lengths.

In addition, we find that after laser excitation, one single Voigt function does not fit the c-CDW peak well, as demonstrated in Fig. 3.4c. The black curve is single-Voigt function and does not fit the data. Instead, we have to use two-Voigt functions to do the fitting. Red curve is the sum of two Voigt functions and the two individual Voigt functions are in dashed lines. Such two-components fitting is appropriate for describing coexistence of static and fluctuating orders, which occurs when a system undergoes a continuous phase transition [87], where additional broadened peak emerges due to critical fluctuations [87]. However here, as the system is spontaneously quenched across the critical point, strong fluctuations are created due to instability under a new energy landscape. The unstable CDW fields represented by these fluctuations will coarsen over time to form the new broken-symmetry order.

To further look at the fluctuations, we examined the peak intensity at the shoulder region (Fig. 3.5b). It is found that while the peak center (red curve) is decreasing in intensity, the

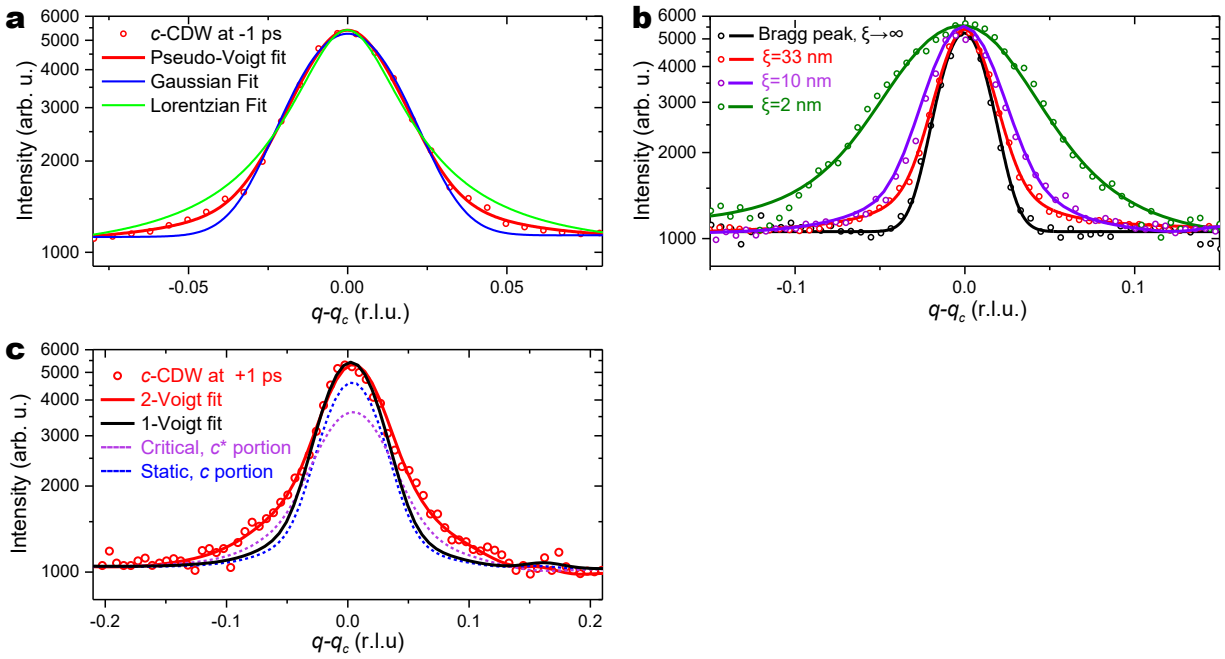

Figure 3.4: The pseudo-Voigt function peak fitting for extracting the correlation length, static, and fluctuating components of a peak. **a**, c-CDW peak at negative time where the fluctuation is small, so a single Voigt function fits it well. Neither a Gaussian nor a Lorentzian would fit. **b**, Voigt function fitting of several CDW peak profiles. The sharpest black curve is a Bragg peak with Gaussian fitting and others are by Voigt function fitting. **c**, c-CDW peak at $+1$ ps, at which a single Voigt function (black curve) does not fit. We have to use two Voigt functions to do the fitting and the two components are in dashed lines corresponding to the static and fluctuating/critical components.

shoulder part (purple curve) normalized to the peak center is actually gaining intensity. Such a phenomenon is indicative of a coarsening process. As seen from the pie chart population change in Fig. 3.5c, the original static order in the blue color is losing population in the first 1 ps, then partially recovers; at the same time, a new c-CDW (hereafter referred as $c^{\dagger}$) in the pink color and a-CDW in green gain population.

Based on KZM, for a initially disordered state after quench, the system goes through the critical point to form an ordered state. Naturally, topological defects would be formed so as to reconcile the phases of the independently grown ordered states in disconnected regions. Such formation of defects could be long-living if the system is rapidly quenched.

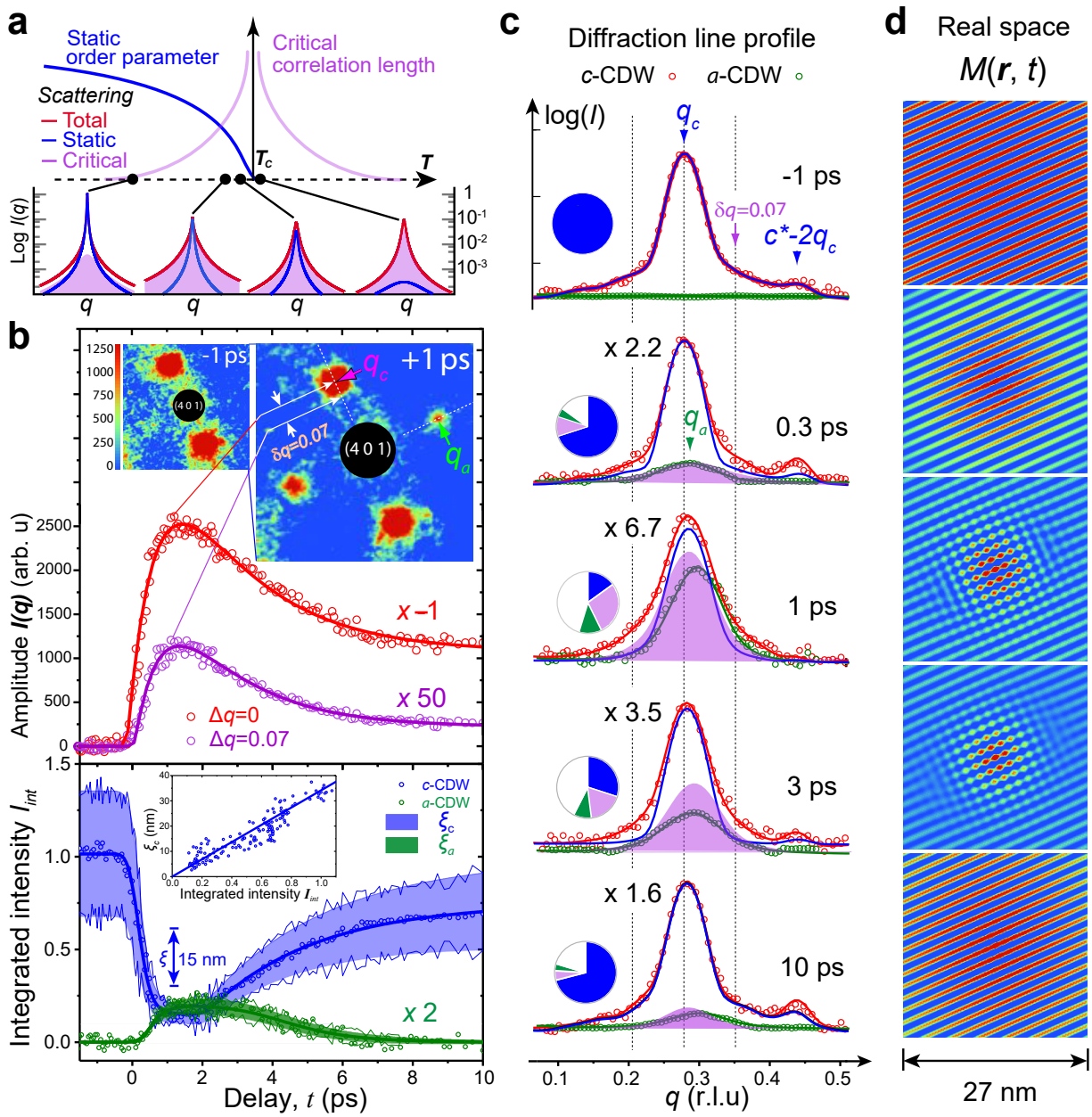

Figure 3.5: Analyses of the fluctuating order and real space reconstruction. **a**, Schematic demonstration of the static and fluctuating orders in correlation length and population near the thermal critical point. **b**, Dynamics of intensity evolution. Top panel is the intensity evolution of peak shoulder ($\delta q = 0.07$) and peak center. Inset are images before and after to show the suppression of c-CDW and appearance of a-CDW. The bottom panel dynamics shows the integrated intensity of c-CDW static portion and a-CDW. Inset shows the linear relation of correlation length and CDW intensity. **c**, Peak profiles and 2-Voigt function fitting. Pie chart shows the population change of each component: blue is c-CDW static part, pink is c-CDW fluctuating order, green is a-CDW portion. **d**, Real space reconstruction based on diffraction patterns, check text for details.

The real-space CDW maps are reconstructed based on the experimental data. First, CDW peak intensities I (a-, $c^{\dagger}$-, and c-CDWs), Q-values, and correlation lengths ξ are extracted from data. Then they are used as input parameters for the CDW order parameters

$$\Psi_e(\mathbf{r},t) = \sum_j \sqrt{I_{int,j}(\mathbf{Q}_j(t))} e^{i(\mathbf{Q}_j(t)\cdot\mathbf{r}+\phi_j)} e^{-\frac{\mathbf{r}-\mathbf{r}_0}{2\xi_j(t)}}. \tag{3.1}$$

For no other good reasons, we simply assign $\phi_j = 0$ and set the reference position $\mathbf{r}_0$ to be at the origin. The real-space CDW map (Fig. 3.5d) is calculated to be

$$M(\mathbf{r},t) = |\Psi_e(\mathbf{r},t)|^2. \tag{3.2}$$

Performing Fourier transform on $M(\mathbf{r},t)$, we can obtain the simulated diffraction pattern (see Fig. 3.6). To refine the reconstruction parameters, simulated diffraction curve is compared with the experimental one (See Fig. 3.5c) by doing the same line scan over the CDW peaks to retrieve the peak profiles.

Besides the change at a single pump fluence, the fluence-dependent responses are also studied and shown in Fig. 3.7. It is found that the a- and c-CDWs have different thresholds with $F_c^{(a)} = 0.6$ mJ/cm^2, $F_c^{(c)} = 1.9$ mJ/cm^2, as indicated in Fig. 3.7b. The a-CDW intensity quickly rises at $F_c^{(a)}$, then plateaus while by contrast, c-CDW intensity drops linearly with fluence in both short and long times.

From the simulation results in Fig. 3.7c, from time zero to 1 ps, the bi-directional orders become more and more prominent. After 1 ps, the bi-directional order starts to "shrink" and decay. Also, topological defects are visible at the bi-directional phase domain boundaries.

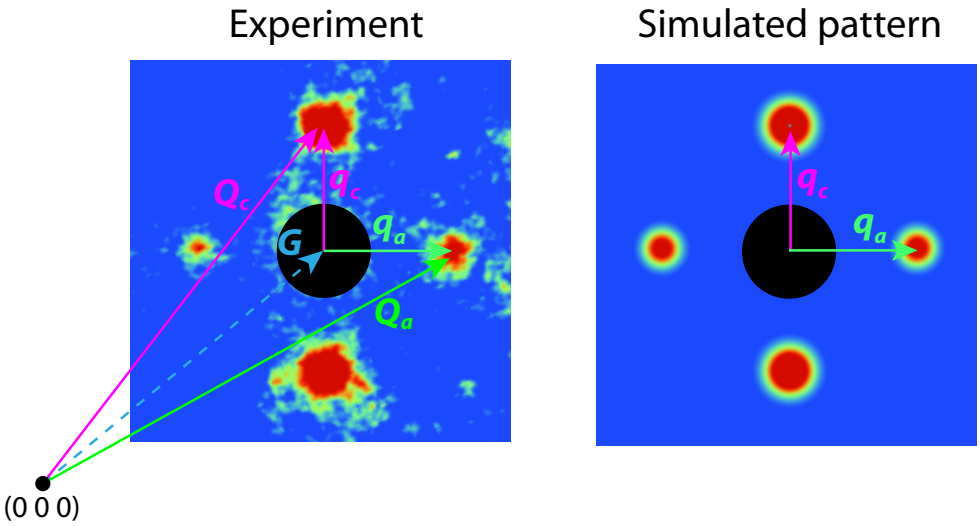

Figure 3.6: Comparison of the experimental pattern with simulated pattern.

3.3 Mechanism for the non-equilibrium phase transition

From previous results, there is clear evidence that a bi-directional phase forms under a nonthermal scenario. But we have not gone into details about why this happens, how we may take advantage of it, and what general implication this experiment might have on other systems.

According to KZM discussed in Sec. 1.2.3, if the system is quenched from a disordered phase to an ordered state at a finite rate, the relaxation time near the critical point would diverge (critical slowing down). As a result, the order parameter might not follow the quench, so there is a lag in the system response, usually behaving as a delay in the growth of the order parameter. Such a delay or lag period is called Kibble-Zurek (KZ) freeze-out time τ_{KZ}. Experimentally, it is not easy to apply a finite rate quench while tracking the order parameter change. The conventional protocol is to track the post-quench topological defect

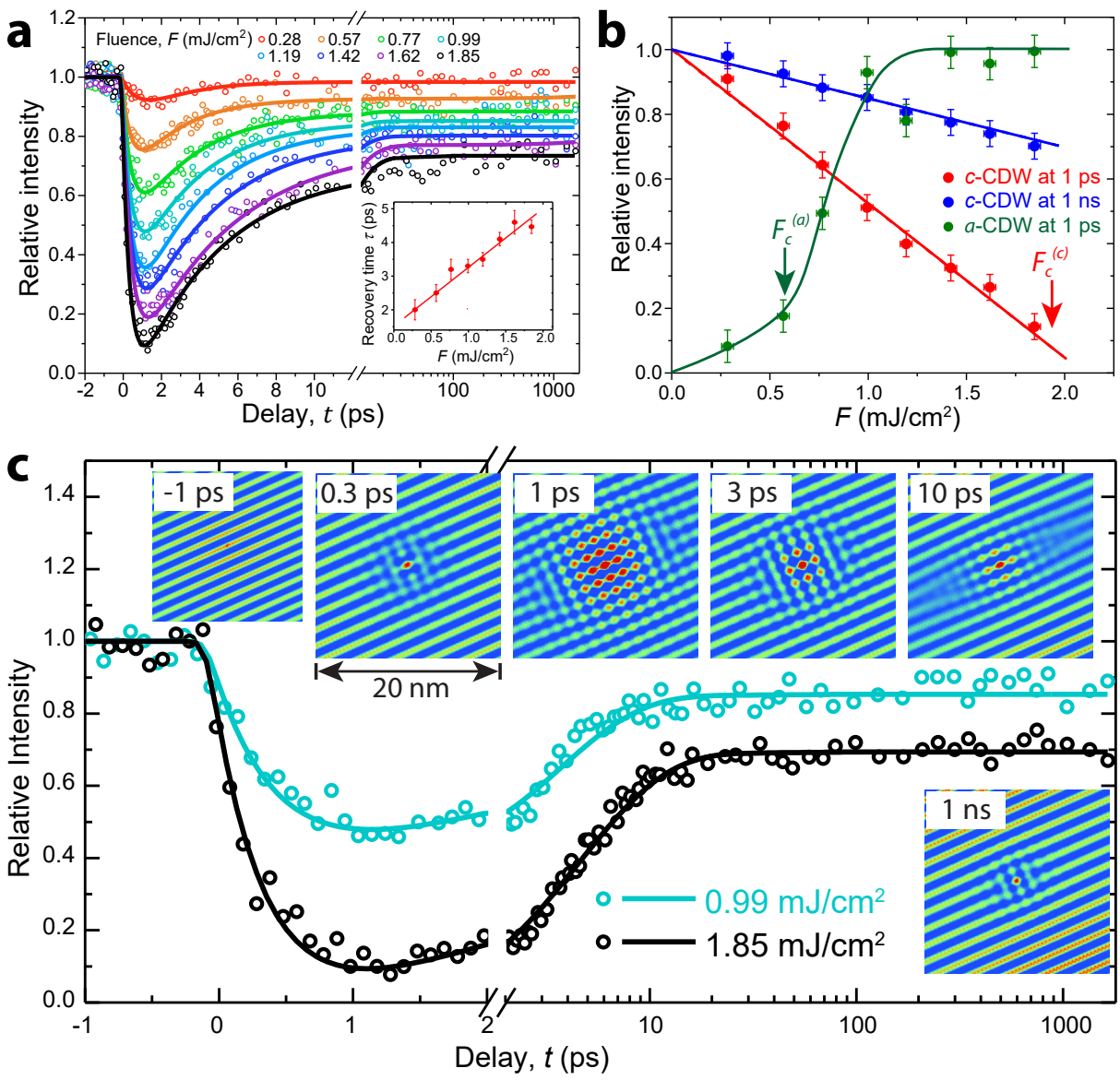

Figure 3.7: The fluence-dependent data and evolution of topological defects. **a**, c-CDW intensity dynamics at different pump fluences. Inset: the characteristic time of the recovery time for c-CDW order at different fluences. **b**, The extracted c-CDW and a-CDW amplitude evolution from fluence scan. The corresponding c- and a-CDW thresholds are indicated. **c**, Dynamics at two fluences above $F_c^{(a)}$. Inset: evolution of topological defects at $F = 1.85$ mJ/cm^2.

density, which is related to the observed correlation length. In this experiment, we have enough time resolution to follow the early non-adiabatic evolution of the order parameter, therefore can shed light on the Kibble-Zurek freeze-out phenomenon.

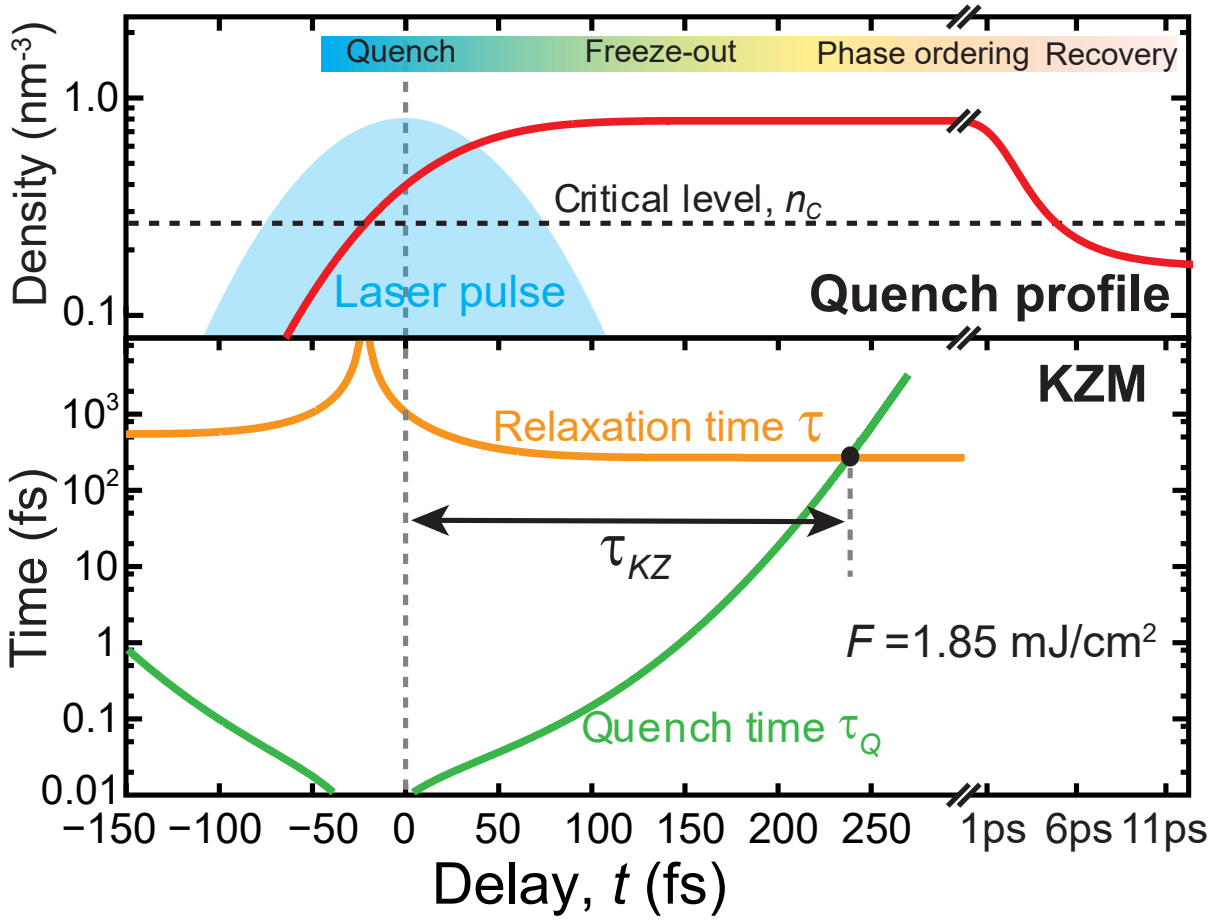

Figure 3.8: Simulations of the quench profile and the Kibble-Zurek freeze-out time.

From Fig. 3.3, after fs quench of the c-CDW state (time-zero), a-CDW order is not immediately formed and there is about 300 fs time delay in the onset of a-CDW ordering. Such a delay, as we will try to explain later, might fit into the KZM freeze-out time hypothesis. Fig. 3.8 is a schematic demonstration of the quench profile and freeze-out time. The top panel is the quench profile and induced carrier density change, which is calculated based on the sample optical constants [88, 89] and the thin film transfer matrix method [90]. The further decay at longer than 1 ps is based on correlation length partial recovery from 1 ps to about 10 ps. In the bottom panel, the orange curve is the relaxation time, calculated based on non-equilibrium relaxation time: $\tau = |\epsilon|^{z\nu}$, where ϵ is reduced temperature: $\epsilon = \frac{T_c - T}{T_c}$. The

green curve corresponds to the quench time, which is inverse of the quench rate at t. When the relaxation rate ($\sim 1/\tau$) catches up with the quench rate, the system becomes adiabatic again.

However, within the freeze-out time, local defects are formed and annihilated, driven by short-range fluctuations. Meanwhile, the coarsening is mediated by the long-wavelength fluctuation to grow to the domain size. At ~ 1 ps, the static a-CDW is established. However, due to the thermalization in the system at longer times, the c-CDW starts to recover and competes with a-CDW. So the a-CDW becomes unstable. But topological defects remain until more than 1 ns as shown in Fig. 3.7c.

Aside from the CDW peaks, we also analyzed Bragg peaks and found interesting dynamics as shown in Fig. 3.9a. From Fig. 2.5, we can see in a CDW system, the Bragg peak and CDW peak intensities are anti-correlated. So in theory, when c-CDW get suppressed, the Bragg peaks along the c-axis should gain intensity, and vice versa for those along the a direction. But in the experiment, what we see is contrary to that: Bragg peak along the a-axis, e.g. peak (6 0 0), gains intensity first then drops; Bragg peak along the c-axis, e.g. peak (0 0 6), has no rise and directly goes down. Such an orthogonal correlation clearly demonstrates that the softened modes associated with both the a- and c-CDWs formations are transverse phonons. This is consistent with a recent density functional perturbation theory study of $RETe_3$, which predicts the soft modes consisting of transverse optical modes [91]. To better explore the CDW formation, we examined all the Bragg peaks of similar s values with peak (6 0 0), as shown in Fig. 3.9a inset.

Bragg peak intensity changes can be treated through the Debye-Waller analysis. Based

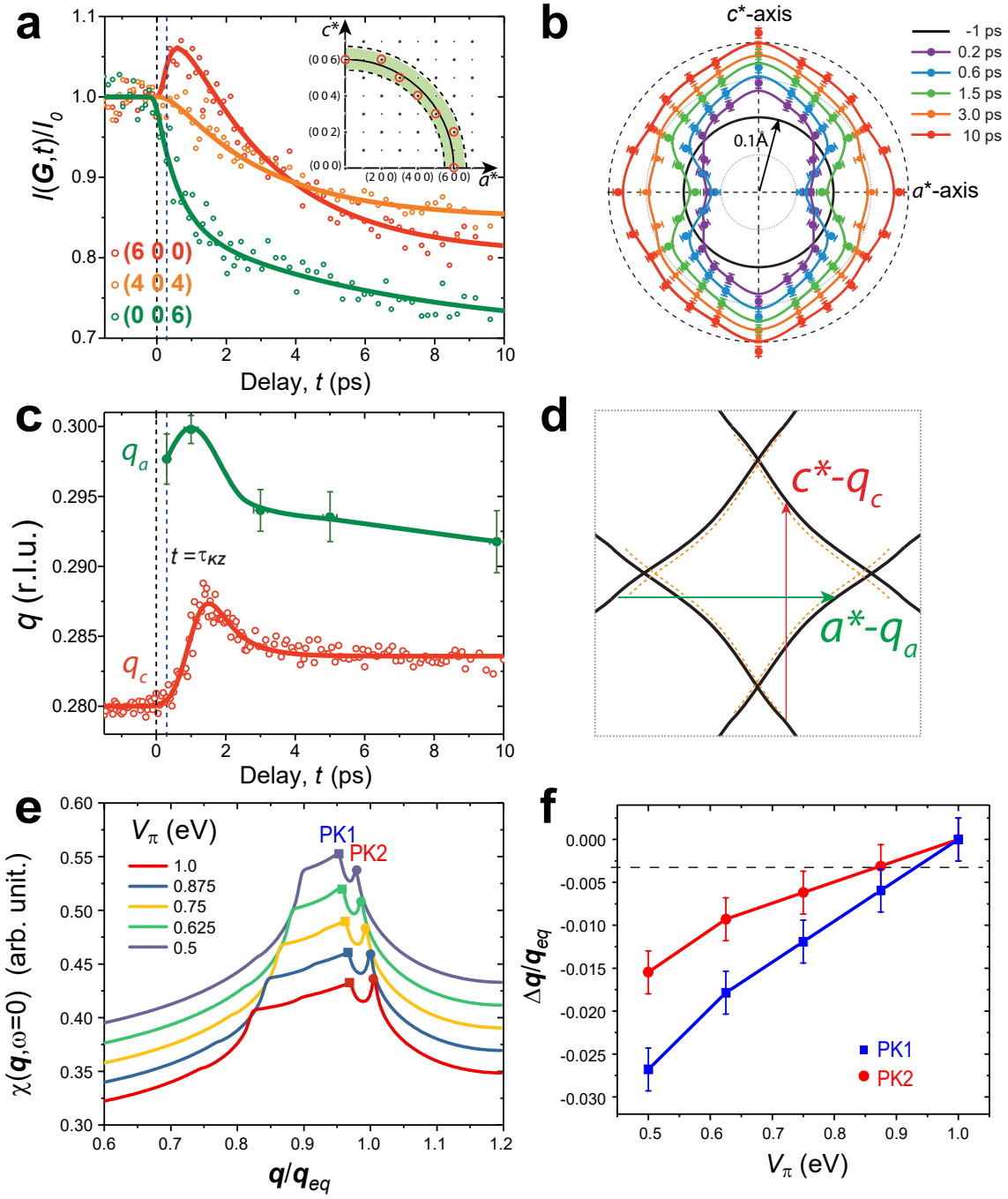

Figure 3.9: The q-dependent Debye-Waller analysis and FSN wave-vector evolution. **a**, Three representative Bragg peaks dynamics at the first 10ps. Inset: the schematic diffraction pattern of $CeTe_3$. Bragg peaks in red-circle in similar s value are used for Debye-Waller analysis in **b**. **b**, the q-dependent Debye-Waller analysis at different time delays. **c**, a- and c-CDWs FS nesting vector changes as a function of time. **d**, Schematic FS structure of the square net Te layer (solid black line). Square gray dashed line is the BZ boundary, dashed orange lines are projected FS change after laser excitation, drawn based on the CDW nesting vector changes in **c**. **e**, Theoretical calculations of the susceptibility (χ) and nesting wave-vector. **f**, Peak position of the electronic susceptibility along the (11) direction

on Eq. 2.26, we get

$$DWF = \frac{I(t)}{I(t<0)} = e^{-\langle(\boldsymbol{s}\cdot\boldsymbol{u(t)})^2-(\boldsymbol{s}\cdot\boldsymbol{u(t<0)})^2\rangle}. \tag{3.3}$$

Then the atomic vibration along that specific Bragg peak direction can be calculated as

$$\langle u(t)^2\rangle = \langle u(t<0)^2\rangle - \frac{1}{s^2}\ln\left(\frac{I(t)}{I(t<0)}\right). \tag{3.4}$$

Initial atomic vibration $\langle u(t<0)^2\rangle$ is estimated to be about 0.008 Å^2 from X-ray measurements [92]. So with Bragg peak intensity change known, we can extract the true root mean square (*rms*) atomic vibration (u) at different directions and different time delays (Fig. 3.9b). Here, we make an assumption that the initial thermal phonon *rms* amplitude is isotropic. The black circle with radius of 0.1 Å represents negative time delay; at 0.2 ps after pump excitation, the *rms* vibration along the a axis becomes smaller and that along the c axis increase, as shown by the purple curve; at 1 ps, the anisotropy becomes maximal; after 1 ps, the system starts to recovery back to an isotropic state; at about 10 ps, the *rms* vibrations along a- and c- axes are already very close.

On the other hand, since CDW formation in $RETe_3$ series is shown to be strongly associated with FS nesting from the photo-emission measurements, it is necessary to explore how the CDW nesting vector changes associated with a laser pump excitation. By tracking the CDW wave-vectors q_a and q_c, it is found that the CDW FS nesting vectors are changing, as shown in Fig. 3.9c. The a-CDW wave-vector is relatively noisy due to weak signal, so only a few averaged data points are shown. But for c-CDW wave-vector, it is clear that the wave-vector is increased by 2.5% at $+1$ ps. With a delay of 300 fs that matches with the

KZ freeze-out time, q_c peaks at $+1.5$ ps, then partially decays back. Fig. 3.9d shows how the FS change after laser excitation (orange dashed line).

In photoemission measurement [93], it has been shown that there is a reduction in transverse coupling $t_\perp$. With theoretical calculations, we show that this reduction leads to the observed change in CDW wave-vector $\boldsymbol{q}_c$. We evaluate the pairing vector by calculating the static charge fluctuation susceptibility $\chi(\boldsymbol{q}_c, \omega = 0)$ based on a model band structure that incorporates the reduction in $t_\perp$. Here, we focus on the underlying susceptibility and its behavior as the V_π ($\propto t_\perp$) is reduced. Fig. 3.9e shows the line cuts of the χ along (11) direction (where the electron-phonon coupling vertex is peaked) for several values of V_π. For both the local maxima labeled as PK1 and PK2, as V_π is reduced, they shift toward smaller nesting wave-vectors. Fig. 3.9f plots the extracted two peak positions at several V_π values to show the trend.

By comparing the Bragg peak and CDW wave-vector dynamics, and associating them with the intensity dynamics, it is clear that the shift in the wave-vector goes hand in hand with the intensity change: both have a freeze-out period, both peaks at about 1 to 1.5 ps. In contrast, the Bragg peak dynamics has no delay and peaks much early.

To prove that the changes we observed here are induced mainly by a nonthermal effect, we performed static TEM measurements to study the thermal phase transition. The TEM measurement is done using a thermal stage in the JEOL 2010F TEM equipped with Gatan OneView 4k x 4k camera (at University of Michigan microscopy center with the help of Dr. Kai Sun). Fig. 3.10a is the full diffraction pattern of $CeTe_3$ at RT while Fig. 3.10b are cropped CDW peaks at 4 different temperatures. The CDW wave-vector is also seen to gradually increase at the beginning then increase significantly faster after 400 K. At the estimated sample temperature (≈ 370 K based on optical absorption, see next paragraph

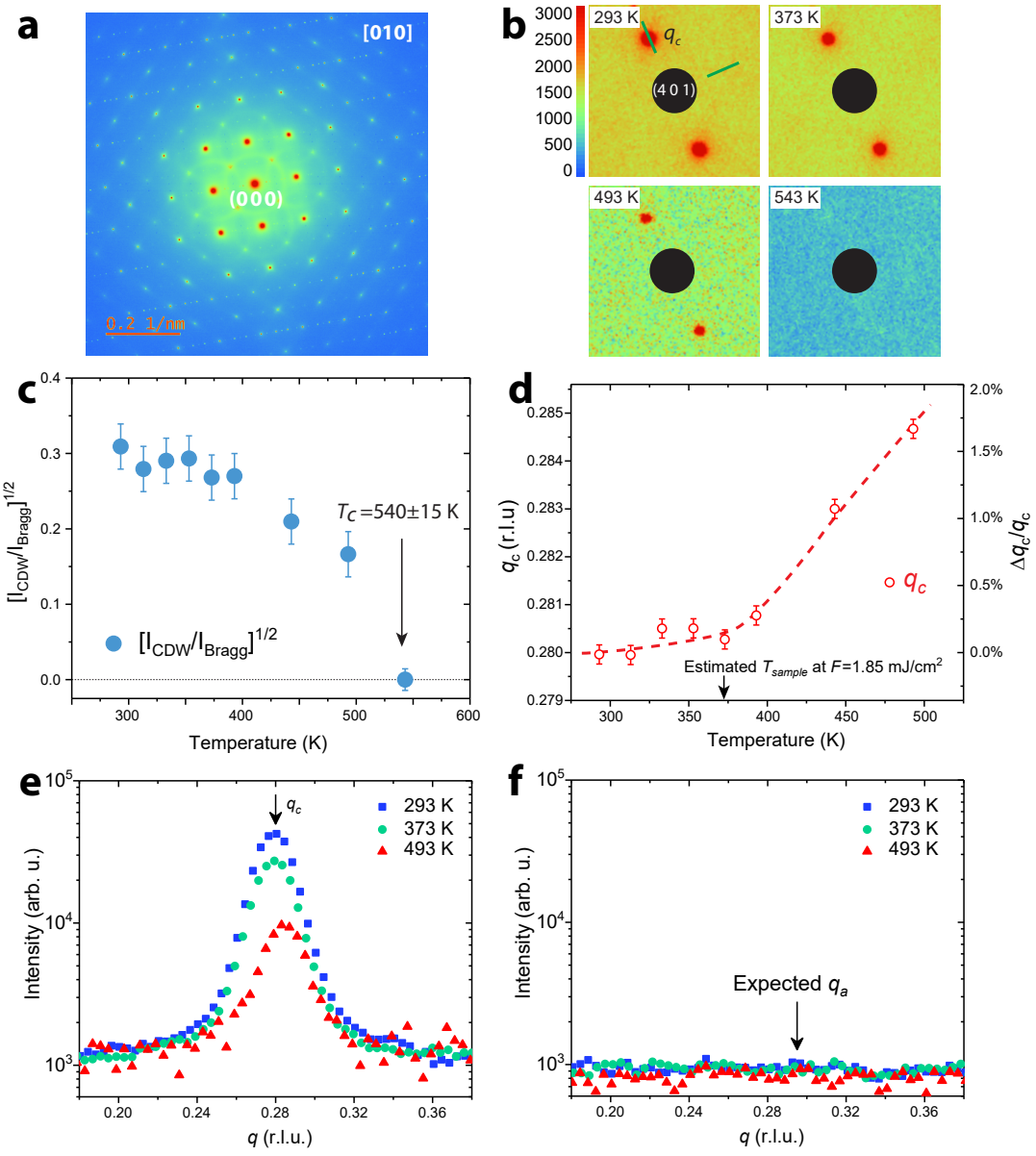

Figure 3.10: Static TEM measurements of $CeTe_3$, **a**, Full TEM diffraction patterns at RT. **b**, Cropped diffraction pattern at several temperatures at fixed scale. **c**, c-CDW peak intensity evolution normalized by Bragg peak intensity. **d**, The CDW wave-vector evolution towards transition temperature. **e**, Line cut along c-CDW peak at three characteristic temperatures. **f**, The same line cut along the potential a-CDW peak position.

for details), the CDW wave-vector is much smaller than the photo-induced change. So the observed $\boldsymbol{q}_c$ change in the UED data is not due to thermal heating. The plot in Fig. 3.10c shows the square root of I_{CDW}/I_{Bragg}. The overall trend defines a transition temperature

of 540 ± 15 K. For c-CDW and a-CDWs intensity profiles as shown in Figs. 3.10e&f, it is clear that the thermal effect can not induce CDW order in the a direction.

Based on optical measurements of $CeTe_3$ [88, 89], we extract the refractive index n and extinction coefficient κ to be 1.04 and 3.45, respectively. With n and κ as the inputs and transfer matrix calculation (refer to Appendix B), the optical absorption is calculated to be 0.32 (45° incidence, p-polarized, 30 nm sample thickness). At $F = 1.85$ mJ/cm^2, the absorbed energy density is calculated to be 1.22 eV/nm^3. According to thermodynamic measurements on $CeTe_3$ and similar compounds [94, 95], the specific heat for $CeTe_3$ at RT is estimated to be 120 J/(mol·K). Then we can estimate the sample temperature rise to be ≈ 75 K.

Finally, based on the previous discussions, we can establish the following phase diagram in Fig. 3.11, in which vertical axis is the equilibrium state and the horizontal axis is the photo-induced non-equilibrium direction. A new hidden bi-directional phase emerges solely due to the interaction-mediated symmetry-recovery in the electronic structure and the decoupling between the microscopic relaxation and CDW collective modes may provide a key window for the hidden state to grow into a stable, meta-stable phase.

3.4 Summary

In conclusion, we have observed a bi-directional CDW state induced by laser pulse illumination, which is thermodynamically forbidden at RT. Such a state is formed over the transiently suppressed c-CDW state, with a threshold of ≈ 0.6 mJ/cm^2 — much smaller than what is needed to suppress c-CDW, which is ≈ 1.9 mJ/cm^2. This threshold defines a nonthermal critical point. The analysis of Bragg peak dynamics and anisotropic atomic vibrational re-

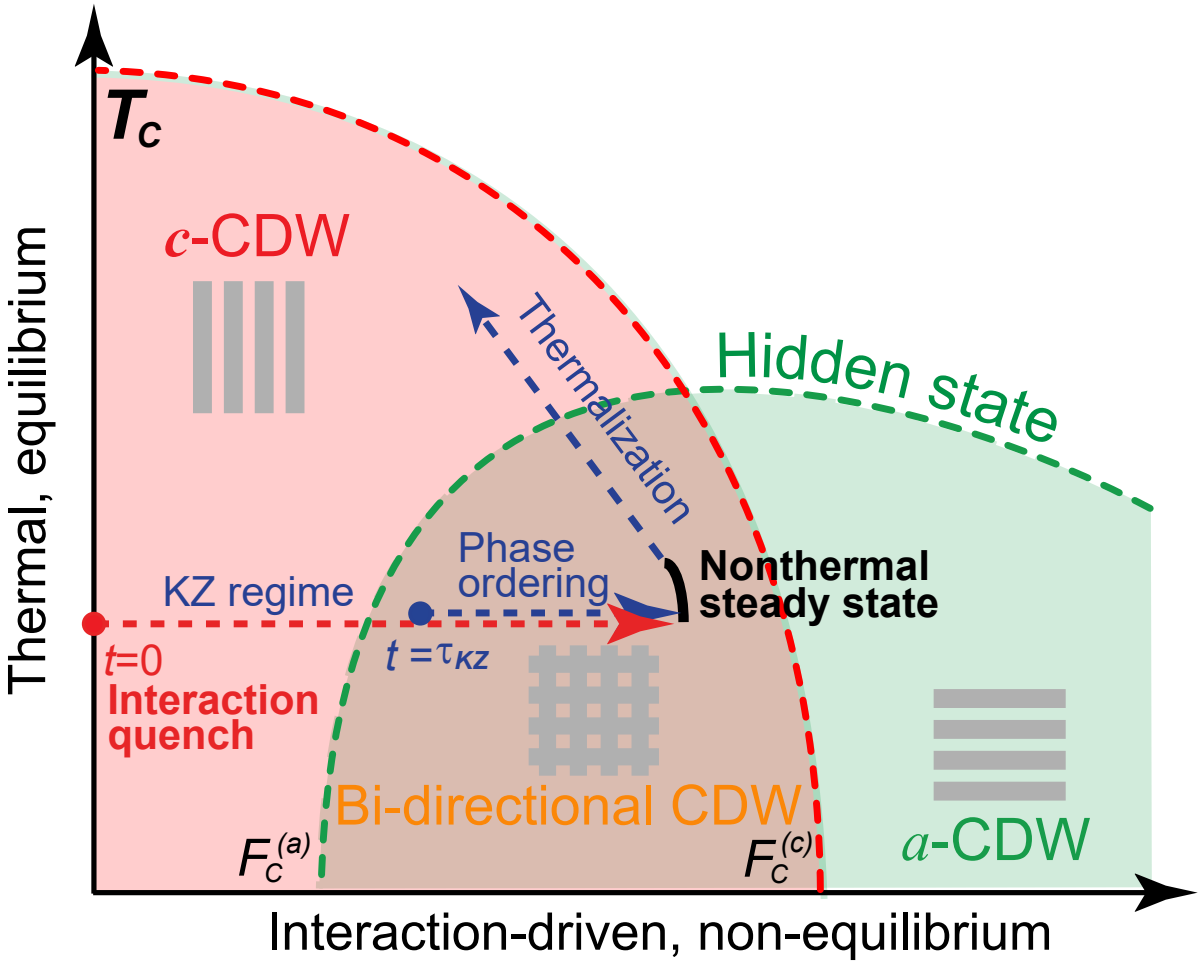

Figure 3.11: The non-equilibrium phase diagram and phase transition pathways of $CeTe_3$.

sponses to the laser excitations prove that the associated symmetry changes involve soft modes, in particular a transverse mode that drives the softening/hardening of phonon dispersions leading to formation/suppression of CDWs. The CDW wave-vector change clearly demonstrates that CDW order parameter evolution follows the FS curvature change resolved by angle-resolved photoemission spectroscopy (ARPES) [93]. This shows that FS nesting enhanced electron-phonon coupling plays a central role in driving the CDW instabilities. Finally, we propose a nonthermal pathway to explain the introduction and stabilization of the hidden interaction-mediated CDW order.

Chapter 4

Symmetry breaking and phase transitions in $ErTe_3$

In the previous chapter, the spontaneous symmetry breaking and hidden states are explored in $CeTe_3$. $CeTe_3$ is optically driven into a hidden bi-directional state via a SSB process involving a nonthermal fixed point. Following this thread, we studied a compound of the same rare-earth tritellutride group: $ErTe_3$, which is on the opposite side of $RETe_3$ series to $CeTe_3$.

$ErTe_3$ has two CDW transition temperatures: above 267 K, the material is in a metallic phase and exhibits no CDW order. Below 267 K, CDW order along the c direction is formed (uni-directional stripe CDW). When temperature is further reduced to 155 K, another CDW order along the a direction is formed (bi-directional CDW). Similar to $CeTe_3$, the CDW is also believed to be formed due to FS nesting: the FS nesting wave-vector matches well with the CDW wave-vector [84]. However, $ErTe_3$ exhibits a richer phase diagram. There is a metallic state at RT. Between 155 K and 267 K, $ErTe_3$ exhibits a stripe CDW state resembling what we see in $CeTe_3$ at RT. Below 155 K, it is likely to have more interesting phenomena due to the interactions between the two CDW orders in a more symmetric FS. So $ErTe_3$ is naturally a further step to give a comprehensive picture for the equilibrium and non-equilibrium CDW for materials in the $RETe_3$ family.

In this chapter, the background on $ErTe_3$ will be introduced first in Sec. 4.1. The dynamics and fluence-dependence data will be discussed in Sec. 4.2. The non-equilibrium melting thresholds for a- and c-CDWs will be investigated at various temperatures. Then at an intermediate temperature between the two transition temperatures, dynamics are discussed in Sec. 4.3. In Sec. 4.4, a new phase diagram is made and the chapter will be summarized.

4.1 Background about $ErTe_3$

According to previous reports [84, 85], $ErTe_3$ has a normal-to-stripe CDW transition at 267 K and stripe-to-bidirectional CDW transition at 155 K. This transition is directly reflected in the diffraction patterns. As shown in Fig. 4.1, at 40 K, the CDW satellite peaks show up in both the $\boldsymbol{a}^*$ (green circles) and $\boldsymbol{c}^*$ (red circles) directions. At an intermediate temperature of 180 K, only CDW satellite peaks along the $\boldsymbol{c}^*$ direction show up.

According to the diffraction and photoemission measurements [84, 85], the CDW along the c-axis has the wave-vector of $\boldsymbol{q}_c = 0.30\boldsymbol{c}^*$ with a band gap of 175 meV. The CDW along the a-axis has the wave-vector of $\boldsymbol{q}_a = 0.315\boldsymbol{a}^*$ and a CDW gap of 50 meV. For comparison, $CeTe_3$ has the transition temperature of $\approx$540 K, $\boldsymbol{q}_c = 0.285\boldsymbol{c}^*$, and the CDW gap of 400 meV. These large differences result in very different s/n of the data.

In our electron diffraction pattern of $CeTe_3$ at RT, the peak intensity of CDW : Bragg $\approx 1:15$. By contrast, for $ErTe_3$ at 25 K, the intensity ratio of c-CDW : Bragg $\approx 1:50$ and the a-CDW intensity is another factor of 5 to 10 weaker than c-CDW's. This makes $ErTe_3$ experiments extremely difficult. It requires a factor of 10 or more probe electrons than $CeTe_3$ in order to get the same level of s/n for studying the CDW dynamics. Another factor that

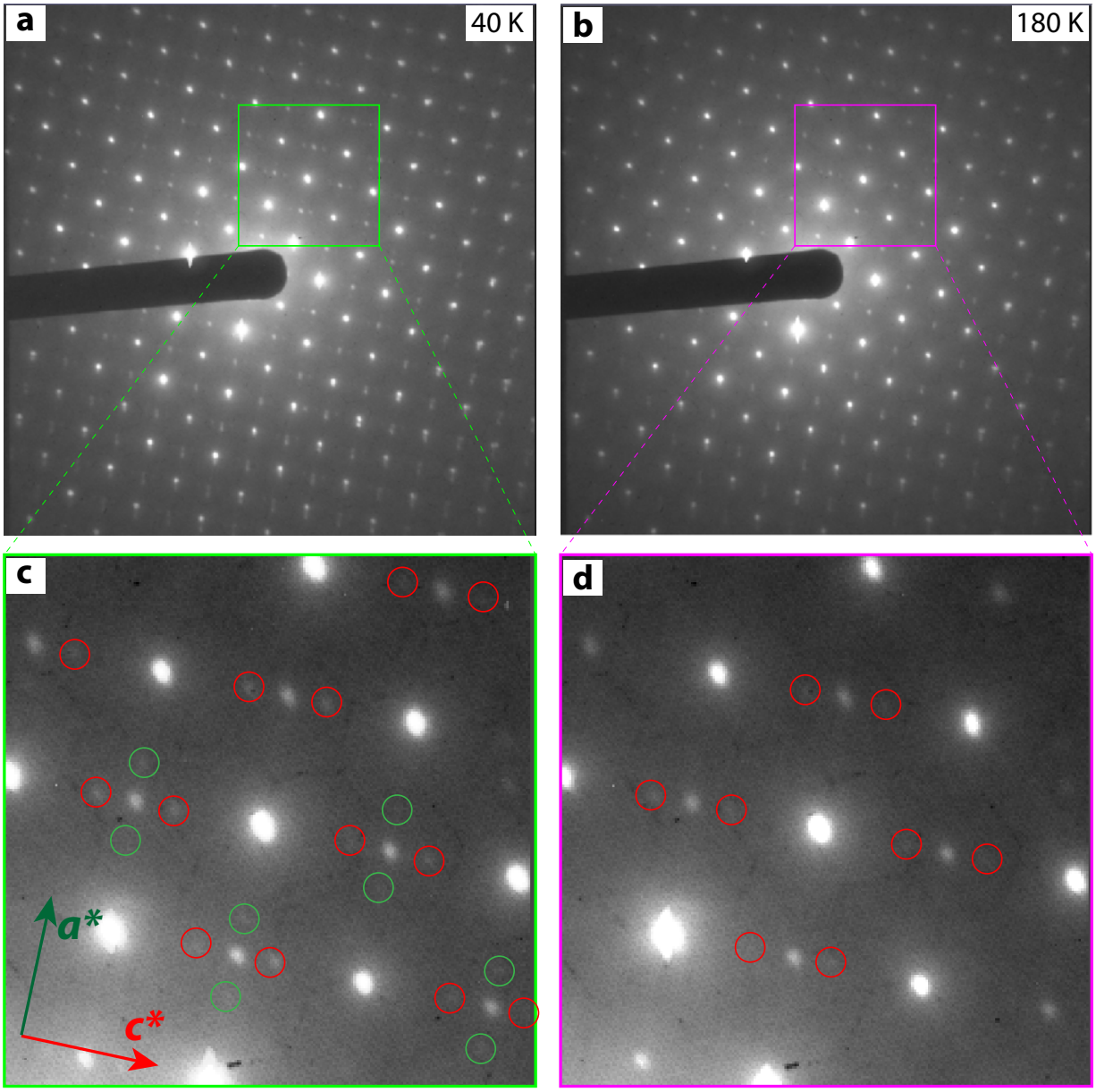

Figure 4.1: The diffraction patterns of $ErTe_3$. **a**&**b**, Full diffraction patterns at 40 K and 180 K. **c**&**d**, Zoom-in view in **a** and **b**. The red circles are c-CDW peaks and green circles are a-CDW peaks. At 40 K, there are both a- and c-CDW orders while at 180 K there is only CDW order along the $\boldsymbol{c}^*$ direction.

makes $ErTe_3$ experiments harder is in the sample preparation step. $ErTe_3$ is very easily oxidized in air, and the surface will be oxidized and sample will become unusable in a few hours. So during sample preparation, it has to be done in a nitrogen-filled glove box. Also, the inter-layer bonding strength in the $ErTe_3$ crystal is much larger than $CeTe_3$ or TaS_2,

making it very hard to exfoliate to very thin flakes. For our collaborators in Northwestern University, they also spent quite some time before resolving the twining problem (mixture of the a and c axes) in $ErTe_3$. After trials and errors, we managed to run a series of experiments to unveil the interesting physics in $ErTe_3$, though the s/n is slightly less than the $CeTe_3$ data reported in the previous chapter.

4.2 Investigations at low temperatures

We first examine the phase transitions at 50 K. With 800 nm pump at the fluence of 2.9 mJ/cm^2, both a- and c-CDW peaks are suppressed to almost zero within the first 1 ps then partially recover to $\sim$40% of the original level (Fig. 4.2a).

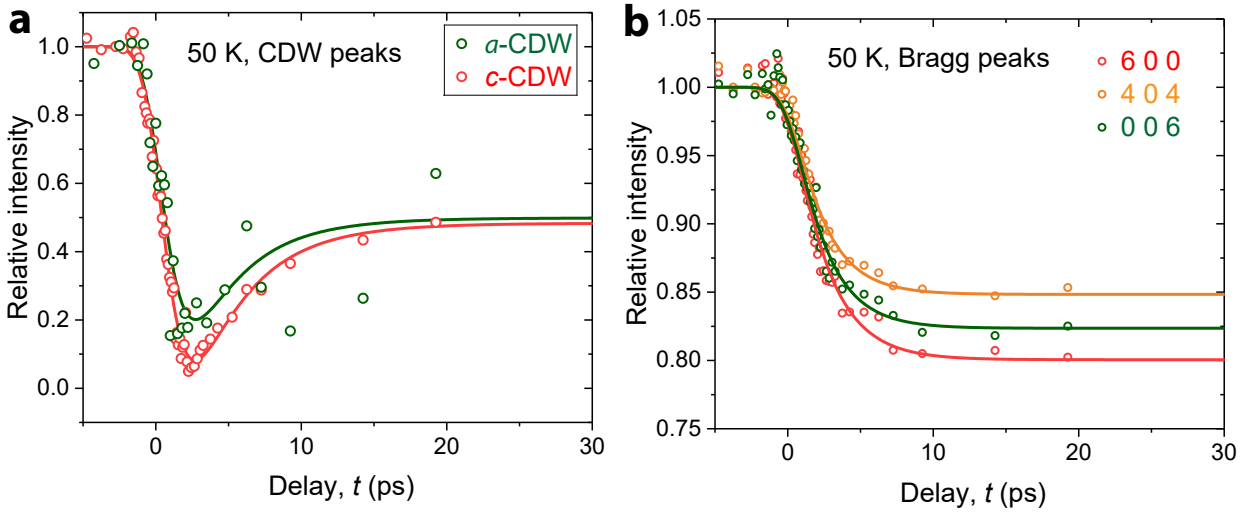

Figure 4.2: The CDW (**a**) and Bragg (**b**) peak dynamics at base temperature of 50 K and pump fluence of 2.9 mJ/cm^2. The a-CDW dynamics data in the first 5 ps are 2-binned for better s/n.

According to phase transitions in the steady state, if one continuously warms the sample up from 50 K across the CDW transition temperatures, the a-CDW will be melted first at 155 K before the c-CDW is melted at 267 K. Naturally, one expects that with laser excitation,

one would drive the melting of a-CDW more efficiently than c-CDW if the thermal heating plays a key role. But experimentally, at about 2 ps, c-CDW is fully melted while a-CDW still has $\sim 20\%$ remaining (Fig. 4.2a).

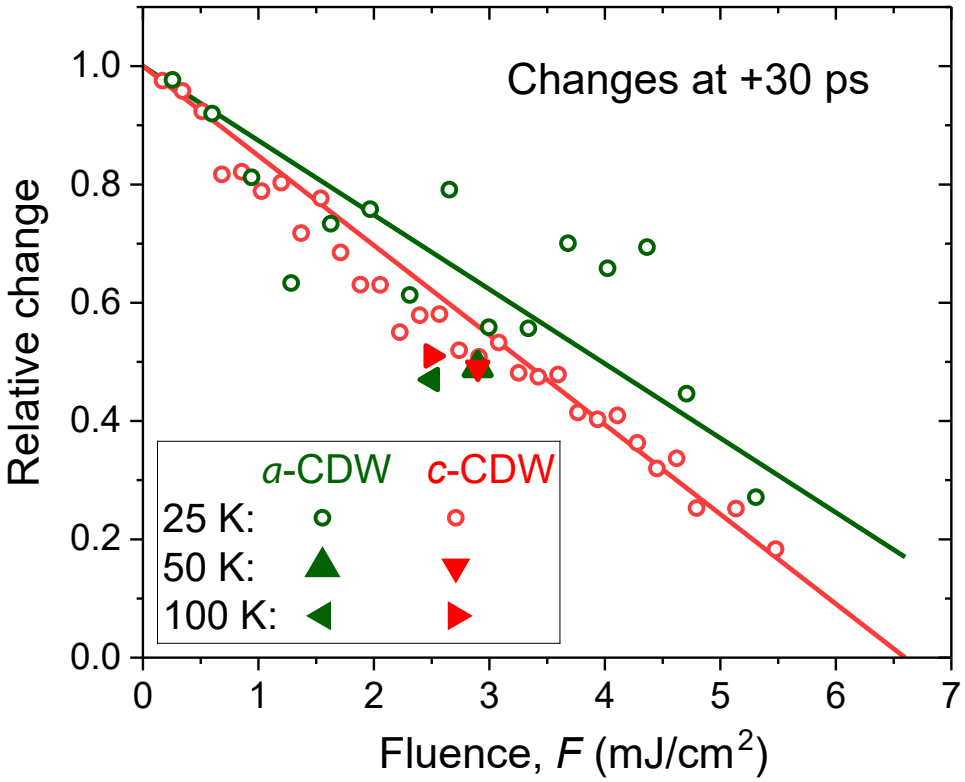

Figure 4.3: The fluence-dependence of the a- and c-CDW peaks relative intensities at 25 K. The a-CDW data are averaged every two points (binning of 2) for better s/n. The data points for 50 K (2.9 mJ/cm^2) and 100 K (2.5 mJ/cm^2) are extracted from the delay scan dynamics.

The anomaly observed in time-dependent dynamics is consistent with what we see in the fluence-dependent data in Fig. 4.3, where we monitor the peak intensity changes at $+30$ ps relative to the negative time value. The c-CDW data in red curve have a relatively good s/n and the trend is quite linear with about $\pm 5\%$ uncertainty bar. The extracted threshold for c-CDW is 6.6 mJ/cm^2. On the other hand, a-CDW in green color is much noisier, limited by s/n. The error bar could be as large as $\pm 15\%$. In the plot, we average every two data

points (binning of 2) for better s/n. However, following the trend line, it is evident that the melting threshold determined at this time scale for a-CDW is not much different from that of c-CDW, or even slightly higher.

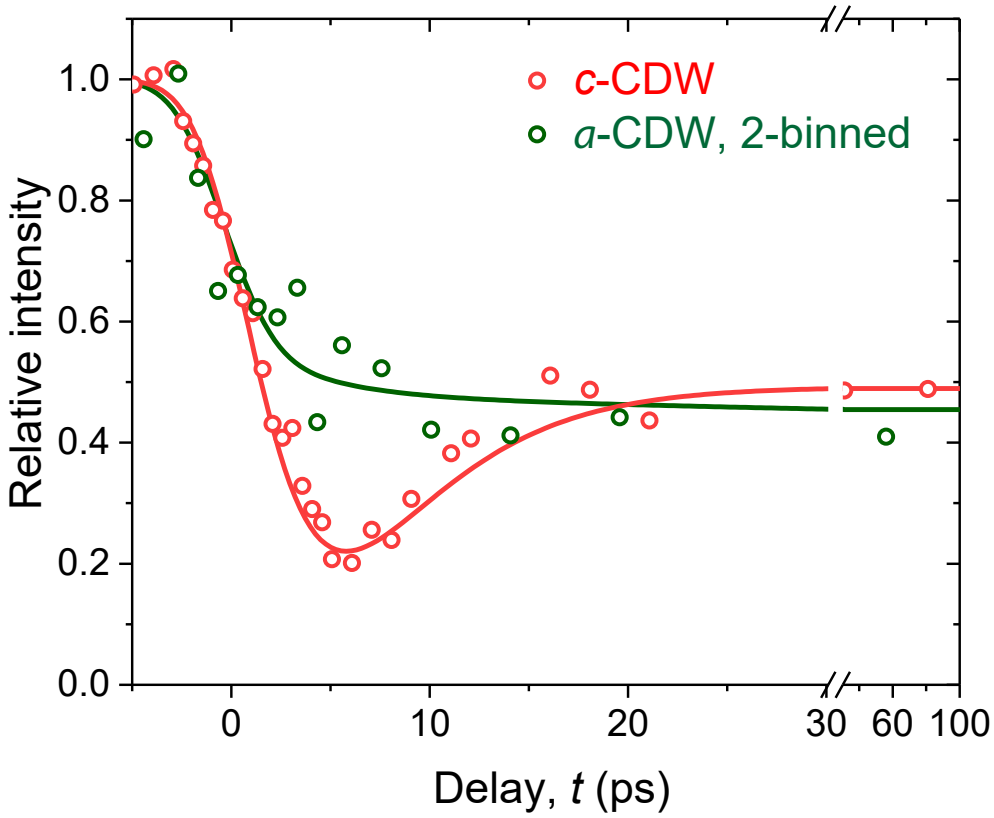

Figure 4.4: The a- and c-CDW peaks dynamics at 100 K. Data points for a-CDW are binned by 2 for better s/n.

This phenomenon can be explained from previous $CeTe_3$ experiments. After photo excitation, there is a reduction in transverse hopping integral. This change leads to a modification in FS curvatures, resulting in a FS nesting that favors a-CDW. This nonthermal effect makes a-CDW state as competitive as c-CDW. Therefore laser-induced quench does not obviously favor one particular stripe order in our presentation.

In terms of anisotropic lattice phonons that we deduce based on the Bragg peak dynamics, $ErTe_3$ shows a smaller anisotropy compared with $CeTe_3$. As shown in Fig. 4.2b, since the

changes along [1 0 0] & [0 0 1] are influenced by soft modes associated with a- and c-CDW states, the smaller anisotropy here reflects a more symmetric energy landscape in $ErTe_3$ at low temperatures than $CeTe_3$ at RT.

We further raise the sample temperature to 100 K and examine the a- and c-CDW peaks responses at pump fluence of 2.5 mJ/cm^2, as shown in Fig. 4.4. While the c-CDW is suppressed to 20% and shows over-damped dynamics before recovering to $\approx 50\%$. The a-CDW intensity is suppressed to $\sim 40\%$ without a clear recovery. We note that judging from the changes at $+30$ ps, both 50 K and 100 K $ErTe_3$ system follow similar fluence-dependence as 25 K (Fig. 4.3). Their early time dynamics reflect disordering of the initial state.

4.3 Phase transitions at intermediate temperature

At temperature of 165 K, which is in between the two transition temperatures, only the c-CDW satellite peak is present. At the pump fluence of 2.9 mJ/cm^2, the c-CDW peaks are suppressed to $\sim 10\%$ (Fig. 4.5a).

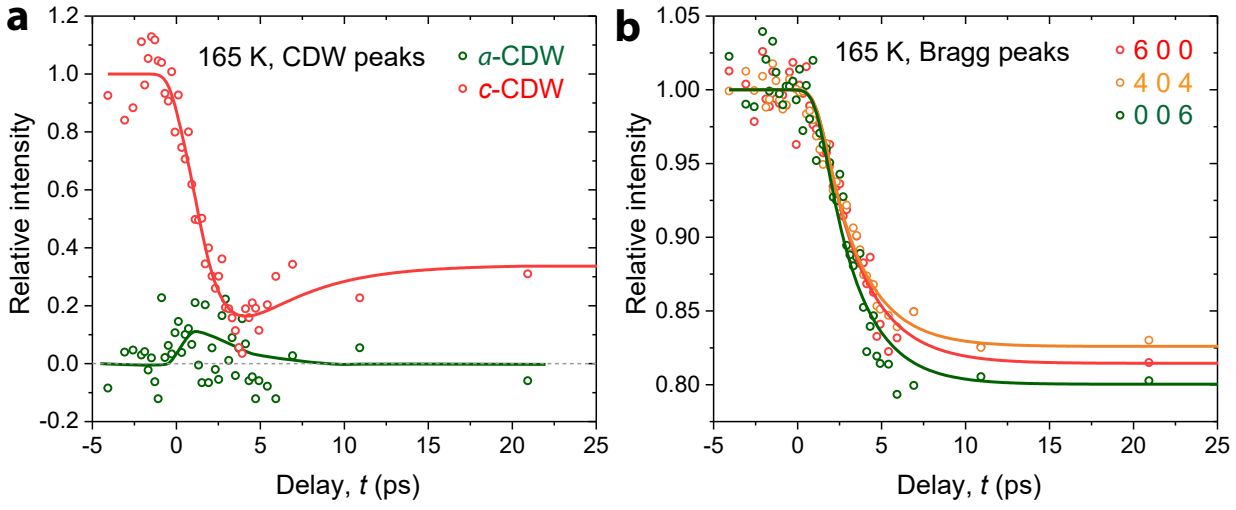

Figure 4.5: The dynamics of CDW (**a**) and Bragg (**b**) peaks at 165 K.

At the location where there is supposed to have a-CDW peak, we gather scattering weight above the background to extract changes induced by laser excitations. As shown in Fig. 4.5, the data are very noisy but do show evidence of an enhancement during the first 5 ps. In the plot, the a-CDW intensity is normalized based on c-CDW intensity (also shown) at negative time.

The state of $ErTe_3$ at 165 K should be very similar to that of $CeTe_3$ at RT. Both have CDW orders only along the c direction. In $CeTe_3$ the laser quench of c-CDW results in the formation of a-CDW. In $ErTe_3$, as we mentioned, the c-CDW order is already a factor of 5 to 10 weaker than that in $CeTe_3$, so the s/n is relatively low and the formation of a-CDW is a little ambiguous. But given the fact that a-CDW order is induced in $CeTe_3$, we expect the signs of a-CDW formation in $ErTe_3$ may be real.

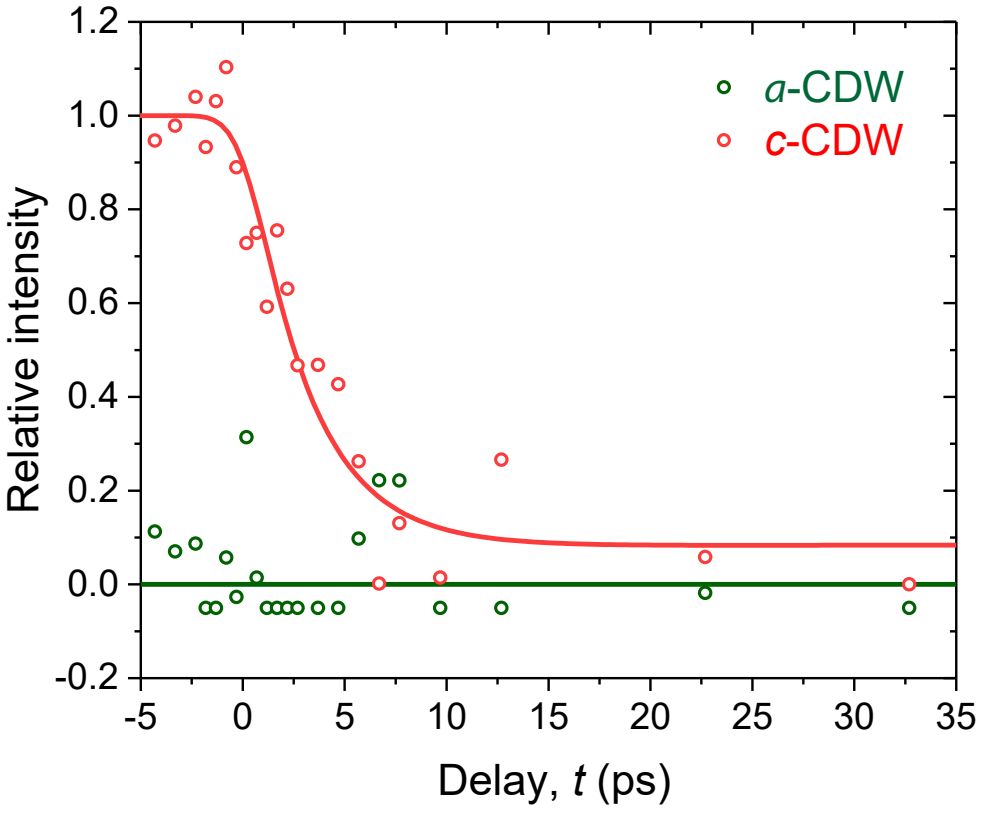

Figure 4.6: The a- and c-CDWs satellite peaks dynamics at 200 K.

For understanding the soft modes dynamics, symmetry breaking/recovery associated Bragg peak intensities are examined. While the weak anisotropic Bragg peak intensity remains to be less suppressed (Fig. 4.5b), but a lower (0 0 6) intensity, instead of (6 0 0), is observed in the low temperature state, which may reflect the stronger soft mode instabilities here associated with a-CDW, which is no longer static at this temperature.

At base temperature of 200 K and fluence of 2.7 mJ/cm^2, c-CDW is suppressed to less than 10% of negative time. We are not able to resolve any presence of a-CDW fluctuation at this temperature. Limited by the s/n in the current UED system, the early non-adiabatic evolution for the two CDW states are not resolved. Further experiments with higher s/n possible with the high-brightness UEM system may resolve these subtle differences in temperature-dependent investigations.

4.4 Non-equilibrium phase diagram and summary

In summary, due to the limited time resolution and s/n, we do not resolve the early symmetry breaking dynamics for $ErTe_3$. But the results presented here do support the key conclusions from $CeTe_3$ that fs laser excitation promotes a-CDW formation. At low temperatures, the energy landscape, compared to that of $CeTe_3$, is already more symmetric. The soft mode features are more isotropic as well.

Based on the Bragg and CDW peak dynamics at various temperatures, we propose the following phase diagram in Fig. 4.7. At low temperatures, the material already resides in the bi-directional CDW state. After laser excitation, both CDW orders are quenched but the a-CDW order has a similar (or even larger) nonthermal melting threshold as the c-CDW. At intermediate temperature of 165 K, which is right above the a-CDW transition

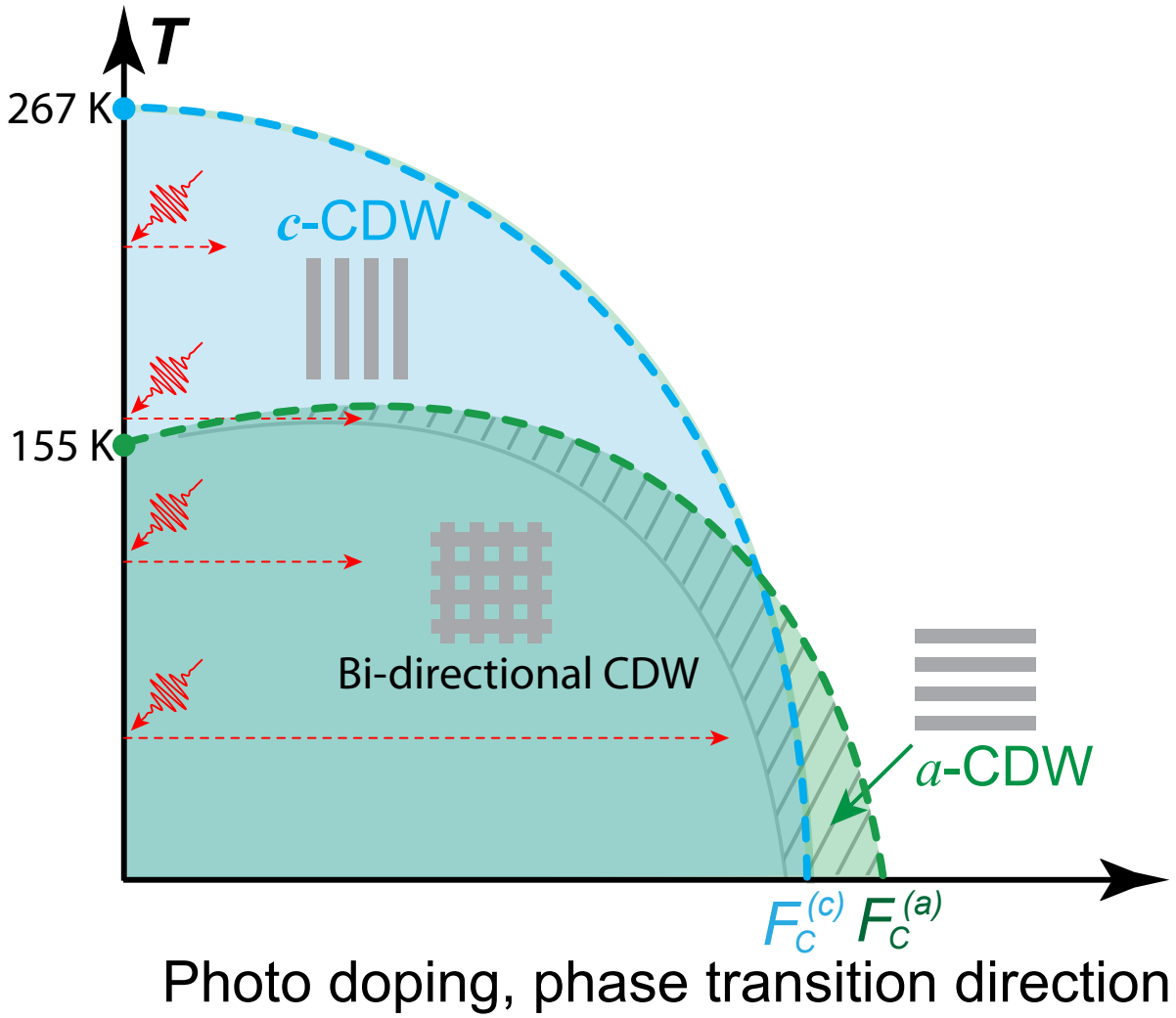

Figure 4.7: The schematic phase diagram of $ErTe_3$ under non-equilibrium conditions. The phase diagram is based on dynamics and fluence-dependent data at various temperatures. The thin gray line shaded-region represents the uncertainties of determining the a-CDW suppression phase boundaries.

temperature (155 K), it is in a uni-directional stripe CDW phase. But with laser excitation, there is signature that a-CDW order is induced after laser excitation, similar to the $CeTe_3$ case at RT. But due to the more than a factor of 10 weakness in CDW intensity compared with $CeTe_3$, the a-CDW is much noisier than the $CeTe_3$ data presented in previous chapter. When the base temperature is further above the 155 K transition temperature (at 200 K), the a-CDW formation is too weak to be observed and only a quench in c-CDW order is

observed.

The non-equivalent axes (a and c) become more symmetric and degenerate after laser excitation. In the non-equilibrium regime, the CDW order is transiently enhanced after laser excitation in the otherwise non-exist a-axis, demonstrating the completely different energy landscape compared with thermodynamic states. Such a non-equilibrium window opens up a new channel for exploring the metastable and hidden phases for possible functional materials. Given the consistency of the results in $CeTe_3$ and $ErTe_3$, we believe the results and conclusions can be extended to other rare-earth tri-telluride compounds as well and other similar symmetry-broken systems with non-equivalent crystal axes.

Chapter 5

Dynamical scaling and phase transitions observed in 1T-TaS_2

Research on quantum materials is a central topic in contemporary condensed matter physics. Of particular interest are 2D materials due to the presence of strong electronic instabilities which are the results of competing interactions at low dimension, frequently leading to a rich phase diagram. 1T-TaS_2 represents such an example of the transition metal dichalcogenides compound where electron-electron interaction leads to novel Mott insulating ground state and even superconductivity at low temperatures, which are entwined with density-wave formations.

In the early years from 1970s to 1990s, by means of X-ray and electron diffraction, and STM measurements, researchers have spent a great deal of effort on understanding how the CDW is formed in 1T-TaS_2 [52, 96], including a series of drastically different CDW formations. Among them, the most intriguing is the periodic domain texture formed in the NC-CDW state [97–100]. In recent years, the low-temperature Mott insulator-to-metal transition (IMT) has attracted a lot of attention with the advances in the time-resolved tools through which one may seek to separate the electron correlation effect from the electron-phonon coupling in the CDW phase transitions [101–107]. It is generally believed that the strong electron-electron correlations are directly responsible for IMT in the low-temperature

C-CDW state. This Mott gap is located in the Γ point of BZ which is decoupled from the CDW gap. With chemical doping [13] or under a high pressure [108, 109], the materials could exhibit superconductivity, which may emerge due to tuning of the electronic structure. An important recent development that draws intense interest is the work by Stojchevska *et al* [110], where they showed that with a single fs laser pulse, 1T-TaS_2 goes from an insulator to a hidden metallic state that lasts very long. This metallic state can be erased by another strong laser pulse. Apart from the nature of this switching, such insulating and metallic transitions are highly promising for optoelectronic devices. Ensuing work [111–116] shows that the hidden states in 1T-TaS_2 may also occur under electrostatic chemical injection, gating with potentials in practical applications.

Even with all the previous work, there are still fundamental questions left unanswered. For example, how exactly the phase transition may happen that to drive the rearrangement of more than billions of atoms in a relatively short time; how an ultrafast laser quench may lead to a hidden state; and what limits the speed of phase switching. In this chapter, we will try to address some of these questions.

In this chapter Sec. 5.1, the background information on 1T-TaS_2 is given and general current problems related to this system is summarized. Then our study with ultrafast electron diffraction is presented in Sec. 5.2, including time-dependent dynamics and the microscopic physical picture of the transition. In Sec. 5.3, we will discuss the universal scaling behavior under non-equilibrium. Then in Sec. 5.4, the ultrafast photo-doping and photo-thermal effects for driving the phase transition will be discussed.

5.1 General properties of 1T-TaS_2

1T-TaS_2 and other transition metal dichalcogenides were studied as early as the 1970s by J. Wilson [52] *et al.* As shown in Fig. 5.1, the layered structure of 1T-TaS_2 with weak inter-layer van der Waals binding makes it easily exfoliatable by the scotch tape for preparing the thin TEM specimen. Within one layer, it has C_3 symmetry with two sulfur layers sandwiching the tantalum layer.

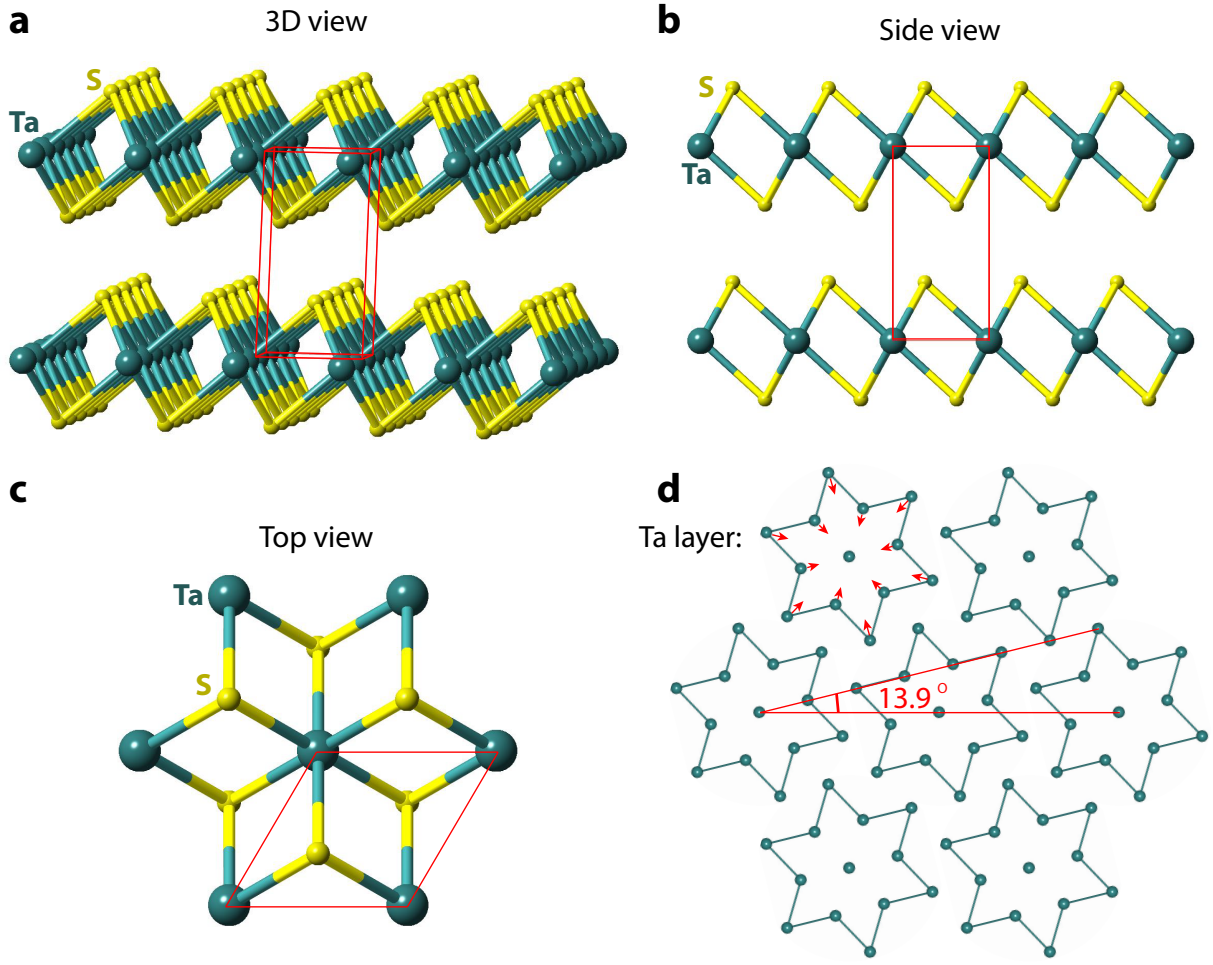

Figure 5.1: The structure of 1T-TaS_2. **a**, 3D view of the structure. Blue balls are Tantalum atoms and yellow represents Sulfur atom as labeled. The red box represents the unit cell. **b**, Side view. **c**, Top view. **d**, Ta layer structure when forming commensurate CDW. Every 13 atoms form Star-of-David supercell with surrounding 12 atoms moving inwards. The CDW superlattice is oriented 13.9° relative to the original lattice.

Despite the simple structure, it exhibits a very rich phase diagram. Below 180 K, the material is in commensurate CDW (C-CDW) state entwined with the Mott insulator state [108]. The C-CDW state unit cell consists of 13 atoms in the so-called Star-of-David (SD) structure formation (Fig. 5.1d). Within one SD supercell, there is in total one electron in the center. The C-CDW is oriented 13.9° from the lattice plane. Upon warming at $\approx$223 K, the system's long range correlation is broken by the formation of stripe order [99, 117]. The CDW orientation angle Φ rotates from 13.9° to about 13°. Further heating to above 283 K, the hexagonal domains with a size of $\approx$7.2 nm are formed and the system is often referred to as the nearly-commensurate CDW (NC-CDW) state with $\Phi \approx 12°$ [97–100, 118]. At T = 353 K, it undergoes yet another transition to the incommensurate CDW (IC-CDW) state, in which CDW is aligned with the lattice plane ($\Phi = 0°$) [98, 119]. At T = 543 K, the IC-CDW is melted and the system becomes metallic.

Details about 1T-TaS_2 phases can be found in Table 5.1.

Based on McMillan's free energy formulation of CDW in transition metal dichalcogenides [120], Nakanishi and Shiba et al proposed that domains in the NC-CDW phase are formed by a series of CDW harmonics [96, 121]. Within the domain, these harmonic states are phase-locked and commensurate with the SD building blocks. Domains are separated by discommensurations characterized by phase jumps. This prediction was later experimentally confirmed in the STM studies by Wu *et al* [97] and Burk *et al* [118], where they observed the 7.2 nm hexagonal domain structures. From a Fourier transform (FT), the high-order CDW wave-vector components obtained from STM images are in agreement with the diffraction results.

The sample studied here was grown by the chemical vapor transport technique by Prof. Kanatzidis group in Northwestern University. Single-crystalline bulk sample is exfoliated

by the Scotch tape method down to ≈30 nm thickness with a lateral size of 20 μm. The thickness is then confirmed by zero-loss electron energy loss spectroscopy (EELS). Details about sample preparation can be found in Appendix A.

Phase	**Temperature** (K)	$\Phi(^\circ)$	**Comments**
Normal	$T > 543$	NA	Metallic phase, no CDW
IC-CDW	$353 < T < 543$	0	Incommensurate CDW
NC-CDW	$283 < T < 353$(warming) $183 < T < 353$(cooling)	11-13	≈7 nm hexagonal domain
Triclinic	$223 < T < 283$ (warming)	12-13	Striped domain
C-CDW	$T < 223$ (warming) $T < 183$ (cooling)	13.9	Lock-in commensurate CDW, no domain

Table 5.1: 1T-TaS_2 phases across different temperatures. Φ refers to the CDW orientation angle away from the lattice plane.

Figs. 5.2a&b are typical optical images of the freestanding samples supported on the TEM grid used in the experiments. The high quality single-crystal sample is reflected in the diffraction patterns as shown in Figs. 5.2c&d. As shown in Fig. 5.2d, in the C-CDW state, the relative angle Φ between the CDW and the lattice is 13.9°. For comparison, Φ is about 12° in the NC-CDW phase (Fig. 5.3a) and 0° in the IC-CDW phase (Fig. 5.3b).

Optical and spectroscopic approaches such as transient optical reflectivity or angle-resolved-photoemission spectroscopy (ARPES) can track the electronics state evolution and closing of the CDW gap. They do not directly confirm the structural transition, which is believed to strongly couple to the evolution in the electronic subsystem. There have been

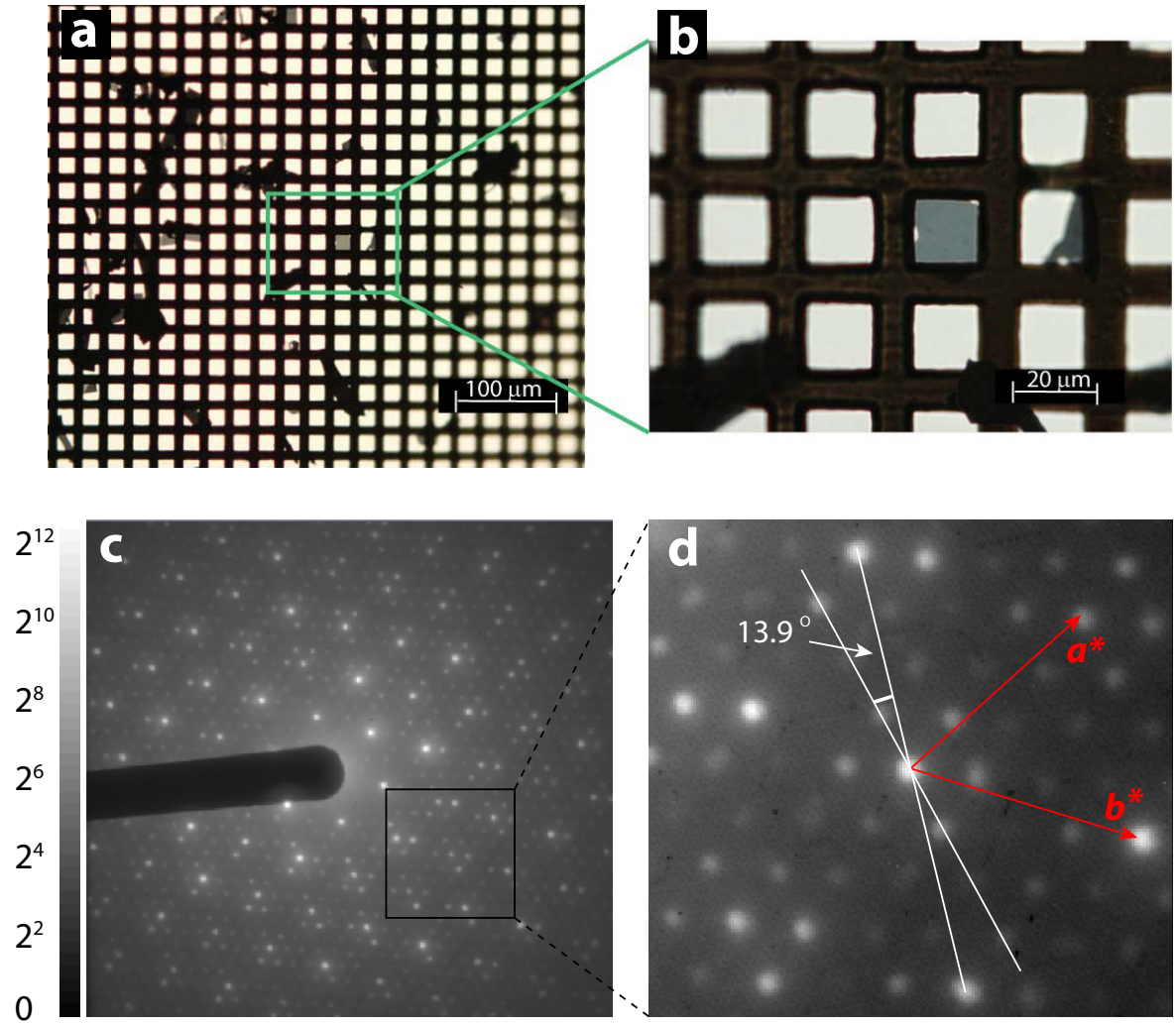

Figure 5.2: The optical images of the sample and electron diffraction patterns. **a**, Freestanding sample flakes on 1000 mesh gold TEM grid. **b**, Zoom-in view of a thin sample piece used for experiment. **c**, The diffraction pattern of 1T-TaS_2 by 30 keV electron beam at 150 K C-CDW phase. **d**, Zoom-in view of the diffraction pattern in **c**. The relative angle between the CDW $\boldsymbol{q}$-vector and the Bragg plane is 13.9°.

several studies of 1T-TaS_2 structural phase transitions by UED and X-ray diffractions. The pioneering UED study of 1T-TaS_2 by Eichberger *et al* [122] discussed the cooperative interaction between the electron and lattice subsystems. But they did not explicitly discuss the mechanism for driving the phase transitions. Han *et al* [106] explored the metastable and hidden phases, transition pathways and photo-doping effect during phase transitions. In

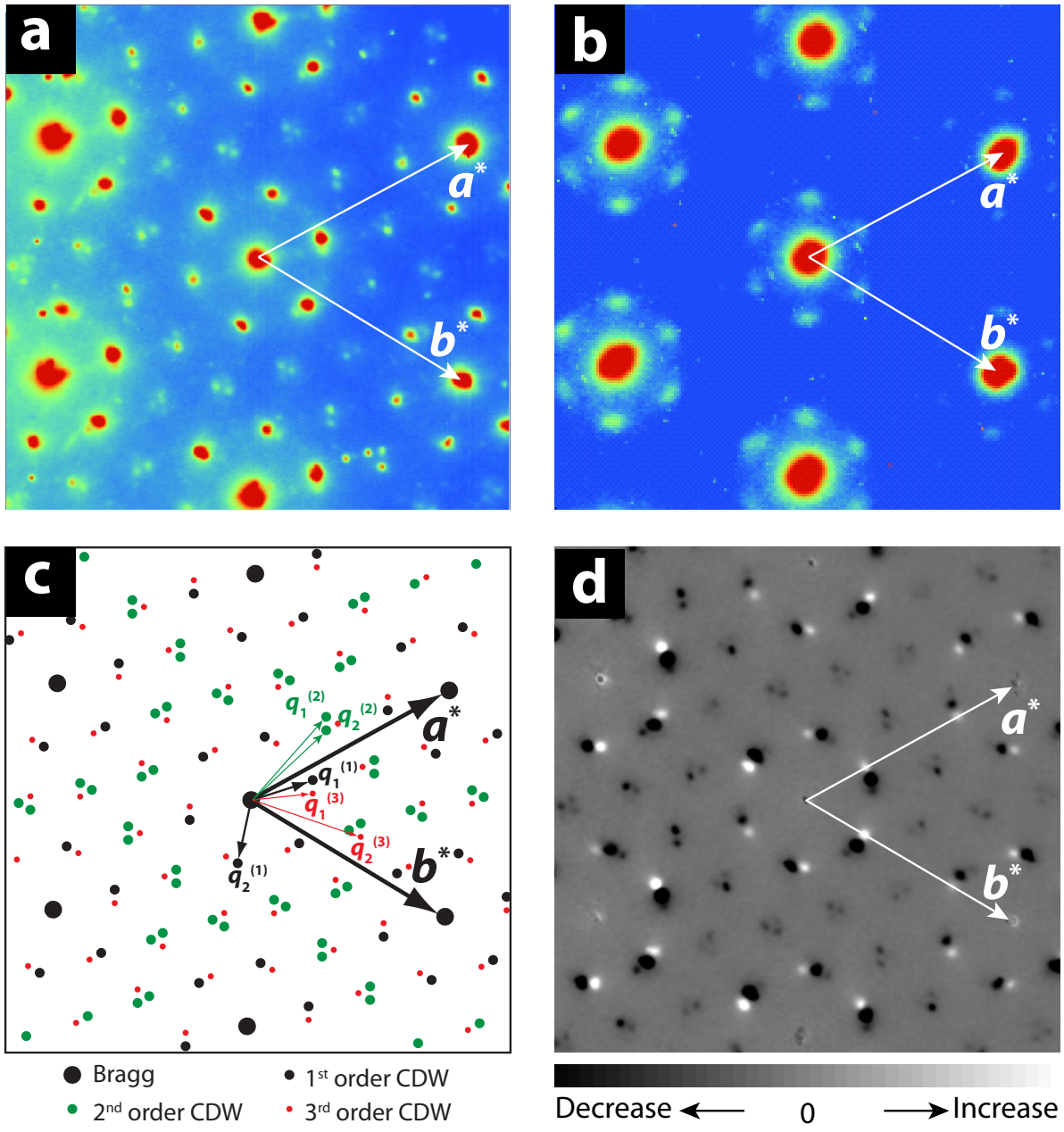

Figure 5.3: The diffraction patterns of 1T-TaS_2 in the NC-CDW phase. **a**, The original diffraction pattern in NC-CDW state. **b**, The diffraction pattern in IC-CDW state. **c**, A schematic diffraction pattern of the NC-CDW phase. Pattern is in the same orientation as that in **a**. The 1^{st}, 2^{nd}, and 3^{rd} CDW peaks are labeled as $q^{(1)}, q^{(2)}, q^{(3)}$, respectively, with each have two peaks differentiated in the subscript by "1" and "2". **d**, The difference diffraction pattern of after laser excitation (IC-CDW phase) minus the pattern before laser excitation (NC-CDW phase).

another UED paper, Haupt *et al* [123] discussed the NC-to-IC CDW phase transformation and suggested IC domain growth after excitation. The work based on X-ray diffraction by Laulhe *et al* [124] tracked the IC phase coarsening process following a power-law with exponent of 1/2. The work by Vogelgesan *et al* [9] discussed the phase ordering kinetics and the power-law growth, but further implicated the involvements of topological defects. From these earlier works, it is clear that the NC to IC transition occurs in the ultrafast time scales and the formation of IC tracked by correlation length follows a power-law. But it is still not entirely clear how the microscopic process can lead to effective switching in the macroscopic systems involving a great number of particles in such relatively short time scales. There are also questions to be reconciled from different approaches with respect to the roles of photo-doping and photo-thermal effects for driving the phase transition.

5.2 Phase transition mechanism of 1T-TaS_2

The key to understand the transformation pathways involves the annihilation of the topological defects (discommensurations) to evolve from NC to IC states. We first discuss how with coherent electron pulses one can resolve the domain structures via UED.

5.2.1 Reconstruction of real-space structures

Diffraction pattern encodes coordinates in the momentum space. To go back and retrieve the real-space structures, a simple Fourier transform (FT) is insufficient because the phase information is missing in the diffraction pattern, which is the so-called phase problem. In a typical microscopy setup with lenses to form an image, the phase information is restored. One method of using coherent diffraction pattern to reconstruct the real-space structure,

generally referred to as coherent diffractive imaging, relies on algorithms to retrieve the phase information. The reconstruction process usually applies a random phase first, then an iterative algorithm involving FT to be performed under preset constraints allows the phase to be retrieved in a self-consistent way. Here in our reconstruction protocol, we do not follow exactly the same protocols of coherent diffractive imaging described above, but instead we rely on the phase information credible to enable successful prediction of the structures at ground state as the constrains for reconstructing the CDW states in real space.

The reconstruction process starts with the effective CDW order parameter

$$\psi_e(\mathbf{r},t) = \sum_j \sqrt{I_{int,j}(t)} e^{-i(\boldsymbol{q}_j(t)\cdot\mathbf{r}+\phi_j)} e^{-\frac{|r-r_0|}{2\xi_j(t)}}, \tag{5.1}$$

where $\boldsymbol{q}_j,\ \phi_j,\ \xi_j$ are the wave-vector, phase, and correlation length of the CDW branch (indexed j) centered on a reference position $\mathbf{r}_0$.

In the NC-CDW phase, considering three-fold rotational symmetry, it has one 1^{st}-order, two 2^{nd}-order, and two 3^{rd}-order NC peaks. The diffraction pattern in Fig. 5.3c mimics that in Fig. 5.3a and has labels for all the CDW peaks. The expression for CDW peaks are as follows. First-order CDW peaks:

$$\boldsymbol{q}_1^{(1)} = 0.249\boldsymbol{a}^* + 0.063\boldsymbol{b}^*; \quad \boldsymbol{q}_2^{(1)} = -0.312\boldsymbol{a}^* + 0.249\boldsymbol{b}^*. \tag{5.2}$$

Second-order CDW peaks:

$$\boldsymbol{q}_1^{(2)} = \boldsymbol{q}_1^{(1)} - \boldsymbol{q}_2^{(1)}; \quad \boldsymbol{q}_2^{(2)} = \boldsymbol{a}^* - 2\boldsymbol{q}_1^{(1)}. \tag{5.3}$$

Third-order CDW peaks:

$$\boldsymbol{q}_1^{(3)} = \boldsymbol{a}^* - 2\boldsymbol{q}_1^{(1)} + \boldsymbol{q}_2^{(1)}; \quad \boldsymbol{q}_2^{(3)} = \boldsymbol{a}^* - \mathbf{q}_1^{(1)} + 2\boldsymbol{q}_2^{(1)}. \tag{5.4}$$

With three-fold rotational symmetry, all the NC-CDW peaks of different orders as well as the IC CDW peak, are included for reconstruction in Eq. 5.1. The key to form the commensurate domain is the requirement of "locked-in", namely the phases ϕ_j from individual harmonic state of NC-CDW are the same at the center of domain defined as position r_0. Here we simply set all $\phi_j = 0$, then the CDW density map can be calculated as

$$M(\mathbf{r}, t) = |\psi_e(\mathbf{r}, t)|^2. \tag{5.5}$$

With CDW present, the lattice is distorted from high symmetry positions with distortion amplitude of $\delta\mathbf{r}_i = \sum_j \delta_c \mathbf{e}_j Re[\psi_e(\mathbf{r}_i, t)]$, where $\mathbf{e}_j$ is the distortion polarization, δ_c is the static distortion of $\approx$0.25 Å for 1T-TaS_2. Then the distorted lattice can be written as

$$I(\mathbf{r}, t) = \sum_{i,j} Z_i^2 e^{-\frac{\delta\mathbf{r}_i^2}{u_i^2}} e^{-\frac{|r-r_0|}{\xi_j(t)}}. \tag{5.6}$$

Then we can get the reconstructed diffraction pattern by doing a FT of the distorted lattice image

$$I_{theo}(\boldsymbol{q}, t) = FFT[I(\mathbf{r}, t)] \otimes G(\boldsymbol{q}), \tag{5.7}$$

where $G(\boldsymbol{q})$ is the Gaussian convolution function representing instrumental resolution.

We can compare the reconstructed theoretical diffraction pattern with experimental patterns to refine the parameters. Fig. 5.4c are examples of CDW density map.

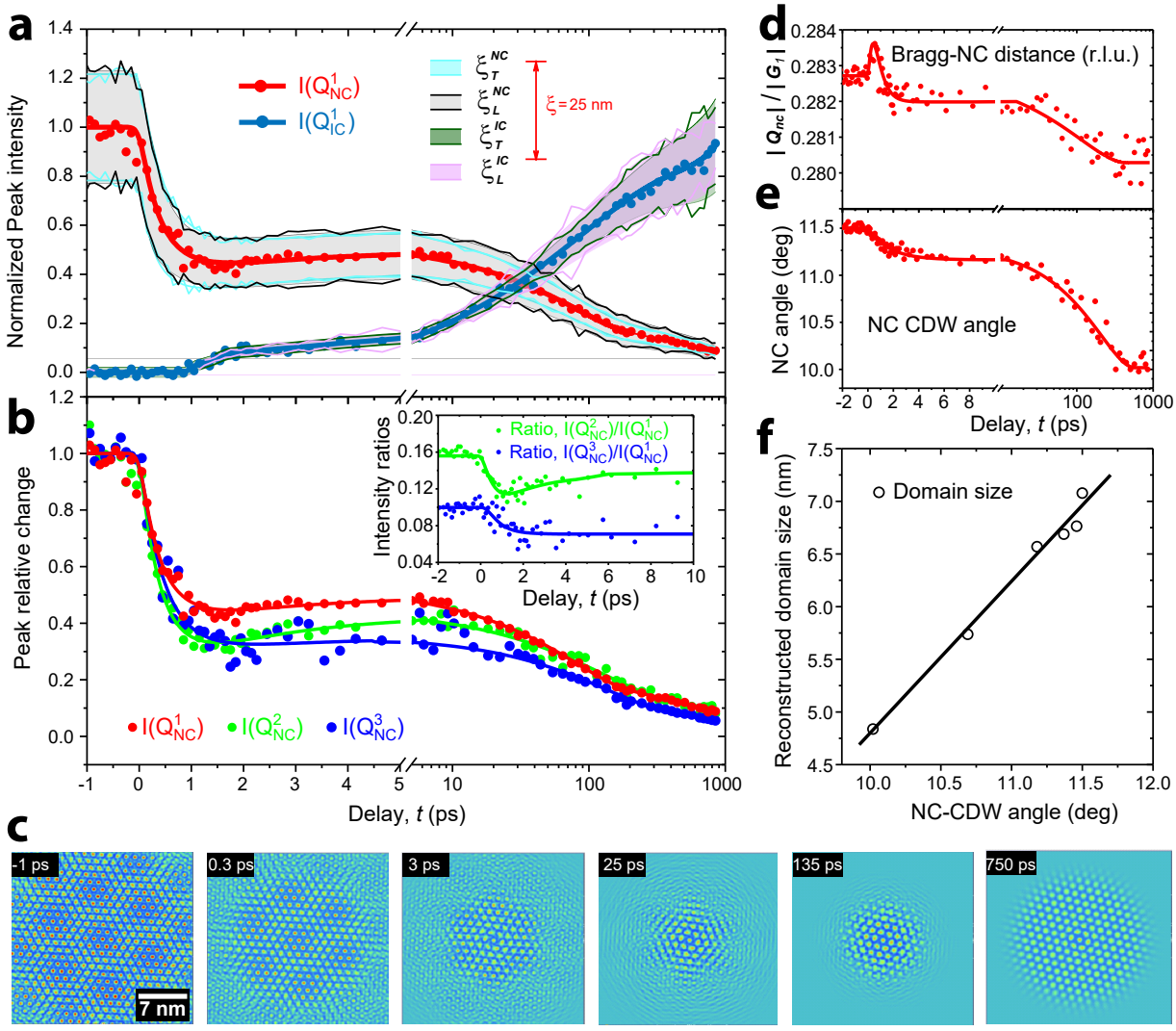

Figure 5.4: The dynamics of different order parameters after laser excitation. **a**, The dynamics of the (first-order) NC and IC peak intensities at fluence of 1.73 mJ/cm^2. Shaded area represents the correlation length of NC and IC order, fitted in the transverse (T) and longitudinal (L) direction. **b**, The dynamics of the 1^{st} (red), 2^{nd} (green), and 3^{rd} (blue)-order CDW peaks. Inset shows the ratio changes of the 2^{nd}– and 3^{rd}-order peak normalized by the 1^{st}-order peak intensity. **c**, The reconstructed CDW intensity map at several critical time delays. **d**, The 1^{st}-order CDW peak radius changes normalized by Bragg peak distance. **e**, The dynamics of 1^{st}-order CDW peak angle relative to Bragg plane. **f**, The NC-CDW domain size-dependence on the NC-CDW angle changes.

5.2.2 CDW peak dynamics and domain evolution

In our experiment, we directly track the Fourier components of the order parameters with electron diffraction and use those to reconstruct the real-space CDW structures, as discussed

in Sec. 5.2.1. Fig. 5.4 shows the evolution of NC-CDW peak of various orders (1^{st}-, 2^{nd}-, and 3^{rd}-orders) and IC-CDW peaks probed by UED. Key parameters, including the CDW amplitude, correlation length, and the wave-vector are extracted from the diffraction analysis. Fig. 5.4c shows the reconstructed CDW density maps. At negative time, the 7 nm NC domains are clearly visible. After laser excitation, the high-order NC-CDW peaks are suppressed more than the first-order peaks (Fig. 5.4b). This is reflected in the less sharp domain structures in the reconstructed images. In the longer time scale, IC phase grows and the visible range expands.

Since the domains resulted from different modulations of the CDW waves, the domain size is found to be almost linearly correlated with NC-CDW angle. In the steady-state measurements, as the temperature increase, the NC-CDW angle decreases [98] and the domain size also shrinks [125]. These measurements are consistent with our reconstruction in Fig. 5.4f, indirectly proving the validity of our method.

5.2.3 General behaviors of dynamical phase transition

There are some generic features in the CDW phase evolution. First off, the NC peak shows well-defined plateau after the initial quench for all the excitations, with different fluences show different plateau duration periods. After the plateau region, the NC peak further drops and IC peak further develops. So this plateau can be seen as a precursor for thermalization and has been observed widely in the post-quench relaxation process in isolated quantum systems [126, 127] — a phenomenon called *prethermalization*.

The term prethermalization comes from the field of cold atoms physics out of equilibrium, where the isolated quantum many-body systems (i.e. cold atoms) reach a quasi-steady state after initial quench but prior to the long-time thermalization. Prethermalization is a fast

loss of memory of the initial conditions due to dephasing after the system is driven out of equilibrium [128–134], typically in nearly-integrable systems [127]. It has been extensively studied in non-equilibrium dynamics in isolated quantum many-body systems theoretically [128–134] and experimentally [126, 135, 136]. This prethermalization plateau is a generic feature of post-quench relaxational dynamics in isolated many-body systems, which may occur due to multiple conserved quantities in the system [40, 137].

5.2.4 The Friedel oscillation and chiral symmetry breaking

There has been extensive literature discussing impacts of chemical doping in a CDW system [11,13,138]. In the presence of charge impurities, there will be local perturbations effect to the CDW system. Such an effect is called *Friedel oscillations* (FO). It is a quantum mechanical analog to the electric charge screening of charged particle in a pool of ions. It depicts the characteristic decay behavior in the fermionic density near the perturbation followed by a damped sine wave. Fig. 5.5 is an example of FO, where the authors use X-ray diffraction to probe vanadium-doped blue bronze. The doped vanadium atoms serve as the defects and modulate the charge-density amplitude and phase nearby, as drawn in the figure. As a result of this modulation, the diffraction peak shows up as an asymmetric tail as shown in the left. This is one of the key phenomena of showing existence of FO and charge impurities.

Here in our data, at $\approx$1 ps, the NC-CDW peak also shows asymmetric tails, as seen in Fig. 5.6a and intensity profile in Fig. 5.6c. To best reconstruct and reproduce experimental data, we go through an iterative process in the reconstruction and find that to explain the emergence of the asymmetric diffraction tail and peak broadening in the plateau region, we only need to apply a phase adjustment that changes from $\boldsymbol{q}_{NC}$ to $\boldsymbol{q}_{IC}$ ($\boldsymbol{Q}_{FO} \propto \boldsymbol{q}_{IC} - \boldsymbol{q}_{NC}$). This phase-only modulation protocol applied here is only similar to the approach applied to

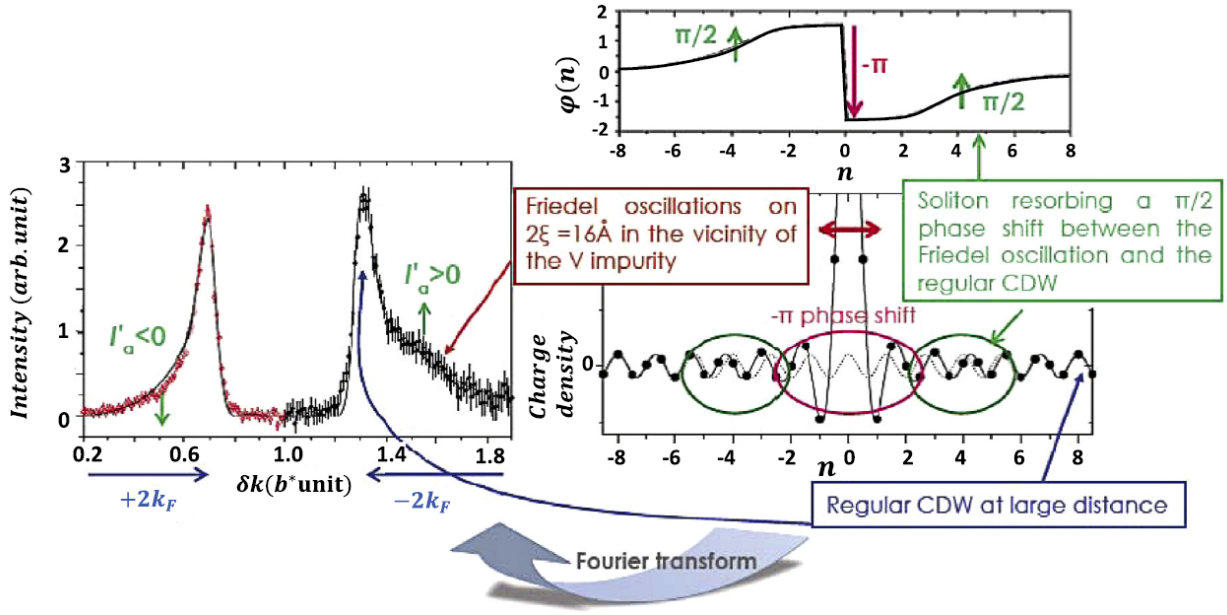

Figure 5.5: An example of the Friedel oscillation in vanadium-doped blue bronze. Adapted from Ref. [11, 12].

model the FO phenomenon in 1D CDW system. The adjustment made here reflect a defect-induced field created by the photo-doping. Unlike the static chemical doping, the mobile charge impurities can self-organize by adjusting to the new energy landscape that drives the NC-CDW to IC-CDW transition. This empirical phase adjustments results in a spiral CDW order emanating from the domain center, manifesting a chiral symmetry breaking within the commensurate domain. FT of this spiral order creates an asymmetric CDW peak that reproduce the experimental feature. Further adjustments in the phase create a tight fit to the data intensity profile as shown in Fig. 5.6c.

The correlation length of FO is about 7 nm with best fit to data and the intensity is the NC intensity after initial quench. Here the chiral symmetry breaking as constructed through phase modulations around the domain center can be seen as a state that exhibits intertwined NC and IC components. This spiral state further develops after prethermalization plateau to shift NC (FO) population into IC state, evidenced from the peak profile evolution where

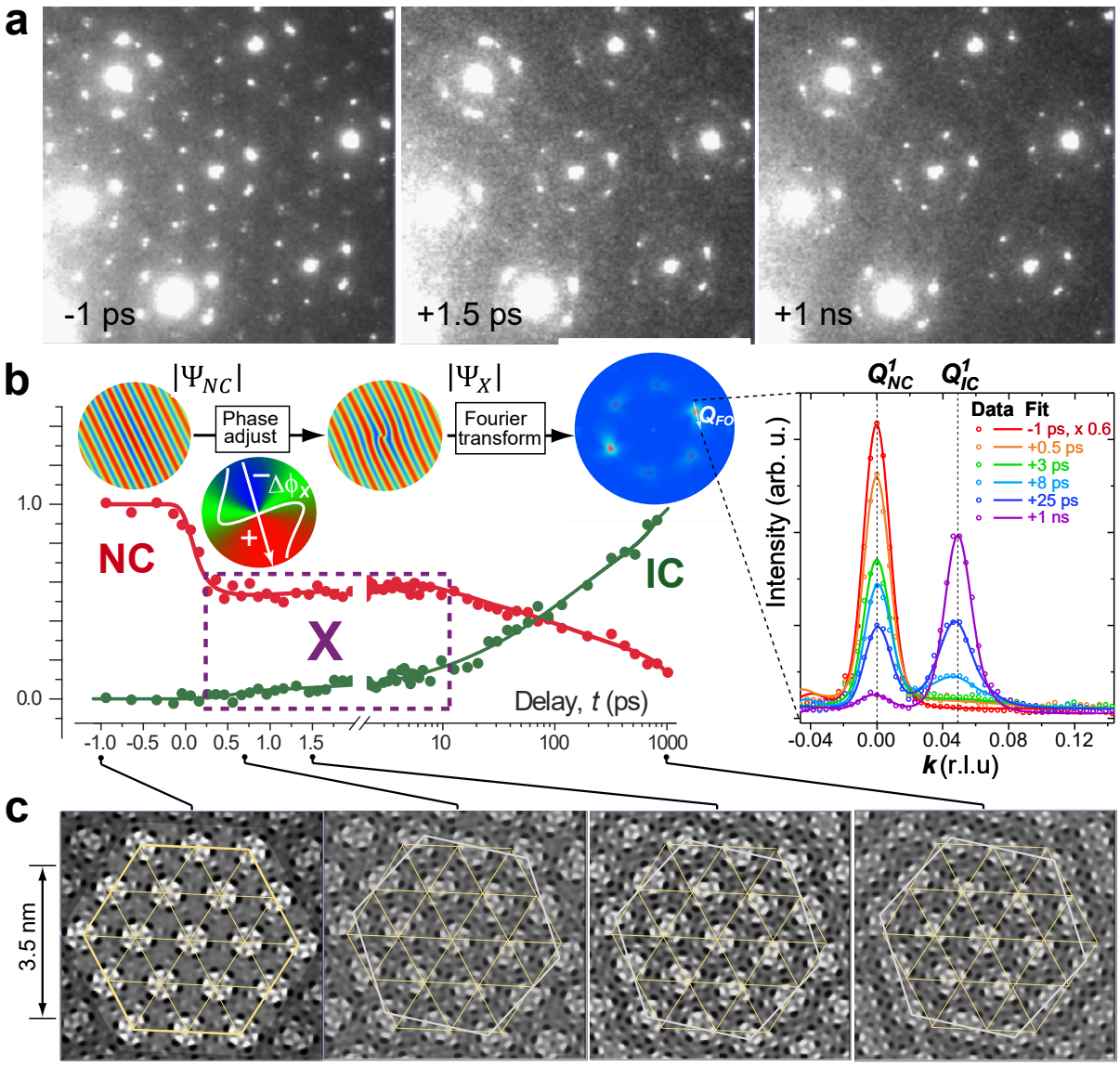

Figure 5.6: The chiral symmetry breaking and Friedel oscillations. **a**, The diffraction patterns at 3 critical time delays. The pattern at + 1.5 ps corresponds to the chiral symmetry breaking and FO region (X state). **b**, Phase modulation imposed on the reconstruction process due to FO. On the right shows the fit of the reconstructed pattern to experimental data. $\mathbf{k} = \mathbf{q} - Q^1_{NC}$. **c**, The reconstructed atomic displacement map. The dark spots represent the loss of atomic density (atoms moving away) and the white spots represent an increase in atomic density (atoms moving towards that spot).

IC peaks grows from the asymmetric tail.

5.2.5 Fluence-dependent studies

Fig. 5.7 reports the NC and IC peak dynamics at various pump excitation fluences, where the symbol $\boldsymbol{m}$ represents normalized intensity of the CDW peak. For NC, the peak intensity is normalized to that at the negative time $I_{NC}(t<0)$ and for IC, peak intensity is normalized by dividing $0.45I_{NC}(t<0)$ — a normalization protocol based on the steady states where the intensity of IC is 0.45 that of NC.

Another key feature is that the changes at short and long times show two thresholds, $F_{c,1}$ and $F_{c,2}$, respectively. Since the change in long time scales corresponds to thermalization, we define $F_{c,1}$ as the thermal threshold. By contrast, $F_{c,2}$ is defined as the nonthermal (doping) threshold.

To better understand the thermal heating effect, we also estimate the temperature rise due to laser heating. Based on 1T-TaS_2 optical measurements on the bulk sample [139], reflectivity $R=0.405$ is derived for 800 nm laser at normal incidence. According to the thin film transfer matrix method [90] and Appendix B, the total reflectivity and transmission are $R=0.35,\ T=0.12$, respectively (note: experimental condition: sample thickness $d=50$ nm, 45° incidence, p-polarized). So the net photon absorption coefficient is: $1-R-T=0.43$. At fluence F, the absorbed energy density on average is calculated to be: $\rho_E=\frac{F(1-R-T)}{d}$. At critical threshold of $F_{c,2}=1.52$ mJ/cm^2, the absorbed energy density $\rho_E=1.0$ eV/nm^3. By integrating the specific heat [119] of 1T-TaS_2 from RT (296 K) to the transition temperature of 353 K, the required thermal density is estimated to be 0.85 eV/nm^3 (including latent heat). At threshold of $F_{c,2}$, assuming all the absorbed photon is converted into heat, then the sample temperature increase would be 71 K (from RT to 367 K). This result is consistent with other measurements in 1T-TaS_2 [122, 123]. As to the doping and nonthermal effect,

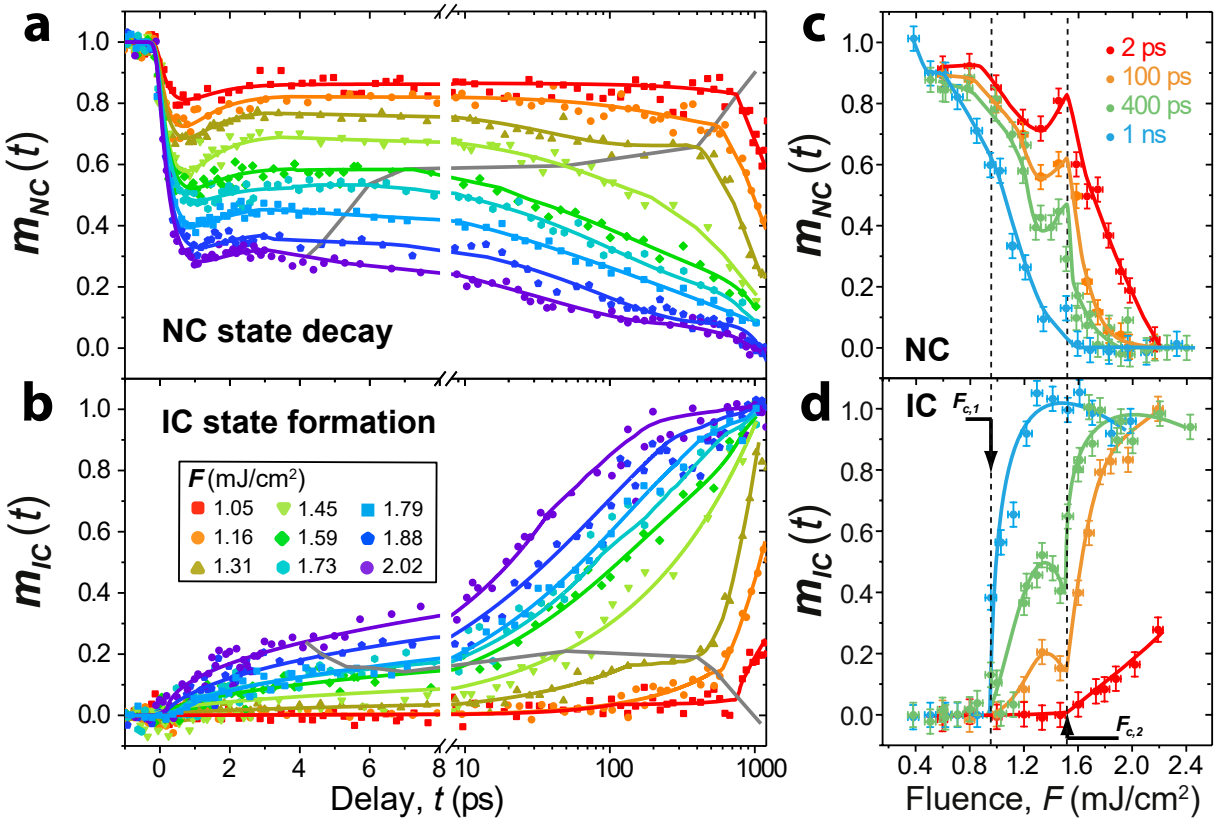

Figure 5.7: The dynamics of NC and IC peaks at various fluences. **a**, The NC peak intensity dynamics. The gray line represents the end of prethermalization and the beginning of thermalization stage. **b**, The IC peak intensity dynamics. **c**, The NC peak intensity changes at several critical time delays. **d**, The normalized IC change at several time delays. Thresholds of $F_{c,1}, F_{c,2}$ are as marked in the figure.

more will be discussed in Sec. 5.4.

5.3 Universal behaviors

As discussed in Chapter 1, phase transitions exhibit critical behavior near the critical point [140]. Even in the non-equilibrium regime, it is predicted to also have universal scaling near the nonthermal fixed point. Recently it has been experimentally observed that the post-quench relaxation process of 1D Bose gas follows a critical scaling [141, 142]. In these experiments, the Bose gas is confined in a 1D tube and perturbed by external field that

mimics a strong cooling quench. Then the post-quench state evolution is monitored with distribution function in real space probe. A FT of the real space distribution yields the momentum space distribution, or correlation function. It is found that within the universal scaling time window, the distribution function can scale horizontally and vertically to collapse into one curve. This critical scaling behavior is a proof of nonthermal fixed point and existence of certain universality class far from equilibrium.

In the case of 1T-TaS_2, the fluence-dependence data unambiguously prove two thresholds in both NC and IC data. In this section, we will discuss the universal scaling behavior at both the prethermalization plateau region and also at the thermalization stage.

5.3.1 Universal scaling in the prethermalization plateau region

The fluence-dependent data reported earlier already indicate that the prethermalization plateau is dependent on fluence, so as the IC switching speed. The life span of prethermalization plateau t_{pre} exhibits slowing down near the thermal threshold of $F_{c,1}$. Similarly, the IC formation time also follows the diverging trend as the pump fluence is tuned near $F_{c,1}$.

The divergence of two characteristic times indicates that the dynamics themselves may be collapsed into a single scaling function (or fixed point). Indeed, with proper assignment of scaling functions and scaling exponents, we found that both the NC and IC curves collapse — into groups of above $F_{c,1}$ and above $F_{c,2}$. In the time domain, we separate the scaling into two parts with different physical origins: prethermalization plateau region and long-time thermalization region. This collapse is performed for both horizontal (t)and vertical ($\boldsymbol{m}$) axis. We base our scaling using the first data curve after each threshold as the reference curve. The scaling exponents are applied to the control parameter, $r = F - F_c$, where F_c could be $F_{c,1}$ or $F_{c,2}$. Now with scaling, the horizontal axis is changed to $t_1 \cdot (r/r_{Ref})^{\kappa}$, where

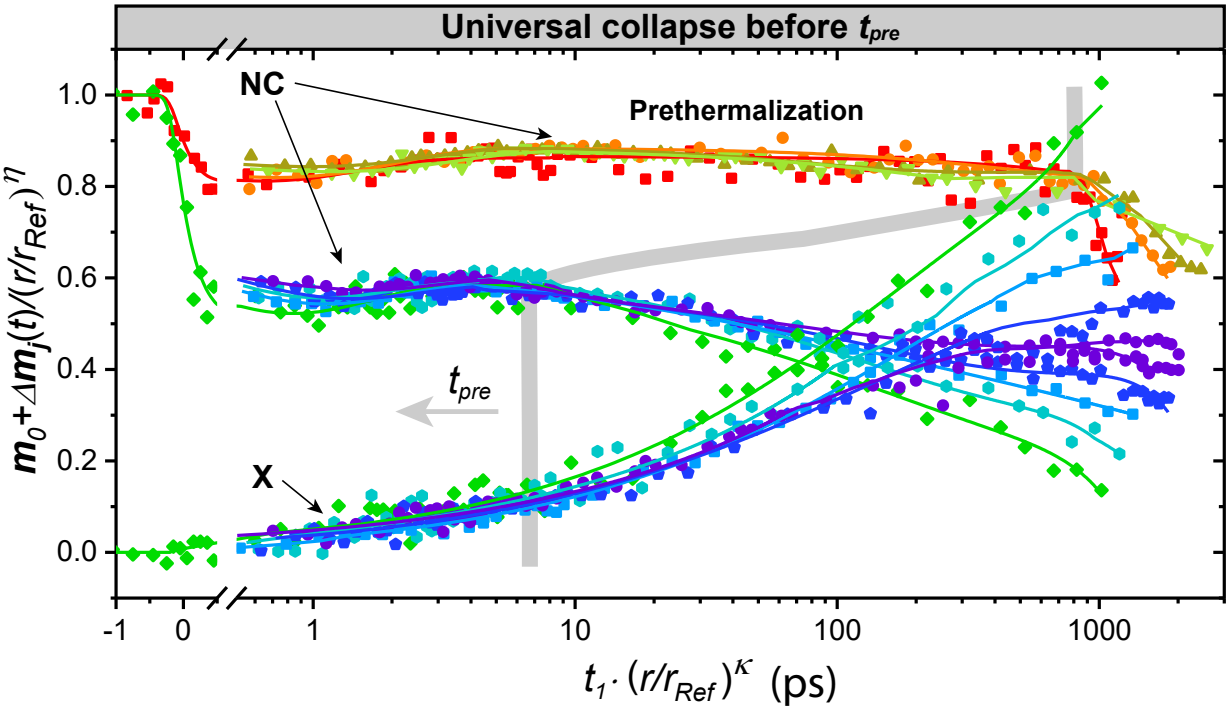

Figure 5.8: The universal scaling dynamics in the prethermalization regime (before t_{pre}) for NC and IC. The horizontal time axis is scaled based on power-law with exponent of κ while the vertical axis is scaled with power-law exponent of η. The r and r_{REF} refer to the distance from the critical threshold $r = F - F_c$ and the distance from the critical threshold for the reference curve, respectively. The reference curves are chosen as the first curve above the thresholds $F_{c,1}$ and $F_{c,2}$. The curves between $F_{c,1}$ and $F_{c,2}$ are scaled to the reference curve of $F = 1.05$ mJ/cm^2; the curves above $F_{c,2}$ are scaled to the reference curve at fluence of $F = 1.59$ mJ/cm^2.

$t_1 = t - 0.5$ ps to ignore the initial quench period. κ refers to the dynamical scaling exponent and here we set $\kappa = 0.5$. In the vertical axis, in the original dynamics plot, it is integrated intensity $\boldsymbol{m}_{NC}$ or $\boldsymbol{m}_{IC}$. In the scaling plot, it is changed to $\boldsymbol{m}_0 + \Delta\boldsymbol{m}_j(t)/(r/r_{Ref})^{\eta}$, where $\boldsymbol{m}_0$ is the offset value for the reference curves, $\Delta\boldsymbol{m}_j(t) = \boldsymbol{m}_j(t) - 1$ for NC so the scaling part is the absolute change while for IC peaks, $\Delta\boldsymbol{m}_j(t) = \boldsymbol{m}_j(t)$ itself. The scaling exponent η is set at 0.5. By applying both scaling, the data collapse well into one curve.

The prethermalization region is by definition region before the system thermalizes. There has been some reports of universal scaling in the thermalization coarsening process [9, 124],

but not in the prethermalization region. This is the first measurement indicating that universal scaling may be observed before thermalization.

5.3.2 Universal scaling in the thermalization stage

After the system passes chiral-symmetry-breaking prethermalization region, the emergent IC-CDW state starts to gain both intensity and correlation length, as shown in Fig. 5.4a. The increase in correlation length is reflected in the 2D map of IC peak evolution shown in Fig. 5.9a, where at each horizontal line scan intensity profile, it is normalized to the IC peak center. So the IC peak center is always at the same color scale. This normalization is to highlight the sharpening in IC peak. A more vivid schematic drawing of the IC peak evolution is drawn in Fig. 5.9b, where the peak profile is a Lorentzian function. Inverse of Lorentzian width scales as t^{β} and the amplitude scales as t^{α}. Fig. 5.9c is an example of the (inverse) peak width and height evolution. Note, the peak is fitted with a Voigt function where Gaussian part represents the instrumental resolution and Lorentzian part represents the overall distribution function. All the Lorentzian width discussed in this section refers to the full width at half maximum of the Lorentzian function. In the plot of Fig. 5.9c, the data in purple are the correlation length, the inverse of the Lorentzian HWHM (half width at half maximum); the data in green are the Lorentzian peak height, which based on a 2D Lorentzian distribution, is the integrated intensity divided by HWHM squared, then divided by the integrated intensity to represent the true profile height.

The scaling region (gray shaded area) starts from t_{pre} and ends until IC is fully formed to a saturated level. The universal scalings in the width and height of the structure factor presented in Fig. 5.9c is just for one sample fluence. In fact, the data at all excitation fluences show such scaling behavior and the scaling exponents α and β are found to be

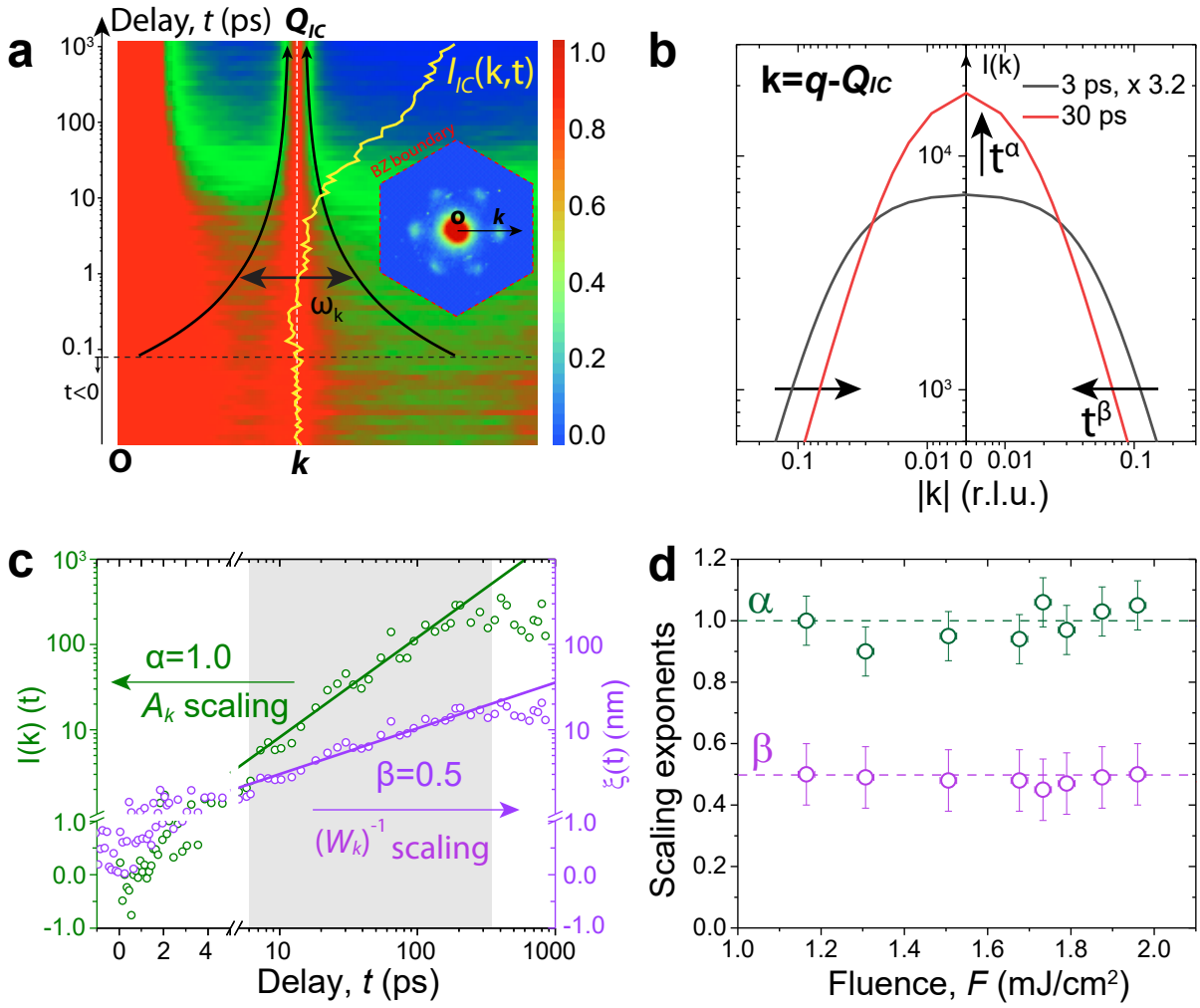

Figure 5.9: The dynamical scaling of IC peak dynamics and IC phase evolution. **a**, The IC peak profile evolution at different time delays. The profile line scan is from Bragg peak (O point in the lower left) to IC peak (Q_{IC}) in the radial direction outwards. Intensity at each time frame is normalized by IC peak to highlight the sharpening of IC peak. **b**, Schematic IC peak profile at two different time delays to illustrate the scaling in peak width W_q and peak height A_q. **c**, The power scaling of IC peak width and peak height scaling across several orders of time evolution (gray shaded area). Pump fluence is 1.73 mJ/cm^2. **d**, The fluence-dependence of the scaling exponents α and β.

fluence-independent, with $\beta = 0.5 \pm 0.05$ and $\alpha = 1.0 \pm 0.1$. Both scaling exponents has physical meanings.

β is for scaling in the correlation length during coarsening, which is the characteristic size of IC domain size. $\beta = 0.5$ means that when the time is 4 times longer, the IC domain

would grow twice larger. Also, $\beta = 0.5$ is universal for phase ordering kinetics for systems with non-conserved order parameter [1].

α is for scaling in the local order parameter of IC-CDW. In our experiments, we show that $\alpha = d\beta$, where $d = 2$ is the dimensionality — a well-accepted result for coarsening under a quench [143].

The scaling exponents are independent of pump fluence. Clearly, the dynamics do show strong fluence-dependence. The difference in dynamics between different excitation fluences lies in the level of scaling: all the correlation length follows 1/2 power-law scaling: $\xi \propto t^{0.5}$, but the coefficients for each fluence are different. Here we can define $\xi = \sqrt{2D \cdot t}$, where D is the diffusion coefficient and it has unit of $\mathrm{nm}^2/\mathrm{ps}$ [143]. Fig. 5.10b shows the diffusion coefficient at different laser fluences. It increases with fluence and changes by an order of magnitude in the applied fluence range.

From the raw dynamics curves at various fluences, the curves are very different. Fig. 5.10a is a plot of the raw data with offset of the prethermalization turning point: delay t is offset by t_{pre}, intensity $\boldsymbol{m}_{IC}(t)$ is offset by $\boldsymbol{m}_{IC}(t) - \boldsymbol{m}_{IC}(t_{pre})$. By simply scaling the horizontal time axis with a coefficient for each fluence, the cures would collapse into a single curve — see Figs. 5.10c&d. The coefficient D_m for each fluence is very similar to the diffusion constant extracted from correlation length fittings D_ξ.

Recent high-impact papers on isolated Bose gas [141, 142] measurements are two of the best examples to demonstrate universal dynamics in the post-quench relaxation process and existence of a nonthermal fixed point, even though theory has been established decades ago. In these experiments, they work on isolated cold atoms, the measurements rely on Fourier transform to extract the distribution and scaling functions. In comparison, our data measure condensed matter systems in the real materials. Our probe is based on scattering and by

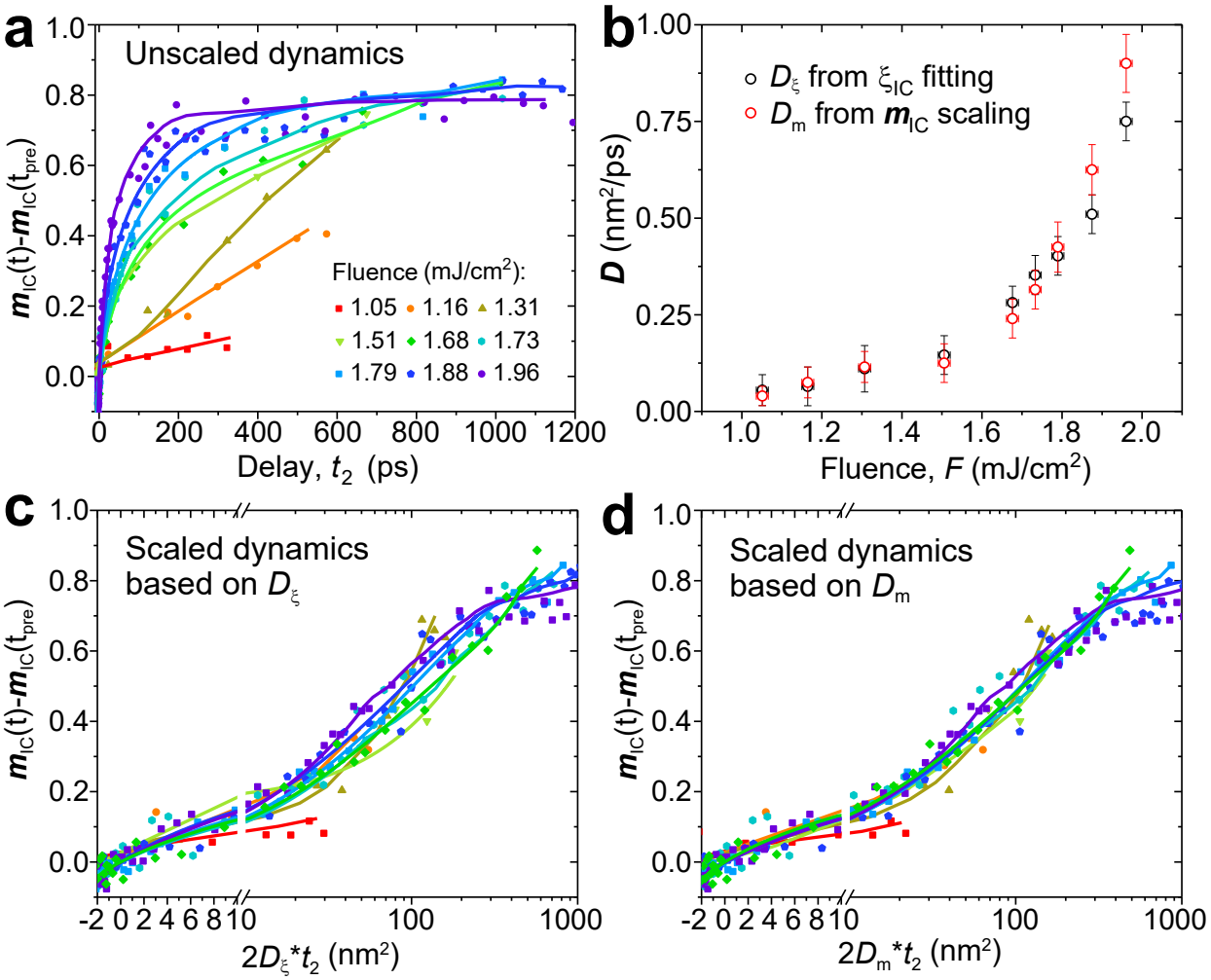

Figure 5.10: The universal scaling of IC peak dynamics across all fluences. **a**, Unscaled IC dynamics after prethermalization. Horizontal time is delay after prethermalization, $t - t_{pre}$. Vertical scale is intensity above prethermalization, $I(t) - I(t_{pre})$. **b**, The fluence-dependence of diffusion coefficients. D_ξ is from correlation length fitting and D_m is from IC universal scaling in the thermalization stage. **c**, IC universal dynamics scaled by diffusion coefficient D_ξ. In the horizontal axis notation, $t_2 = t - t_{pre}$. **d**, IC universal dynamics scaled by diffusion coefficient D_m.

nature it is a direct representation of correlation functions (scaling functions). The high coherence and time resolution of our electron probe allow us to directly monitor the correlation function (i.e. peak profile) evolution. This level of resolution and sensitivity represents a significant step forward in studying non-equilibrium dynamics in complex materials.

5.4 Phase transitions induced by 2500 nm laser

In recent years, there has been a lot of interests in developing novel optoelectronic devices based on graphene, transition metal dichalcogenides (TMD), and heterostructures of layered materials [144–149]. Due to the high flexibility in controlling photodoping density, fast write/erase cycles and vast variety of materials to choose from, laser-based optoelectronic devices are promising to find vast applications in the future.

For a material such as 1T-TaS_2 in optoelectronic applications, there are many concerns one like to get answers for. For example, what is the intrinsic switching speed and can we improve it? How do we deal with heat dissipation problem? In this section, based on our results, we will provide a possible solution for improving the switching speed and at the same time depositing much less energy to avoid heating problem in applications.

In a rigid lattice, for example in silicon or gold [150–152], there is no lattice symmetry change by laser excitation. So the post-excitation behavior is mainly governed by the carrier relaxation and subsequent lattice heating effect. By contrast, in symmetry-broken complex materials for example VO_2 [153–155] or 1T-TaS_2 [106, 122], where there are both strong electron-electron and electron-phonon couplings, disruption to the electronic system instantaneously modifies the lattice potential energy surface and ions will spontaneously proceed to a high symmetry state. Such a process does not necessarily require lattice temperature rise, although lattice heating is inevitable through electron-phonon coupling in the long timescale. To clarify whether the phase transition is primarily thermally-driven or via photo-doping effect, we designed experiments by using 2500 nm and 800 nm lasers to induce phase transitions in 1T-TaS_2 and compare the results.

The photon energy between 2500 nm and 800 nm differs by a factor of 3, as illustrated

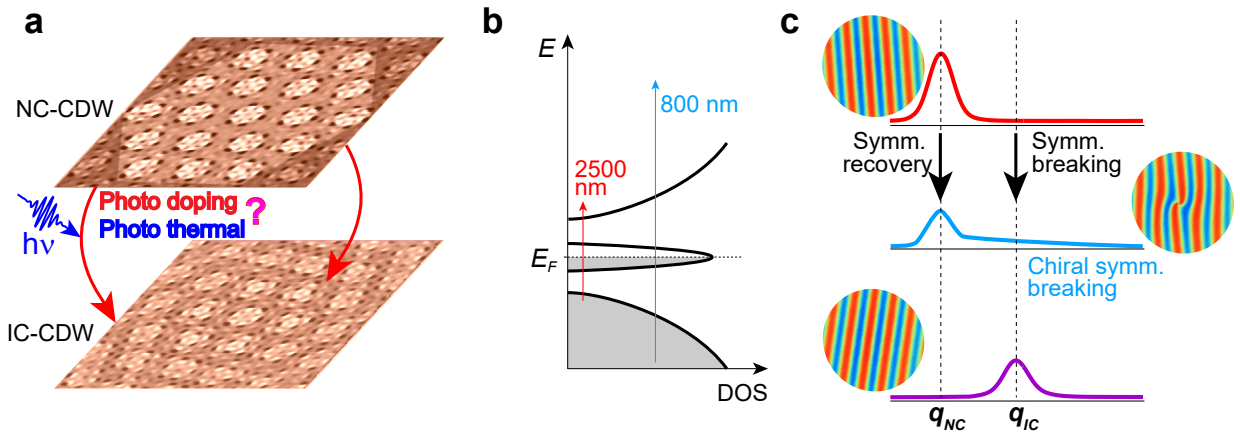

Figure 5.11: The schematic drawing of phase transitions by 2500 nm and 800 nm lasers. **a**, Phase switching between NC- and IC-CDWs by means of either photo-doping or photo-thermal effect. **b**, The schematic drawing of density of states (DOS) near the FS for 1T-TaS_2 at RT, adapted from Ref. [13]. **c**, The schematic drawing of the transition from NC-CDW to IC-CDW via chiral symmetry breaking.

in Fig. 5.11b, while for both of them, each absorbed photon creates one pair of electron and hole, ignoring nonlinear effects. This gives us a unique opportunity to do comparative experiments to clarify whether phase transition is induced by photo-thermal or photo-doping effect. Photo-thermal refers to the thermal and lattice heating effect by laser excitation. Photo-doping is similar to chemical doping, which is generally related to changes in the electronic states independent of lattice heating.

Fig. 5.12 shows the fluence-dependent dynamics induced by 2500 nm laser. As we can see, there is also distinct prethermalization plateaus as seen in 800 nm. From the peak profile analysis, the 2500 nm excitation also has asymmetric tails in the NC peaks — signatures of FO and chiral symmetry breaking (see Fig. 5.11c).

From the fluence-dependent data, we can extract the characteristic time of IC state formation (Fig. 5.12c). Here, we use the time it takes to reach 1/2 of the IC intensity and define this time as $\tau_{1/2}$. In both cases, the photo-doping enables a new dynamical pathway driving phase transitions. Accordingly, we determine the excitation density to be 0.68 and

0.75 nm^{-3} for 800 nm and 2500 nm, respectively. The difference is within 10%. But in contrast, the corresponding absorbed energies are 1.05 and 0.37 eV/nm^3, respectively — a factor of 3 difference.

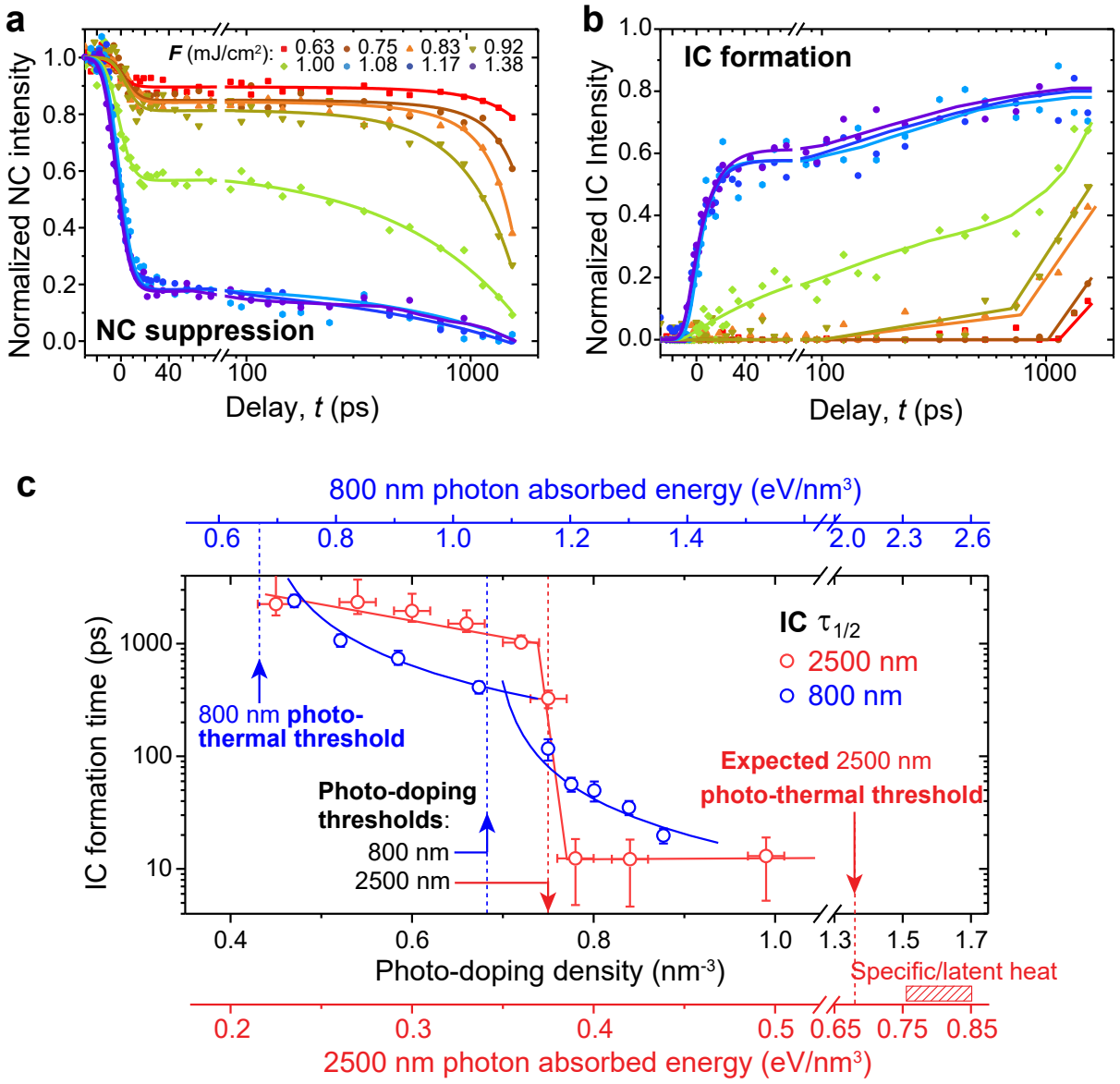

Figure 5.12: The fluence-dependent data of 2500 nm dynamics and thresholds comparison. **a**, The NC-CDW peak intensity evolution at various pump fluences by 2500 nm laser. **b**, IC-CDW peak growth at various pump fluence, the same color code as **a**. **c**, Comparison of the IC formation time for 800 nm and 2500 nm and determination of photo-doping, photo-thermal thresholds.

Note: the absorbed photon and energy density are calculated based on the following:

based on 1T-TaS_2 optical measurements on the bulk sample [139], for 2500 nm laser, reflectivity is $R = 0.534$ at normal incidence. According to thin film transfer matrix method [90] and Appendix B, the total reflectivity and transmission are $R = 0.42$, $T = 0.22$, respectively (experimental conditions: sample thickness $d = 59$ nm, 45° incidence, p-polarized). So the photon absorption coefficient is: $1 - R - T = 0.36$. The absorbed energy density is calculated to be: $\rho_E = \frac{F(1-R-T)}{d}$. At critical threshold of $F_c = 1.04$ mJ/cm^2, the absorbed energy density $\rho_E = 0.37$ eV/nm^3, corresponding to absorbed photon density of 0.75 photon/nm^3.

The coincidence in photo-doping density at the phase transition threshold suggests that the phase transition is more coupled to the photo-doping effect (excited carrier density) than photo-thermal effect (thermal heating). The absorbed photon density at the threshold level of ~ 0.7 photon/nm^3 corresponds to 0.52 absorbed photon per Star-of-David, which coincides with the iron-doped 1T-TaS_2 [13]. Comparing with the specific heat measurement [119], 800 nm at the critical level $F_{c,2}$ is above the thermal requirement but the 2500 nm threshold is way below that. This observation is consistent with a previous report by Han and coworkers [106].

More evidences on doping and thermal effects are shown in the time-resolved dynamics in Fig. 5.13, where both 800 nm and 2500 nm are at a similar absorbed photon density level of ≈ 0.75 nm^{-3}. In Fig. 5.13a, we examine the satellite intensity integral. The overall changes in NC satellite intensities are very similar whereas clear differences are shown in IC intensities. IC peak change with 2500 nm excitation is seen to rise very fast to 20% in the first 2 ps while 800 nm excitation does not lead to an obvious initial rise. Another difference is 2500 nm excitation only reaches to 0.8 while 800 nm data rise to 1. This difference is also revealed in the previous fluence scan plot. Without enough thermal energy deposition, the 2500 nm data can only reach 80% of the level reached in 800 nm data in the thermalization

process.

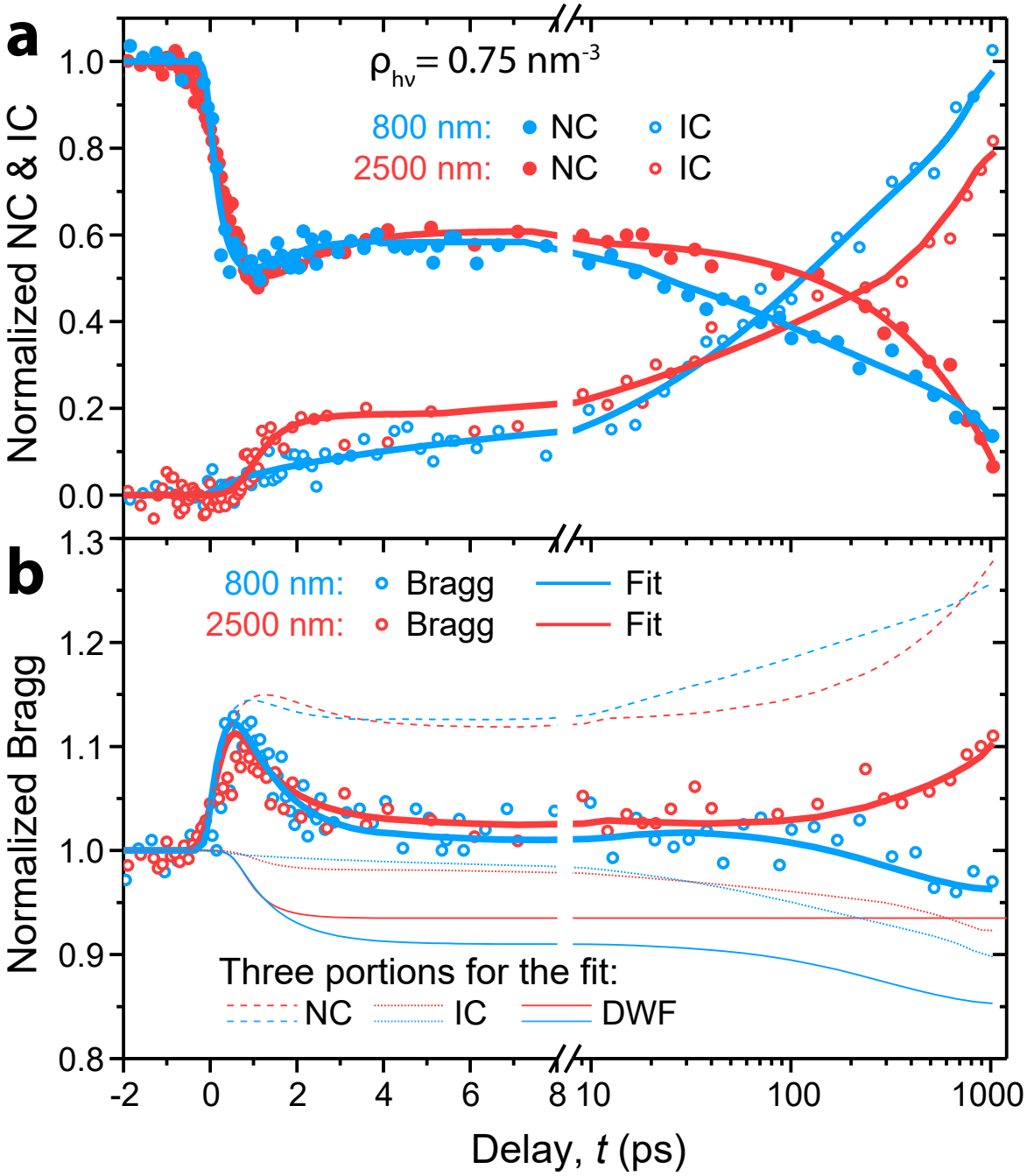

Figure 5.13: The CDW and Bragg peak dynamics at $\rho_{h\nu} \approx 0.75$ nm^{-3} for both 800 nm and 2500 nm pump excitation. **a**, NC and IC peak intensity evolution. **b**, The Bragg peak dynamics comparison and corresponding fit guidelines for the fit model.

The Bragg peak dynamics plotted in Fig. 5.13b reveals more information. To simulate

and understand the Bragg peak data, we propose the following simple model. Bragg peak intensity change has three contributions: 1, the intensity increase due to NC state suppression (symmetry recovery); 2, the intensity drop due to IC phase formation (symmetry breaking); 3, the intensity drop due to thermal heating (Debye-Waller effect). For the Debye-Waller (DW) factor, it is a convention to assume an exponential decay (two-temperature model) with the characteristic electron-phonon coupling time. For considering the static lattice distortion due to the NC and IC states, it is necessary to refer to the structure factors of CDW.

According to Giuliani and Overhauser [156], the structure factor of a CDW system can be written in the following way

$$S(\mathbf{q}) = \sum_{\boldsymbol{G}} \sum_{n=-\infty}^{+\infty} \delta[\boldsymbol{q} - (\boldsymbol{G} + n\boldsymbol{Q})] J_n^2(\boldsymbol{q}\cdot\boldsymbol{A}) F_n^{\phi} F_n^{A} F^{DW}(\boldsymbol{q}), \tag{5.8}$$

where $\boldsymbol{q}$ is the scattering wave-vector, $\boldsymbol{G}$ is the reciprocal lattice vector, $\boldsymbol{Q}$ and $\boldsymbol{A}$ are the CDW wave-vector and lattice distortion vector, respectively. J_n is Bessel function of the first kind of order n, with $n=0$ corresponds to Bragg peak, $n=1$ (2) corresponds to first- (second-) order CDW peaks. F_n^{ϕ} and F_n^{A} are the phase and amplitude factors and $F^{DW}(\boldsymbol{q},\boldsymbol{u}) = \exp\big(-\langle(\boldsymbol{q}\cdot\boldsymbol{u})^2\rangle\big)$ is DW factor with atomic vibration amplitude u. With small amplitude approximations at an initial CDW distortion amplitude A_0, CDW intensity can be written as: $I_{CDW}(\boldsymbol{q},\boldsymbol{A}_0) = J_1^2(\boldsymbol{q}\cdot\boldsymbol{A}_0) \approx \frac{1}{4}(\boldsymbol{q}\cdot\boldsymbol{A}_0)^2 F_1^{\phi} F_1^{A}$. Bragg peak intensity: $I_{Bragg}(\boldsymbol{q},\boldsymbol{A}_0) = J_0^2(\boldsymbol{q}\cdot\boldsymbol{A}_0) F^{DW}(\boldsymbol{q},\boldsymbol{u}) \approx [1 - \frac{1}{2}(\boldsymbol{q}\cdot\boldsymbol{A}_0)^2] F^{DW}(\boldsymbol{q},\boldsymbol{u})$.

After laser excitation, assuming that the lattice distortion changes from $\boldsymbol{A}_0$ to $\boldsymbol{A}_1$, the

normalized CDW peak intensity can be written as

$$I_{CDW}^{norm} = \frac{I_{CDW}(\boldsymbol{q}, \boldsymbol{A}_1)}{I_{CDW}(\boldsymbol{q}, \boldsymbol{A}_0)} = \frac{A_1^2}{A_0^2}. \tag{5.9}$$

Normalized Bragg peak intensity can be written as

$$I_{Bragg}^{norm} = \frac{I_{Bragg}(\boldsymbol{q}, \boldsymbol{A}_1)}{I_{Bragg}(\boldsymbol{q}, \boldsymbol{A}_0)} = \frac{1 - 0.5(\boldsymbol{q} \cdot \boldsymbol{A}_0)^2 I_{CDW}^{norm}}{1 - 0.5(\boldsymbol{q} \cdot \boldsymbol{A}_0)^2} \exp\Big[-q^2(u_1^2 - u_0^2)\Big]. \tag{5.10}$$

Assuming NC- and IC-CDWs are independent, the normalized 1T-TaS_2 Bragg peak intensity can be written as follows

$$I_{Bragg}^{norm} = [\frac{1 - 0.5(\boldsymbol{q} \cdot \boldsymbol{A}_0)^2 \cdot I_{NC}^{norm}}{1 - 0.5(\boldsymbol{q} \cdot \boldsymbol{A}_0)^2}] \cdot [1 - 0.5(\boldsymbol{q} \cdot \boldsymbol{A}_0)^2 \cdot 0.45 I_{IC}^{norm}] \cdot [a \cdot \exp[-t/\tau_{DW}] + 1 - a], \tag{5.11}$$

where the first part is the contribution from NC (dashed line in Fig. 5.13b), the second part is related to IC (dotted line in Fig. 5.13b), the third part is the DWF, where we assume an exponential decay with a time constant τ_{DW} and amplitude of a. In this simple model, I_{NC}^{norm} and I_{IC}^{norm} are independently measured (Fig. 5.13a). τ_{DW} is estimated to be 1 ps, a typical value for electron-phonon coupling time constant and it fits our data well. So the only fitting parameters left are $(\boldsymbol{q} \cdot \boldsymbol{A}_0)$ and DWF amplitude a.

To best fit the 2500 nm data, $|\boldsymbol{q} \cdot \boldsymbol{A}_0| = 0.68$ and $a = 0.06$ are obtained. The Bragg peaks in the plot has a q-value of 5.6 Å^{-1}. Considering the maximum lattice distortion for 1T-TaS_2 is $\sim$0.2 Å [157] at RT, $|\boldsymbol{q} \cdot \boldsymbol{A}_0| = 0.68$ is a reasonable estimate. Using the same $|\boldsymbol{q} \cdot \boldsymbol{A}_0|$, τ_{DW}, and DW amplitude a to fit the 800 nm data, the data and fit agree well in the first several ps. But there is another decay process that is much longer than 1 ps in the thermalization region. To capture the longer time scale, we have to impose another

DW exponential decay with a time constant of $\sim$300 ps and amplitude of 0.09. With this addition, it fits the data quite well. The total effective DW decay amplitude for 800 nm is 0.15, a factor of 2.5 that of 2500 nm data. Based on absorbed energy density calculations, the temperature rises from 2500 nm and 800 nm pump are 23 K and 71 K, respectively. This a factor of 3 in energy deposition in general agreement with the factor of 2.5 in DW decay amplitudes.

In the fit model of Bragg peak dynamics, we first use the CDW intensities (both NC and IC) to extract the static distortions. Then the static distortions are applied in the Bragg peak intensity formula to fit the Bragg peak dynamics. In this process, both CDW and Bragg peak intensity formulas use small-amplitude approximations in the Bessel functions. To verify the validity of this approximation, we estimate the error bars based on NC-CDW intensity (IC -CDW has weaker intensity thus smaller error bars). When NC-CDW intensity is 1 at negative time, the calculations with both Bessel function and approximations reveal the same result: the error bar is zero. When NC-CDW intensity drops to 50%, the difference between Bessel function and small-amplitude approximation is 1.2% in Bragg peak intensity calculation. When NC-CDW intensity drops to 10%, the difference is 2.2%. When NC-CDW intensity drops to 0, the difference is zero. So through out the NC-CDW peak evolution, the error bar is less than 2.5%. This small difference between Bessel function and approximation verifies that the small-amplitude approximation is good enough for the calculations.

With a higher excitation fluences, at similar doping level of 0.9 and 1.0 nm^{-3} for 800 nm and 2500 nm, respectively, the NC and IC peak evolutions are plotted for comparison in Fig. 5.14. From the results, while NC peaks also show similar levels of change initially, IC peak dynamics are drastically different. It takes 2 ps and 15 ps to reach 40% and 80%, respectively, by 2500 nm laser excitation. In comparison, to reach the same level of changes,

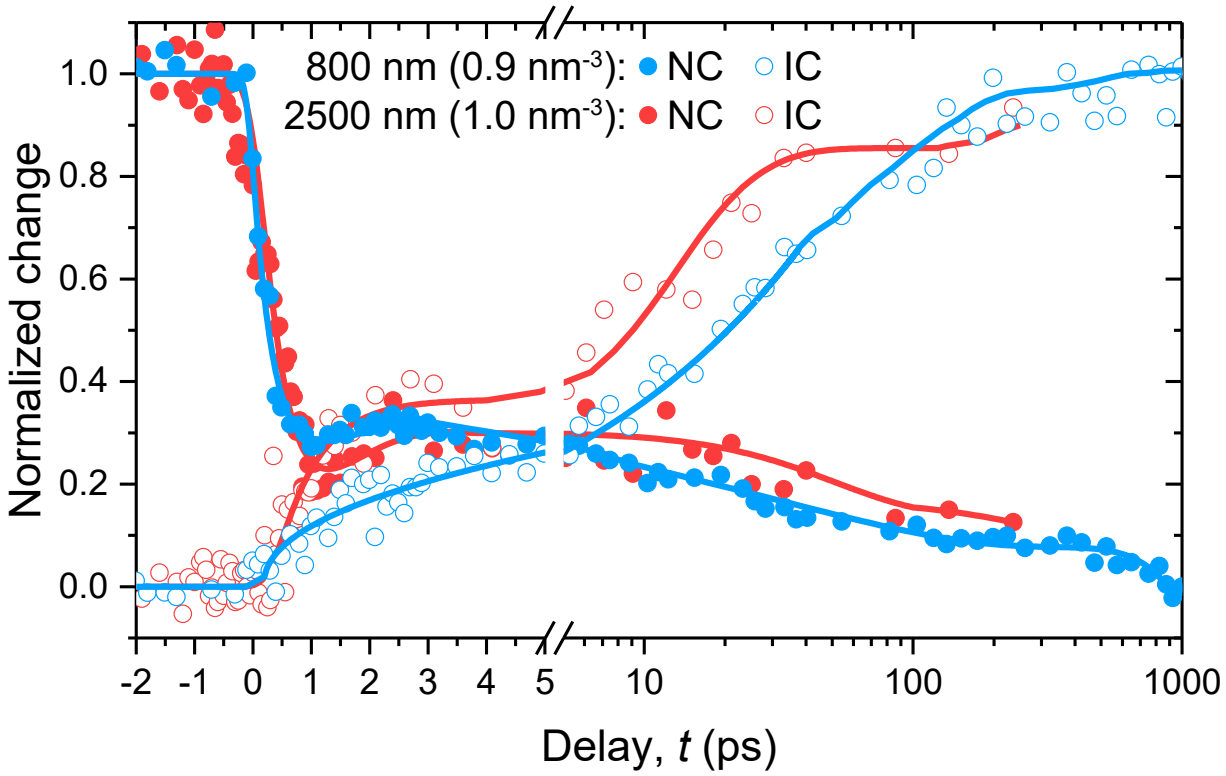

Figure 5.14: The CDW peak dynamics at excitation density of $\rho_{h\nu} = 0.9$ and 1.0 nm^{-3} for 800 nm and 2500 nm lasers, respectively.

it takes 14 ps and 80 ps, respectively, for 800 nm laser — more than a factor of 5 slower than 2500 nm excitation. A faster switching speed from 2500 nm excitation is obvious.

From previous data, one of the main differences between the two excitation lasers is the IC formation. Fig. 5.15a shows the IC relative intensity at various fluences at 10 ps ant 1 ns with 2500 nm laser excitation. In the short time scale (10 ps), there is a sharp jump that defines the photo-doping threshold. In the long time scale (1 ns), the sub-threshold doping produces partial IC growth in activated processes than thermalization. In comparison with 800 nm data as shown in Fig. 5.15b, 800 nm data do not have such a sharp jump at the threshold.

In summary, the NC to IC phase transition in 1T-TaS_2 is closely coupled to the photo-doping density rather than the energy density. With 2500 nm laser excitation, it deposits

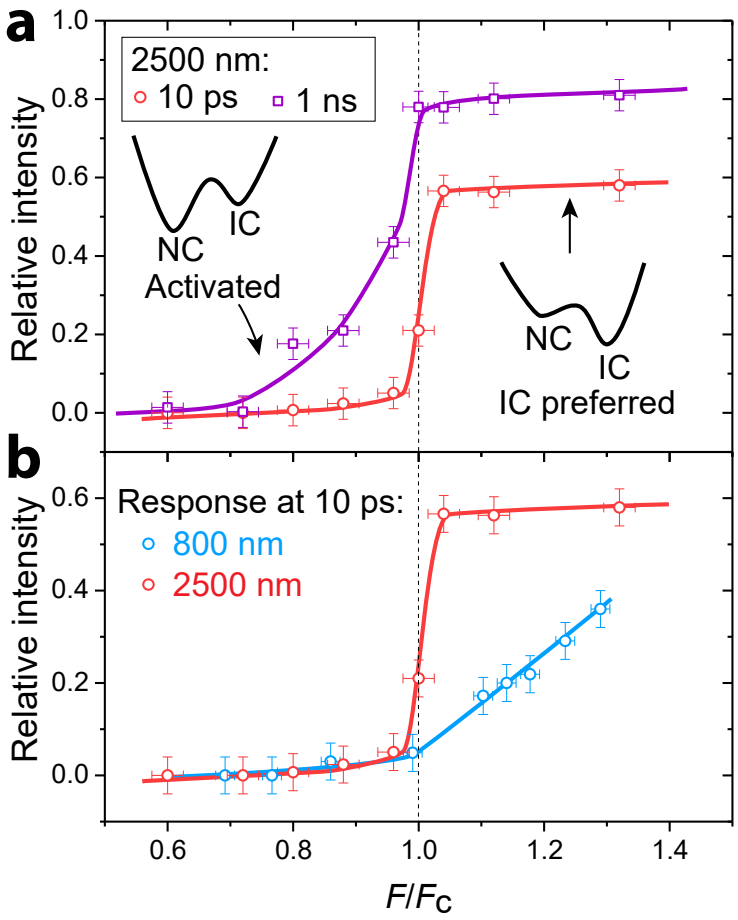

Figure 5.15: The comparison of IC formation for the two excitation lasers. **a**, IC relative intensity at 10 ps and 1 ns by 2500 nm laser excitation. **b**, Comparison of IC peak relative intensity at 10 ps with 800 nm and 2500 nm excitation.

less energy while showing a faster initial switching speed. In the long time thermalization regime, both 800 nm and 2500 nm data show scaling in the IC coarsening process. But 2500 nm has a much slower coarsening rate than 800 nm due to the lack of thermal energy. The less energy deposition, faster initial switching speed and distinct threshold behavior of 2500 nm excitation all point toward a better choice than 800 nm in optoelectronic applications.

5.5 Summary

To summarize, in this chapter, we explored phase transitions in 1T-TaS_2. The dynamics separates well in the time domain — initial order parameter quench in the first 0.5 ps, followed by prethermalization plateau (chiral-symmetry-breaking period), then by thermalization and coarsening in the longer timescale. The dynamics have well-defined universal scaling behaviors in each regime. Microscopically, a chiral-symmetry-breaking mechanism is proposed and proved by reconstruction and simulations. With 2500 nm laser excitation for comparison, the phase transition is proved to be connected to the photo-doping effect. Phase transition thresholds for such a novel transition pathway are primarily determined by photo-doping densities by comparing the data from 800 nm and 2500 nm laser excitations. Lack of excess thermal energy in the 2500 nm data proves to be more first order-like with faster switching speed.

Chapter 6

Study of iron chalcogenides by ultrafast electron diffraction

Superconductivity (SC) is an old but fascinating topic ever since its first discovery in 1911 by H. K. Onnes [158]. Five Nobel Prizes in physics have been given related to superconductivity (in the years of 1913, 1972, 1973, 1987, 2003) across almost a century. Realization and understanding of SC is the dream of many condensed matter physicists. A major step forward in this field was the discovery of SC in copper oxide in 1986 [159]. In the following 20 years, most records in T_c were related to the copper-based SC. This made people believe that copper oxide plays a magic role in SC. But in 2008, an iron pnictide compound was found to have SC with T_c of 26 K [160], which promoted a new field of iron-based SC (Fe-SC). In the same year, another iron pnictide compound was reported to have a T_c of 55 K [161] and iron chalcogenide FeSe was also shown to have SC with T_c of 8 K [162]. In 2012, it was demonstrated that single-layer FeSe on the $SrTiO_3$ substrate exhibits T_c of 77 K — ten times higher than the bulk FeSe. Another work reported the T_c could reach 109 K in single-layer FeSe on $SrTiO_3$ substrate [163]. Iron chalcogenide is the simplest form of Fe-SC materials and will be the main discussion in this chapter, particularly from structural point of view.

Superconductivity in Fe-SC arises from the proximity of anti-ferromagnetic (AFM) order.

The electron pairing mechanism is not BCS-type so Fe-SC is unconventional SC [164]. It is believed that the AFM correlations are important for understanding SC in Fe-SC. Moreover, the occurrence of AFM is always accompanied by a structural transition. On the high temperature side, it is paramagnetic with tetragonal structure. On the low temperature side, it is AFM or spin-density wave order with a lower structural symmetry, usually orthorhombic or monoclinic order. The low temperature state is often referred to as the nematic order because the 4-fold rotational symmetry is reduced to 2-fold. This nematic phase is a precursor of SC. So it is crucial to understand how the structural phase transition happens and the formation mechanism of the nematic phase in order to better understand and manipulate the SC in Fe-SC.

FeTe is the most stable iron chalcogenide, but it is non-superconducting. On the other hand, FeSe is superconducting with T_c of 8 K (bulk). With substitution of Te by Se, the compound with a formula of $FeSe_{0.5}Te_{0.5}$ is reported to have the highest T_c of 15 K [165]. In this chapter, we will show the UED studies of all three compounds: FeTe, $FeSe_{0.44}Te_{0.56}$, and FeSe. In Sec. 6.1, the background information on iron chalcogenide systems will be provided. Then ultrafast studies of FeTe at both low and high temperatures will be presented in Sec. 6.2. Structural transition from low temperature monoclinic to high temperature tetragonal phase was observed and will be discussed. In Sec. 6.3, we will show the ultrafast responses in an optimally-doped sample of $FeSe_{0.44}Te_{0.56}$. We report ultrafast dynamics of FeSe in Sec. 6.4. Finally, a summary is presented in Sec. 6.5.

6.1 Background and properties of iron chalcogenide compounds

Iron chalcogenide is the simplest form of Fe-SC class. It is composed of layered structure as shown in Fig. 6.1. In one unit cell, there are three layers with two chalcogen layers sandwiching the Fe layer, which is responsible for SC, as well as magnetic orders. A zoom-in view of the structural order is also plotted. One Se/Te atom forms bonds with 4 Fe atoms in a pyramid shape. Around one Fe atom, 4 Se/Te atoms form a tetrahedron structure. At above ≈ 75 K, both FeSe and FeTe have tetragonal structure with lattice constant $a = b$. Below that temperature, it transforms into the orthorhombic (FeSe) or monoclinic (FeTe) phase with a change of the unit cell and lattice constant $a \neq b$ (Fig. 6.1d).

The binary phase diagram between FeTe and FeSe is presented in Fig. 6.2a (from Ref. [15]). The green curve represents the T_c. It goes from 8 K in FeSe to about 15 K at $x \approx 0.5$. With Te concentration higher than 0.5, the Tc drops and it is non-superconducting in FeTe. The structural phase transition temperature T_s is anti-correlated with T_c. At the optimal-doping of $x \approx 0.5$, there is no longer a structural transition all the way down to zero temperature. In FeTe, the structural transition is accompanied by a AFM/SDW orders along $\mathbf{a}^*$ direction. The structural transition is observed by peak broadening or peak splitting while SDW order is seen through emergence of new peak — see Fig. 6.2b.

Superconductivity in FeSe is found to be enhanced under external pressure. The T_c increases to above 20 K at 4 GPa pressure (Fig. 6.2c). At the same time, the height of Se above Fe layer is decreasing with pressure (Fig. 6.2d). A more direct way of demonstrating how the structural order affects SC is shown in Fig. 6.2d, where all the Fe-SC materials are summarized. There exists an optimal anion height that generates the highest T_c. The

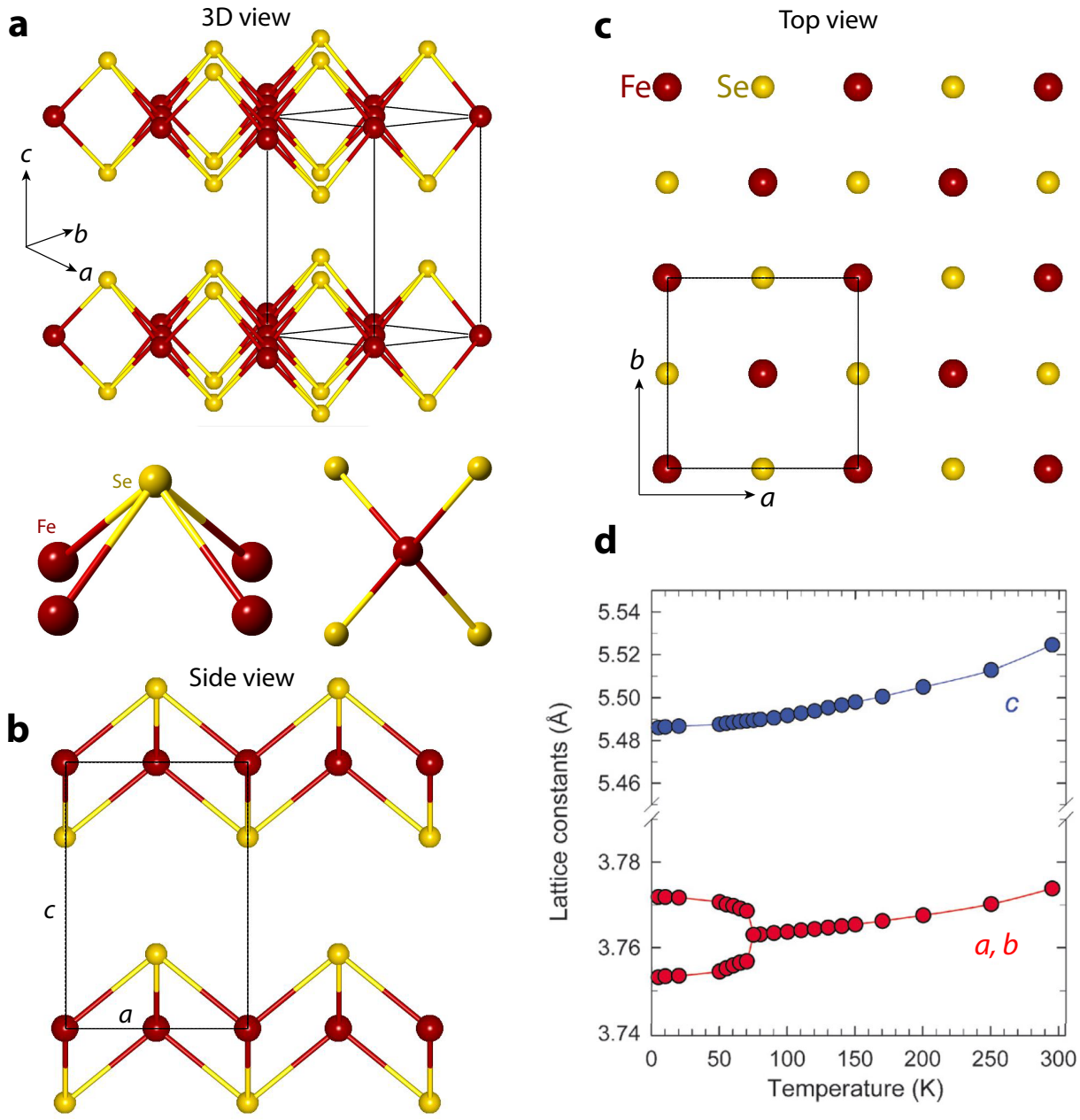

Figure 6.1: The structures of FeTe/FeSe in the high temperature tetragonal phase. **a**, 3D view of the ball-stick model structures. Cuboid with solid line represents the unit cell. **b**&**c**, Side and top view of FeTe/FeSe structure, respectively. **d**, Lattice constant changes across the tetragonal-orthorhombic structural transition for $FeSe_{0.92}$, reprinted from Ref. [14].

FeSe under pressure is plotted in open red circle symbols and it follows the trend relatively well. For our measurements using the electron probe, we are interested in exploring how the structure transforms after laser excitation to provide evidences and potential answers for

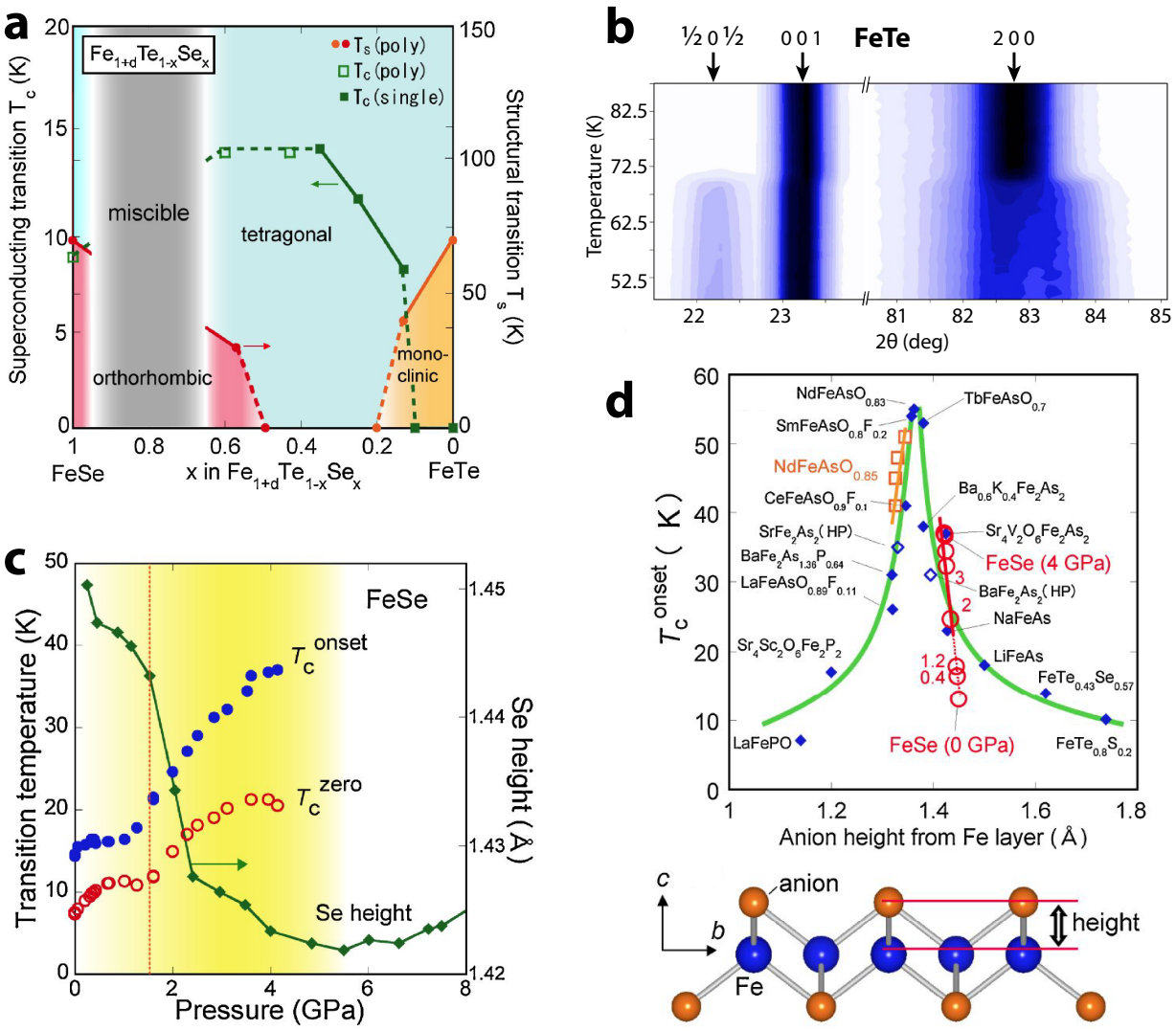

Figure 6.2: The phase diagrams of iron chalcogenides. **a**, The phase diagram of $FeTe_{1-x}Se_x$, figure from Ref. [15]. **b**, Neutron scattering measurement of FeTe to demonstrate simultaneous emergence of AFM order and structural transition, figure from Ref. [16]. **c**, The pressure-dependence of Se height and superconducting temperature T_c in FeSe. **d**, The anion height dependence of T_c of typical Fe-SC materials. Figure is reprinted from Ref. [15]. The overall trend indicates there exists an optimal anion height for the highest T_c.

understanding SC in Fe-SC.

6.2 Ultrafast phase transitions in FeTe

At room temperature, FeTe is in tetragonal phase with space group of P4/nmm. The unit cell contains 2 Te and 2 Fe atoms (lattice constants: $a = b = 3.822$ Å, $c = 6.285$ Å). At 72.5 K, it transforms into monoclinic phase with space group of $P2/_1$ m. Each unit cell contains 4 Te and 4 Fe atoms (lattice constants: $a = 5.331$ Å, $b = 5.308$ Å, $c = 5.485$ Å, Ref. [16]). For the diffraction pattern taken at RT, it is labeled in the following way: Bragg peak (1 0 0) to (0 0 0) has length of $a^* = 2\pi/a$ and Bragg peak (0 1 0) to (0 0 0) has length of $b^* = 2\pi/b$, where a and b are lattice constants in tetragonal phase. In the monoclinic phase, there is a change in unit cell thus in the labeling. The (2 2 0) peak in tetragonal phase splits into (4 0 0) and (0 0 4) peak in monoclinic state (Ref. [14]). In fact all the peaks with component in the a-b plane exhibit splitting or broadening, as shown by X-ray diffraction measurements in a previous paper [16]. This is also what we observed for the first time with ultrafast electron diffraction.

Diffraction patterns in Figs. 6.3d&e are taken at similar electron beam conditions (30 keV electron energy, ≈ 5000 e^-/pulse) but at different sample temperatures. The differences are quite visible: all the peaks are very sharp at RT while the peaks at 23 K are blurry (broadened), especially at higher s values. The difference image between RT and 23 K shown in Fig. 6.3f indicates the movement and broadening of the peaks.

The time-dependent measurements in Fig. 6.4 track the peak position and width induced by laser excitation at the following experimental conditions: the sample is cooled to 23 K and pumped by 2500 nm laser at $F = 2.7$ mJ/cm^2 and 1 kHz repetition rate. The anisotropy in the lattice along a and b axes can be distinguished from the static diffraction pattern, where the distances between (6 0 0) to (-6 0 0) and (0 6 0) to (0 -6 0) differs by about 2

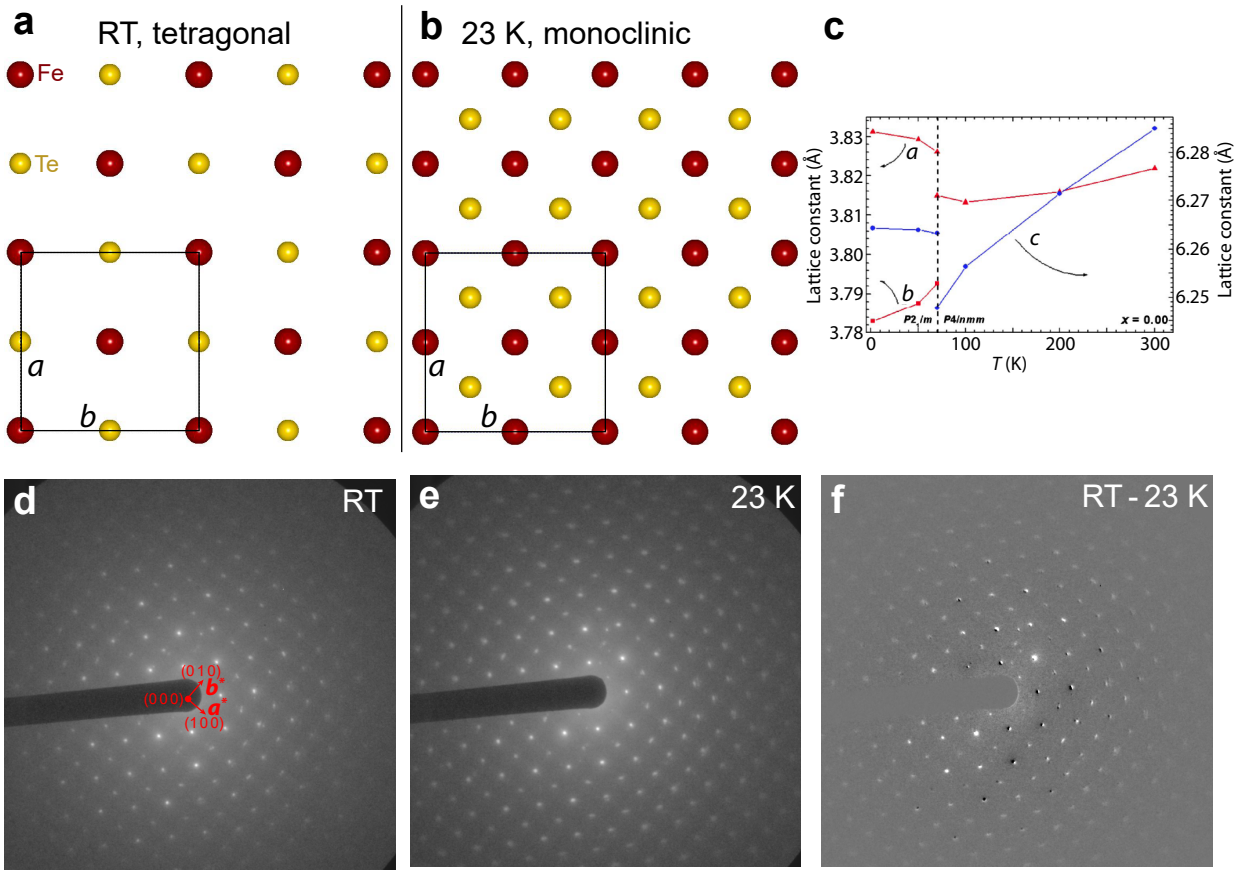

Figure 6.3: The structure and diffraction patterns of FeTe in the RT tetragonal and low-temperature monoclinic phase. **a**, Top view of the RT tetragonal structure. Lattice constants $a = b = 3.822$ Å. **b**, Top view of monoclinic structure at 23 K. Lattice constants a and b expand by a factor of $\approx \sqrt{2}$, with $a = 5.418$ Å, $b = 5.350$ Å due to unit cell doubling. **c**, FeTe lattice constant changes across the structural transition at ≈ 72 K [16]. **d**&**e**, Full diffraction pattern of FeTe at RT and 23 K, respectively. Electron diffraction pattern of FeTe at RT. 30 keV electron beam is along the [0 0 1] zone axis. The labeling is based on $a^* = 2\pi/a$ and $b^* = 2\pi/b$, where a and b are the tetragonal lattice constants. **f**, The difference diffraction pattern of RT minus that of 23 K. Both patterns are acquired at the same beam conditions and exposure times. The peak shift and sharpening/broadening can be clearly visible from the difference image.

pixels. After laser excitation, the peaks move toward more symmetric positions. The lattice constant changes are plotted in Fig. 6.4a. The lattice constant a decreases by 0.1% while b increases by 0.2%. By comparing with thermodynamic X-ray measurements [16], the lattice constants change at the first-order phase transition are -0.42% and +0.76% for a and b, respectively. Our measurements are overall a factor of 4 smaller than the reported values. It

is likely that either our laser fluence is not high enough or only 25% of the sample is driven to the tetragonal phase while the rest 75% is still in the monoclinic state.

To validate this, we estimate the temperature increase induced by laser. Based on optical measurements of $Fe_{1.05}Te$ [166], the optical reflectivity $R = 0.65$ and the real part of optical conductivity $\sigma_1 = 2.7 * 10^5\ \Omega^{-1}\mathrm{m}^{-1}$ at 2500 nm at 23 K. We assume the same values apply to FeTe. With this, the imaginary part of electrical permittivity ϵ_2 is calculated to be 4.14 and optical refractive index $n = 0.834$. The extinction coefficient $\kappa = 2.48$, which derives a penetration depth of 80 nm for 2500 nm photon. With transfer matrix method described in Appendix B, the optical absorption is calculated to be 0.34. The absorbed energy density with fluence of 2.7 $\mathrm{mJ/cm}^2$ is calculated to be 0.72 $\mathrm{eV/nm}^3$ (sample thickness ≈ 80 nm). Based on the specific heat of FeTe [167], the absorbed energy would raise the sample temperature from 23 K base temperature to 130 K, assuming all the absorbed energy is converted into heat and no heat loss.

This estimated final temperature is way above the structural transition temperature of 72.5 K. This discrepancy might because of several reasons: 1, the temperature estimate is not considering heat dissipation from sample to TEM grid; 2, the absorbed energy density is overestimated due to the inaccurate values of optical constant input, which are extrapolated from $Fe_{1.05}Te$ measurements instead of FeTe; 3, in the specific heat integration, the latent heat is not mentioned in the paper and it is underestimated in the calculation. The latent heat in a first-order phase transition could be very large compared to the specific heat integration. For example, in VO_2, from 0 K to 340 K, the integration of specific heat (not including latent heat) is only twice that of latent heat in the monoclinic to tetragonal transition at 340 K, which is the same type of structural transition as in FeTe. The specific heat is generally increasing from 0 at 0 K and gradually plateaus at some value around 300

K. For FeTe, the transition temperature (72.5 K) is much lower than that of VO_2 (340 K). If the latent heat in FeTe is similar to that of VO_2, then it would be easily several times higher than the total specific heat integration from 23 K to 72.5 K, reducing the estimated temperature rise to below 72.5 K.

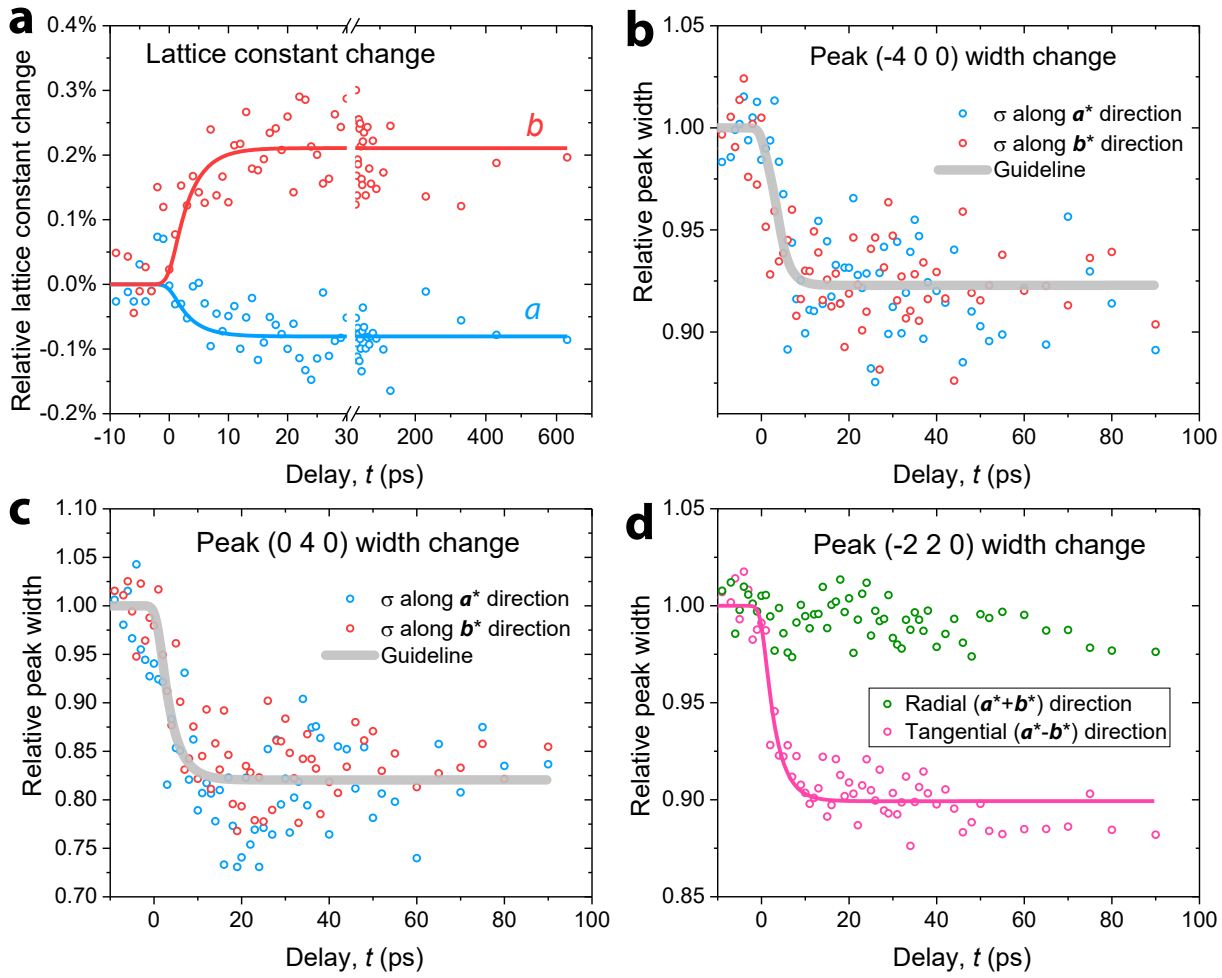

Figure 6.4: The time evolution of FeTe lattice constants and peak width at base temperature of 23 K (sample a, 2500 nm pump laser, 2.7 mJ/cm^2). **a**, The lattice constant changes along a and b directions, extracted from (4 0 0) and (0 4 0) peak movement relative to the center (0 0 0) peak. **b**, **c**&**d**, Peak sharpening after laser excitation with Gaussian profile fit for peak (-4 0 0), (0 4 0), and (-2 2 0), respectively. The width σ here refers to σ of a Gaussian fitting.

Aside from lattice constant change to demonstrate the structural transition, there is also peak sharpening (merging). Figs. 6.4b-d shows three typical peaks become sharper after

laser excitation. Peaks are fitted with Gaussian fitting and the presented peak width is normalized to sigma at the negative time. While peaks along $\boldsymbol{a}^*$ and $\boldsymbol{b}^*$ direction sharpens isotropically, the peaks with index of (h h 0) shows anisotropic change with sharpening mainly in the tangential direction (relative to center peak (0 0 0)) and almost no change in the radial direction.

In terms of peak intensity, it is found that the peak intensity has oscillations with period of $\approx$40 ps — see Fig. 6.5a and different peak oscillations have different phase about 90° apart. This oscillation corresponds to phonon frequency of 0.025 THz, which is most likely an acoustic phonon. Fig. 6.5b is a schematic diffraction pattern that shows the peaks with oscillations. About 1/3 of the peaks have very clear intensity oscillations. This peak oscillation is also reproducible in other samples. Fig. 6.5c shows oscillations in another two samples. But interestingly, instead of 40 ps as seen in sample a, the other two samples (b&c) have an oscillation period of 60 ps. The oscillations last for about two periods before damping away. These very large amplitude oscillations without consistent pattern and the periodicity seem to suggest that the oscillations are sample-dependent. It's likely to originate from sample warping after laser pulse excitation. The change of sample flatness affects the Ewald's sphere cutting of the reciprocal rods thus the intensities. However, at high temperatures, the oscillations are not clearly visible, as shown in Fig. 6.5d.

6.3 Ultrafast structural dynamics in $\mathbf{FeSe_{0.44}Te_{0.56}}$

$FeSe_{0.44}Te_{0.56}$ is reported to have the highest T_c among the $FeSe_xTe_{1-x}$ series. At the same time, it seems the structural and magnetic transitions are competing with SC. So with the highest T_c, the structural transition is quench down to unmeasurable — no thermodynamical

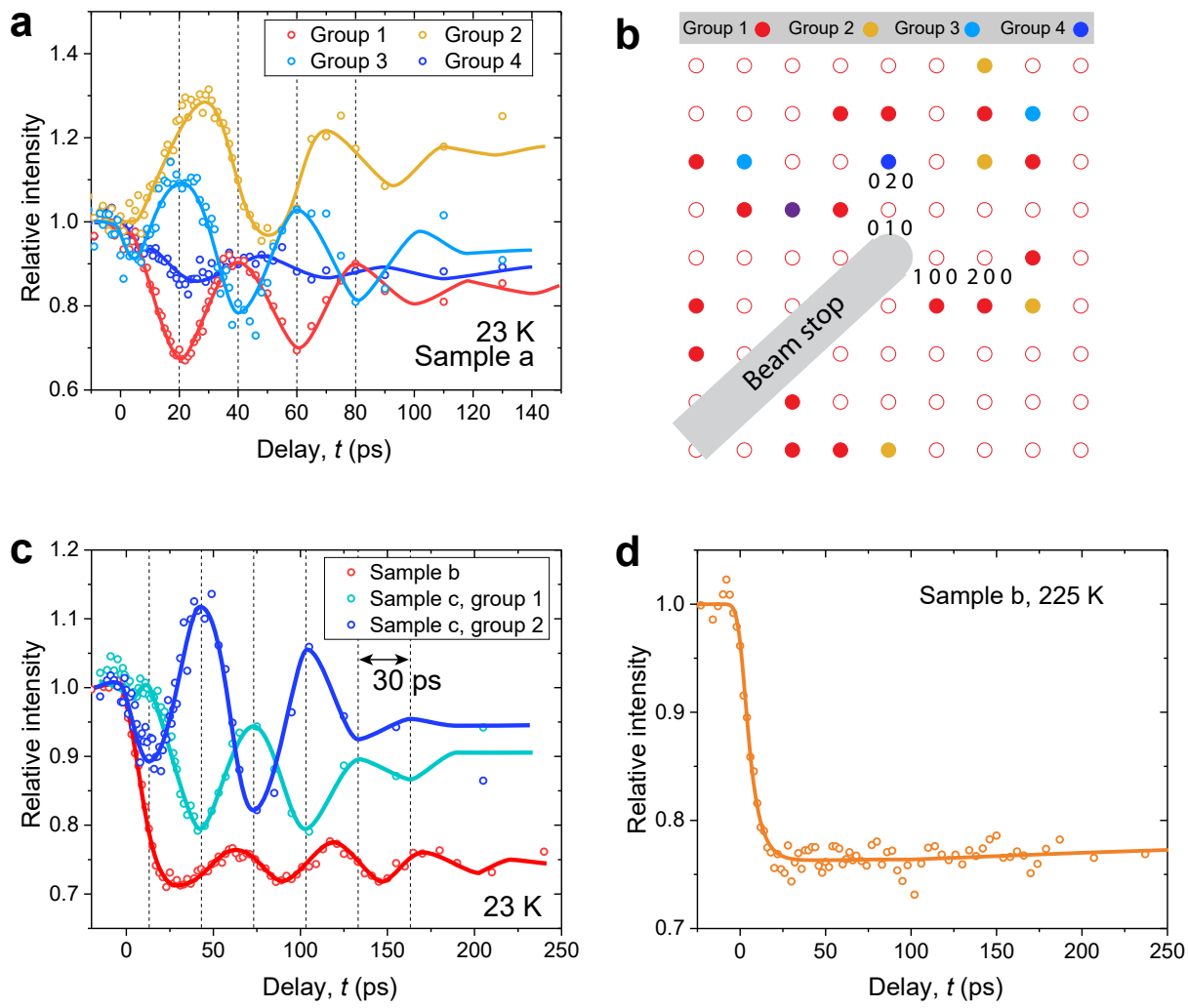

Figure 6.5: FeTe peak intensity evolution at low and high temperatures. **a**, Four groups of peaks evolution in sample a ($\lambda = 2500$ nm, $F = 2.7$ mJ/cm^2). **b**, Peak notation of 4 different groups in an artificial diffraction pattern. **c**, The oscillations observed in another two samples at low temperature, with a period of 60 ps instead of 40 ps seen in sample a. Experimental conditions: for sample b: $\lambda = 2500$ nm, $F = 2.3$ mJ/cm^2; for sample c: $\lambda = 606$ nm, $F = 1.4$ mJ/cm^2. **d**, The peak intensity evolution of sample b at 225 K, $\lambda = 2500$ nm, $F = 1.8$ mJ/cm^2. No oscillations are observed at high temperature.

structural transition has been observed and the system remains in tetragonal phase down to 0 K. The lack of structural transformation is confirmed with the ultrafast measurements, where even at a low temperature (23 K), the diffraction pattern peaks remain sharp and no peak broadening is seen (Figs. 6.6a&b) after applying a laser fluence of 1.1 mJ/cm^2 (2500

nm laser). Also, from the difference image, the lack of peak movement and sharpening is evident (Fig. 6.6c).

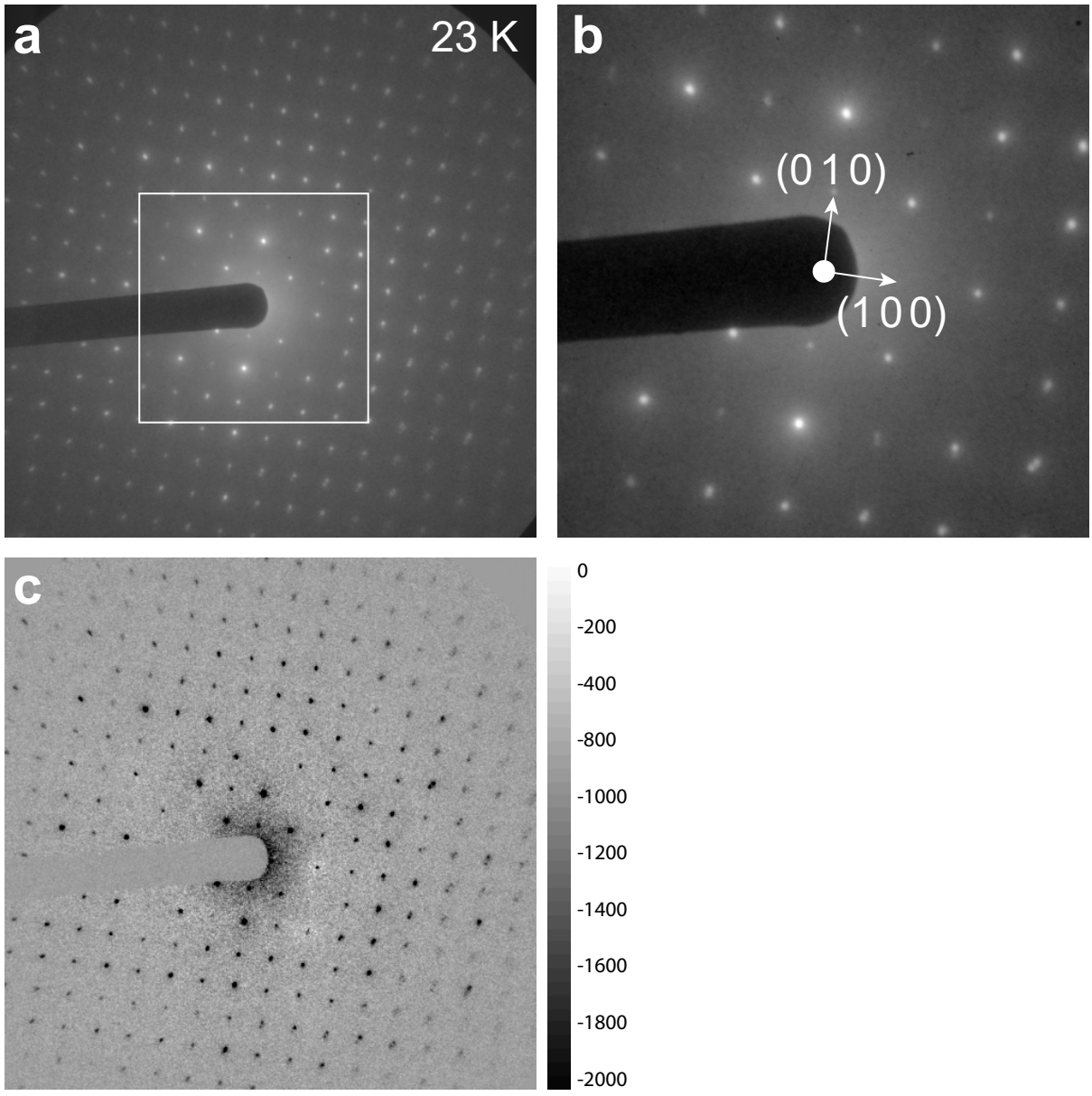

Figure 6.6: Diffraction patterns of $FeSe_{0.44}Te_{0.56}$. **a**, Original diffraction pattern of $FeSe_{0.44}Te_{0.56}$ at 23 K. **b**, Zoom-in view of pattern in **a**. **c**, Difference diffraction pattern of positive time (+ 40 ps) minus negative time (- 20 ps) under 2500 nm laser pumping at F = 1.1 mJ/cm^2.

While the lack of lattice structure modifications is observed within our observable window (up to $\approx$ 200 ps), as shown in Figs. 6.7a&b, the peak intensity at different Bragg reflection

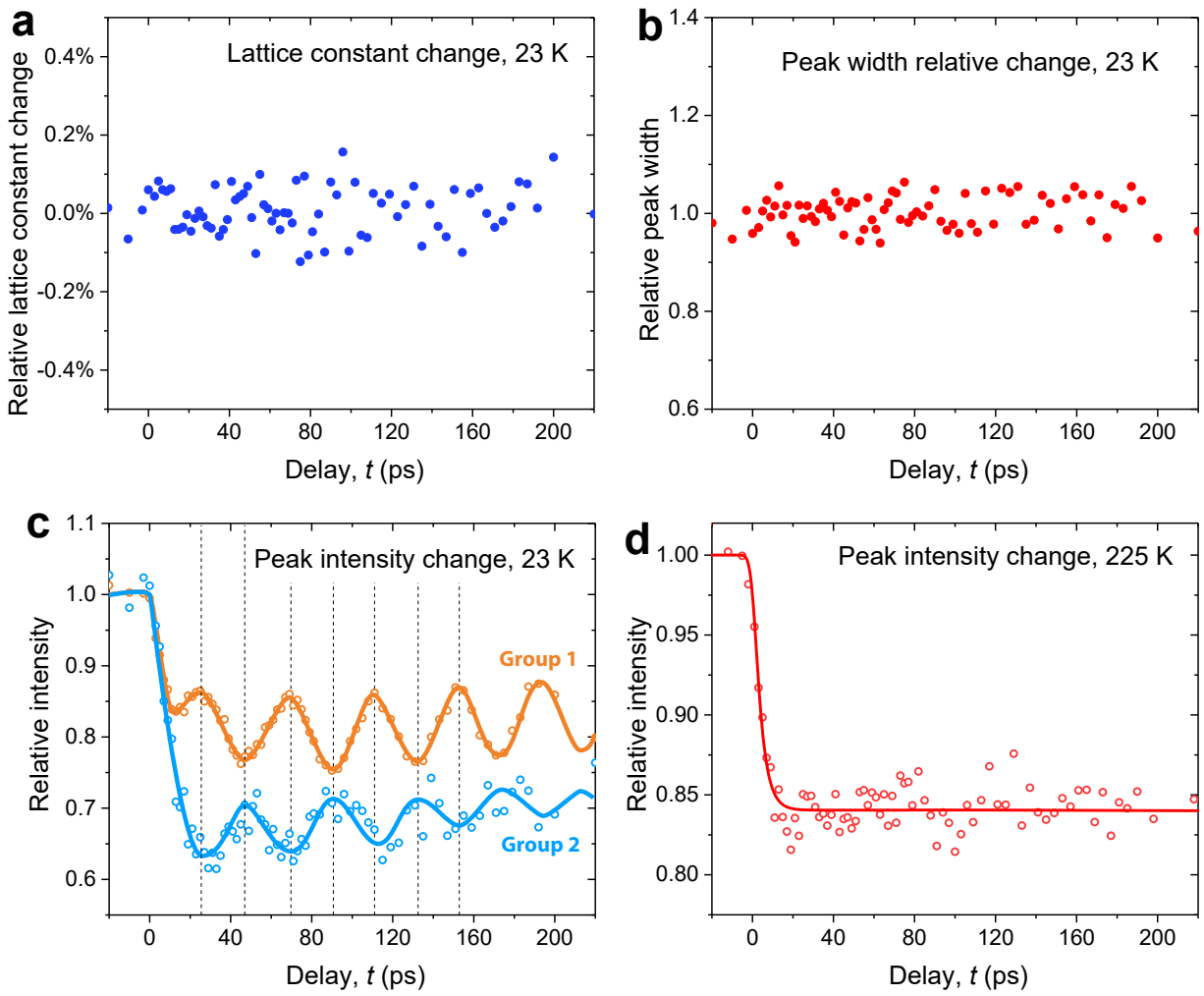

Figure 6.7: The peak dynamics of $FeSe_{0.44}Te_{0.56}$ at low and high temperatures ($\lambda = 2500$ nm, $F = 1.1$ mJ/cm^2). **a**, The lattice constant changes after laser excitation at base temperature of 23 K. **b**, The peak width changes at 23 K. **c**, The intensity oscillations observed at 23 K. **d**, The peak intensity dynamics at base temperature of 225 K. No oscillations are observed.

exhibit oscillations with a period of ≈ 40 ps, similar to the case of FeTe, as shown in Fig. 6.7c. But these oscillations are only seen at low temperatures. Such oscillation occur over a single-step decay in the intensity integral, indicating that optical energy is indeed transferred to the lattice system. Interestingly, raising the sample temperature to 225 K, the peak intensity does not show oscillatory behaviors but only a one-step drop.

6.4 Ultrafast dynamics in FeSe

In FeSe, we expect to see a structural transition similar to that of FeTe in terms of *ab*-plane lattice constant change (see Fig. 6.1d and Fig. 6.3d) when pumping at low temperatures. However, the data we acquired do not show any signs of such phase transition: the lattice constant is not observed to change within the measurement resolution; the peak is not seen to sharpen as expected, but rather an overall of 2.5% broadening is seen, as shown in Figs. 6.8b&c. While we believe, given what is observed in FeTe at $F = 2.7$ mJ/cm^2, the applied fluence here (1.1 mJ/cm^2) may be too low to reach the thermal threshold for the phase transition. The peak broadening phenomenon points to a different type of dynamics from phase transformation. The peak intensity is also not seen to have any oscillations, even at low temperature of 23 K.

Another interesting phenomenon observed in the FeSe dynamics is oscillations at absolute peak positions at 225 K. As shown in Fig. 6.9a, the peak intensity evolution also has no oscillations. But the peak position is seen to vibrate quite obviously, mainly along the $\boldsymbol{b}^*$ direction. All peaks show oscillations with the same amplitude and phase along the same direction. Figs. 6.9c&d are snap-shots at two time delays. It is clear from these images that all the peaks move together. Such an oscillation starts even at negative time and the oscillation frequency damps down over time.

This collective shifts in absolute positions of the Bragg peaks in the diffraction pattern could be due to either the electron beam drifting or the sample tilts/oscillates. It is unlikely to have periodic modulation to the electron beam, so it is more likely that the sample is vibrating. From the sample geometry as shown in Fig. 6.9e, one side of the sample is in good contact with the TEM grid while the other side is freestanding. From the oscillation

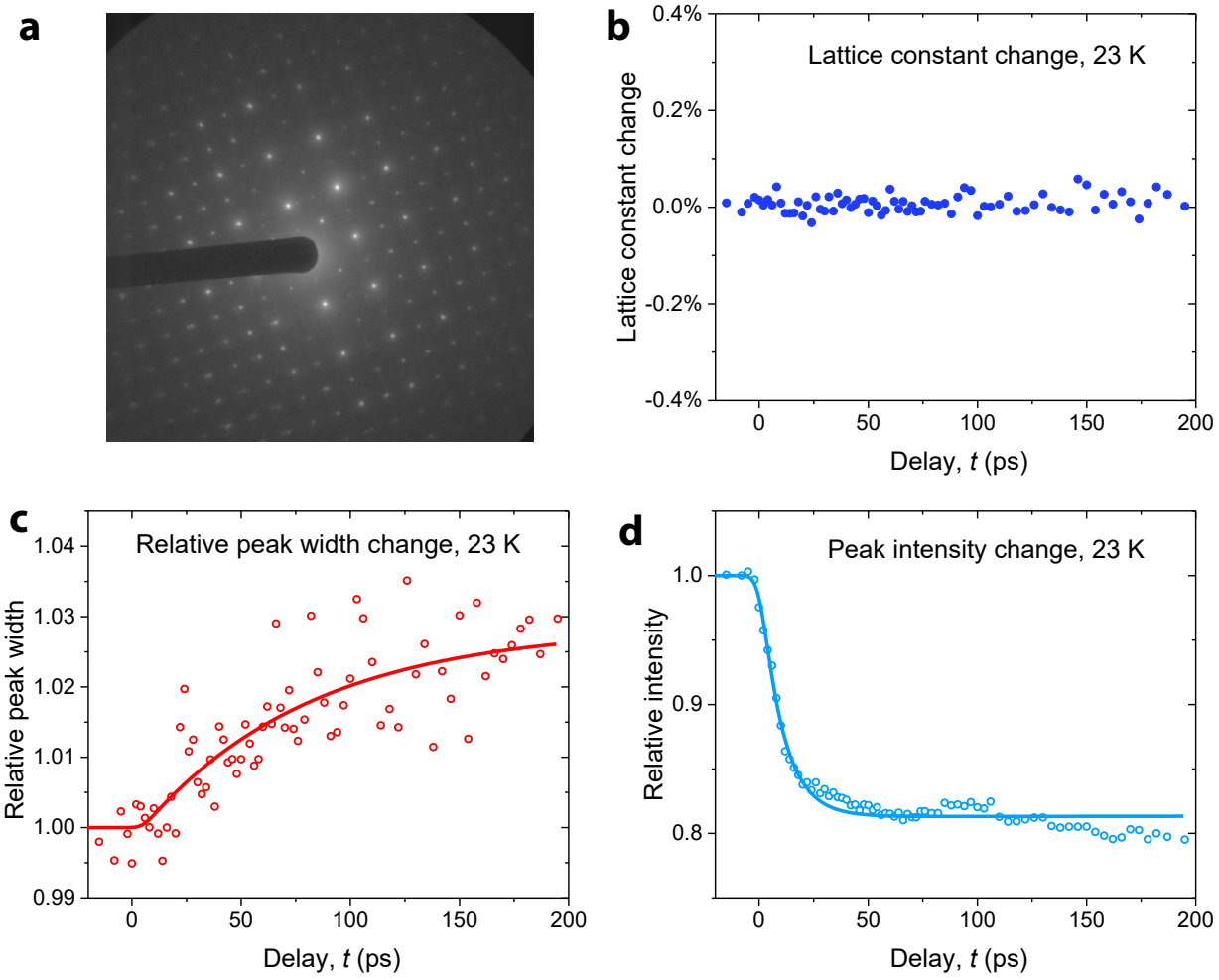

Figure 6.8: The diffraction patterns and dynamics of FeSe at 23 K (2500 nm pump laser, $F = 1.1$ mJ/cm^2). **a**, The diffraction pattern of FeSe at 23 K. **b**, Lattice constant change of FeSe at 23 K, a and b axes are similar: no clear lattice constant changes are observed. **c**, The peak broadening after laser excitation observed at 23 K. **d**, The peak intensity change at 23 K.

direction shown, if the sample vibrates around the contact side, then this matches well with the observed oscillation direction.

It is very likely that the various oscillation phenomena here are nuanced, resulting from a large pump area that generates acoustic wave across the interface between the supporting metal grid and the free-standing specimen. The observation that the onset of the oscillation (in FeSe) even begins at the negative time, indicating the source for those oscillations does

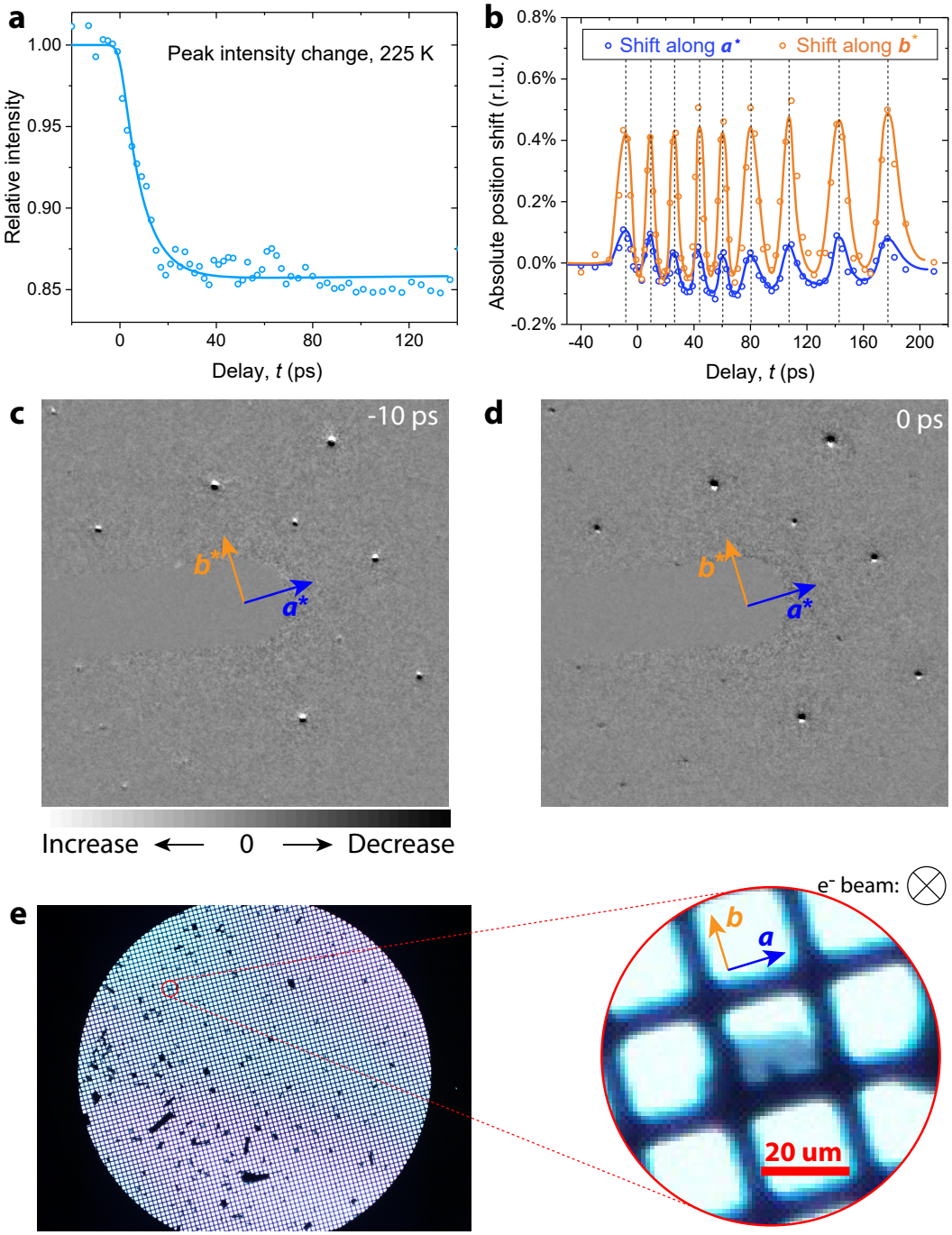

Figure 6.9: The dynamics of FeSe at 225 K ($\lambda = 2500$ nm, $F = 1.1$ mJ/cm^2). **a**, Peak intensity evolution at base temperature of 225 K. **b**, Peak shift along $\boldsymbol{a}^*$ and $\boldsymbol{b}^*$ direction. **c**&**d**, Snapshots of different images at - 10 ps and 0 ps (both minus the diffraction pattern at - 100 ps). All peaks exhibit similar drifts in amplitude and phase, mainly along $\boldsymbol{b}^*$ direction. **e**, The sample grid and zoom-in view of the sample used for the experiments.

not start at the probed sample region. We have also observed such oscillations in other specimen with wide irradiation footprint. But reducing the pump size by an aperture to limit the exposure of the laser pulse only to the specimen has suppressed such nuanced oscillation.

6.5 Summary

To summarize, the iron chalcogenide compounds studied here show very interesting results in the Bragg peak dynamics. The properties and main experimental results are summarized in Table 6.1.

In FeTe at below the transition temperature, the peaks are observed to sharpen and the changes in lattice constants agree with the structural phase transition. The observation of ultrafast phase transitions in FeTe is never reported before with time-resolved X-ray or electron diffraction tools. This is the first report of FeTe phase transitions in ultrafast time scale. Based on the estimated temperature rise, it is likely that the sample is indeed heated above the transition temperature. The Bragg peak intensities show the sophisticated large-amplitude oscillations, likely due to laser-induced acoustic phonons in the system. We do not yet know exactly the sources that drive this interesting phenomenon, but given that it occurs only in the monoclinic state, such acoustic wave generation may be tied to the hydrodynamics modes in the system which involves collective orders (AFM). At high temperature, as expected, there is no phase transition observed.

In the low-temperature state of $FeSe_{0.44}Te_{0.56}$ (23 K) right above T_c (15 K), there is no phase transition observed as expected. But we observed very strong Bragg peak intensity oscillations. The period of this oscillation (40 ps) coincides with that observed in FeTe. Given

Compound	**FeTe**	**$FeSe_{0.44}Te_{0.56}$**	**FeSe**
SC	No	Yes	Yes
AFM order	Yes	No	No
Structural PT	Yes	No	Yes
Experiments at 23 K ($\lambda = 2500$ nm):			
F (mJ/cm^2)	2.7	1.1	1.1
DWF	0.69	0.78	0.80
Estd. ΔT (K)	90	40	40
Peak width	Sharpen	No change	Broaden
a, b change	Yes	No	No
Intensity osc.	Yes	Yes	No
Position osc.	No	No	No
Phase transition	Yes	No	No
Experiments at 225 K ($\lambda = 2500$ nm):			
F (mJ/cm^2)	1.8	1.1	1.1
DWF	0.76	0.83	0.86
Estd. ΔT (K)	60	35	35
Peak width	No change	No change	Broaden
a, b change	No	No	No
Intensity osc.	No	No	No
Position osc.	No	No	Yes
Phase transition	No	No	No

Table 6.1: Summary of the properties and experimental results for all three iron chalcogenide compounds. "DWF" represents the relative intensity at + 40 ps of the Bragg peaks analyzed. The "Estd. ΔT (K)" means the estimated sample temperature rise based on applied fluences and the DWF analyses.

that the oscillations have a very high s/n and last for more than 5 periods with little changes in frequency, the observed acoustic phonons here might also be intrinsic to $FeSe_{0.44}Te_{0.56}$.

In the low-temperature state of FeSe (23 K), the system is expected to exhibit laser-induced structural transition but our data do not show signs of any lattice constant change or peak sharpening. This is likely due to the low excitation fluence. Based on both the specific heat estimate and the DWF analysis, the final sample temperature is indeed below the transition temperature. The observation of Bragg peak broadening is contradictory to the expected peak sharpening effect. According to a recent work on FeSe [168], there are nanoscale local nematicities that persist in a large range of temperature even above the structural transition temperature. From the point of local nematicity and local stress, the peak broadening phenomenon observed here can be explained based on laser-enhanced local stress. This laser-induced instability in the stress-field exhibits peak broadening, which is seen at both low and high temperatures. (peak broadening at high temperature is similar to that observed at low temperature but not plotted in the figures.) At high temperature, the peak positions are observed to have very strong oscillations. Given the facts that the oscillation starts at negative time, oscillation frequency is damping down, and that the oscillation polarization matches well with sample orientations, this phenomenon is very likely due to the sample vibrations, not related to the intrinsic structural responses of these systems.

The phase transition observed in FeTe has never been observed by UED or other ultrafast measurements. The very strong acoustic phonon oscillations observed in $FeSe_{0.44}Te_{0.56}$ are also new and highly interesting. The enhanced local stress seen in FeSe is surprising and may give information to help understand the nematic and superconductivity phase. In the meantime, these results call for experiments with better spatial/temporal resolutions to further clarify the questions such as the nature of these excited acoustic phonons and role of local stress/nematicity to SC formation in FeSe.

Chapter 7

Conclusion

The results presented here demonstrate the great potential of using ultrashort laser pulses to explore phase transitions in complex materials in the non-equilibrium regime. With all the results presented in this dissertation, it is evident that photo-induced phase transitions (PIPT) follow different paths from that of steady state. The PIPT process, while frequently proceeding at a high temperature, acts very much like an interaction-mediated phase transition, which shares key characteristics with the quantum phase transitions. This thus opens up a new dimension in studying novel states in the material phase diagrams. Moreover, in a quantum phase transition, there exists a quantum critical point due to competing phase orders. The same is true for PIPT processes. In a PIPT, the competition between different states also leads to the existence of a nonthermal fixed point. Near the nonthermal fixed point, the system order parameters follow universal scaling laws and exhibit critical divergence behaviors.

In $CeTe_3$, the system is shown to be driven to a hidden bi-directional order that cannot exist at thermal equilibrium. In the first 200 to 300 fs after laser excitation, the order parameter field is highly unstable, exhibiting characteristics of the so-called Kibble-Zurek freeze-out time. After the KZ freeze-out time, the a-CDW order starts to form, together with the $c^{\dagger}$-CDW order. The coincidence in time scales and amplitude between a-CDW and $c^{\dagger}$-CDW orders indicates that the hidden state may emerge in a more symmetric electronic

energy landscape that prefers a checkerboard order over a stripe order. By examining the CDW wave-vector change, it is found the nesting vector change is in agreement with the photoemission measurements [93]. The photo-excited electrons cause a reduction in the transverse coupling constant, and thus the FS nesting vector. The discovery here proves another solid example of photo-induced metastable and hidden states in complex materials. The study in $ErTe_3$ is one step further based on the $CeTe_3$ results. $ErTe_3$ exhibits an even richer phase diagram due to the existence of two CDW orders. The dynamics at various temperatures show a-CDW may have a larger non-thermal melting threshold like in the case of $CeTe_3$. This unexpected result, together with those in $CeTe_3$, provide a more comprehensive picture of PIPT in the $RETe_3$ series: the system follows transition pathways different from that in thermal equilibrium and the ac-plane becomes more symmetric (non-degenerate to degenerate). The same may be true for other "asymmetric" systems with nonequivalent crystal axes.

In 1T-TaS_2, the system is shown to observe universal scaling at both non-thermal and thermalization regimes. Such universal dynamics in the nonthermal regime is the first example of such universality observed in the prethermalization stage. The phase ordering kinetics are also highly interesting in the thermalization stage. Although such results are predicted theoretically and validated recently in cold quantum gas experiments, our experiments exhibit subtleties that warrant further theoretical investigation. By comparison of the 2500 nm and 800 nm results, we emphasize the photo-doping effect in driving the non-thermal phase transition in complex materials. The phase transition by 2500 nm shows much less energy deposition and faster switching speed, giving promises for better optoelectronic applications with long-wavelength laser.

In the study of iron chalcogenides, we observed the ultrafast phase transition and exci-

tation of acoustic phonons. SC in iron-based superconductor arises near the AFM order. The pairing mechanism is believed to be correlated with the spin order. At the same time, the spin order is directly coupled with the structural order. The ultrafast structural phase transition in non-superconducting compound FeTe presented here is first observed with UED measurements. In the superconducting compound of $FeSe_{0.44}Te_{0.56}$, at a temperature close to T_c, the observed strong acoustic phonon oscillations might be intrinsic to the system. But further high-resolution experiments are needed to clarify the roles of the acoustic phonons and how they are related to SC. The observed laser-induced local stress in FeSe is also highly interesting. It is still unclear what the role of nematic order is in the formation of SC. The observation of enhanced stress field after laser excitation may promote understanding of SC in FeSe. However, given the limited s/n and available data set, experiments with better temporal and higher coherence length are needed.

These results presented here show promising directions of using fs laser to explore metastable and hidden phases in complex materials, as well as helping to understand the physics in the equilibrium states. One of the ultimate goals in condensed matter physics is to realize photo-induced superconductivity at high temperature or even room temperature. Even though it is a long way ahead, the results presented here, along with other similar experiments in recent years with different approaches, show promises towards that goal.

APPENDICES

Appendix A

2D sample preparation procedure

For the two-dimensional (2D) materials discussed in this dissertation, the popular "scotch tape" method [169] is used for sample preparation.

The 2D bulk material is first cleaved to have a flat and clean surface, which may require a few times of exfoliation. Then press a clean scotch tape onto the clean surface to peel off a big and uniform sample piece, which could be more or less 1 μm thick (Fig. A.1a). Use another clean tape to exfoliate with the one that has sample on for several times. As the exfoliation times increase, the sample pieces would be thinner and smaller. Typically after exfoliating 6 to 8 times, the sample pieces should be good for the next step (Fig. A.1b). The sample quality can be checked by examining the transparency under optical microscope. Fig. A.1 is an example. After measuring thickness of some freestanding sample on TEM grid with TEM zero-loss energy spectroscopy thickness map, the sample transparency can be determined to correspond to thickness. This thickness-transparency correlation can be used to quickly determine the sample thickness on tape

Once the sample is properly exfoliated on the tape (usually make sure there is a significant percentage of samples below 50 nm), we can drop cast two drops of acetone onto 1 cm x 1 cm silicon wafer and press the tape evenly onto the wafer with a glass piece. Press and hold the glass piece for 2 minutes until acetone all evaporates. Then gently separate the tape from Si wafer. Now most of the samples are on the Si wafer (Fig. A.1c). Place the wafer in

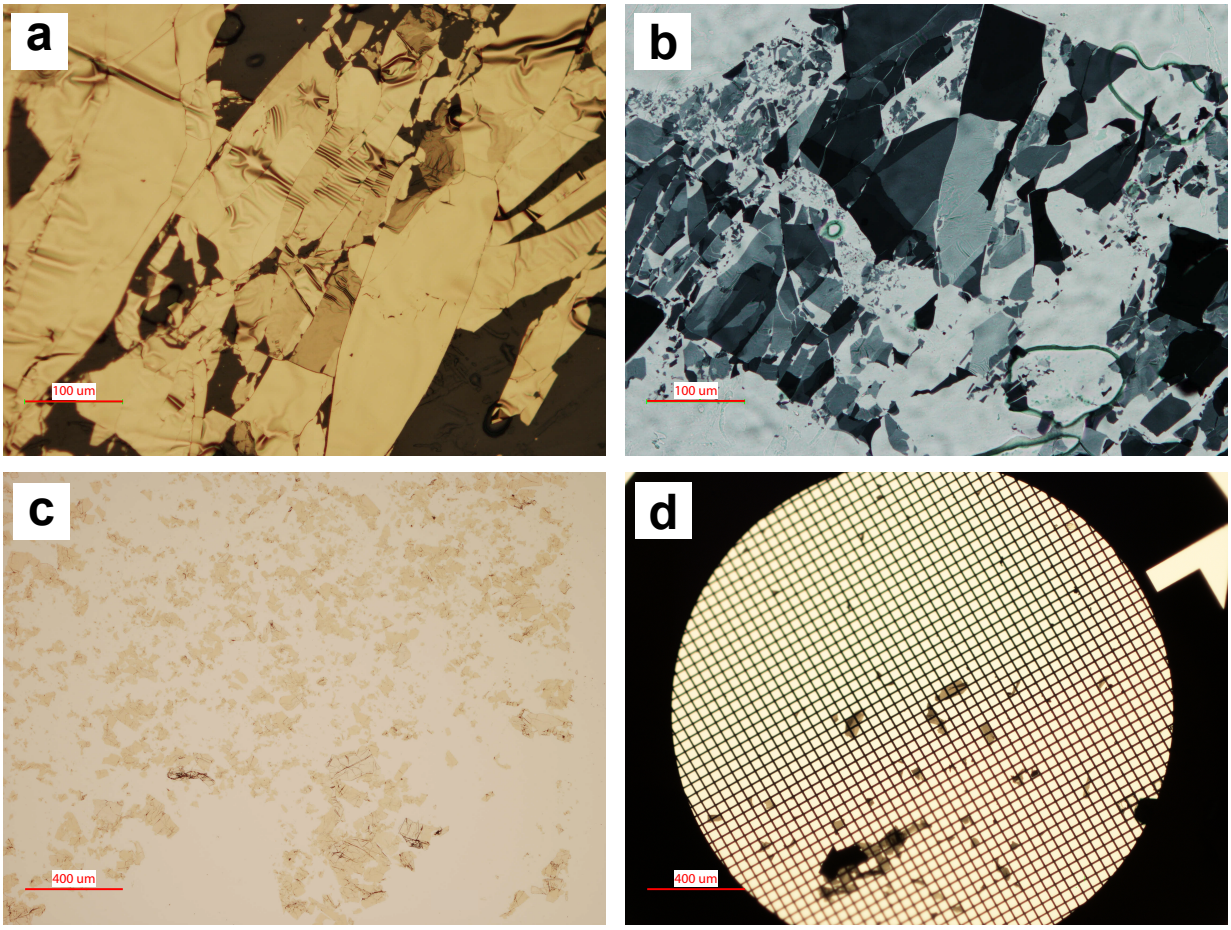

Figure A.1: Typical sample images during sample preparation process. **a**, 1T-TaS_2 sample on scotch tape. Light is reflected from sample surface so we see the gold metallic color. **b**, Typical 1T-TaS_2 samples on scotch tape after a few times of exfoliation. Light is transmitting through the sample to show the transparency. **c**, Sample flakes on silicon wafer. **d**, Typical optical image of the samples transferred to the TEM grid.

a clean beaker and put several ml of acetone. Put the beaker in a ultrasonicator for a few seconds to make sure samples come off from the wafer into the acetone.

Drop cast two drops of acetone sample solution onto TEM grid. Wait for about 1 minute to let acetone evaporate. Then the samples would be left on the grid for experiment use. The density of sample is kept more or less as the one shown in Fig. A.1d to avoid sample overlap (too dense) as well as enough samples for experiments.

Appendix B

Transfer matrix method for optical absorption calculations

In UED or other optical experiments, to estimate the absorbed optical density or energy density, it is necessary to know the optical constants to calculate the absorption coefficient. Since we are dealing with thin film samples of tens of nm, the interference effect at sample interfaces should be considered in order to calculate the true absorption coefficient. This is where the transfer matrix method is involved for the calculation.

In the following part, I will first list a few common optical parameters that are frequently seen in literature then list their relationships, then introduce the transfer matrix method.

Reflectivity: R

Electrical permittivity: ϵ

Refractive index: n

Extinction coefficient: κ

Attenuation coefficient (absorption coefficient): α

Optical conductivity: σ

The relative electrical permittivity ϵ_r is related with refractive index by the relation: $\epsilon_r = n^2$ (for non-magnetic materials). Considering that both of them are complex numbers, $\epsilon_r = \epsilon_1 + i\epsilon_2, n = n_0 + i\kappa$, we can get the following relation: $n_0^2 - \kappa^2 = \epsilon_1$ and $2n_0\kappa = \epsilon_2$.

Optical conductivity σ is also complex: $\sigma = \sigma_1 + i\sigma_2$ and by definition it is related with electrical permittivity by: $\epsilon_r = 1 + \frac{i}{\epsilon_0\omega}\sigma$. Thus, $\epsilon_1 = 1 - \frac{1}{\epsilon_0\omega}\sigma_2$ and $\epsilon_2 = \frac{1}{\epsilon_0\omega}\sigma_1$, where ϵ_0 is vacuum permittivity and ω is the photon angular frequency. The attenuation coefficient α is related with extinction coefficient κ by: $\alpha = \frac{4\pi\kappa}{\lambda}$, where λ is optical wavelength. The optical penetration depth δ is usually defined as inverse of the attenuation coefficient: $\delta = \frac{1}{\alpha} = \frac{\lambda}{4\pi\kappa}$.

From optical measurements in literature, the most direct measurement is reflectivity spectrum normal to bulk sample surface. Through the Kramers-Kronig analysis (for example refer to the paper [139]), the real and imaginary part of optical conductivity (σ_1 and σ_2) or permittivity (ϵ_1 and ϵ_2) can be derived, with which we can get the refractive index (n), extinction coefficient (κ), etc. n_0 and κ are our input parameters for the following transfer matrix calculations.

Consider a N-layer sample structure as shown in Fig. B.1. We assume the m^{th} layer has a thickness of δ_m and refractive index of n_m. The incident optical wave has an electric field of amplitude E_0^+. The forward field is labeled as + sign and backward field has - sign. At the m^{th} interface, the electric field at before and after the interface has the following relationship:

$$\begin{pmatrix} E_{m-1}^+ \\ E_{m-1}^- \end{pmatrix} = \frac{1}{t_{m-1,m}} \begin{bmatrix} 1 & r_{m-1,m} \\ r_{m-1,m} & 1 \end{bmatrix} \begin{pmatrix} E_m^+ \\ E_m^- \end{pmatrix} \tag{B.1}$$

where $r_{m-1,m}$, $t_{m-1,m}$ are the reflectance and transmittance coefficients, respectively, at the m^{th} interface. They can be calculated based on the Fresnel equations.

At the m^{th} medium, the electric field has the following relation:

$$\begin{pmatrix} E_m'^+ \\ E_m'^- \end{pmatrix} = \begin{bmatrix} e^{-i\delta m} & 0 \\ 0 & e^{i\delta m} \end{bmatrix} \begin{pmatrix} E_m^+ \\ E_m^- \end{pmatrix} \tag{B.2}$$

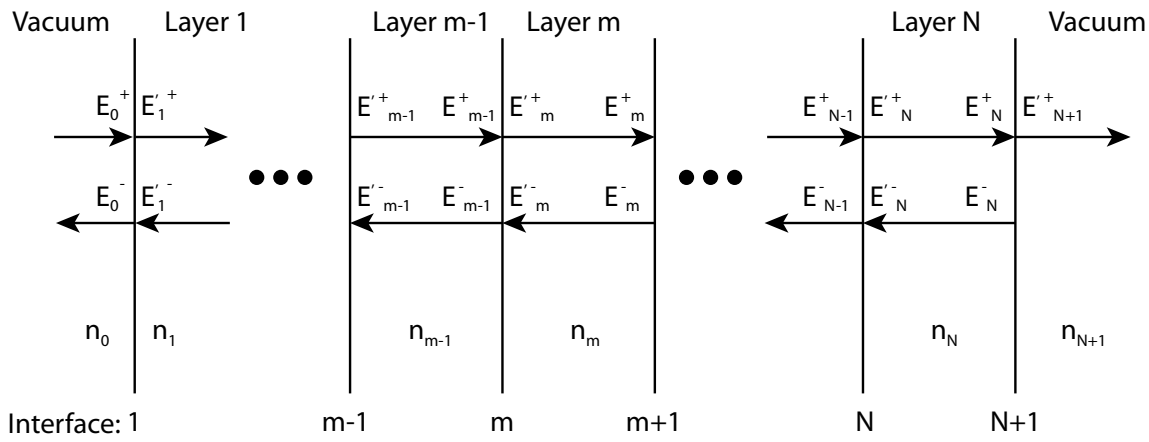

Figure B.1: The schematic drawing of N-layer sample. The electric field amplitude is labeled at each interface for both forward and backward waves.

At this point, the answer is straight forward for the N-layer problem: simply multiply all the transfer matrices from the left to right for each medium layer and medium interface:

$$\begin{aligned}\begin{pmatrix} E_0^+ \\ E_0^- \end{pmatrix} &= \frac{1}{t_{0,1}} \begin{bmatrix} 1 & r_{0,1} \\ r_{0,1} & 1 \end{bmatrix} \begin{bmatrix} e^{-i\delta_1} & 0 \\ 0 & e^{i\delta_1} \end{bmatrix} \frac{1}{t_{1,2}} \begin{bmatrix} 1 & r_{1,2} \\ r_{1,2} & 1 \end{bmatrix} \begin{bmatrix} e^{-i\delta_2} & 0 \\ 0 & e^{i\delta_2} \end{bmatrix} \\ &\quad ... \frac{1}{t_{N,N+1}} \begin{bmatrix} 1 & r_{N,N+1} \\ r_{N,N+1} & 1 \end{bmatrix} \begin{pmatrix} E'^+_{N+1} \\ 0 \end{pmatrix} \\ &= [T_{0,1}T_{1,2} \ ... \ T_{N-1,N}] * \frac{1}{t_{N,N+1}} \begin{bmatrix} 1 & r_{N,N+1} \\ r_{N,N+1} & 1 \end{bmatrix} \begin{pmatrix} E'^+_{N+1} \\ 0 \end{pmatrix}\end{aligned} \tag{B.3}$$

where the $T_{m-1,m} = \frac{1}{t_{m-1,m}} \begin{bmatrix} 1 & r_{m-1,m} \\ r_{m-1,m} & 1 \end{bmatrix} \begin{bmatrix} e^{-i\delta_m} & 0 \\ 0 & e^{i\delta_m} \end{bmatrix}$.

For Eq. B.3, with each side divided by E_0^+, the total reflectance and transmittance (in E-field amplitude) are $r = \frac{E_0^-}{E_0^+}$ and $t = E'^+_{N+1}$, respectively. The total reflectivity and transmission (in laser intensity) would be $R = (r^*) * (r), T = (t^*) * (t)$. Correspondingly, the

absorption coefficient A can be extracted from the reflectivity and transmission: $A = 1 - R - T$. With absorption coefficient estimated, for one-layer sample, assuming homogeneous excitation for thin samples, the absorbed energy density is

$$\rho_E = \frac{F(1-R-T)}{\delta} \tag{B.4}$$

where F is the laser fluence, δ is the sample thickness.

The absorbed photon density is the energy density divided by photon energy $h\nu$

$$\rho_{h\nu} = \frac{\rho_E}{h\nu} \tag{B.5}$$

For two dimensional layered materials under study discussed in this dissertation, for example 1T-TaS_2, $CeTe_3$, $ErTe_3$, etc., the system is a one-layer problem, as shown by the schematic drawing in Fig. B.2a. In our real experiment, the pump laser incident angle is 45° as shown in the figure. For 1T-TaS_2, from reference [139], with 800 nm laser, $n_0 = 3.00, \kappa = 2.09$; with 2500 nm laser, $n_0 = 5.60, \kappa = 1.79$. With n_0 and κ as the inputs, we can calculate the optical reflection, transmission, and absorption coefficients by the above discussed transfer matrix method in Mathematica. These parameters are plotted as a function of sample thickness in Fig. B.3. From the results, 800 nm data get stable after 100 nm while 2500 nm data become stable after 400 nm. The interference effect is observable from the oscillations as a function of sample thickness variation. For more direct comparisons of the regular calculation (ignore interference effect) and transfer matrix calculations, Table. B.1 is made for a 50 nm thick sample for 800 nm and 2500 nm laser. In this table, for the regular method without considering interference effect, the optical reflectivity is taken from literature

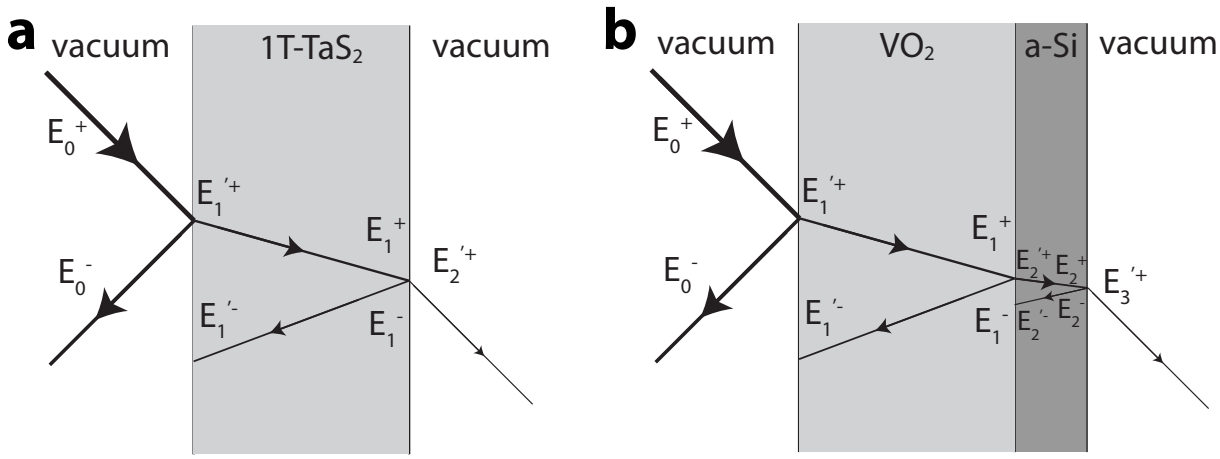

Figure B.2: The schematic drawing of the wave propagation in (**a**) 1T-TaS_2 and (**b**) VO_2 film deposited on 9 nm amorphous silicon film.

[139]; transmission is calculated based on formula: $T = (1 - R)e^{-a/\delta}$ and the absorption is calculated based on: $A = (1 - R)(1 - e^{-a/\delta})$, where a is the sample thickness and δ is the optical penetration depth. From the result, the absorption coefficient is very similar for 800 nm with two methods; but the absorption for 2500 nm pump differs by a factor of two.

For the thin film VO_2 deposited on 9 nm amorphous silicon film, the sample is a two-layer system. From optical measurements in reference [155, 170], for 800 nm laser, $n_0 = 2.88, \kappa = 0.42$; for 2000 nm laser, $n_0 = 3.25, \kappa = 0.13$. With this input, the optical reflection, transmission, and absorption coefficients are calculated as a function of VO_2 film thickness, plotted in Fig. B.4. For this two-layer system, the interference effect is more pronounced from the oscillation amplitude. Note, for the absorption calculations in VO_2, the absorption by amorphous silicon film is negligible. So the absorption by VO_2 film takes the total absorption of VO_2 and silicon film combined.

Condition	**Reflection, *R***	**Transmission, *T***	**Absorption, *A***
800 nm, w/o interference	0.405	0.113	0.482
800 nm, transfer matrix calc.	0.352	0.122	0.526
2500 nm, w/o interference	0.534	0.291	0.175
2500 nm, transfer matrix calc.	0.423	0.222	0.355

Table B.1: Comparison of the optical coefficients for 50 nm-thick 1T-TaS_2 by using the regular method and transfer matrix method for 800 nm and 2500 nm lasers.

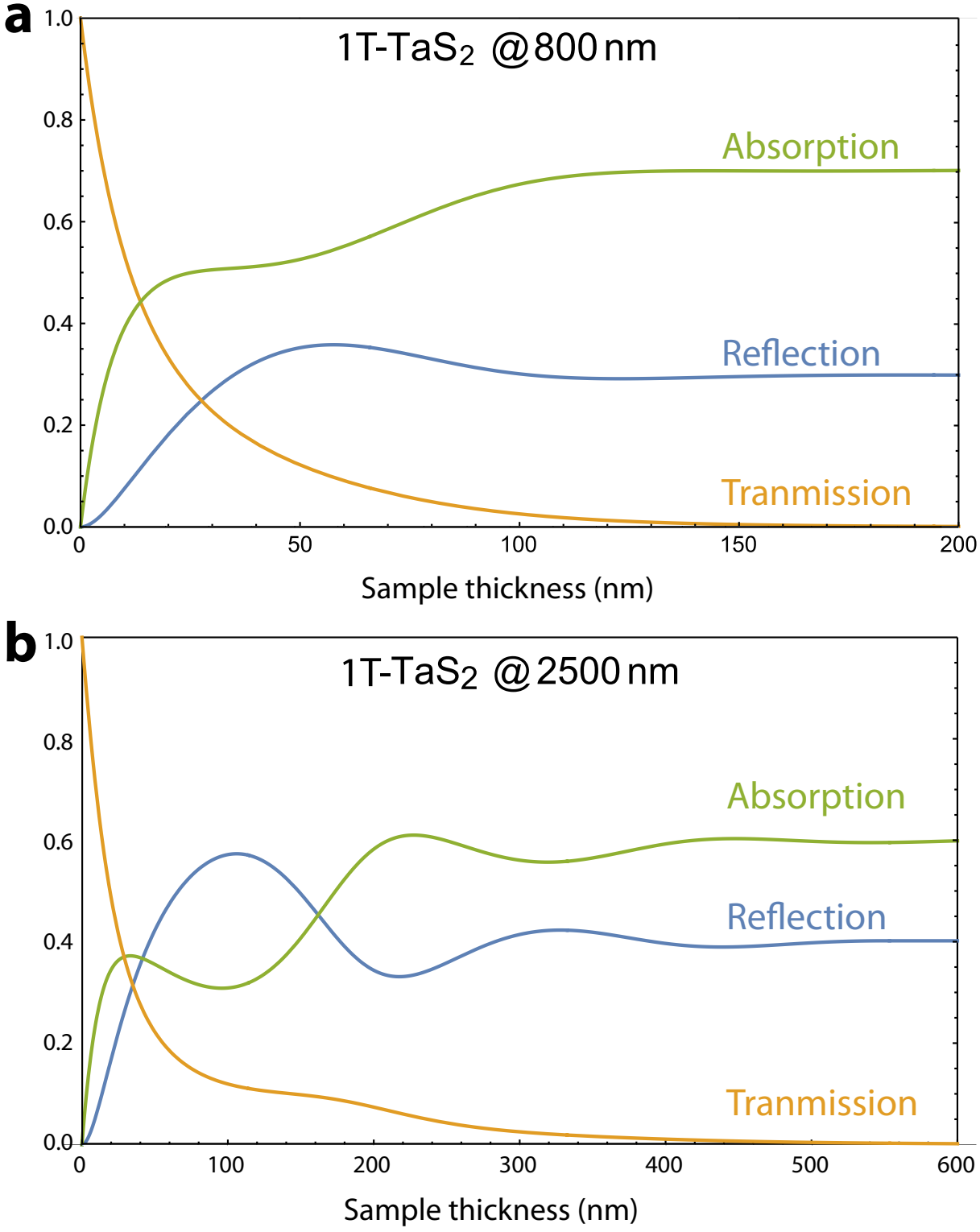

Figure B.3: 1T-TaS_2 optical reflection, transmission, and absorption coefficients as a function of sample thickness for 800 nm (**a**) and 2500 nm (**b**) lasers. The pump laser is 45° incident on the sample and p-polarized for the calculation, the same as experimental conditions.

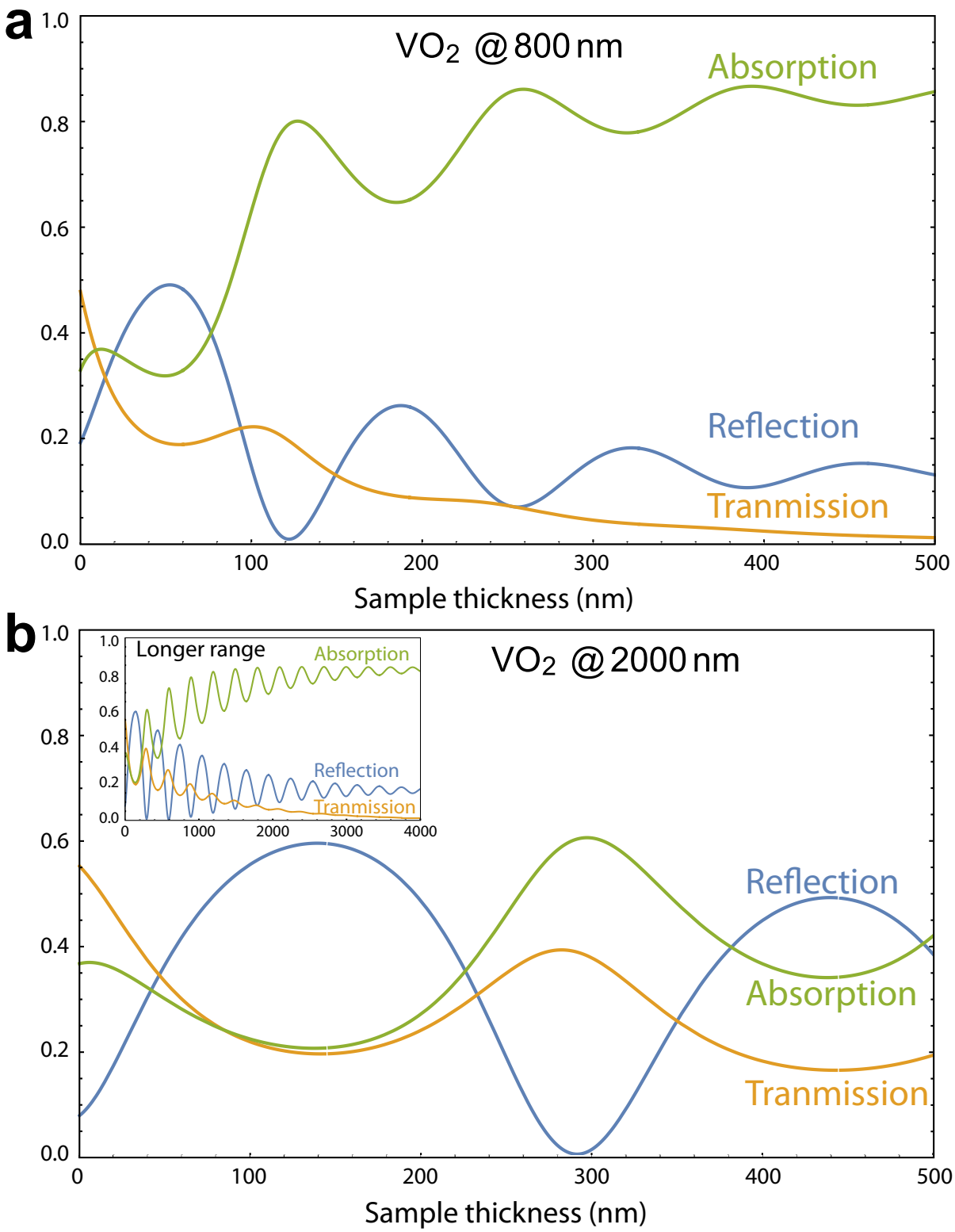

Figure B.4: The optical reflection, transmission, and absorption coefficients as a function of VO_2 film thickness for 800 nm (**a**) and 2500 nm (**b**) lasers. Inset of **b** are the same data but plotted up to 4 um thick. VO_2 film is deposited on 9 nm amorphous silicon film. Laser pulse is 45° incident on the sample and p-polarized for the calculation, the same as experimental conditions.

Appendix C

Photo diode box-car integrator (PD-BCI) system for pump power measurement, monitor, and calibration

In a UED pump-probe experiment, it is crucial to have a good pump-probe overlap and monitor the pump conditions. Due to the temperature or humidity change in the lab, the pump power might change or pump position could drift (which eventually also results in pump power change at the sample). In the long time delay experiment over 2 or 3 ns, the delay stage might not be perfectly aligned so the pump beam would drift at different time delays. Another issue is that the regular power meter can only measure up to ± 0.1 mW precision. Such a resolution might not be fine enough in a fluence scan, especially near the threshold where 5% change in pump power could result in 100% change in diffraction signals.

To solve these issues, we designed a photo diode-box car integrator (PD-BCI) system to measure and monitor the pump fluence in real time for each diffraction image at each time delay. This system is computer controlled while acquiring diffraction images. The pump fluence for each diffraction pattern is automatically stored in the image info. Ideally, with

this system and computer-controlled variable NDQ pump laser filter, students do not even need to be in the lab to measure or adjust the pump power when running delay scan or fluence scan experiments — minimal perturbation to the experiment conditions.

The schematic for this setting is drawn in Fig. C.1a, where the pump laser is split into two paths: one goes into the chamber as excitation pump, the other is directed to a photo-diode. A 50 μm pin hole is placed right in front of the photo diode (PD) and the distance from beam splitter (BS) to sample and BS to pin hole is the same. Also, the 50 μm pin hole mimics the sample size to allow the same amount of photon goes into the PD as the amount of photon illuminating on the sample. The PD output is fed into a device called box-car integrator (BCI), which performs the function of integrating and averaging the PD signal and outputs a voltage signal that is proportional to laser power. This voltage signal is automatically recorded in the diffraction images.

The BCI (Stanford Research Systems, model: SR250) is a gated device that needs proper input signals to trigger and reset. Fig. C.1b shows the signal diagram into and out of BCI. The PD input and trigger signals are both at 1 kHz repetition rate. The trigger signal is chosen to use the camera image intensifier (I.I.) gate signal instead of direct trigger from laser Timing Delay Generator (TDG) box because the I.I. gate signal is "1" only in the period of camera acquisition while the laser TDG box trigger signal is always on independent of camera acquisition. This avoids the noise accumulation when camera is not acquiring.

With the trigger signal, PD input, and proper settings in the delay and integration width, the BCI would integrate only tens of ns duration when the input signal is present and avoids accumulating the noise. BCI calculates the exponential moving average of the signal inputs. For example, if we set the number of average to be 1000, then BCI would reach 66.7% of its true value in one second (1000 pulses). To reach 99% of its true value, it usually requires

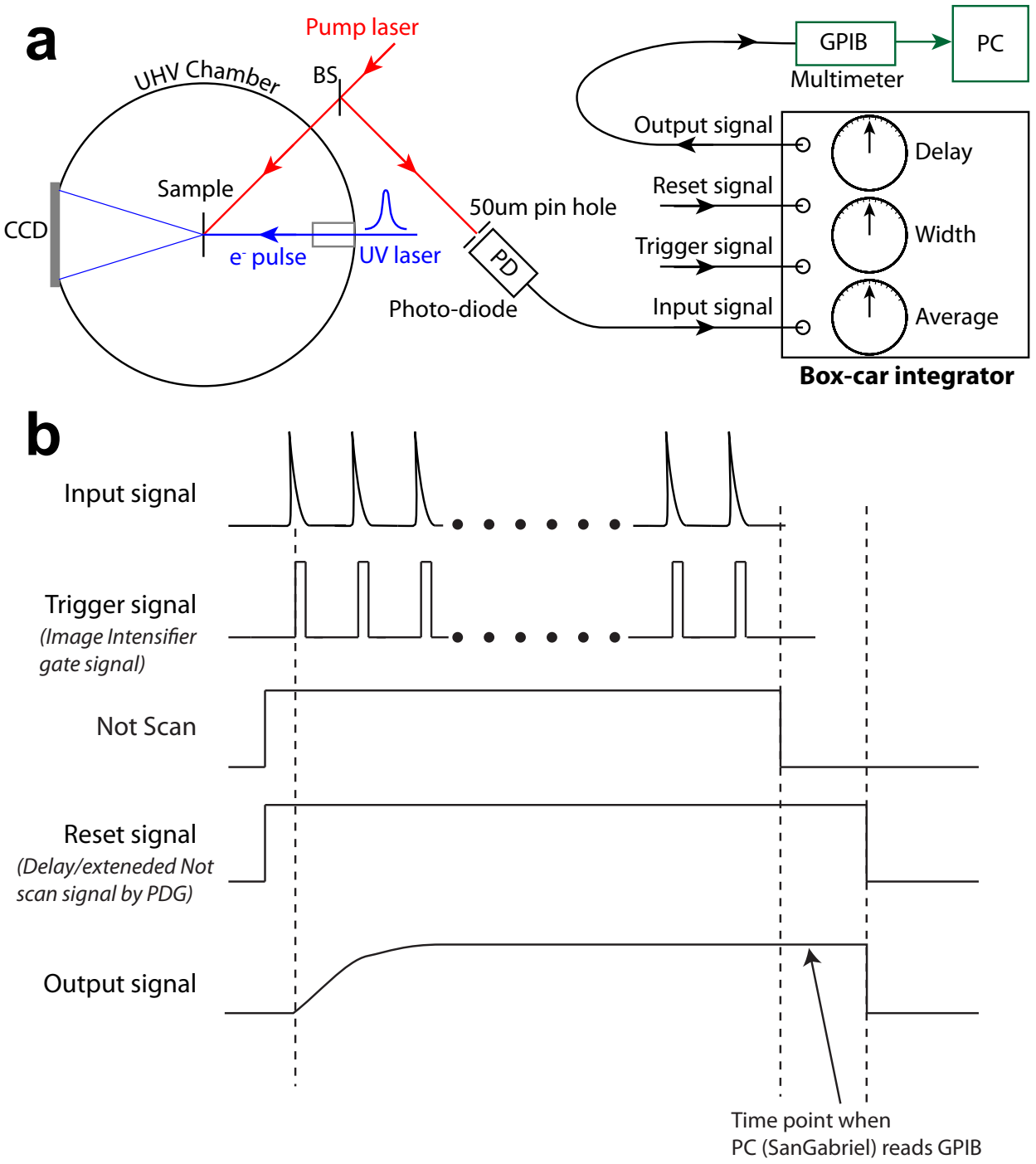

Figure C.1: The photo diode-box car integrator system schematic drawing and signal wave forms for input/output signals. **a**, The schematic drawing for the box-car integrator system. The pump laser is split to feed into a photo diode. The four input/output signals and three main adjusting knobs are drawn. **b**, The wave forms of input/output signals

a few seconds. To record the pump power reading after diffraction image acquisition, the computer would takes one to two seconds to read the GPIB voltage. So the output has to hold for about two seconds for the computer to read the GPIB output, but at the same time it gets reset before the next image acquisition. To fulfill such requirements, we use the NOT SCAN signal from camera and extend it for three seconds using a pulse delay generator. This three seconds period is when the computer reads GPIB output. After the three seconds period, the BCI output gets reset to get ready for the next image acquisition.

To use such a system to run experiments, for example on a fluence scan, we first find pump-probe overlap on the sample by scanning pump beam on the sample grid at certain positive time delay. The maximum response from sample would be overlap position. At the same time delay, we optimize the PD and pin hole positions to have a maximum reading. With proper settings on the BCI, we calibrate the output vs. power meter reading as shown in Fig. C.2a. Then without people in the lab, the computer can control the variable laser attenuation filter then measure the pump power with this system. At proper pump fluence, we can start the delay scan or fluence scan. Once the scan finishes, one uses the computer to adjust pump fluence remotely and moves to the next fluence point and restarts the scan. In this way, very consistent and convenient way of running experiments can be achieved at high precision.

Fig. C.2b is an example of 1T-TaS_2 phase transition delay scan with 2500 nm laser excitation. 2500 nm laser is generated by an optical parametric amplifier through nonlinear processes. So if there is some fluctuation in source 800 nm laser, the 2500 nm laser power could be unstable. Fig. C.2b is such an example of unstable 2500 nm laser power as well as bad alignment in the delay stage. As we can see, the pump power stays relatively stable in the first 500 ps. But after 500 ps, it starts to increase due to bad alignment and has

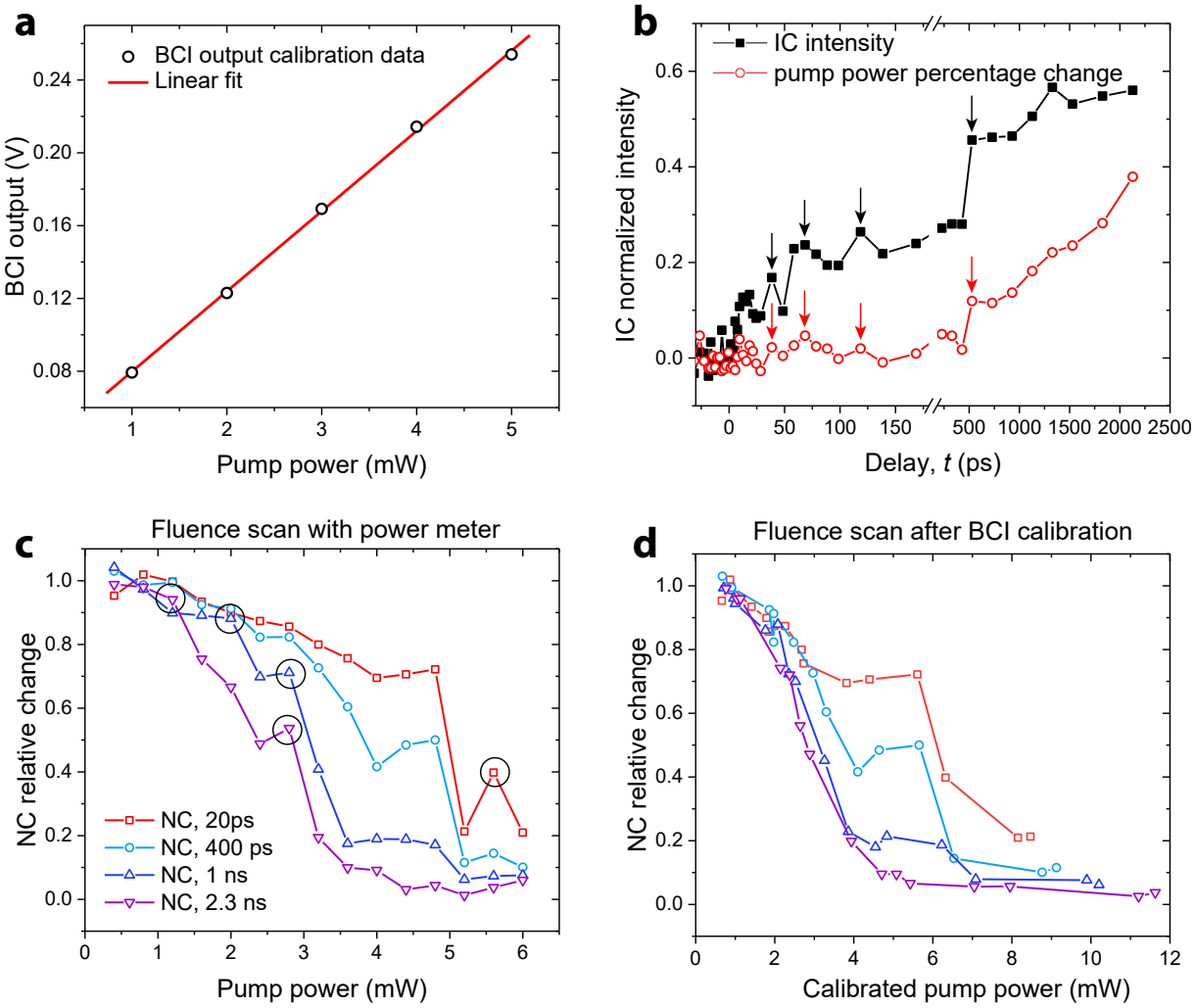

Figure C.2: Applications of the PD-BCI system in UED experiments. **a**, Calibration of BCI output voltage relative to pump power. **b**, Delay scan of 1T-TaS_2 IC peak dynamics with PD-BCI system calibration with 2500 nm pump. The arrows indicate strong correlation between the data noise and pump power fluctuations. **c**, The fluence-dependent data of 1T-TaS_2 NC-CDW peak changes at several critical delays before calibration. Horizontal labeled power is measured by power meter. The few black circles are "noisy/jumping" data points before calibration. **d**, Fluence scan data the same as that in **c** but after power calibration with the PD-BCI system.

$\approx 40\%$ rise in power at $+2.2$ ns. The black curve is the typical raw dynamics we would see after analyzing the data. Typically, these noisy, jumping points marked by black arrows are just treated as noise from somewhere we do not know. But with this PD-BCI system, it is strikingly clear that the jumping data points are directly correlated with jumps in the pump

power.

Figs. C.2c&d are another examples of fluence scan done with PD-BCI system calibration. Fig. C.2c is the typical fluence scan we would get in 1T-TaS_2 NC-CDW peak response. As we can see, there are some kinks and jumping points, making it hard to judge which kinks are real which kinks are noise. With this PD-BCI system installed, after calibration, the curves become very smooth and noisy points are gone, demonstrating the high dependence of data noise on pump power.

With these examples and demonstrations, we believe this is a very reliable system that can greatly improve the s/n of UED experiments, especially when the laser power is unstable or the delay stage alignment is not perfect. Moreover, it allow a person to do experiments remotely without being in the lab to perturb the experimental conditions.

BIBLIOGRAPHY

BIBLIOGRAPHY

[1] P. C. Hohenberg and B. I. Halperin, "Theory of dynamic critical phenomena," *Rev. Mod. Phys.*, vol. 49, pp. 435–479, 1977.

[2] M. Vojta, "Quantum phase transitions," *Reports on Progress in Physics*, vol. 66, no. 12, p. 2069, 2003.

[3] J. Allam, M. T. Sajjad, R. Sutton, K. Litvinenko, Z. Wang, S. Siddique, Q.-H. Yang, W. H. Loh, and T. Brown, "Measurement of a reaction-diffusion crossover in exciton-exciton recombination inside carbon nanotubes using femtosecond optical absorption," *Phys. Rev. Lett.*, vol. 111, p. 197401, 2013.

[4] D. Williams and C. Carter, *Transmission Electron Microscopy: A Textbook for Materials Science*. Springer US, 2009.

[5] S. K. Sundaram and E. Mazur, "Inducing and probing non-thermal transitions in semiconductors using femtosecond laser pulses," *Nature Materials*, vol. 1, pp. 217 EP –, 2002.

[6] R. P. Chatelain, V. R. Morrison, B. L. M. Klarenaar, and B. J. Siwick, "Coherent and incoherent electron-phonon coupling in graphite observed with radio-frequency compressed ultrafast electron diffraction," *Phys. Rev. Lett.*, vol. 113, p. 235502, 2014.

[7] E. J. Sie, C. M. Nyby, C. D. Pemmaraju, S. J. Park, X. Shen, J. Yang, M. C. Hoffmann, B. K. Ofori-Okai, R. Li, A. H. Reid, S. Weathersby, E. Mannebach, N. Finney, D. Rhodes, D. Chenet, A. Antony, L. Balicas, J. Hone, T. P. Devereaux, T. F. Heinz, X. Wang, and A. M. Lindenberg, "An ultrafast symmetry switch in a weyl semimetal," *Nature*, vol. 565, no. 7737, pp. 61–66, 2019.

[8] M. Z. Mo, V. Becker, B. K. Ofori-Okai, X. Shen, Z. Chen, B. Witte, R. Redmer, R. K. Li, M. Dunning, S. P. Weathersby, X. J. Wang, and S. H. Glenzer, "Determination of the electron-lattice coupling strength of copper with ultrafast MeV electron diffraction," *Review of Scientific Instruments*, vol. 89, no. 10, p. 10C108, 2018.

[9] S. Vogelgesang, G. Storeck, J. G. Horstmann, T. Diekmann, M. Sivis, S. Schramm, K. Rossnagel, S. Schäfer, and C. Ropers, "Phase ordering of charge density waves traced by ultrafast low-energy electron diffraction," *Nature Physics*, vol. 14, pp. 184 EP –, 2017.

[10] M. J. Stern, L. P. René de Cotret, M. R. Otto, R. P. Chatelain, J.-P. Boisvert, M. Sutton, and B. J. Siwick, "Mapping momentum-dependent electron-phonon coupling and

nonequilibrium phonon dynamics with ultrafast electron diffuse scattering," *Phys. Rev. B*, vol. 97, p. 165416, 2018.

[11] S. Rouzière, S. Ravy, J.-P. Pouget, and S. Brazovskii, "Friedel oscillations and charge-density wave pinning in quasi-one-dimensional conductors: an X-ray diffraction study," *Phys. Rev. B*, vol. 62, pp. R16231–R16234, 2000.

[12] J.-P. Pouget, "The Peierls instability and charge density wave in one-dimensional electronic conductors," *Comptes Rendus Physique*, vol. 17, no. 3, pp. 332–356, 2016.

[13] R. Ang, Y. Tanaka, E. Ieki, K. Nakayama, T. Sato, L. J. Li, W. J. Lu, Y. P. Sun, and T. Takahashi, "Real-space coexistence of the melted mott state and superconductivity in Fe-substituted 1T-TaS_2," *Phys. Rev. Lett.*, vol. 109, p. 176403, 2012.

[14] S. Margadonna, Y. Takabayashi, M. T. McDonald, K. Kasperkiewicz, Y. Mizuguchi, Y. Takano, A. N. Fitch, E. Suard, and K. Prassides, "Crystal structure of the new $FeSe_{1-x}$ superconductor," *Chemical Communications*, no. 43, pp. 5607–5609, 2008.

[15] Y. Mizuguchi and Y. Takano, "Review of Fe chalcogenides as the simplest Fe-based superconductor," *Journal of the Physical Society of Japan*, vol. 79, no. 10, p. 102001, 2010.

[16] A. Martinelli, A. Palenzona, M. Tropeano, C. Ferdeghini, M. Putti, M. R. Cimberle, T. D. Nguyen, M. Affronte, and C. Ritter, "From antiferromagnetism to superconductivity in $Fe_{1+y}Te_{1-x}Se_x$ ($0 \leq x \leq 0.20$): neutron powder diffraction analysis," *Phys. Rev. B*, vol. 81, p. 094115, 2010.

[17] S. Sachdev and B. Keimer, "Quantum criticality," *Physics Today*, vol. 64, no. 2, pp. 29–35, 2011.

[18] J. Orenstein, "Ultrafast spectroscopy of quantum materials," *Physics Today*, vol. 65, no. 9, pp. 44–50, 2012.

[19] L. Landau, "On the theory of phase transitions," *Phys. Z. Sow.*, vol. 11, 1937.

[20] D. Ter Haar, "On the theory of phase transitions," in *Collected Papers of L.D. Landau*, pp. 193 – 216, Pergamon, 1965.

[21] K. G. Wilson, "Renormalization group and critical phenomena. I. renormalization group and the Kadanoff scaling picture," *Phys. Rev. B*, vol. 4, pp. 3174–3183, 1971.

[22] K. G. Wilson, "Renormalization group and critical phenomena. II. phase-space cell analysis of critical behavior," *Phys. Rev. B*, vol. 4, pp. 3184–3205, 1971.

[23] E. A. Guggenheim, "The principle of corresponding states," *The Journal of Chemical Physics*, vol. 13, no. 7, pp. 253–261, 1945.

[24] L. Onsager, "Crystal statistics. I. a two-dimensional model with an order-disorder transition," *Phys. Rev.*, vol. 65, pp. 117–149, 1944.

[25] C. N. Yang, "The spontaneous magnetization of a two-dimensional Ising model," *Phys. Rev.*, vol. 85, pp. 808–816, 1952.

[26] M. R. Moldover and W. A. Little, "Specific heat of He^3 and He^4 in the neighborhood of their critical points," *Phys. Rev. Lett.*, vol. 15, pp. 54–56, 1965.

[27] L. P. Kadanoff, "Scaling laws for Ising models near T_c," *Physics Physique Fizika*, vol. 2, pp. 263–272, 1966.

[28] K. G. Wilson and M. E. Fisher, "Critical exponents in 3.99 dimensions," *Phys. Rev. Lett.*, vol. 28, pp. 240–243, 1972.

[29] J. Bardeen, L. N. Cooper, and J. R. Schrieffer, "Theory of superconductivity," *Phys. Rev.*, vol. 108, pp. 1175–1204, 1957.

[30] M. Aizenman, "Proof of the triviality of ${\phi_d}^4$ field theory and some mean-field features of Ising models for d>4," *Phys. Rev. Lett.*, vol. 47, pp. 1–4, 1981.

[31] R. Guida and J. Zinn-Justin, "Critical exponents of the N-vector model," *Journal of Physics A: Mathematical and General*, vol. 31, no. 40, p. 8103, 1998.

[32] H. Nakanishi and H. E. Stanley, "Scaling studies of percolation phenomena in systems of dimensionality two to seven: cluster numbers," *Phys. Rev. B*, vol. 22, pp. 2466–2488, 1980.

[33] D.Stauffer, "Scaling theory of percolation clusters," *Phys. Rep.*, vol. 54, no. 1, pp. 1–74, 1979.

[34] J. Adler, Y. Meir, A. Aharony, and A. B. Harris, "Series study of percolation moments in general dimension," *Phys. Rev. B*, vol. 41, pp. 9183–9206, 1990.

[35] I. Jensen, "Low-density series expansions for directed percolation: I. a new efficient algorithm with applications to the square lattice," *Journal of Physics A: Mathematical and General*, vol. 32, no. 28, p. 5233, 1999.

[36] C. A. Voigt and R. M. Ziff, "Epidemic analysis of the second-order transition in the Ziff-Gulari-Barshad surface-reaction model," *Phys. Rev. E*, vol. 56, pp. R6241–R6244, 1997.

[37] I. Jensen, "Critical behavior of the three-dimensional contact process," *Phys. Rev. A*, vol. 45, pp. R563–R566, 1992.

[38] H.-K. Janssen and U. C. Täuber, "The field theory approach to percolation processes," *Annals of Physics*, vol. 315, no. 1, pp. 147 – 192, 2005.

[39] B. Derrida, A. J, and C. Godreche, "Non-trivial exponents in the zero temperature dynamics of the 1D Ising and Potts models," *Journal of Physics A: Mathematical and General*, vol. 27, no. 11, pp. L357–L361, 1994.

[40] G. Odor, "Universality classes in nonequilibrium lattice systems," *Rev. Mod. Phys.*, vol. 76, pp. 663–724, 2004.

[41] A. del Campo and W. H. Zurek, "Universality of phase transition dynamics: topological defects from symmetry breaking," *International Journal of Modern Physics A*, vol. 29, 2014.

[42] T. Kibble, "Topology of cosmic domains and strings," *Journal of Physics A: Mathematical and General*, vol. 9, no. 8, pp. 1387–1398, 1976.

[43] T. Kibble, "Some implications of a cosmological phase transition," *Physics Reports*, vol. 67, no. 1, pp. 183 – 199", 1980.

[44] W. H. Zurek, "Cosmological experiments in superfluid helium," *Nature*, vol. 317, no. 6037, pp. 505–508, 1985.

[45] A. del Campo and W. H. Zurek, "Universality of phase transition dynamics: topological defects from symmetry breaking," *International Journal of Modern Physics A*, vol. 29, no. 08, p. 1430018, 2014.

[46] R. Peirels, *Quantum Theory of Solids*. Clarendon Press, 1955.

[47] W. Kohn, "Image of the Fermi surface in the vibration spectrum of a metal," *Phys. Rev. Lett.*, vol. 2, pp. 393–394, 1959.

[48] R. Comès, M. Lambert, H. Launois, and H. R. Zeller, "Evidence for a Peierls distortion or a Kohn anomaly in one-dimensional conductors of the type $K_2Pt(CN)_4Br_{0.3x}H_2O$," *Phys. Rev. B*, vol. 8, pp. 571–575, 1973.

[49] J. P. Pouget, S. K. Khanna, F. Denoyer, R. Comès, A. F. Garito, and A. J. Heeger, "X-ray observation of $2k_F$ and $4k_F$ scatterings in tetrathiafulvalene-tetracyanoquinodimethane (TTF-TCNQ)," *Phys. Rev. Lett.*, vol. 37, pp. 437–440, 1976.

[50] W. Fogle and J. H. Perlstein, "Semiconductor-to-metal transition in the blue potassium molybdenum bronze, $K_{0.3}MoO_3$; example of a possible excitonic insulator," *Phys. Rev. B*, vol. 6, pp. 1402–1412, 1972.

[51] P. Monçeau, N. P. Ong, A. M. Portis, A. Meerschaut, and J. Rouxel, "Electric field breakdown of charge-density-wave-induced anomalies in $NbSe_3$," *Phys. Rev. Lett.*, vol. 37, pp. 602–606, 1976.

[52] J. Wilson, F. D. Salvo, and S. Mahajan, "Charge-density waves and superlattices in the metallic layered transition metal dichalcogenides," *Advances in Physics*, vol. 24, no. 2, pp. 117–201, 1975.

[53] J. A. Wilson, "Bands, bonds, and charge-density waves in the $NbSe_3$ family of compounds," *Phys. Rev. B*, vol. 19, pp. 6456–6468, 1979.

[54] G. Grüner, *Density Waves In Solids*. Frontiers in physics, 2009.

[55] X. Zhu, Y. Cao, J. Zhang, E. W. Plummer, and J. Guo, "Classification of charge density waves based on their nature," *Proceedings of the National Academy of Sciences*, vol. 112, no. 8, pp. 2367–2371, 2015.

[56] P. A. Lee, T. M. Rice, and P. W. Anderson, "Fluctuation effects at a Peierls transition," *Phys. Rev. Lett.*, vol. 31, pp. 462–465, 1973.

[57] B. Renker, H. Rietschel, L. Pintschovius, W. Gläser, P. Brüesch, D. Kuse, and M. J. Rice, "Observation of giant Kohn anomaly in the one-dimensional conductor $K_2Pt(CN)_4Br_{0.3}{\cdot}3H_2O$," *Phys. Rev. Lett.*, vol. 30, pp. 1144–1147, 1973.

[58] G. Shirane, S. M. Shapiro, R. Comès, A. F. Garito, and A. J. Heeger, "Phonon dispersion and Kohn anomaly in tetrathiafulvalene-tetracyanoquinodimethane (TTF-TCNQ)," *Phys. Rev. B*, vol. 14, pp. 2325–2334, 1976.

[59] J. P. Pouget, S. M. Shapiro, G. Shirane, A. F. Garito, and A. J. Heeger, "Elastic- and inelastic-neutron-scattering study of tetrathiafulvalenium-tetracyanoquinodimethanide (TTF-TCNQ): new results," *Phys. Rev. B*, vol. 19, pp. 1792–1799, 1979.

[60] H. Requardt, J. E. Lorenzo, P. Monceau, R. Currat, and M. Krisch, "Dynamics in the charge-density-wave system $NbSe_3$ using inelastic X-ray scattering with meV energy resolution," *Phys. Rev. B*, vol. 66, p. 214303, 2002.

[61] J.-P. Pouget, "The Peierls instability and charge density wave in one-dimensional electronic conductors," *Comptes Rendus Physique*, vol. 17, no. 3, pp. 32 – 356, 2016.

[62] J. P. Pouget, B. Hennion, C. Escribe-Filippini, and M. Sato, "Neutron-scattering investigations of the Kohn anomaly and of the phase and amplitude charge-density-wave excitations of the blue bronze $K_{0.3}MoO_3$," *Phys. Rev. B*, vol. 43, pp. 8421–8430, 1991.

[63] V. Brouet, W. L. Yang, X. J. Zhou, Z. Hussain, N. Ru, K. Y. Shin, I. R. Fisher, and Z. X. Shen, "Fermi surface reconstruction in the CDW state of $CeTe_3$ observed by photoemission," *Phys. Rev. Lett.*, vol. 93, p. 126405, 2004.

[64] C. D. Malliakas and M. G. Kanatzidis, "Divergence in the behavior of the charge density wave in $RETe_3$ (RE = Rare-Earth element) with temperature and RE element," *Journal of the American Chemical Society*, vol. 128, no. 39, pp. 12612–12613, 2006.

[65] K. Rossnagel, "On the origin of charge-density waves in select layered transition-metal dichalcogenides," *Journal of Physics: Condensed Matter*, vol. 23, no. 21, p. 213001, 2011.

[66] M. D. Johannes and I. I. Mazin, "Fermi surface nesting and the origin of charge density waves in metals," *Phys. Rev. B*, vol. 77, p. 165135, 2008.

[67] K. Rossnagel, E. Rotenberg, H. Koh, N. V. Smith, and L. Kipp, "Fermi surface, charge-density-wave gap, and kinks in 2H-$TaSe_2$," *Phys. Rev. B*, vol. 72, p. 121103, 2005.

[68] G. Ghiringhelli, M. Le Tacon, M. Minola, S. Blanco-Canosa, C. Mazzoli, N. B. Brookes, G. M. De Luca, A. Frano, D. G. Hawthorn, F. He, T. Loew, M. M. Sala, D. C. Peets, M. Salluzzo, E. Schierle, R. Sutarto, G. A. Sawatzky, E. Weschke, B. Keimer, and L. Braicovich, "Long-range incommensurate charge fluctuations in $(Y,Nd)Ba_2Cu_3O_{6+x}$," *Science*, vol. 337, no. 6096, pp. 821–825, 2012.

[69] E. H. da Silva Neto, P. Aynajian, A. Frano, R. Comin, E. Schierle, E. Weschke, A. Gyenis, J. Wen, J. Schneeloch, Z. Xu, S. Ono, G. Gu, M. Le Tacon, and A. Yazdani, "Ubiquitous interplay between charge ordering and high-temperature superconductivity in cuprates," *Science*, vol. 343, no. 6169, pp. 393–396, 2014.

[70] D. Rez, P. Rez, and I. Grant, "Dirac–Fock calculations of X-ray scattering factors and contributions to the mean inner potential for electron scattering," *Acta Crystallographica Section A*, vol. 50, no. 4, pp. 481–497, 1994.

[71] P. Brown, A. G. Fox, E. N. Maslen, M. A. O'Keefe, and B. T. M. Willis, *International Tables for Crystallography*, vol. C. Kluwer Academic Publishers, 2006.

[72] N. Mott and H. Massey, *The theory of atomic collisions*. Clarendon Press, 3rd ed., 1965.

[73] A. R. Stokes and A. J. C. Wilson, "The diffraction of X-rays by distorted crystal aggregates - I," *Proceedings of the Physical Society*, vol. 56, no. 3, p. 174, 1944.

[74] G. Williamson and W. Hall, "X-ray line broadening from filed aluminium and wolfram," *Acta Metallurgica*, vol. 1, no. 1, pp. 22 – 31, 1953.

[75] T. H. de Keijser, J. I. Langford, E. J. Mittemeijer, and A. B. P. Vogels, "Use of the Voigt function in a single-line method for the analysis of X-ray diffraction line broadening," *Journal of Applied Crystallography*, vol. 15, no. 3, pp. 308–314, 1982.

[76] A. H. Zewail, "Femtosecond transition-state dynamics," *Faraday Discuss. Chem. Soc.*, vol. 91, pp. 207–237, 1991.

[77] J. C. Williamson and A. H. Zewail, "Structural femtochemistry: experimental methodology," *Proceedings of the National Academy of Sciences*, vol. 88, no. 11, pp. 5021–5025, 1991.

[78] J. Williamson, M. Dantus, S. Kim, and A. Zewail, "Ultrafast diffraction and molecular structure," *Chemical Physics Letters*, vol. 196, no. 6, pp. 529 – 534, 1992.

[79] M. Dantus, S. B. Kim, J. C. Williamson, and A. H. Zewail, "Ultrafast electron diffraction. 5. experimental time resolution and applications," *The Journal of Physical Chemistry*, vol. 98, no. 11, pp. 2782–2796, 1994.

[80] J. C. Williamson, J. Cao, H. Ihee, H. Frey, and A. H. Zewail, "Clocking transient chemical changes by ultrafast electron diffraction," *Nature*, vol. 386, no. 159, pp. 159–162, 1997.

[81] Y. Jiang, Z. Chen, Y. Han, P. Deb, H. Gao, S. Xie, P. Purohit, M. W. Tate, J. Park, S. M. Gruner, V. Elser, and D. A. Muller, "Electron ptychography of 2D materials to deep sub-ångström resolution," *Nature*, vol. 559, no. 7714, pp. 343–349, 2018.

[82] O. Krivanek, T. Lovejoy, N. Bacon, G. Corbin, N. Dellby, P. Hrncirik, M. Murfitt, G. Skone, Z. Szilagyi, P. Batson, and et al., "High energy resolution monochromated EELS-STEM system," *Microscopy and Microanalysis*, vol. 19, no. S2, p. 1124–1125, 2013.

[83] V. Brouet, W. L. Yang, X. J. Zhou, Z. Hussain, R. G. Moore, R. He, D. H. Lu, Z. X. Shen, J. Laverock, S. B. Dugdale, N. Ru, and I. R. Fisher, "Angle-resolved photoemission study of the evolution of band structure and charge density wave properties in RTe_3 ($R =$ Y, La, Ce, Sm, Gd, Tb, and Dy)," *Phys. Rev. B*, vol. 77, p. 235104, 2008.

[84] R. G. Moore, V. Brouet, R. He, D. H. Lu, N. Ru, J.-H. Chu, I. R. Fisher, and Z.-X. Shen, "Fermi surface evolution across multiple charge density wave transitions in $ErTe_3$," *Phys. Rev. B*, vol. 81, p. 073102, 2010.

[85] N. Ru, C. L. Condron, G. Y. Margulis, K. Y. Shin, J. Laverock, S. B. Dugdale, M. F. Toney, and I. R. Fisher, "Effect of chemical pressure on the charge density wave transition in rare-earth tritellurides RTe_3," *Phys. Rev. B*, vol. 77, p. 035114, 2008.

[86] C. D. Malliakas and M. G. Kanatzidis, "Divergence in the behavior of the charge density wave in $RETe_3$ (RE = Rare-Earth element) with temperature and RE element," *Journal of the American Chemical Society*, vol. 128, no. 39, pp. 12612–12613, 2006.

[87] Y. Feng, J. Wang, R. Jaramillo, J. van Wezel, S. Haravifard, G. Srajer, Y. Liu, Z.-A. Xu, P. B. Littlewood, and T. F. Rosenbaum, "Order parameter fluctuations at a buried quantum critical point," *Proceedings of the National Academy of Sciences*, vol. 109, no. 19, pp. 7224–7229, 2012.

[88] A. Sacchetti, L. Degiorgi, T. Giamarchi, N. Ru, and I. R. Fisher, "Chemical pressure and hidden one-dimensional behavior in rare-earth tri-telluride charge-density wave compounds," *Phys. Rev. B*, vol. 74, p. 125115, 2006.

[89] B. F. Hu, P. Zheng, R. H. Yuan, T. Dong, B. Cheng, Z. G. Chen, and N. L. Wang, "Optical spectroscopy study on $CeTe_3$: evidence for multiple charge-density-wave orders," *Phys. Rev. B*, vol. 83, p. 155113, 2011.

[90] C. C. Katsidis and D. I. Siapkas, "General transfer-matrix method for optical multilayer systems with coherent, partially coherent, and incoherent interference," *Appl. Opt.*, vol. 41, no. 19, pp. 3978–3987, 2002.

[91] M. Maschek, D. A. Zocco, S. Rosenkranz, R. Heid, A. H. Said, A. Alatas, P. Walmsley, I. R. Fisher, and F. Weber, "Competing soft phonon modes at the charge-density-wave transitions in $DyTe_3$," *Phys. Rev. B*, vol. 98, p. 094304, 2018.

[92] H. J. Kim, C. D. Malliakas, A. T. Tomić, S. H. Tessmer, M. G. Kanatzidis, and S. J. L. Billinge, "Local atomic structure and discommensurations in the charge density wave of $CeTe_3$," *Phys. Rev. Lett.*, vol. 96, p. 226401, 2006.

[93] L. Rettig, R. Cortés, J.-H. Chu, I. R. Fisher, F. Schmitt, R. G. Moore, Z.-X. Shen, P. S. Kirchmann, M. Wolf, and U. Bovensiepen, "Persistent order due to transiently enhanced nesting in an electronically excited charge density wave," *Nature Communications*, vol. 7, pp. 10459 EP –, 2016.

[94] N. Ru and I. R. Fisher, "Thermodynamic and transport properties of YTe_3, $LaTe_3$, and $CeTe_3$," *Phys. Rev. B*, vol. 73, p. 033101, 2006.

[95] P. Saint-Paul, M.;Monceau, "Survey of the thermodynamic properties of the charge density wave systems," *Advances in Condensed Matter Physics*, vol. 2019, 2019.

[96] K. Nakanishi, H. Takatera, Y. Yamada, and H. Shiba, "The nearly commensurate phase and effect of harmonics on the successive phase transition in 1T-TaS_2," *Journal of the Physical Society of Japan*, vol. 43, no. 5, pp. 1509–1517, 1977.

[97] X. L. WU and C. M. LIEBER, "Hexagonal domain-like charge density wave phase of TaS_2 determined by scanning tunneling microscopy," *Science*, vol. 243, no. 4899, pp. 1703–1705, 1989.

[98] T. Ishiguro and H. Sato, "Electron microscopy of phase transformations in 1T-TaS_2," *Phys. Rev. B*, vol. 44, pp. 2046–2060, 1991.

[99] R. E. Thomson, B. Burk, A. Zettl, and J. Clarke, "Scanning tunneling microscopy of the charge-density-wave structure in 1T-TaS_2," *Phys. Rev. B*, vol. 49, pp. 16899–16916, 1994.

[100] A. Spijkerman, J. L. de Boer, A. Meetsma, G. A. Wiegers, and S. van Smaalen, "X-ray crystal-structure refinement of the nearly commensurate phase of 1T-TaS_2 in $(3 + 2)$-dimensional superspace," *Phys. Rev. B*, vol. 56, pp. 13757–13767, 1997.

[101] J. Demsar, L. Forró, H. Berger, and D. Mihailovic, "Femtosecond snapshots of gap-forming charge-density-wave correlations in quasi-two-dimensional dichalcogenides 1T-TaS_2 and 2H-$TaSe_2$," *Phys. Rev. B*, vol. 66, p. 041101, 2002.

[102] L. Perfetti, P. A. Loukakos, M. Lisowski, U. Bovensiepen, H. Berger, S. Biermann, P. S. Cornaglia, A. Georges, and M. Wolf, "Time evolution of the electronic structure of 1T-TaS_2 through the insulator-metal transition," *Phys. Rev. Lett.*, vol. 97, p. 067402, 2006.

[103] S. Hellmann, M. Beye, C. Sohrt, T. Rohwer, F. Sorgenfrei, H. Redlin, M. Kalläne, M. Marczynski-Bühlow, F. Hennies, M. Bauer, A. Föhlisch, L. Kipp, W. Wurth, and K. Rossnagel, "Ultrafast melting of a charge-density wave in the mott insulator 1T-TaS_2," *Phys. Rev. Lett.*, vol. 105, p. 187401, 2010.

[104] N. Dean, J. C. Petersen, D. Fausti, R. I. Tobey, S. Kaiser, L. V. Gasparov, H. Berger, and A. Cavalleri, "Polaronic conductivity in the photoinduced phase of 1T-TaS_2," *Phys. Rev. Lett.*, vol. 106, p. 016401, 2011.

[105] J. C. Petersen, S. Kaiser, N. Dean, A. Simoncig, H. Y. Liu, A. L. Cavalieri, C. Cacho, I. C. E. Turcu, E. Springate, F. Frassetto, L. Poletto, S. S. Dhesi, H. Berger, and A. Cavalleri, "Clocking the melting transition of charge and lattice order in 1T-TaS_2 with ultrafast extreme-ultraviolet angle-resolved photoemission spectroscopy," *Phys. Rev. Lett.*, vol. 107, p. 177402, 2011.

[106] T.-R. T. Han, F. Zhou, C. D. Malliakas, P. M. Duxbury, S. D. Mahanti, M. G. Kanatzidis, and C.-Y. Ruan, "Exploration of metastability and hidden phases in correlated electron crystals visualized by femtosecond optical doping and electron crystallography," *Science Advances*, vol. 1, no. 5, 2015.

[107] W. Shen, Y. Ge, A. Y. Liu, H. R. Krishnamurthy, T. P. Devereaux, and J. K. Freericks, "Nonequilibrium "melting" of a charge density wave insulator via an ultrafast laser pulse," *Phys. Rev. Lett.*, vol. 112, p. 176404, 2014.

[108] B. Sipos, A. F. Kusmartseva, A. Akrap, H. Berger, L. Forró, and E. Tutis, "From mott state to superconductivity in 1T-TaS_2," *Nature Materials*, vol. 7, pp. 960 EP –, 2008.

[109] T. Ritschel, J. Trinckauf, G. Garbarino, M. Hanfland, M. v. Zimmermann, H. Berger, B. Büchner, and J. Geck, "Pressure dependence of the charge density wave in 1T-TaS_2 and its relation to superconductivity," *Phys. Rev. B*, vol. 87, p. 125135, 2013.

[110] L. Stojchevska, I. Vaskivskyi, T. Mertelj, P. Kusar, D. Svetin, S. Brazovskii, and D. Mihailovic, "Ultrafast switching to a stable hidden quantum state in an electronic crystal," *Science*, vol. 344, no. 6180, pp. 177–180, 2014.

[111] Y. Yu, F. Yang, X. F. Lu, Y. J. Yan, Y.-H. Cho, L. Ma, X. Niu, S. Kim, Y.-W. Son, D. Feng, S. Li, S.-W. Cheong, X. H. Chen, and Y. Zhang, "Gate-tunable phase transitions in thin flakes of 1T-TaS_2," *Nature Nanotechnology*, vol. 10, pp. 270 EP –, 2015.

[112] M. J. Hollander, Y. Liu, W.-J. Lu, L.-J. Li, Y.-P. Sun, J. A. Robinson, and S. Datta, "Electrically driven reversible insulator-metal phase transition in 1T-TaS_2," *Nano Letters*, vol. 15, no. 3, pp. 1861–1866, 2015.

[113] A. W. Tsen, R. Hovden, D. Wang, Y. D. Kim, J. Okamoto, K. A. Spoth, Y. Liu, W. Lu, Y. Sun, J. C. Hone, L. F. Kourkoutis, P. Kim, and A. N. Pasupathy, "Structure and control of charge density waves in two-dimensional 1T-TaS_2," *Proceedings of the National Academy of Sciences*, vol. 112, no. 49, pp. 15054–15059, 2015.

[114] M. Yoshida, R. Suzuki, Y. Zhang, M. Nakano, and Y. Iwasa, "Memristive phase switching in two-dimensional 1T-TaS_2 crystals," *Science Advances*, vol. 1, no. 9, 2015.

[115] L. Ma, C. Ye, Y. Yu, X. F. Lu, X. Niu, S. Kim, D. Feng, D. Tománek, Y.-W. Son, X. H. Chen, and Y. Zhang, "A metallic mosaic phase and the origin of mott-insulating state in 1T-TaS_2," *Nature Communications*, vol. 7, pp. 10956 EP –, 2016.

[116] I. Vaskivskyi, I. A. Mihailovic, S. Brazovskii, J. Gospodaric, T. Mertelj, D. Svetin, P. Sutar, and D. Mihailovic, "Fast electronic resistance switching involving hidden charge density wave states," *Nature Communications*, vol. 7, pp. 11442 EP –, 2016.

[117] S. C. Bayliss, A. M. Ghorayeb, and D. R. P. Guy, "Thermal and transport evidence for a phase transition in 1T-TaS_2 observed at 282 K upon warming," *Journal of Physics C: Solid State Physics*, vol. 17, no. 21, pp. L533–L537, 1984.

[118] B. Burk, R. E. Thomson, A. Zettl, and J. Clarke, "Charge-density-wave domains in 1T-TaS_2 observed by satellite structure in scanning-tunneling-microscopy images," *Phys. Rev. Lett.*, vol. 66, pp. 3040–3043, 1991.

[119] A. Suzuki, M. Koizumi, and M. Doyama, "Thermal evidences for successive CDW phase transitions in 1T-TaS_2," *Solid State Communications*, vol. 53, no. 2, pp. 201–203, 1985.

[120] R. N. Bhatt and W. L. McMillan, "Theory of phonon dynamics near a charge-density-wave instability," *Phys. Rev. B*, vol. 12, pp. 2042–2044, 1975.

[121] K. Nakanishi and H. Shiba, "Domain-like incommensurate charge-density-wave states and the first-order incommensurate-commensurate transitions in layered tantalum dichalcogenides. I. 1T-polytype," *Journal of the Physical Society of Japan*, vol. 43, no. 6, pp. 1839–1847, 1977.

[122] M. Eichberger, H. Schäfer, M. Krumova, M. Beyer, J. Demsar, H. Berger, G. Moriena, G. Sciaini, and R. J. D. Miller, "Snapshots of cooperative atomic motions in the optical suppression of charge density waves," *Nature*, vol. 468, pp. 799 EP –, 2010.

[123] K. Haupt, M. Eichberger, N. Erasmus, A. Rohwer, J. Demsar, K. Rossnagel, and H. Schwoerer, "Ultrafast metamorphosis of a complex charge-density wave," *Phys. Rev. Lett.*, vol. 116, p. 016402, 2016.

[124] C. Laulhé, T. Huber, G. Lantz, A. Ferrer, S. O. Mariager, S. Grübel, J. Rittmann, J. A. Johnson, V. Esposito, A. Lübcke, L. Huber, M. Kubli, M. Savoini, V. L. R. Jacques, L. Cario, B. Corraze, E. Janod, G. Ingold, P. Beaud, S. L. Johnson, and S. Ravy, "Ultrafast formation of a charge density wave state in 1T-TaS_2: observation at nanometer scales using time-resolved X-ray diffraction," *Phys. Rev. Lett.*, vol. 118, p. 247401, 2017.

[125] X. L. Wu and C. M. Lieber, "Direct observation of growth and melting of the hexagonal-domain charge-density-wave phase in 1T-TaS_2 by scanning tunneling microscopy," *Phys. Rev. Lett.*, vol. 64, pp. 1150–1153, 1990.

[126] M. Gring, M. Kuhnert, T. Langen, T. Kitagawa, B. Rauer, M. Schreitl, I. Mazets, D. A. Smith, E. Demler, and J. Schmiedmayer, "Relaxation and prethermalization in an isolated quantum system," *Science*, vol. 337, no. 6100, pp. 1318–1322, 2012.

[127] T. Mori, T. N. Ikeda, E. Kaminishi, and M. Ueda, "Thermalization and prethermalization in isolated quantum systems: a theoretical overview," *Journal of Physics B: Atomic, Molecular and Optical Physics*, vol. 51, no. 11, p. 112001, 2018.

[128] J. Berges, S. Borsányi, and C. Wetterich, "Prethermalization," *Phys. Rev. Lett.*, vol. 93, p. 142002, 2004.

[129] M. Marcuzzi, J. Marino, A. Gambassi, and A. Silva, "Prethermalization in a nonintegrable quantum spin chain after a quench," *Phys. Rev. Lett.*, vol. 111, p. 197203, 2013.

[130] N. Nessi, A. Iucci, and M. A. Cazalilla, "Quantum quench and prethermalization dynamics in a two-dimensional Fermi gas with long-range interactions," *Phys. Rev. Lett.*, vol. 113, p. 210402, 2014.

[131] E. Kaminishi, T. Mori, T. N. Ikeda, and M. Ueda, "Entanglement pre-thermalization in a one-dimensional Bose gas," *Nature Physics*, vol. 11, pp. 1050 EP –, 2015.

[132] T. Langen, R. Geiger, and J. Schmiedmayer, "Ultracold atoms out of equilibrium," *Annual Review of Condensed Matter Physics*, vol. 6, no. 1, pp. 201–217, 2015.

[133] K. Mallayya, M. Rigol, and W. De Roeck, "Prethermalization and thermalization in isolated quantum systems," *Phys. Rev. X*, vol. 9, p. 021027, 2019.

[134] P. Reimann and L. Dabelow, "Typicality of prethermalization," *Phys. Rev. Lett.*, vol. 122, p. 080603, 2019.

[135] T. Langen, R. Geiger, M. Kuhnert, B. Rauer, and J. Schmiedmayer, "Local emergence of thermal correlations in an isolated quantum many-body system," *Nature Physics*, vol. 9, pp. 640 EP –, 2013.

[136] C. Eigen, J. A. P. Glidden, R. Lopes, E. A. Cornell, R. P. Smith, and Z. Hadzibabic, "Universal prethermal dynamics of Bose gases quenched to unitarity," *Nature*, vol. 563, no. 7730, pp. 221–224, 2018.

[137] A. Bray, "Theory of phase-ordering kinetics," *Advances in Physics*, vol. 43, no. 3, pp. 357–459, 1994.

[138] O. R. Albertini, A. Y. Liu, and M. Calandra, "Effect of electron doping on lattice instabilities in single-layer 1H-TaS_2," *Phys. Rev. B*, vol. 95, p. 235121, 2017.

[139] A. R. Beal, H. P. Hughes, and W. Y. Liang, "The reflectivity spectra of some group VA transition metal dichalcogenides," *Journal of Physics C: Solid State Physics*, vol. 8, no. 24, pp. 4236–4234, 1975.

[140] A. Piñeiro Orioli, K. Boguslavski, and J. Berges, "Universal self-similar dynamics of relativistic and nonrelativistic field theories near nonthermal fixed points," *Phys. Rev. D*, vol. 92, p. 025041, 2015.

[141] S. Erne, R. Bücker, T. Gasenzer, J. Berges, and J. Schmiedmayer, "Universal dynamics in an isolated one-dimensional Bose gas far from equilibrium," *Nature*, vol. 563, no. 7730, pp. 225–229, 2018.

[142] M. Prüfer, P. Kunkel, H. Strobel, S. Lannig, D. Linnemann, C.-M. Schmied, J. Berges, T. Gasenzer, and M. K. Oberthaler, "Observation of universal dynamics in a spinor Bose gas far from equilibrium," *Nature*, vol. 563, no. 7730, pp. 217–220, 2018.

[143] U. C. Täuber, *Critical Dynamics: a Field Theory Approach to Equilibrium and Non-Equilibrium Scaling Behavior*. Cambridge University Press, 2014.

[144] Q. H. Wang, K. Kalantar-Zadeh, A. Kis, J. N. Coleman, and M. S. Strano, "Electronics and optoelectronics of two-dimensional transition metal dichalcogenides," *Nature Nanotechnology*, vol. 7, pp. 699 EP –, 2012.

[145] L. Ju, J. Velasco Jr, E. Huang, S. Kahn, C. Nosiglia, H.-Z. Tsai, W. Yang, T. Taniguchi, K. Watanabe, Y. Zhang, G. Zhang, M. Crommie, A. Zettl, and F. Wang, "Photoinduced doping in heterostructures of graphene and boron nitride," *Nature Nanotechnology*, vol. 9, pp. 348 EP –, 2014.

[146] C. Sun, M. T. Wade, Y. Lee, J. S. Orcutt, L. Alloatti, M. S. Georgas, A. S. Waterman, J. M. Shainline, R. R. Avizienis, S. Lin, B. R. Moss, R. Kumar, F. Pavanello, A. H. Atabaki, H. M. Cook, A. J. Ou, J. C. Leu, Y.-H. Chen, K. Asanovic, R. J. Ram, M. A. Popovic, and V. M. Stojanovic, "Single-chip microprocessor that communicates directly using light," *Nature*, vol. 528, pp. 534 EP –, 2015.

[147] T. Leydecker, M. Herder, E. Pavlica, G. Bratina, S. Hecht, E. Orgiu, and P. Samorì, "Flexible non-volatile optical memory thin-film transistor device with over 256 distinct levels based on an organic bicomponent blend," *Nature Nanotechnology*, vol. 11, pp. 769 EP –, 2016.

[148] D. Xiang, T. Liu, J. Xu, J. Y. Tan, Z. Hu, B. Lei, Y. Zheng, J. Wu, A. H. C. Neto, L. Liu, and W. Chen, "Two-dimensional multibit optoelectronic memory with broadband spectrum distinction," *Nature Communications*, vol. 9, no. 1, p. 2966, 2018.

[149] T. Liu, D. Xiang, Y. Zheng, Y. Wang, X. Wang, L. Wang, J. He, L. Liu, and W. Chen, "Nonvolatile and programmable photodoping in $MoTe_2$ for photoresist-free complementary electronic devices," *Advanced Materials*, vol. 30, no. 52, p. 1804470, 2018.

[150] M. Harb, R. Ernstorfer, T. Dartigalongue, C. T. Hebeisen, R. E. Jordan, and R. J. D. Miller, "Carrier relaxation and lattice heating dynamics in silicon revealed by femtosecond electron diffraction," *The Journal of Physical Chemistry B*, vol. 110, no. 50, pp. 25308–25313, 2006.

[151] K. Sokolowski-Tinten, X. Shen, Q. Zheng, T. Chase, R. Coffee, M. Jerman, R. K. Li, M. Ligges, I. Makasyuk, M. Mo, A. H. Reid, B. Rethfeld, T. Vecchione, S. P. Weathersby, H. A. Dürr, and X. J. Wang, "Electron-lattice energy relaxation in laser-excited thin-film Au-insulator heterostructures studied by ultrafast Mev electron diffraction," *Structural Dynamics*, vol. 4, no. 5, p. 054501, 2017.

[152] M. Bernardi, D. Vigil-Fowler, J. Lischner, J. B. Neaton, and S. G. Louie, "Ab initio study of hot carriers in the first picosecond after sunlight absorption in silicon," *Phys. Rev. Lett.*, vol. 112, p. 257402, 2014.

[153] P. Baum, D.-S. Yang, and A. H. Zewail, "4D visualization of transitional structures in phase transformations by electron diffraction," *Science*, vol. 318, no. 5851, pp. 788–792, 2007.

[154] V. R. Morrison, R. P. Chatelain, K. L. Tiwari, A. Hendaoui, A. Bruhács, M. Chaker, and B. J. Siwick, "A photoinduced metal-like phase of monoclinic VO_2 revealed by ultrafast electron diffraction," *Science*, vol. 346, no. 6208, pp. 445–448, 2014.

[155] Z. Tao, F. Zhou, T.-R. T. Han, D. Torres, T. Wang, N. Sepulveda, K. Chang, M. Young, R. R. Lunt, and C.-Y. Ruan, "The nature of photoinduced phase transition and metastable states in vanadium dioxide," *Scientific Reports*, vol. 6, pp. 38514 EP –, 2016.

[156] G. F. Giuliani and A. W. Overhauser, "Structure factor of a charge-density wave," *Phys. Rev. B*, vol. 23, pp. 3737–3743, 1981.

[157] R. Brouwer and F. Jellinek, "The low-temperature superstructures of 1T-$TaSe_2$ and 2H-$TaSe_2$," *Physica B+C*, vol. 99, no. 1, pp. 51–55, 1980.

[158] D. van Delft and P. Kes, "The discovery of superconductivity," *Physics Today*, vol. 63, no. 9, pp. 38–43, 2010.

[159] J. G. Bednorz and K. A. Müller, "Possible high-Tc superconductivity in the Ba-La-Cu-O system," *Zeitschrift für Physik B Condensed Matter*, vol. 64, no. 2, pp. 189–193, 1986.

[160] Y. Kamihara, T. Watanabe, M. Hirano, and H. Hosono, "Iron-based layered superconductor La[$O_{1-x}F_x$]FeAs (x = 0.05-0.12) with Tc = 26 K," *Journal of the American Chemical Society*, vol. 130, no. 11, pp. 3296–3297, 2008.

[161] Z.-A. Ren, W. Lu, J. Yang, W. Yi, X.-L. Shen, Z.-C. Li, G.-C. Che, X.-L. Dong, L.-L. Sun, F. Zhou, and Z.-X. Zhao, "Superconductivity at 55 K in iron-based F-doped layered quaternary compound Sm[$O_{1-x}F_x$]FeAs," *Chinese Physics Letters*, vol. 25, no. 6, pp. 2215–2216, 2008.

[162] F.-C. Hsu, J.-Y. Luo, K.-W. Yeh, T.-K. Chen, T.-W. Huang, P. M. Wu, Y.-C. Lee, Y.-L. Huang, Y.-Y. Chu, D.-C. Yan, and M.-K. Wu, "Superconductivity in the PbO-type structure α-FeSe," *Proceedings of the National Academy of Sciences*, vol. 105, no. 38, pp. 14262–14264, 2008.

[163] J.-F. Ge, Z.-L. Liu, C. Liu, C.-L. Gao, D. Qian, Q.-K. Xue, Y. Liu, and J.-F. Jia, "Superconductivity above 100 K in single-layer FeSe films on doped $SrTiO_3$," *Nature Materials*, vol. 14, pp. 285 EP –, 2014.

[164] Q. Si, R. Yu, and E. Abrahams, "High-temperature superconductivity in iron pnictides and chalcogenides," *Nature Reviews Materials*, vol. 1, pp. 16017 EP –, 2016.

[165] K.-W. Yeh, T.-W. Huang, Y.-l. Huang, T.-K. Chen, F.-C. Hsu, P. M. Wu, Y.-C. Lee, Y.-Y. Chu, C.-L. Chen, J.-Y. Luo, D.-C. Yan, and M.-K. Wu, "Tellurium substitution effect on superconductivity of the α-phase iron selenide," *Europhysics Letters*, vol. 84, no. 3, p. 37002, 2008.

[166] R.-H. Yuan and N.-L. Wang, "Optical spectroscopy studies on $FeTe_{1-x}Se_x$ and $A_xFe_{2-y}Se_2$ (A=K, Rb, Cs): a brief overview," *Chinese Physics B*, vol. 22, no. 8, p. 87404, 2013.

[167] P. K. Maheshwari, V. R. Reddy, and V. P. S. Awana, "Heat capacity and Mössbauer study of self-flux grown FeTe single crystal," *Journal of Superconductivity and Novel Magnetism*, vol. 31, no. 6, pp. 1659–1663, 2018.

[168] T. Konstantinova, L. Wu, M. Abeykoon, R. J. Koch, A. F. Wang, R. K. Li, X. Shen, J. Li, J. Tao, I. A. Zaliznyak, C. Petrovic, S. J. L. Billinge, X. J. Wang, E. S. Bozin, and Y. Zhu, "Photoinduced dynamics of nematic order parameter in FeSe," *Phys. Rev. B*, vol. 99, p. 180102, 2019.

[169] K. S. Novoselov, A. K. Geim, S. V. Morozov, D. Jiang, Y. Zhang, S. V. Dubonos, I. V. Grigorieva, and A. A. Firsov, "Electric field effect in atomically thin carbon films," *Science*, vol. 306, no. 5696, pp. 666–669, 2004.

[170] H. W. Verleur, A. S. Barker, and C. N. Berglund, "Optical properties of VO_2 between 0.25 and 5 eV," *Phys. Rev.*, vol. 172, pp. 788–798, 1968.